Improving Speed of Transmission Line Protection: Exploring the Use of Dynamic Phasors, Transients, and Incremental Components

By

Jagannath Wijekoon

A thesis submitted to the Faculty of Graduate Studies of
The University of Manitoba
in partial fulfillment of the requirements of the degree of

DOCTOR OF PHILOSOPHY

Department of Electrical and Computer Engineering
University of Manitoba
Winnipeg, Manitoba

Abstract

High penetration of inverter-based resources (IBRs) in modern power grids reduces system inertia and short circuit levels, emphasizing the need for fast and reliable transmission line protection to maintain grid stability. This thesis presents novel algorithms to improve the speed and reliability of line distance protection and faulted phase selection.

This thesis explores two new approaches to improve the speed of line distance protection. The first algorithm uses the dynamic phasor model of a transmission line and the dynamic phasors of the measured currents and voltages to estimate the impedance from the relay location to the fault point. The second line protection algorithm uses the Clarke equivalent networks of a transmission line and the Clarke components of instantaneous incremental currents to estimate the inductance and the resistance from the relay location to the fault point and compare them against the reach settings. The algorithm employs least squares estimation to determine fault loop inductance and resistance. This algorithm is faster than the traditional phasor-based protection algorithms and remains consistent irrespective of fault location and fault resistance while maintaining equal or better dependability and security.

The thesis also examines the problem of determining fault type and faulted phases and proposes two new algorithms. The first algorithm uses current transients in a selected frequency band. A set of indices is computed considering various ratios of the rate of change of the Clarke components of these bandpass-filtered currents. The algorithm makes the decisions based on the values of these indices calculated within a short time window of 0.75 ms after detecting a fault. The second algorithm determines the faulted phases based on the ratios of the rate of change of instantaneous

incremental currents computed using a pair of phases at a time, offering simpler implementation and reliable identification within 6 ms.

The performance of the proposed algorithms was validated through extensive simulation studies. The new protection algorithms presented in this thesis can improve the speed of operation of transmission line protection without compromising reliability and requiring expensive highly specialized hardware.

Use of Copyrighted Material

I hereby acknowledge the use of content from the following publications during the preparation of this thesis with the permission of all co-authors. Only the contents of the publications where I am the first author are included in the main text of this thesis.

Publication in Elsevier Journals

- **J. Wijekoon**, and A.D. Rajapakse, "Fast Transmission Line Protection Using Instantaneous Clarke Components," in *Electric Power Systems Research*, *(Accepted for Publication).*
- **J. Wijekoon**, and A.D. Rajapakse, "Instantaneous incremental current-based faulted phase selection algorithm," in *Electric Power Systems Research*, vol. 220, pp. 1-12, Jul. 2023.

Publication in IET Journals

- **J. Wijekoon**, and A. D. Rajapakse, "Investigation of using dynamic phasors for improving the speed of distance protection," in *IET Generation, Transmission & Distribution*, vol. 16, no. 16, pp. 3282–3296, Jun. 2022.

Publication in IEEE Journals

- **J. Wijekoon**, A. D. Rajapakse and N. M. Haleem, "Fast and Reliable Method for Identifying Fault Type and Faulted Phases Using Band Limited Transient Currents," in *IEEE Transactions on Power Delivery*, vol. 36, no. 5, pp. 2839-2850, Oct. 2021.

Patents

- A. D. Rajapakse, N. M. Haleem, and **J. S Wijekoon**, "Method for determining conductors involved in a fault on a power transmission line and fault location using local current measurements," US11971440B2, April 30, 2024.

Acknowledgments

Firstly, I would like to express my sincere gratitude to my advisor, Prof. Athula Rajapakse, for his continuous support throughout my Ph.D. program. It has been an honor and a privilege to work under his guidance.

I would also like to thank the internal committee members, Prof. Shaahin Filizadeh, Prof. BingChen Wang, and Dr. Nuwan Perera, for their valuable feedback on my research work. Additionally, I extend my thanks to the external examiner, Prof. Tarlochan Sidhu, for critically reading my thesis and providing insightful suggestions.

My appreciation extends to the University of Manitoba, the Natural Sciences and Engineering Research Council (NSERC) of Canada, Mitacs, ERL Phase Power Technologies, and Kalkitech Pvt. Ltd for funding this research.

I am grateful to all my instructors for the invaluable knowledge they imparted during the coursework. I also thank the staff of the Electrical and Computer Engineering Department for their unwavering support. My heartfelt thanks go to all my friends in Winnipeg for their encouragement and support over the years.

A special thank you goes to my wife, Rashmi Boragolla, for her support and patience throughout my graduate studies. Finally, I extend my deepest gratitude to my parents. Without their encouragement, I would not have achieved this milestone.

Contents

List of Tables

List of Figures

List of Abbreviations

AC	Alternating Current
ADC	Analog-to-Digital Converter
BPF	Band Pass Filter
CCT	Critical Clearing Time
CHIL	Control Hardware In the Loop
CSV	Comma Separated Values
CT	Current Transformer
DC	Direct Current
DFT	Discrete Fourier Transform
DP	Dynamic Phasor
DRTS	Digital Real Time Simulator
EMT	Electro-Magnetic Transient type
EMTDC	Electromagnetic Transients including DC
FACTS	Flexible AC Transmission Systems
GAM	Generalized Average Model
GNSS	Global Navigation Satellite System
GOOSE	Generic Object-Oriented Substation Events
HV	High Voltage
HVDC	High Voltage DC
IBR	Inverter Based Resources
IEC	International Electrotechnical Commission
IEEE	Institute of Electrical and Electronics Engineers
JA	Jiles-Atherton
KCL	Kirchoff's Current Law
KVL	Kirchoff's Voltage Law
LAN	Local area network
LLS	Linear Least Squares
LPF	Low Pass Filter

MFLOPS	Million Floating Points Per Second
PM	Permanent Magnet
PSCAD	Power System Computer Aided Design
PT	Potential Transform
QUAD	Quadrilateral
ROCOC	Rate Of Change Of Current
ROCOIC	Rate Of Change Of Incremental Current
RPM	Revolutions Per Minute
SV	Sampled Values
TKF	Taylor Kalman Filter
TWLS	Taylor Weighted Least Square
WTG	Wind Turbine Generator

Chapter 1

Introduction

1.1 Background

An electrical power system is a complex network of electrical components working in synchronism to generate, transmit, and distribute power. The main components of a power system include generators, transmission lines, transformers, and loads. Generation of electric power is carried out wherever it achieves the most economical generation cost, and the generated power is transferred to load centers using the transmission systems while the distribution systems carry the power to the furthest customer using an appropriate level of voltage.

The primary goal of a power system is to provide electricity to the customers at an acceptable level of reliability, quality, safety, and price. Therefore, a power system must be properly designed and maintained to limit the number of faults that disrupt the continuous supply of power. Regardless of how well a power system is designed, faults cannot be completely avoided. Factors such as lightning discharges, ice buildup, vandalism, deterioration of insulators, and contact with tree branches are some of the principal causes of faults [1]. These faults can generate fault currents with a very high magnitude which could be hazardous to both the equipment and humans.

Furthermore, frequent interruptions and system-wide blackouts caused by cascading fault events could potentially minimize the return on the investment made in developing the power system. Moreover, a sustaining fault is likely to cause the individual generators in a power station, or groups of generators in different stations to lose synchronism and fall out of step resulting in the consequent splitting of the system. To avoid these situations, it is imperative to have a properly designed and reliable protection system in place.

The purpose of a protection system is to prevent or minimize damage to the system and people during faults and abnormal operating conditions. This is achieved by swiftly isolating the directly affected part or power system element from the rest of the system. The healthy sections of the power system must not be disconnected in this process to minimize unnecessary interruptions to customers. A properly designed protection scheme should be reliable, sensitive, fast, simple, and economical. A typical protection system consists of measuring devices such as current transformers (CT) and potential transformers (PT), protection relays, and interrupting devices such as circuit breakers as shown in Fig 1.1.

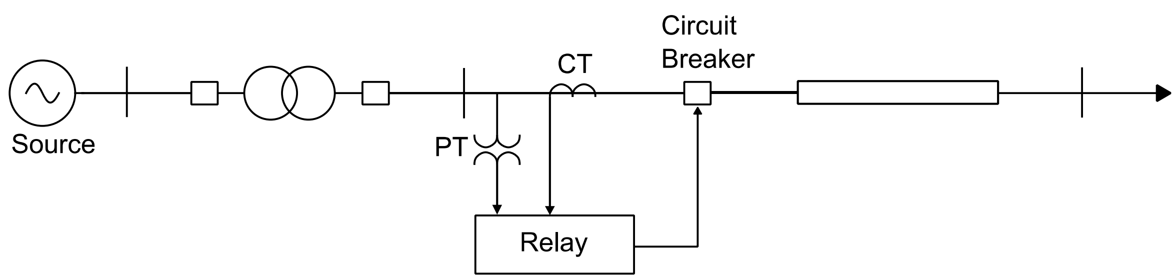

Fig 1.1 Typical Elements of a Protection System

1.2 Transmission Line Protection

Transmission lines play a pivotal role in power systems by transporting bulk power generated at generating stations to urban load centers. Transmission line protection emerged at the beginning of the twentieth century with the introduction of the first electromechanical overcurrent relay, which was introduced in 1902 [2]. Since then, the technologies associated with transmission line protection have developed into a massive industry. Most of the transmission line protection schemes were developed in the first few decades after the introduction of overcurrent protection as the preferred method for transmission line protection. These principles are still applied in protection schemes today, even though the technology used to implement these principles has changed substantially.

At present, transmission line protection methods can be categorized into two main categories. They are phasor-based methods and non-phasor-based methods. Phasor-based methods include methods such as distance protection and line current differential methods. Methods based on traveling waves and incremental quantities fall into non-phasor-based methods.

1.2.1 History

The earliest relays were all electromechanical and based on the over-current principle. These devices had to detect a fault based on the torque generated by the fault current. Upon detection of a fault, the relay energizes a trip coil of the associated circuit breaker to interrupt the fault current. Due to its inherent delays and lack of sensitivity, over-current relays were replaced with differential relays, which needed a pilot wire connection to convey the information from one end of the feeder to the other end. As a result, the distance relaying principle was introduced in 1923 [2], which measures the apparent line impedance at the relay point, which is proportional to the physical distance to the fault. Using only the locally measured currents and voltages, a distance relay responds to a fault that occurs inside a predetermined reach, set by the user [3]. Selective and dependable tripping, simple time coordination, fast operation, and the ability to provide both primary and backup protection from the same scheme are some of the advantages provided by distance protection. These advantages led to the widespread adoption of distance relays for the protection of high-voltage networks. Ideally, this reach is independent of the fault current level, pre-fault load, fault type, or fault resistance. However, these factors affect the fault coverage in practice.

Distance relays were implemented using electromechanical relays until the 1940s [2]. These electromechanical distance relays implemented in the form of induction cup Mho relays achieved high accuracy [4]. Therefore, Mho relays are used as starting units in most distance relay schemes to this day. Static relays were introduced in the 1940s with the advent of transistors. This led the way to the implementation of different distance protection schemes. Static relays allowed the designers to have full control over the balance between speed and accuracy in the designs. Static relay technology was quickly replaced by numerical protection relays in the 1980s. The concept of sampling and holding allowed the switch from static relays to numerical relays. Initially, the performance of numerical relays was limited by their sampling and processing rates even though numerical relays delivered new functions and advantages. Modern microprocessor-based distance relays with powerful processors use phasors calculated within a sub-cycle data window such as a half-cycle window.

1.2.2 Distance Protection

Modern-day distance relays calculate the apparent impedance and the fault location using sampled voltage and current signals. The impedance seen by the relay is proportional to the distance between the fault and the relaying point.

Distance relay characteristics are usually presented as a region in the R-X plane. In the R-X plane, the protected line is represented by a straight line drawn from the origin to the point corresponding to the impedance of the line in steady-state. The impedance reach or operating characteristics are represented by a fixed shape. At normal operation, the impedance seen by the relay is the load impedance whereas, during a fault, the impedance moves into the area of the operating characteristic of the distance relay. The process is depicted in Fig 1.2. Based on the shape of characteristics the distance relays are categorized. The distance relays started as concentric elements and then evolved into other characteristics such as offset impedance, Mho, Mho polarized, reactance, and quadrilateral characteristics, some of which are presented in Fig 1.3. Out of these, the Mho relay is the most commonly used type of distance relay due to its advantages. Apart from that, polygonal and quadrilateral characteristics are particularly useful for short lines.

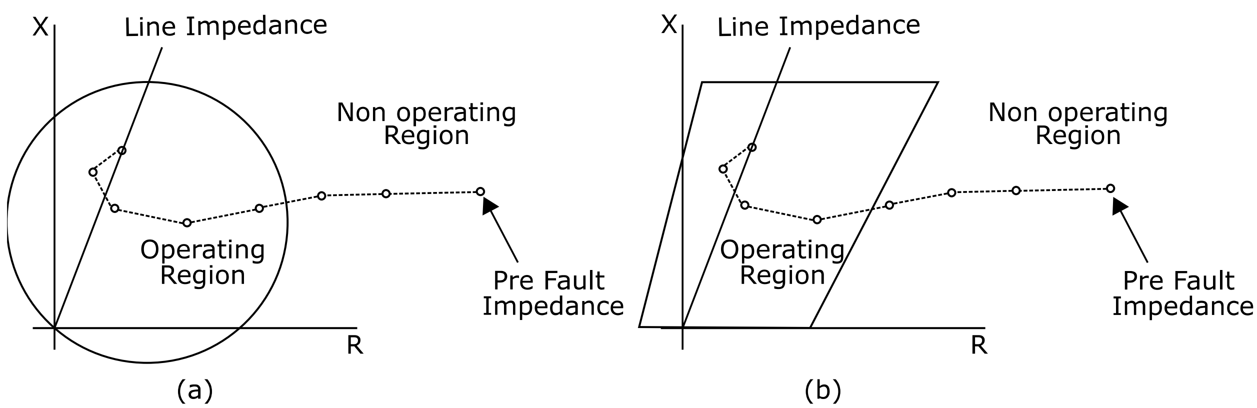

Fig 1.2 Impedance Trajectory during a Fault (a) Mho Relay, (b) Quadrilateral relay

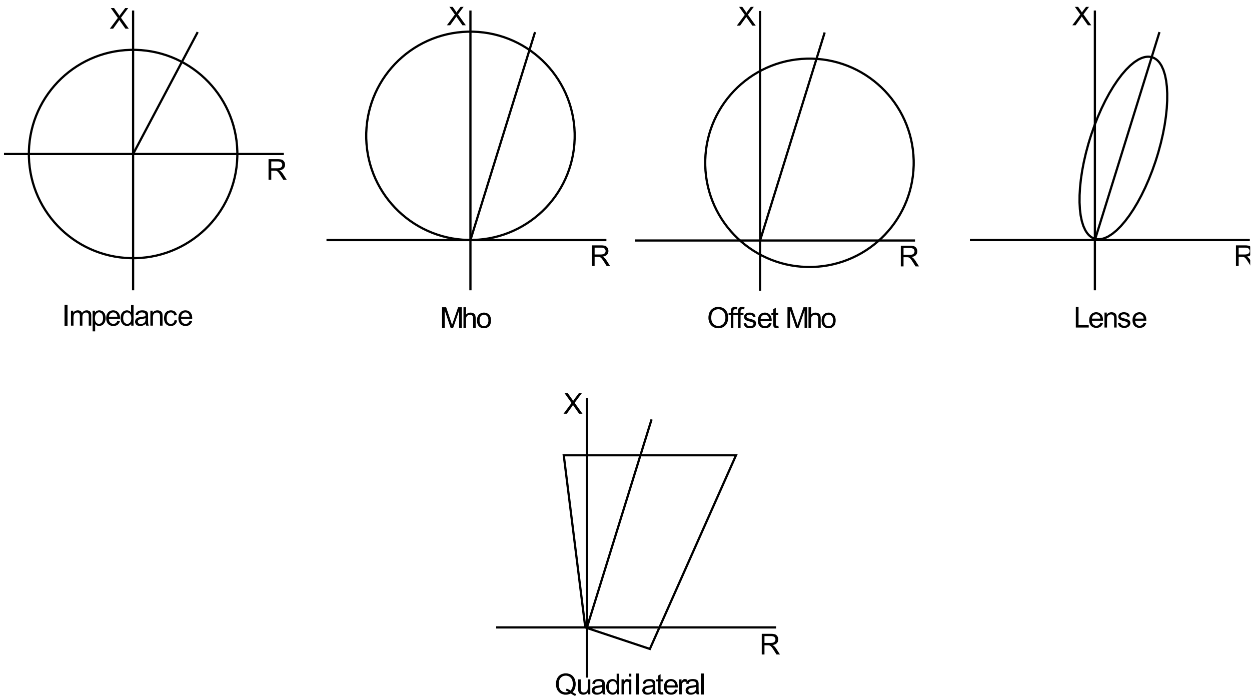

Fig 1.3 Different Types of Distance Relay Characteristics

Modern distance relays typically use 6 fault loops: three ground loops (AG, BG, CG), and three phase loops (AB, BC, and CA) by selecting the appropriate voltage and current combination for each distance element [3]. A simple impedance calculation does not constitute a distance relay. Practical distance relays include extra functions such as voltage polarization, phase identification, load encroachment supervision, power swing blocking, and other supervisory functions such as loss-of-potential, overcurrent supervision, and open pole supervision to address several operational issues and improve performance. The typical steps involved in the digital implementation of a distance relay are depicted in Fig 1.4.

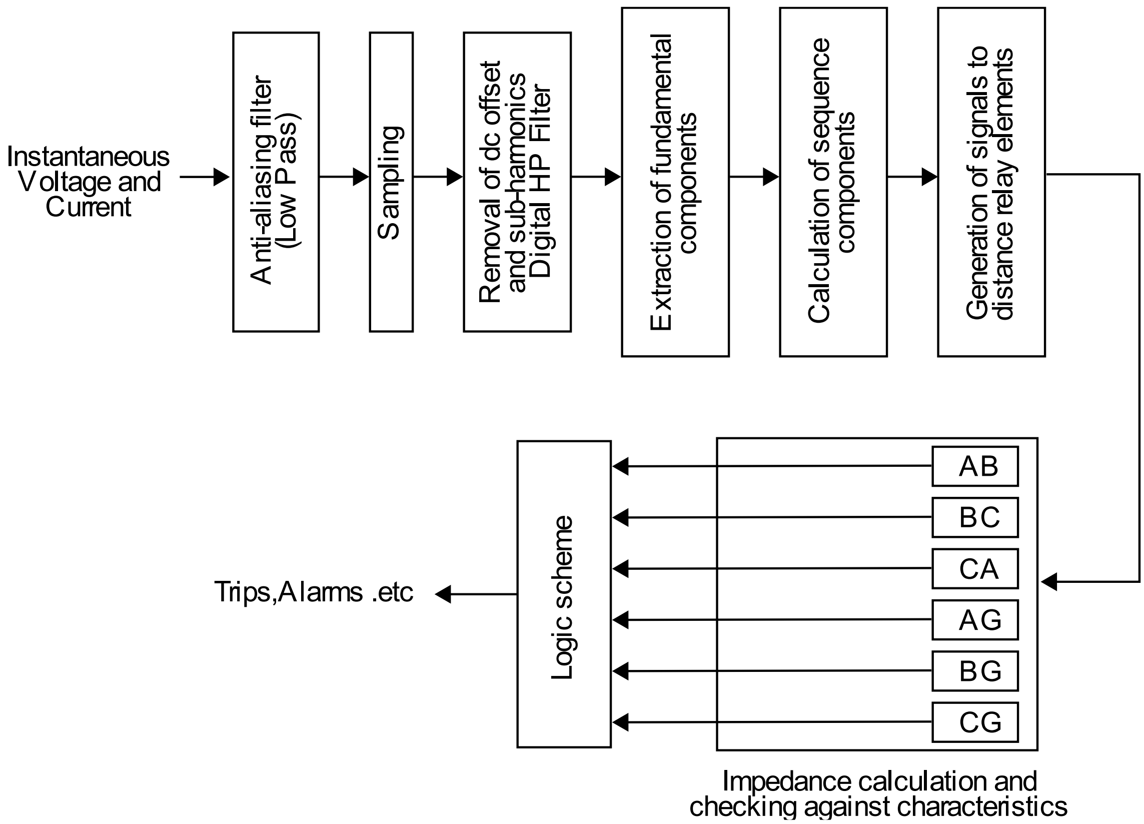

Fig 1.4 Main Processing Steps in a Digital Distance Relay

A trip decision made in a distance relay is not solely dependent on the distance calculation logic. Several other supervisory functions play a major role in deciding whether to issue a trip signal or not. The operating time of these major supervisory functions contributes to the time it takes to issue a trip signal in distance relaying algorithms in addition to the distance calculation time. If the HV circuit breaker operating time of 2 – 3 cycles is considered [5], the typical fault clearance time would be in the range of 3 – 4.5 cycles after considering the time of 1 – 1.5 cycles [5] required by a traditional phasor-based relay to issue a trip signal. The various supervisory functions and extra logic used in practical distance relays are described in the following sections.

1.2.2.1 Voltage Polarization

The primary use of voltage polarization is to ensure a correct directional response for close-up short circuit faults both in the forward and reverse direction, where the fault-loop voltage sensed by the protection relay may be very low. Therefore, instead of using the loop voltage for polarization, several other methods are used in practice.

1) Cross Polarization

   Cross polarization uses voltages from healthy phases. For example, a relay may use the BC voltage in the AG fault loop measurement since BC voltage does not collapse during a Phase-A-to-Ground fault and is shifted by 90^{o} with respect to the Phase-A voltage. Positive-sequence polarization is a form of cross-phase polarization.

2) Memory Polarization

   Memory polarization uses the pre-fault voltage for polarization. The principle is founded on the observation that large synchronous generators do not change their angular position quickly during a fault. Hence the angle of the pre-fault voltage is an accurate representation of the angle of the fault voltage even if the fault voltage collapses to zero.

3) Mixed Mode Polarization

   This uses a combination of voltage during and before a fault. It has the benefit of providing polarization for instantaneous tripping (memory action) and for time-delayed trips when the memory part of the polarization signal expires. Memorized positive-sequence voltage is the most popular way of polarization in modern distance relays.

1.2.2.2 Phase Selection

As mentioned earlier, modern distance relays use six fault loops (AG, BG, CG, AB, BC, and CA) and select which loop or loops to operate based on the fault type [3]. Even though this method accurately calculates the distance in the faulted loops, it could lead to an undesirable response in healthy fault loops. Therefore, a phase selection logic is required to be implemented in a distance relay to allow the faulted loops to operate while restraining the healthy fault loops. Furthermore, accurate phase selection enables single-pole tripping and reclosing schemes by differentiating single-phase faults and multi-phase faults. Apart from that, phase selection schemes block specific distance elements during some faults. For example, the phase-selection scheme can block the Phase-to-Ground distance element during a Phase-to-Phase-to-Ground fault [6]. Hence faulted phase selection plays a major role among the supervisory functions in generating accurate trip signals in distance relays. The angle between the negative sequence current and the zero sequence or incremental positive-sequence current is a very fast and reliable indicator of the fault type and is commonly used in many phasor-based distance relays.

1.2.2.3 Load Encroachment Supervision

In some situations, the impedance of the load can be less than the impedance of faults. Therefore, during these situations, there may be an overlap between the protection zone and the load areas which could lead to trip conditions in heavily loaded long lines. A load-encroachment characteristic intentionally blocks a distance element during load conditions to allow applications on long, heavily loaded lines. One way to avoid maloperation due to load encroachment is to change the characteristic shape of the impedance tripping zone. However, this approach reduces the coverage for certain types of resistive faults. The second approach is implementing load blinders. When the measured impedance is within the load blinder region, the over-reaching distance elements are blocked from tripping.

1.2.2.4 Power Swing Blocking

A power swing may cause the apparent impedance to encroach on the distance element characteristic. A power swing blocking element is used to assert a blocking signal if the apparent impedance traverses the impedance plane at a speed indicative of a swing (a slow trajectory). During a fault, the impedance traverses the impedance plane almost abruptly. Blinder schemes are implemented to detect power swing conditions. These can be either a) Single Blinder Schemes or b) Double Blinder Schemes.

Single blinder schemes have a right and a left blinder and detect unstable power swings when the time interval required to cross the distance between the right and left blinders exceeds a minimum time setting. Double blinder schemes measure the time that it takes the impedance trajectory to cross the distance between the outer and inner blinders. A power swing is detected when the measured time interval is longer than a set time delay.

1.3 Current Challenges and Existing Solutions

The protection of transmission lines has always been a major concern for utilities due to its crucial role in power transmission from generation centers to urban load centers. Even though these high-voltage transmission systems are designed to be highly reliable, faults do occur due to a variety of unavoidable reasons. The continuous expansion of power systems in scale and complexity has compelled utilities to operate transmission lines at their maximum capacity. This has been intensified by factors such as economic, right-of-way, and environmental concerns.

Therefore, identifying and clearing faults in transmission lines accurately and promptly has become of utmost importance to maintain the stability of power systems [7] and to prevent a fault in a single element from evolving into a system-wide blackout. The need for accurate operation of protection relays has been further intensified since the transmission lines are among the power system components with the highest fault incidence rate, [8] mainly due to their exposure to the environment.

In a digital distance relay, the impedance seen by the relay is calculated from the fundamental frequency component of the voltage and current signals. The accuracy of the impedance estimation depends on how accurately the fundamental components are extracted from the signal samples. The process of sampling and extracting phasor components involves filtering which incorporates a delay. Since the impedance is a phasor quantity, it takes time for the impedance to change from a load condition value to a fault condition value which directly affects the fault-clearing time. This inherent delay is common to the phasor-based faulted phase identification schemes as well.

The rapid increase of inverter-based resources (IBR) is creating new challenges to phasor-based distance and faulted phase identification schemes. Typically, distance relays use some form of voltage polarization to provide coverage for close-in faults. This provides expanded coverage, and the expansion is proportional to the source impedance behind the relay [9]. Since the short circuit currents in IBRs depend on the control system, the source impedance behind the relay is dependent on the control system of the IBR. Therefore, the expansion of the mho circle can be anywhere on the R-X plane for a forward fault threatening the reliability of the protection system. Furthermore, a distance relay operation is supervised by some minimum phase current. If the IBR output current drops below this minimum value before the relay's inherent or intentionally added time-delay that relay takes to operate, the relay will fail to trip. Apart from that, the lack of negative sequence currents during ground faults is also creating issues in distance protection schemes especially in faulted phase identification schemes that utilize the presence of negative sequence currents.

Furthermore, since renewable energy sources do not provide rotational inertia in the same way as traditional synchronous generators, high penetration of renewable energy resources can decrease the overall grid stability [10] - [12]. System inertia is the inherent response from synchronously connected generators that resists decay in frequency after a sudden loss in supply. In electricity networks, the loss of a large energy generator can cause a rapid frequency decline. The kinetic energy in synchronously connected generators slows the rate of change of frequency, providing a time interval for the quick start of the generators or cut-off loads to correct the imbalance in supply and demand [10]. On the other hand, the ability of generators to output electrical power becomes greatly restricted during the faults and the generators accelerate at a rate determined by their inertia. If a fault is not cleared within a certain time interval, commonly known as the critical clearing time (CCT), some generators can lose the synchronism with the power system. If the system operators or automatic remedial action schemes fail to take corrective action, it could lead to large-scale blackouts and potential damage to generators. Since IBRs such as wind and solar do not provide any inertia to the system, the critical clearing time is greatly reduced with the increasing penetration of IBRs to the power system. Hence, to preserve the stability of a power system with high penetration of IBRs, faults in the transmission lines need to be cleared before its consequential critical clearing time. Therefore, the need for fast protection schemes has increased with the rapid increase of IBRs.

Hence, attempts have been made in the past to improve the speed of distance protection. Some of these methods focus on faster phasor calculation and adaptive window widths to reduce the operating time of distance protection [13] - [16]. However, the accuracy of phasor estimation using a sub-cycle/adaptive data window is compromised by the initial fault transient, and the speed improvements usually come at the cost of reliability. In addition to using faster phasor calculation and adaptive window widths, phasor domain incremental quantities [17] based line distance protection has also been proposed to improve the speed of distance protection. Similar to other phasor-based methods, the speed gain is limited by the phasor calculation time. Line differential schemes have also been proposed to overcome the challenges presented by the IBR generation. Even though line current differential protection which is immune to problems faced by traditional distance protection such as power swings, load encroachment, and mutual coupling problems does not provide backup protection, and remains a less economical solution for long transmission lines due to their dependence on a reliable dedicated communication system. Apart from that, line current differential protection schemes need to address sample misalignment, CT saturation issues, high resistance faults in heavily loaded lines, and line charging currents [18].

Traveling wave-based techniques have been proposed as an alternative approach to improve the performance of distance protection systems. Traveling wave-based methods use backward and forward traveling waves generated by faults to detect and generate trip signals. Protection devices using traveling waves as relaying signals use specific algorithms to time stamp the arrival times of the traveling waves. In this aspect, traveling wave protection schemes use filters such as differentiator smoother [19], discrete wavelet transform [20], [21], Kalman filtering [20], principle component analysis [22], [23], and empirical mode decomposition to extract the desired high-frequency components from the fault induced voltage/current signals. From the time delays of arrival times, fault location can be calculated easily with high accuracy. If the topology of the power system gets more complicated, e.g. with multiple buses, adjacent lines, and parallel lines, the algorithms in the protection devices need to discriminate the reflected traveling waves from the various points with discontinuities in the topology.

However, traveling wave-based protection schemes have been known to face reliability issues in accurately detecting close-up faults due to repeated reflections leading to high-frequency transients and the inability to detect ground faults occurring at voltage zero crossing due to a lack of steep wavefronts. Furthermore, traveling wave-based methods have limitations in providing backup protection to remote lines. A more reliable double-ended traveling wave algorithm requires measurement from the remote end and thus needs a communication channel and precise time synchronization of measurements. High sampling frequencies are required by all traveling wave-based methods, typically in the vicinity of the MHz range.

Methods based on instantaneous values have also been proposed in the literature as an attractive solution [24] - [28]. These algorithms have some advantages over the traveling wave-based methods and show some potential for enhancing the speed of line protection. Unlike the traveling wave-based methods, instantaneous values-based methods do not rely on high-frequency waves, and therefore, very high sampling rates are not required. Since the instantaneous value-based algorithms are applied to the whole signal including the fundamental frequency component, they are not critically affected by the fault inception angle. However, closer analysis showed that the reported methods account only for faults in the forward direction; the response for the reverse faults has not been defined/investigated. Furthermore, methods reported in the literature [24] - [28] use arbitrary thresholds to make trip decisions and are not set up to provide backup for adjacent elements.

Methods based on instantaneous incremental components have also been proposed in the recent literature [29] - [31]. An incremental quantities-based protection scheme uses fault-generated voltage and current signals by subtracting the pre-fault steady-state signals from fault-measured signals [2]. The most commonly used method to obtain incremental components is using the measured signals taken exactly one cycle before as the instantaneous estimate of the steady-state signal [2]. Subsequently, the incremental signals are low-pass filtered to remove undesired components in the signal. An alternative approach is to use a high pass filter to filter the steady-state signal so that only the transient signal components are available.

The method in [29] considers the concept of replica current. It involves the comparison of the relay reach point incremental voltage against a calculated restraint voltage. If the fault is inside the selected reach, the relay reach point incremental voltage is greater than the restraint voltage value. Even though the method is fast, it is less dependable for faults with fault resistance. Furthermore, it requires the system impedance behind the relay, which can vary with the system topology changes, as a parameter to calculate the replica currents. Similar voltage comparison scheme-based incremental distance protection schemes have been proposed in [26], [28].

1.4 Problem Definition

The discussion presented in Section 1.3 highlighted that there is still a need to improve the speed of distance protection. The speed of existing phasor-based solutions is limited by the phasor calculation speed which is usually around a full cycle time. The traveling wave-based solutions proposed to improve the speed of distance protection face a different set of challenges which include the effect reflections, voltage zero crossings, requirement of specialized hardware, and complexity. Even though the instantaneous value-based methods provide a simpler solution than traveling wave-based methods they rely on thresholds that cannot be determined straightforwardly.

Therefore, it is important to explore solutions that improve the speed of distance protection that use only local measurements, are less complex, and do not rely on arbitrary thresholds. The efforts should include improving the speed of critical supporting functions such as phase selection as they are integral to the decision-making and impact the speed of operation.

1.5 Objectives and Contributions

The main objective of this research is to explore solutions that improve the speed of distance protection. The following contributions were made in this research while achieving this objective.

1. Development of a line distance protection algorithm with coverage for both forward and reverse faults using the dynamic phasor theory and the dynamic phasor model of a transmission line, and evaluation of the algorithm under a wide range of system conditions and fault scenarios using detailed electromagnetic transient (EMT) simulations.
2. Development of a line distance protection algorithm using the Clarke components of instantaneous incremental quantities and the Clarke equivalent networks of a transmission line, and detailed evaluation of the method through EMT simulation studies.
3. Development of a fast fault type and faulted phase selection algorithm using the transients in the Clark components of the instantaneous currents, and validation of its performance under high penetration of IBRs through Control Hardware in the Loop testing (CHIL).
4. Development of an improved fast fault type and faulted phase selection algorithm using the incremental components of the instantaneous currents and validation through EMT simulation studies.

5. Testing and verification of the line distance protection scheme and the phase selection algorithm on a larger power system with inverter-based generation.

1.6 Thesis Overview

The rest of the chapters in this thesis are arranged as follows, starting with the introduction provided in this chapter.

Chapter 2: Provides a detailed overview of the background theories used in this thesis.

Chapter 3: Investigates the concept of dynamic phasors and their applicability in distance protection. Presents a distance protection scheme developed using the dynamic phasor model of the transmission line and analyzes its performance against the standard distance protection algorithm.

Chapter 4: Implements a distance protection algorithm using Clarke equivalent networks. Detailed modeling of fault loop equations is presented. The method was validated using EMT simulations and the performance was compared against the standard distance protection algorithm.

Chapter 5: Presents a faulted phase selection algorithm developed using transients in the Clarke components of instantaneous currents. The method was validated using EMT case studies. It was further validated through a CHIL case study implemented in a Digital Real-Time Simulator (DRTS).

Chapter 6: Implements another faulted phase selection algorithm based on instantaneous incremental currents. The method was validated using EMT simulations. The method overcame some of the challenges identified during the validation process of the phase selection algorithm presented in Chapter 5.

Chapter 7: The results of the complete distance protection scheme, which combines the protection scheme proposed in Chapter 4 with the Clarke component phase selection scheme proposed in Chapter 5 and validated on a larger power system with inverter-based resources using EMT simulations, are presented.

Chapter 8: Presents the conclusions drawn from the results of this thesis and suggests topics for further research.

Chapter 2

Theoretical Background and Definitions

This thesis investigates methods to improve the speed of fault type and faulted phase selection and distance protection. The methods proposed in this thesis involve the use of (i) dynamic phasors, (ii) incremental quantities, and (iii) high-frequency current transients. The objective of this chapter is to provide an overview of transmission line protection and briefly summarize the theories used in the research. First, the transmission line theory is described followed by the theory of traveling waves. Next, the theory of dynamic phasors is summarized followed by the concept of incremental quantities.

2.1 Transmission Line Models and Traveling Waves

A system of conductors that transmit electric power from one location to another is defined as a transmission line [4]. The lumped parameter model is the simplest method to model transmission lines where the transmission lines are represented as a simple R-L circuit or as a PI circuit model depending on the length of the line [32]. In the case where high accuracy and proper representation of wave nature is required, the distributed parameter transmission line model, which provides results for a wide range of frequencies, is used.

2.1.1 Single-Phase Transmission Line Model

This section reviews the theory related to the distributed parameter model of a single-phase transmission line. The transmission line parameters, including inductance (L), resistance (R), capacitance (C), and conductance (G), are considered distributed along the transmission line, in contrast to the lumped parameter model. In this distributed model, these parameters are characterized per unit length. Fig 2.1 depicts the distributed parameter model of an incremental section of length Δz from a distance z from the terminal of a lossy transmission line.

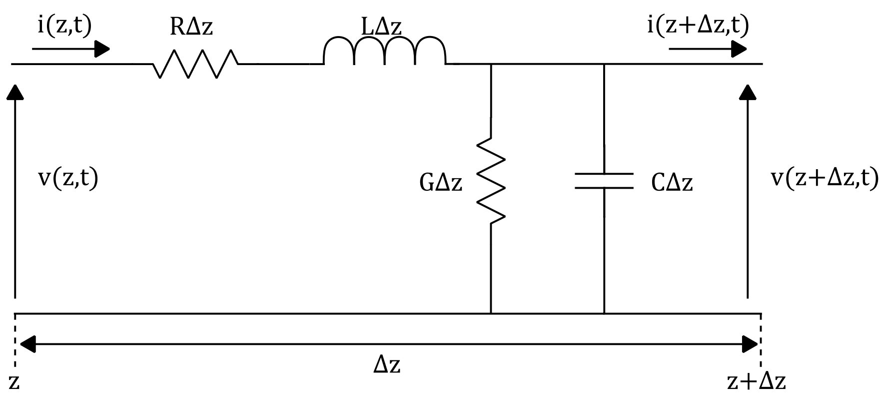

Fig 2.1 Distributed parameter model of an elemental section of a single-phase lossy transmission line [4]

The voltage and current waveforms are functions of time t and distance z is measured along the line as shown in Fig 2.1 and can be represented as given in ((2.1) and ((2.2)

$$v = v(x,t) \tag{2.1}$$

$$i = i(x,t) \tag{2.2}$$

Writing Kirchhoff's voltage law (KVL) around the loop gives:

$$v(z+\Delta z,t) - v(z,t) = -Ri(z,t)\Delta z - L\Delta z\frac{\partial i(z,t)}{\partial t} \tag{2.3}$$

Dividing both sides in ((2.3) by Δz and taking the limit as $\Delta z \rightarrow 0$ yields the first transmission line equation [33] :

$$\frac{\partial v(z,t)}{\partial z} = -Ri(z,t) - L\frac{\partial i(z,t)}{\partial t} \tag{2.4}$$

Similarly, writing Kirchhoff's current law (KCL) at the upper node gives

$$i(z+\Delta z,t) - i(z,t) = -Gv(z+\Delta z,t)\Delta z - C\Delta z\frac{\partial v(z+\Delta z,t)}{\partial t} \tag{2.5}$$

Dividing both sides in ((2.5) by Δz and taking the limit as $\Delta z \to 0$ gives the second transmission line equation given in ((2.6)

$$\frac{\partial i(z,t)}{\partial z} = -Gv(z,t) - C\frac{\partial v(z,t)}{\partial t} \tag{2.6}$$

For the sinusoidal steady-state condition with cosine-based phasors [34], ((2.4) and ((2.6) become

$$\frac{dV(z)}{dz} = -(R + j\omega L)I(z) \tag{2.7}$$

$$\frac{dI(z)}{dz} = -(G + j\omega C)V(z) \tag{2.8}$$

The wave equations for $I(z)$ and $V(z)$ are derived from eliminating the $I(z)$ and $V(z)$ from ((2.7) and ((2.8).

$$\frac{d^2V(z)}{dz^2} - \gamma^2 V(z) = 0 \tag{2.9}$$

$$\frac{d^2I(z)}{dz^2} - \gamma^2 I(z) = 0 \tag{2.10}$$

Equations ((2.9) and ((2.10) are second-order differential equations that have solutions of the form:

$$V(z) = V_0^+ e^{-\gamma z} + V_0^- e^{\gamma z} \tag{2.11}$$

$$I(z) = I_0^+ e^{-\gamma z} + I_0^- e^{\gamma z} \tag{2.12}$$

where the propagation constant is

$$\gamma = \alpha + j\beta = \sqrt{(R + j\omega L)(G + j\omega C)} \tag{2.13}$$

In a physical sense, $V_0^+ e^{-\gamma z}$ and $I_0^+ e^{-\gamma z}$ are forward-traveling waves (moving in the $+z$ direction) and $V_0^- e^{\gamma z}$ and $I_0^- e^{\gamma z}$ are backward traveling waves (moving in the $-z$ direction).

In the case of lossless transmission lines, it is permissible to neglect the series resistance (R) and shunt conductance (G).

2.1.2 Three-Phase Transmission Line Model

The equivalent circuit of an incremental section of length Δz from a distance z from the terminal of a three-phase transmission line including the ground return path is depicted in Fig 2.2. In Fig 2.2, R_1,L_1 and C_1 are the positive sequence components and R_0 , L_0 and C_0 are the zero sequence components.

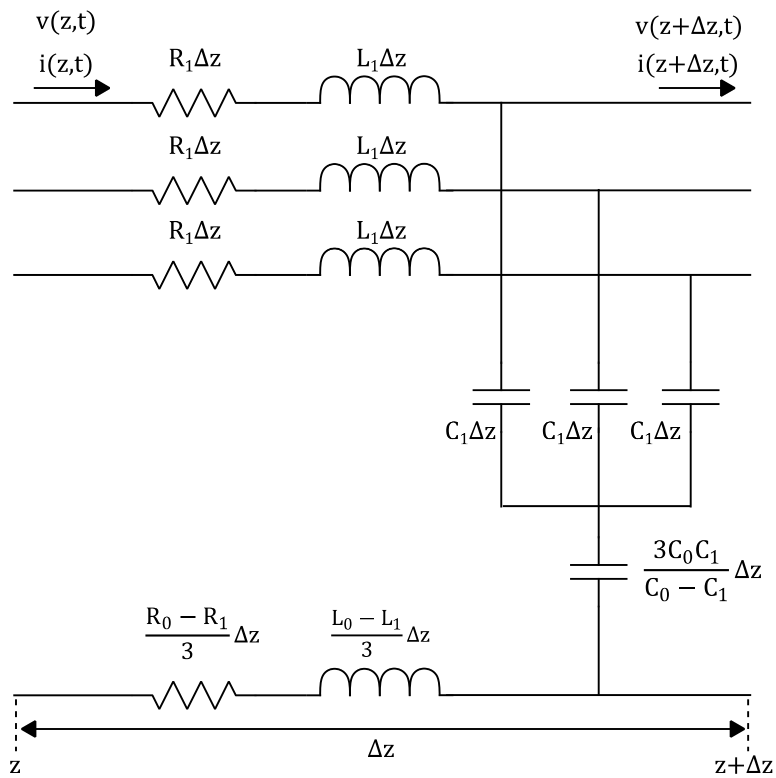

Fig 2.2 Distributed parameter model of a three-phase transmission line [4]

The following set of equations can be derived by applying the KVL to the loops formed by each conductor pair and the KCL at the junction of each capacitor [4]

$$-\frac{\partial}{\partial z}\begin{bmatrix} v_a(z,t) \\ v_b(z,t) \\ v_c(z,t) \end{bmatrix} = \frac{1}{3}\begin{bmatrix} Z_{p_s} & Z_{p_m} & Z_{p_m} \\ Z_{p_m} & Z_{p_s} & Z_{p_m} \\ Z_{p_m} & Z_{p_m} & Z_{p_s} \end{bmatrix}\begin{bmatrix} i_a(z,t) \\ i_b(z,t) \\ i_c(z,t) \end{bmatrix} \tag{2.14}$$

$$-\frac{\partial}{\partial t}\begin{bmatrix} v_a(z,t) \\ v_b(z,t) \\ v_c(z,t) \end{bmatrix} = \frac{1}{3}\begin{bmatrix} Z_{q_s} & Z_{q_m} & Z_{q_m} \\ Z_{q_m} & Z_{q_s} & Z_{q_m} \\ Z_{q_m} & Z_{q_m} & Z_{q_s} \end{bmatrix}\frac{\partial}{\partial z}\begin{bmatrix} i_a(z,t) \\ i_b(z,t) \\ i_c(z,t) \end{bmatrix} \tag{2.15}$$

where,

$$Z_{p_s} = (R_0 + 2R_1) + (L_0 + 2L_1)\frac{\partial}{\partial t} \tag{2.16}$$

$$Z_{p_m} = (R_0 - R_1) + (L_0 - L_1)\frac{\partial}{\partial t} \tag{2.17}$$

$$Z_{q_s} = \left(\frac{1}{C_0} + \frac{2}{C_1}\right) \tag{2.18}$$

$$Z_{q_m} = \left(\frac{1}{C_0} - \frac{1}{C_1}\right) \tag{2.19}$$

Applying the Laplace transform will result in the following equations.

$$-\frac{d}{dz}\begin{bmatrix} V_a(z,s) \\ V_b(z,s) \\ V_c(z,s) \end{bmatrix} = \frac{1}{3}\begin{bmatrix} Z_{p_0} + 2Z_{p_1} & Z_{p_0} - Z_{p_1} & Z_{p_0} - Z_{p_1} \\ Z_{p_0} - Z_{p_1} & Z_{p_0} + 2Z_{p_1} & Z_{p_0} - Z_{p_1} \\ Z_{p_0} - Z_{p_1} & Z_{p_0} - Z_{p_1} & Z_{p_0} + 2Z_{p_1} \end{bmatrix}\begin{bmatrix} I_a(z,s) \\ I_b(z,s) \\ I_c(z,s) \end{bmatrix} \tag{2.20}$$

$$-\begin{bmatrix} V_a(z,s) \\ V_b(z,s) \\ V_c(z,s) \end{bmatrix} = \frac{1}{3}\begin{bmatrix} Z_{q_0} + 2Z_{p_1} & Z_{q_0} - Z_{q_1} & Z_{q_0} - Z_{q_1} \\ Z_{q_0} - Z_{q_1} & Z_{q_0} + 2Z_{q_1} & Z_{q_0} - Z_{q_1} \\ Z_{q_0} - Z_{q_1} & Z_{q_0} - Z_{q_1} & Z_{q_0} + 2Z_{q_1} \end{bmatrix}\frac{d}{dx}\begin{bmatrix} I_a(z,s) \\ I_b(z,s) \\ I_c(z,s) \end{bmatrix} \tag{2.21}$$

where $Z_{p_0} = R_0 + sL_0$,$Z_{p_1} = R_1 + sL_1, Z_{q_0} = 1/sC_0$ and $Z_{q_1} = 1/sC_1$

Laplace transformed equations can be written in the general form according to (2.22) and (2.23)

$$-\frac{d}{dx}[V] = \frac{1}{3}[Z_p][I] \tag*{2.22}$$

$$-[V] = \frac{1}{3}[Z_Q]\frac{d}{dx}[I] \tag*{2.23}$$

A second-order differential equation can be written by eliminating the current matrix $[I]$

$$\frac{d^2}{dx^2}[V] - [Z][V] = 0 \tag{2.24}$$

where, $[Z] = [Z_P][Z_Q]^{-1}$

The impedance matrix $[Z]$ obtained is not a diagonal matrix due to the mutual coupling between the conductors in the three-phase system. Therefore, to diagonalize the impedance matrix, a transformation matrix has to be used which results in an independent set of modes. This transform method is known as the modal transform.

2.1.3 Modal Transform

If the transformation matrix is considered as $[T]$, a new set of voltages $[U]$ can be written as,

$$[U] = [T][V] \tag{2.25}$$

The differential equation for $[V]$ can be rewritten as,

$$\frac{d^2}{dx^2}[U] - [Z_M][U] = 0 \tag{2.26}$$

where, $[Z_M]$ is given by,

$$[Z_M] = [T]^{-1}[Z][T] \tag{2.27}$$

By selecting the appropriate transformation matrix $[T]$, $[Z_M]$ can be made a diagonal matrix which results in three independent modes. One of the most commonly used transformations is the Clarke transform. The Clarke transformation matrix is given by,

$$[T] = \frac{1}{3}\begin{bmatrix} 1 & 1 & 1 \\ 2 & -1 & -1 \\ 0 & \sqrt{3} & \sqrt{3} \end{bmatrix} \tag{2.28}$$

The use of modal components eliminates the mutual coupling between conductors. This feature has been used in the current transient-based faulted phase identification scheme implemented in Chapter 5 of this thesis. Furthermore, equivalent networks of power systems can be derived using the Clarke transformation. Different equivalent networks can be derived for each of the fault loops (AG, BG, CG, ABG, BCG, ACG, AB, BC, CA, ABC). These Clarke equivalent networks are the basis of the distance protection scheme presented in Chapter 4 of this thesis.

2.1.4 Traveling Waves

The relationship between the voltage and current of a traveling wave that propagates along a transmission line is governed by its characteristic impedance, Z_c. This can change in the case of a discontinuity where the traveling wave reaches a transition point at which there is an abrupt change in circuit constants, such as an open or short-circuited terminal or a junction with another line. A part of the energy associated with the traveling wave is transmitted into the second transmission line and the rest will be transmitted back [35]. The incoming wave is called an incident wave while the two waves generated at the transition point are called the transmitted and reflected wave, respectively.

When a fault occurs on a transmission line, the sudden discharge of line charges at the fault location generates traveling waves (transient waves). These traveling waves propagate along the transmission line at a velocity close to the speed of light. These fault-induced traveling waves provide information about the fault type, location of the fault, and fault inception angle [2]. The traveling wave phenomena can be illustrated using the Bewley Lattice diagram [35]. Fig 2.3 depicts the Bewley lattice diagram of a single-phase power system. Three sources connect at busbars A, D, and C creating a T-junction at busbar B. In Fig 2.3, $f_i(t)$, $f_t(t)$ and $f_r(t)$ are the incident, transmitted and reflected traveling waves respectively. Currents corresponding to each traveling wave are also shown in Fig 2.3. The gradient of the propagation lines is proportional to the velocity of the lines. The voltage and currents are measured at busbar A. For a relay protecting line AB located at busbar A, the forward direction is considered AB. When a Phase-to-Ground fault occurs in the forward direction at point F, the fault-generated wavefronts will travel along in both directions of the line from the fault location.

The wavefronts that travel from fault location F towards the measuring point A under a forward fault are known as backward traveling waves. These wavefronts will reflect at busbar A and travel back towards the fault location F. The wavefronts that travel toward the forward direction from the relay location are known as forward-traveling waves. When these waves reach F, part of it will reflect from the fault point F while the remaining part propagates towards busbar B. Two transmission lines with different characteristic impedances are connected at busbar B. Hence at busbar B, part of the traveling wave will be reflected, and the rest will propagate along lines 2 and 3 as transmitted waves. These transmitted waves will reflect at busbars C and D respectively.

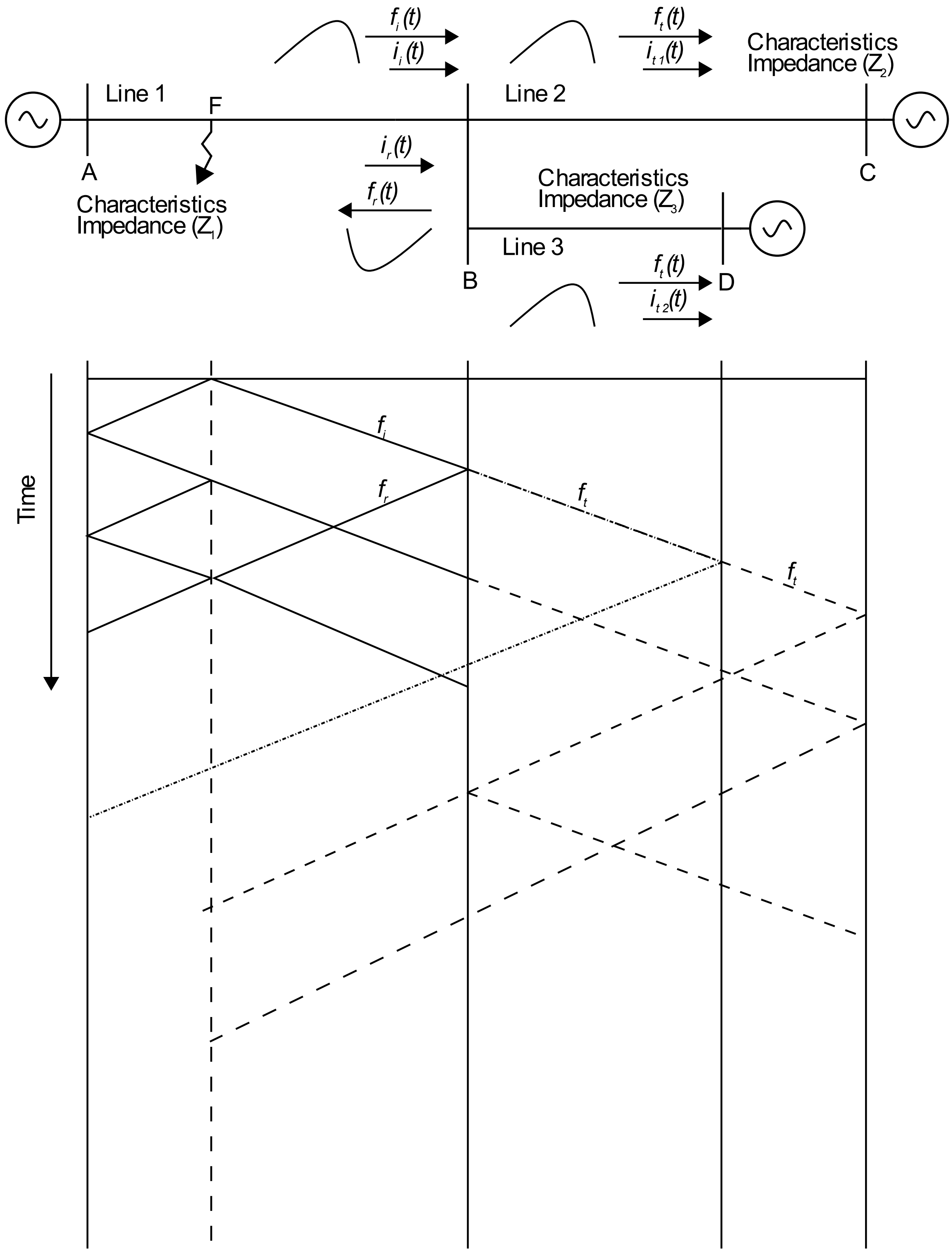

Fig 2.3 Bewley Lattice Diagram of Wavefronts Generated by a Fault

The equations governing the transmission and reflection waves can be derived as follows. The relationship between the voltages and the currents of the traveling waves is given by,

$$i_i(t) = \frac{f_i(t)}{Z_1}, i_r(t) = -\frac{f_r(t)}{Z_1}, i_{t1}(t) = \frac{f_t(t)}{Z_2}, and\ i_{t2}(t) = \frac{f_t(t)}{Z_3} \tag{2.29}$$

Since the total voltage and the current on either side of the junction must be the same,

$$f_t(t) = f_i(t) + f_r(t), and\ i_{t1}(t) + i_{t2}(t) = i_i(t) + i_r(t) \tag{2.30}$$

The transmission (G_T) and reflection (G_R) can be obtained by solving ((2.29) and ((2.30).

$$G_T = \frac{f_t(t)}{f_i(t)} = \frac{2Z_2Z_3}{Z_1Z_2 + Z_1Z_3 + Z_2Z_3} \tag{2.31}$$

$$G_R = \frac{f_r(t)}{f_i(t)} = \frac{Z_2 + Z_3 - Z_1Z_2Z_3}{Z_2 + Z_3 + Z_1Z_2Z_3} \tag{2.32}$$

In real transmission systems, the positions of the conductors are periodically swapped to reduce the mutual coupling between conductors such that each phase experiences an equal distance in each position between the sending and receiving end. This process is known as conductor transposition. However, wave interference does occur at the transition points of the transmission line. Furthermore, conductor transposition gives rise to repetitive resonance effects at certain critical frequencies [36], which could create issues in the reliability of traveling wave-based protection schemes.

2.2 Dynamic Phasors

This section presents the basics of dynamic phasors, which are used to implement a distance protection scheme using the dynamic phasor model of the transmission line. The dynamic phasor concept was first introduced into power systems in the early 90s and was referred to as "time-varying phasors" [37], [38]. Even though it was introduced into power systems in the 90s, the time-varying phasor concept has been used in communication theory for a long time. Since its introduction to power systems, the dynamic phasor concept has been used in many areas of power systems, especially as an efficient modeling approach that lies in between the traditional steady-state phasor models and the detailed electromagnetic transient models, in the area of power system dynamic analysis. The traditional phasor analysis represents sinusoidal quantities in steady-state as complex numbers using constant magnitudes and phase angles. On the other hand, in a dynamic phasor, the magnitude and phase angle are considered as time-varying quantities [39]. This allows the representation of some fast dynamics in electrical networks without significantly increasing the computational burden. Since its introduction to the power systems domain, dynamic phasors have been applied in a wide variety of areas such as modeling and simulation of power electronic devices [38], controller design in HVDC and FACTS devices [40], transient stability analysis [41], [42], and machine modeling [43], and simulation [44].

2.2.1 Basic Dynamic Phasor Theory

Consider the modulated signal $u(t)$ where the carrier frequency equals to ω_c. The modulated signal can be written as [42]:

$$u(t) = A(t)\, cos\big(\omega_c t + \delta(t)\big) \tag{2.33}$$

where $A(t)$ is the magnitude and $\delta(t)$ is the angle.

The signal $u(t)$ can be represented in the dynamic phasor domain as:

$$U(t) = A(t)e^{j\delta(t)} = A(t)\angle\delta(t) \tag{2.34}$$

where, $U(t)$ is the dynamic phasor of the modulated signal. The modulated signal $u(t)$ can be rewritten using the dynamic phasor signal $U(t)$ as given in ((2.35):

$$u(t) = \Re\left\{A(t)e^{j(\omega_c t + \delta(t))}\right\} = \Re\left\{U(t)e^{j\omega_c t}\right\} \tag{2.35}$$

Here $\Re$ is the real part of the complex signal.

The main difference between traditional phasor signals and dynamic phasor is the way it handles differential equations [42]. The derivative property of a dynamic phasor can be obtained considering the time derivative of the modulated signal $u(t)$ given in ((2.35):

$$\frac{du(t)}{dt} = \Re\left\{\frac{d}{dt}\left(U(t)e^{j\omega_c t}\right)\right\} = \Re\left\{\left(\frac{dU(t)}{dt} + j\omega_c U(t)\right)e^{j\omega_c t}\right\} \tag{2.36}$$

According to ((2.36), in the dynamic phasor domain, taking the time derivative of a signal is equal to the addition of the derivative of the dynamic phasor signal, and the $j\omega_c$ multiplied by the dynamic phasor signal. In addition to the derivative property, the dynamic phasor of a product of two time-domain signals can be obtained from a discrete-time convolution of the corresponding dynamic phasors of each signal [43].

Using the differentiation property, differential equations for the voltage across a capacitor and the current through an inductor can be written as ((2.39) and ((2.40).

$$i_c(t) = C\frac{d}{dt}v_C(t) \tag{2.37}$$

$$v_L(t) = L\frac{d}{dt}i_L(t) \tag{2.38}$$

Taking dynamic phasor of both sides of ((2.37) and ((2.38):

$$I_C(t) = C\frac{d}{dt}V_C(t) + j\omega_c C V_C(t) \tag{2.39}$$

$$V_L(t) = L\frac{d}{dt}I_L(t) + j\omega_c L I_L(t) \tag{2.40}$$

where signals $I_C(t)$, $V_C(t)$, $V_L(t)$, and $I_L(t)$ are dynamic phasor voltages and currents. The above equations have been derived for the fundamental frequency component.

2.3 Incremental Quantities

A faulted network can be solved by separately analyzing the pre-fault network and the fault network. The pre-fault network consists of load voltages and currents and the fault network contains only the fault-generated components of voltages and currents. The Thevenin source at the fault location energizes the fault network and before a fault, the equivalent network is not energized, and the voltages and currents are zero. The Thevenin source voltage is equal to the negative of the voltage at the fault point in the pre-fault network. The fault network goes through a transient state and settles into the fault steady state after the occurrence of a fault. The voltages and currents in the fault network are incremental quantities and they are valid both for the transient and steady state of the fault network. These fault-generated incremental quantities are not affected by the load and only depend on the network parameters. Only the initial conditions of the Thevenin source are affected by the power system sources and load flow. This process is depicted in Fig 2.4.

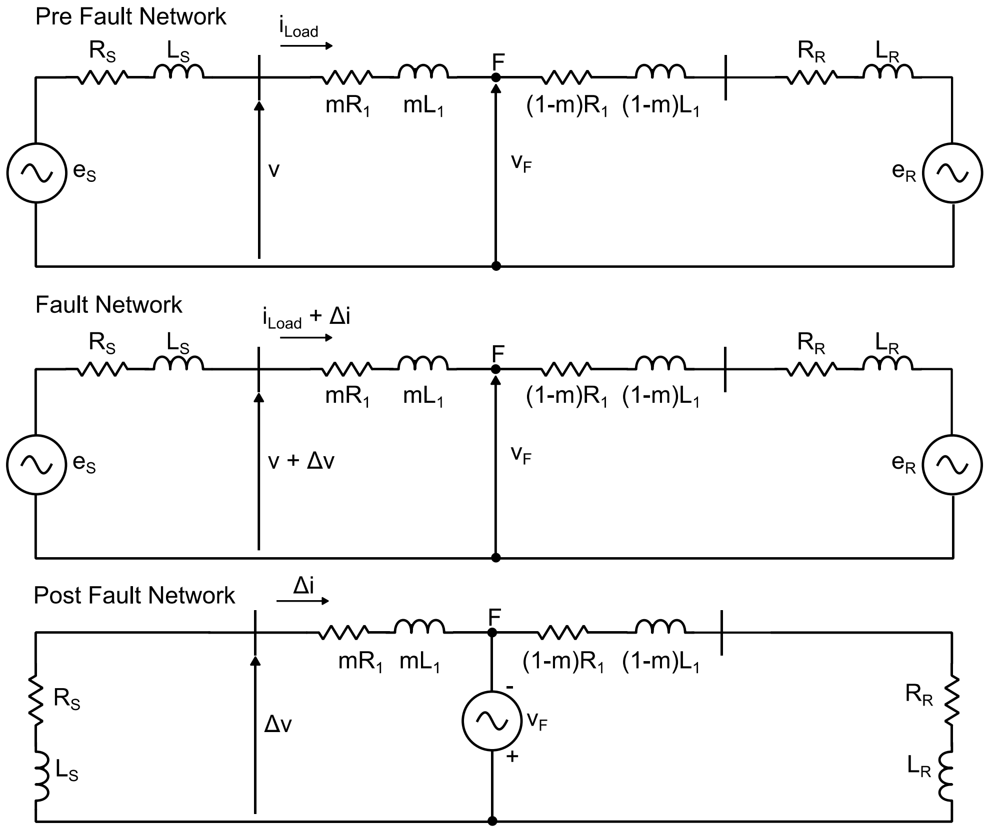

Fig 2.4 Pre-Fault, Fault, and Post-Fault Networks

The term “Incremental Quantities” is a broad term, and based on the filtering frequency range three types of incremental quantities can be defined. These are i) Instantaneous incremental quantities, (ii) Phasor incremental quantities, and (iii) High-frequency incremental quantities as depicted in Fig 2.5.

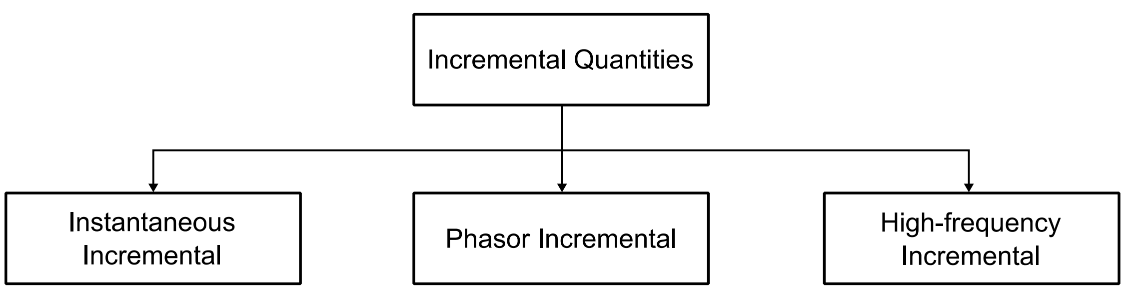

Fig 2.5 Types of Incremental Quantities Based on Filter Frequency

Phasor incremental quantities only contain the fundamental frequency component of the fault component, and it comes at the expense of the filter latency and slower operation whereas high-frequency incremental components are obtained by high pass filtering and are short-lived. On the other hand, instantaneous incremental quantities contain all the frequency components including the decaying DC component, the fault component of the fundamental frequency, and the high-frequency transients. The instantaneous incremental quantities are calculated using ((2.41).

$$\Delta q(t) = q(t) - q(t - pT) \tag{2.41}$$

where:

Δq – Instantaneous incremental quantity

q – Measured instantaneous value

T – Period of the measured quantity

p – Number of periods

The value of p is selected depending on the intended usage of the incremental quantity. Typical values would be 2 to 3 power cycles.

2.4 Summary

The main theoretical background to this research was described in this chapter. The chapter includes the transmission line theory, theory of traveling waves, dynamic phasor theory, and incremental quantities. The background knowledge provided in this chapter will be useful in understanding the details and the need for proposed methods in later chapters.

Chapter 3

Investigation of Distance Protection Using Dynamic Phasors

The concept of Dynamic Phasors (DP) is gaining attention as an efficient modeling approach that lies in between the traditional steady-state phasor models and the detailed electromagnetic transient models in power system dynamic analysis. This chapter investigates the use of dynamic phasors as a modeling approach to derive a line distance protection scheme starting from the dynamic phasor model of the transmission line. Furthermore, the chapter also explores whether the ability of dynamic phasors to preserve some of the dynamics without increasing the computational burden thus can help improve the speed of line distance protection.

3.1 Introduction

In protection applications, transmission lines are modeled in the time domain as simple RL or π circuits depending on the line length. The standard distance protection relay equations are derived assuming a lumped parameter model of the transmission line and using the quasi-stationary phasor approach where the amplitude and the phase of the signal are assumed to be in a steady state. However, this approach is invalid during the post-fault transient period since the amplitude and phase deviate from steady-state values. Therefore, there is an inherent time delay associated with the traditional phasor-based distance relays in estimating the fault loop impedance. The dynamic phasor line models can be used to accommodate the time-varying nature of current and voltage signal amplitudes and phase angles, which could lead to more accurate estimates of inductance and resistance estimates of the faulted line section during fault-generated transients.

A transmission line parameter estimation method using dynamic phasors was introduced in [45]. The authors in [45] proposed two direct methods and one indirect method to estimate the line parameters of a transmission line during a fault condition. The proposed methods were compared with the recursive least-square estimator in the discrete-time domain and with a conventional stationary phasor solution. Results revealed that the proposed methods are faster and more accurate, especially under severe signal distortions. However, the direct methods proposed by the authors only provide useful results if the sampling time is less than one-tenth of the line time constant. Even though the indirect method is more stable and provides more accurate results, it is complex. Furthermore, the authors have not considered the fault loops (Phase-to-Ground and Phase-to-Phase) when deriving the parameter estimation equation which could lead to incorrect estimation of parameters for more common asymmetrical faults.

Different methods have been proposed in the literature to estimate the dynamic phasor of a signal [46] - [48]. The concept of fast time-varying phasors was one of the earliest methods of dynamic phasor extraction methods in power system applications [46] where a transform named Blondel-Park transformation is used to extract the dynamic phasor from the time domain signal. The Generalized Averaging Method (GAM) [47] is another method that has been used since the 1990s to extract dynamic phasors from time-domain signals. However, this method does not consider the decaying DC component when extracting phasors from time-domain signals. Several papers detail the methods to estimate dynamic phasors from instantaneous measurements. An algorithm to approximate the dynamic phasors using a second-order Taylor polynomial is presented in [48]. In this approach, dynamic phasor estimation is formulated considering a truncated Taylor polynomial around the center of any observation interval and the coefficients of the Taylor expansion correspond to the estimates of the dynamic phasor and its derivatives. However, the dynamic phasor concept presented in this paper is different from the concept presented in [38] where the waveform $x(t)$ can be approximated in the interval $\tau \in (t-T, t]$ to arbitrary accuracy with a Fourier series. In [48], the dynamic phasor is understood as the complex envelope of the bandpass signal model of the oscillation, which includes the Fourier transforms of $x(\tau)$, $\tau x(\tau)$, and $\tau^2 x(\tau)$. Main drawback of this estimation method is it cannot estimate the phasors instantaneously. Therefore, to overcome this drawback and estimate the phasors instantaneously, the authors of [48] proposed a method to estimate the phasors instantaneously using Kalman filters. This method was further improved to include the DC component and higher-order harmonics [49]. However, the Kalman gain used in this method needs to be frozen at a predetermined steady state to avoid oscillations in the estimates. This steady state must be determined by simulation studies. Several other methods have been reported in the literature to estimate dynamic phasors. In [50] a Taylor weighted least square filter has been used to estimate the dynamic phasors. This method improves the accuracy at off-nominal frequencies. However, this method can only estimate the fundamental components. A double suboptimal-scaling-factor adaptive strong tracking Kalman filter was used in [51] to estimate dynamic phasor. An autoregressive moving average model-based dynamic phasor estimation method was also introduced in [52].

The Taylor-Kalman-Fourier (TKF) filter-based phasor estimation method presented in [49] has been used in several applications. In [53] the TKF filter presented in [49] has been used as the input signal to a phase comparator in a digital distance relay. The performance has been compared with the well-known Fourier and Cosine filter and the results indicated that the method presented in [49] improves the relay's steady-state and transient responses. A similar comparison has been done in [54] where the TKF filter has been compared with traditional DFT and Cosine filter methods. The results revealed that the TKF filter improves the transient performance and provides better rejection of the decaying DC component, which is a significant issue in digital distance relaying, and the TKF reaches the protection zone in the shortest time. A dynamic-phasor estimation-based fault location algorithm has been presented in [55]. This method computes the variation of resistance over time based on the fact that the power loss increases during a fault. The phasors are computed using dynamic phasor estimation. The results revealed that the dynamic phasor produced better results after applying the proposed method. However, none of the above-mentioned methods consider the modeling of the transmission line using a dynamic phasor approach. The application of the above-mentioned methods is limited to the use of phasors extracted using dynamic phasor signal models as inputs to the distance protection algorithms developed considering traditional static phasor definition [53] - [56]

3.2 Dynamic Phasor Estimation

Approximating the dynamic phasor signal using a Taylor polynomial is more commonly observed in contemporary dynamic phasor estimation methods. This approach helps to identify the fundamental component as well as the higher-order derivatives of the dynamic phasor based on the signal model. A least squares-based algorithm to approximate the dynamic phasor using a second-order Taylor polynomial is presented in [48]. Dynamic phasors are estimated by a truncated Taylor polynomial about the center of any observation interval and the coefficients of the Taylor expansion correspond to the estimates of the dynamic phasor and its derivatives. In addition to least square-based methods, Kalman filter-based methods have also been reported in the literature to extract dynamic phasors from the time-domain signals based on the Taylor polynomial signal model [51], [57]. However, none of the above-mentioned dynamic phasor estimation methods explicitly address the removal of decaying DC components in fault-generated current signals which is an important issue in protective relaying since decaying DC components can lead to oscillations in the phasor estimates causing overreach or underreach in distance relay operation. Phasor estimation algorithms based on traditional phasor definition have addressed this by including the DC component in the signal model [58] - [61] and designing steps to remove it. Therefore, a similar approach can be employed to remove the decaying DC component from the dynamic phasor estimate is essential to preserve the reliability of the protection algorithm.

A modified Taylor Weighted Least Square (TWLS) method incorporating decaying DC components in the signal model has been proposed in [62]. The method in [62] uses a second-order Taylor polynomial to model the phasor signal while modeling the decaying DC signal using a first-order Taylor polynomial. A similar approach is used in this thesis, but the representation of the phasor signal was approximated with a first-order Taylor polynomial in place of the second-order Taylor polynomial used in [62]. The use of the first-order Taylor polynomial to model the phasor signals allows the estimation of the fundamental component of the dynamic phasor and its first derivative simultaneously.

The dynamic phasor model of a power system voltage/current signal can be given as in ((3.1) where $a(t)$ is the amplitude, $\varphi(t)$ is the phase, and ω is the angular frequency of the signal $x(t)$. The term $Ce^{-\frac{t}{\tau}}$ denotes the decaying DC component where τ is the time constant.

$$x(t) = a(t)\, cos\big(\omega t + \varphi(t)\big) + Ce^{-\frac{t}{\tau}} \tag{3.1}$$

The expression in ((3.1) can be rewritten as a complex exponential function as:

$$\begin{aligned} x(t) &= \frac{1}{2}\left(p(t)e^{j\omega t} + \bar{p}(t)e^{-j\omega t}\right) + Ce^{-\frac{t}{\tau}} \\ &= \Re\left\{p(t)e^{j\omega t}\right\} + Ce^{-\frac{t}{\tau}} \end{aligned} \tag{3.2}$$

where, $p(t) = a(t)e^{j\varphi(t)}$ is the dynamic phasor of the signal and $\bar{p}(t) = a(t)e^{-j\varphi(t)}$ is the complex conjugate of $p(t)$. The dynamic phasor signal and the decaying DC component can be approximated by a first-order Taylor polynomial around a reference time of t_0 as:

$$x(t_0) = \Re\left\{\left[p(t_0) + \frac{\dot{p}(t_0)(t - t_0)}{1!}\right]e^{j\omega(t-t_0)}\right\} + C - \frac{C(t - t_0)}{\tau} \tag{3.3}$$

Assuming that the signal is sampled at a sampling frequency of f_s (at N_1 samples per cycle), consider a sample window of $N = 2N_h + 1$ samples where the center of the sampling window is considered as the reference time of the phasor estimate. Then the phasor and its first derivative can be estimated using least squares.

$$[X] = ([A]^H A)^{-1} A^H x_r \tag{3.4}$$

in which:

$[X] = \begin{bmatrix} p_1^*/2 & p_0^*/2 & p_0/2 & p_1/2 & C & -\frac{C}{\tau} \end{bmatrix}^T$ where H, T, and $*$ denotes the Hermitian, transposition, the complex conjugate and $p_1 = p'(t_0)/(1!\,f_s)$, $p_0 = p(t_0)$. The vector x_r is the vector holding $2N_h + 1$ samples.

$$x_r = [x(-N_h) \;\; x(-N_h + 1) \ldots x(0) \ldots x(N_h - 1) \;\; x(N_h)]^T$$

The matrix A is a $(2N_h + 1) \times 6$ matrix. A row in matrix A can be denoted by a_n where n goes from $-N_h$ to N_h and $\theta = \frac{2\pi}{N_1}$.

$$a_n = [ne^{-jn\theta} \quad e^{-jn\theta} \quad e^{jn\theta} \quad ne^{jn\theta} \quad 1 \quad n]$$

$$A = \begin{bmatrix} -N_h e^{-j(-N_h)\theta} & e^{-j(-N_h)\theta} & e^{j(-N_h)\theta} & -N_h e^{j(-N_h)\theta} & 1 & -N_h \\ \vdots & \vdots & \vdots & \vdots & \vdots & \vdots \\ 0 & 1 & 1 & 0 & 1 & 0 \\ \vdots & \vdots & \vdots & \vdots & \vdots & \vdots \\ N_h e^{-jN_h\theta} & e^{-jN_h\theta} & e^{jN_h\theta} & N_h e^{jN_h\theta} & 1 & N_h \end{bmatrix}_{(2N_h+1)\times 6}$$

Matrix A can be pre-calculated and stored in the memory for online phasor estimation. The amplitude, phase, and derivatives of the dynamic phasor can be obtained as:

$$\hat{a}(t_0) = 2|p_0| \tag{3.5}$$

$$\hat{\varphi}(t_0) = \angle p_0 \tag{3.6}$$

$$\hat{a}'(t_0) = 2\Re\{p_1 e^{-j\varphi(t_0)}\} \tag{3.7}$$

$$\hat{\varphi}'(t_0) = \frac{2}{\hat{a}(t_0)} \Im\{p_1 e^{-j\varphi(t_0)}\} \tag{3.8}$$

where $\Im$ denotes the imaginary component, $\hat{a}(t_0)$ and $\hat{\varphi}(t_0)$ denotes the magnitude and angle of the dynamic phasor estimates at the fundamental frequency whereas $\hat{a}'(t_0)$ and $\hat{\varphi}'(t_0)$ denotes the magnitude and angle of the estimates of the first derivative of the fundamental dynamic phasor, which correspond to the term $dU(t)/dt$ in (2.32). In Section 2.2.1, the frequency of the dynamic phasor has been defined as a constant quantity. However, during fault scenarios, the frequency starts to deviate from the steady state frequency. These frequency deviations appear as phase angle changes in the dynamic phasor.

3.2.1 Signal Model, Window Length, and Derivative Estimate of Phasor Extraction Method

The signal model used in [62] considers the second-order terms in its signal model. However, using second-order terms in the signal model necessitates the use of window lengths of at least two cycles. Although a two-cycle long window may be acceptable for applications concerned with control or electromechanical dynamics, protection applications need a faster response. The frequency response of the signal models that use the first and second-order Taylor polynomials are compared in Fig 3.1. In both cases, the decaying DC component was represented by a first-order Taylor polynomial. Even though a smoother magnitude response can be achieved by adding the second-order terms in the signal model, it needs at least a two-cycle long data window length to obtain an appropriately shaped frequency response that rejects DC and higher frequency interfering signal components as evident from Fig 3.1 (b). It is also evident from Fig 3.1 (a) that an appropriate frequency response can be obtained with window lengths shorter than two cycles for the case of the first-order signal model. These results, therefore, justify the selection of the first-order model for the phasor signal as mentioned in Section 3.2.

Fig 3.2 shows the frequency response of the first-order signal model at 4 different window lengths (1-cycle, 1.25-cycle, 1.5-cycle, and 2-cycle) over a larger frequency range. From Fig 3.2 it is evident that using a window length of 2-cycle provides the maximum rejection for higher-order harmonics compared to all the other considered window lengths. On the other hand, a 1-cycle window amplifies the second harmonic and is not suitable. The use of a 2-cycle window increases the operating time of the protection by a significant margin. As a compromise, a window length of 1.25 cycles is used for generating the main results. The use of a 1.25-cycle is not new to distance relaying. It has been used as an alternative to mimic filters in digital protective relays to remove decaying DC components [63]. The performance with a 1.5-cycle window will also be examined for comparison. Since the rectangular window provides the most accurate results for short-time windows [64], a rectangular window is used to estimate the dynamic phasors instead of using a special windowing function as in [62].

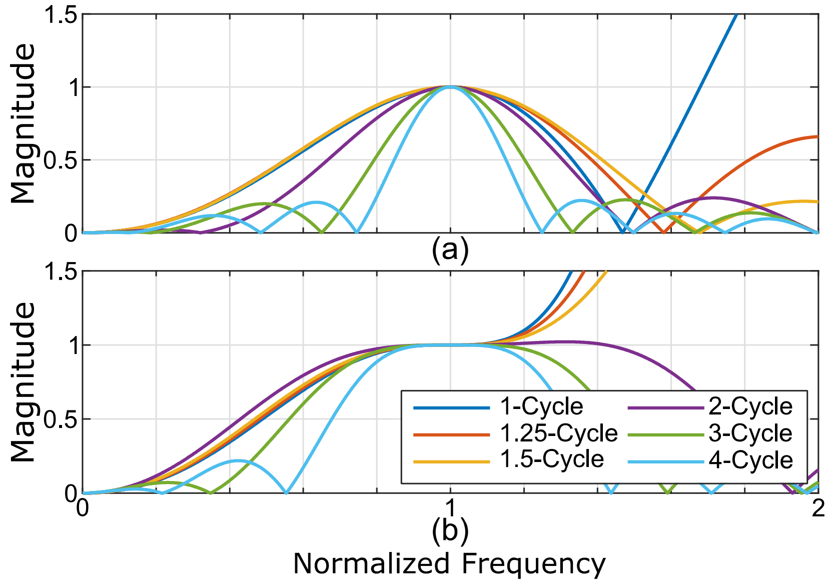

Fig 3.1 Magnitude Response for the (a) First and (b) Second-Order Signal Models at Different Window Lengths

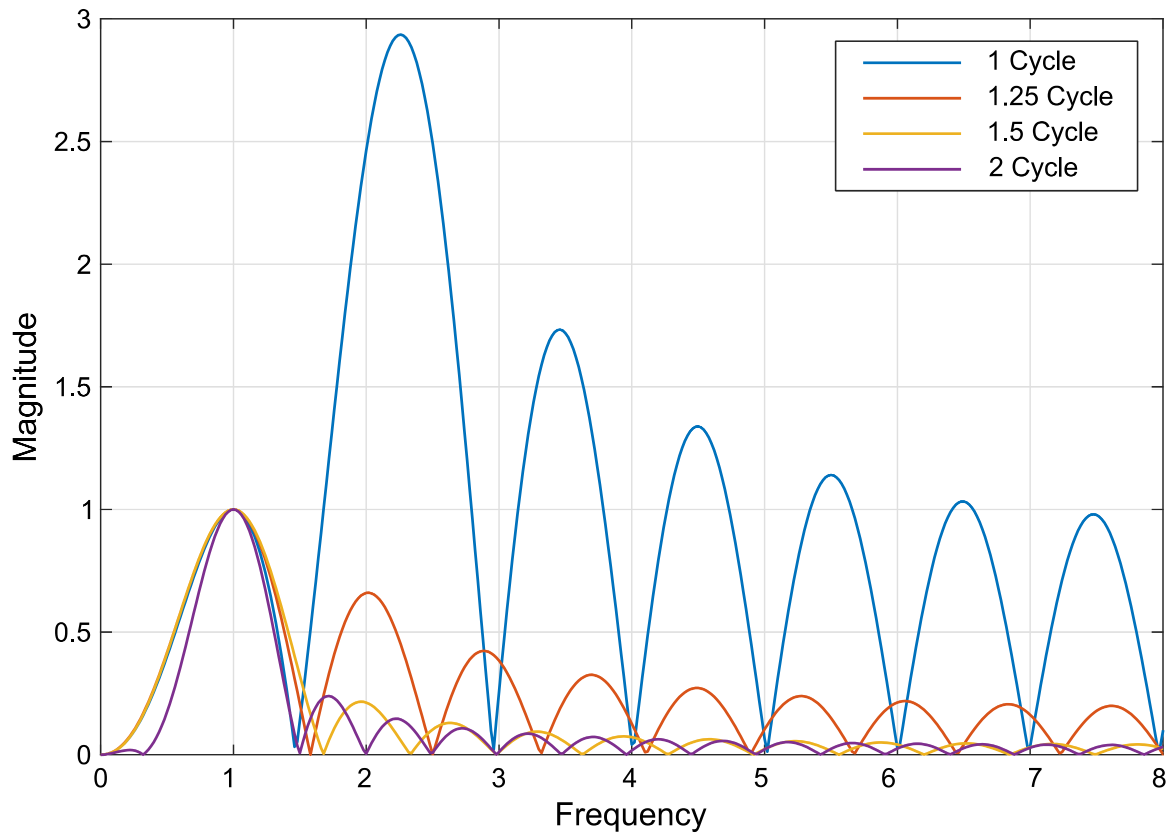

Fig 3.2 Frequency Response of the First-Order Signal Model at Different Window Lengths

Fig 3.3 (a) - (e) shows the variation of the instantaneous current signal, the real component of the fundamental phasor, the derivative of the real component, and the imaginary component of the fundamental phasor and its derivative respectively during a Phase-A-to-Ground fault. The DP estimation method is capable of correctly estimating the fundamental phasor in terms of its real and imaginary parts accurately even with a large decaying dc component in the instantaneous current signal. However, when comparing the variations of the real/imaginary components and their respective derivatives, it is evident that the derivative estimates are inconsistent during the post-fault transient period. Thus, the use of derivative estimates can result in spurious trip signals. Further investigations showed that although the dynamic phasor estimation method is capable of accurately tracking the first derivative of the signals with slowly varying amplitude/phase angles, it fails to do so during fault scenarios where current signals undergo sudden changes.

Therefore, the first-order derivatives input to the relay algorithm were calculated by differentiating the fundamental estimates instead of using the derivative estimates. Hence the derivative terms in the comparator equations were approximated with first-order differences as $\dot{x}_k = (x_k - x_{k-1})/\Delta T$ where $\dot{x}_k$ is the derivative of the estimate of the fundamental at k^{th} time step, x_k and x_{k-1} are the estimates of the fundamental components at k^{th} and $(k-1)^{th}$ time steps and ΔT is the sampling time. Although the estimated derivatives are no longer used, the first-order signal model was kept as proposed in Section 3.2, because the signal model with the first-order polynomial improves the fundamental phasor estimate, as compared to a zeroth-order model, which has also been confirmed in [48].

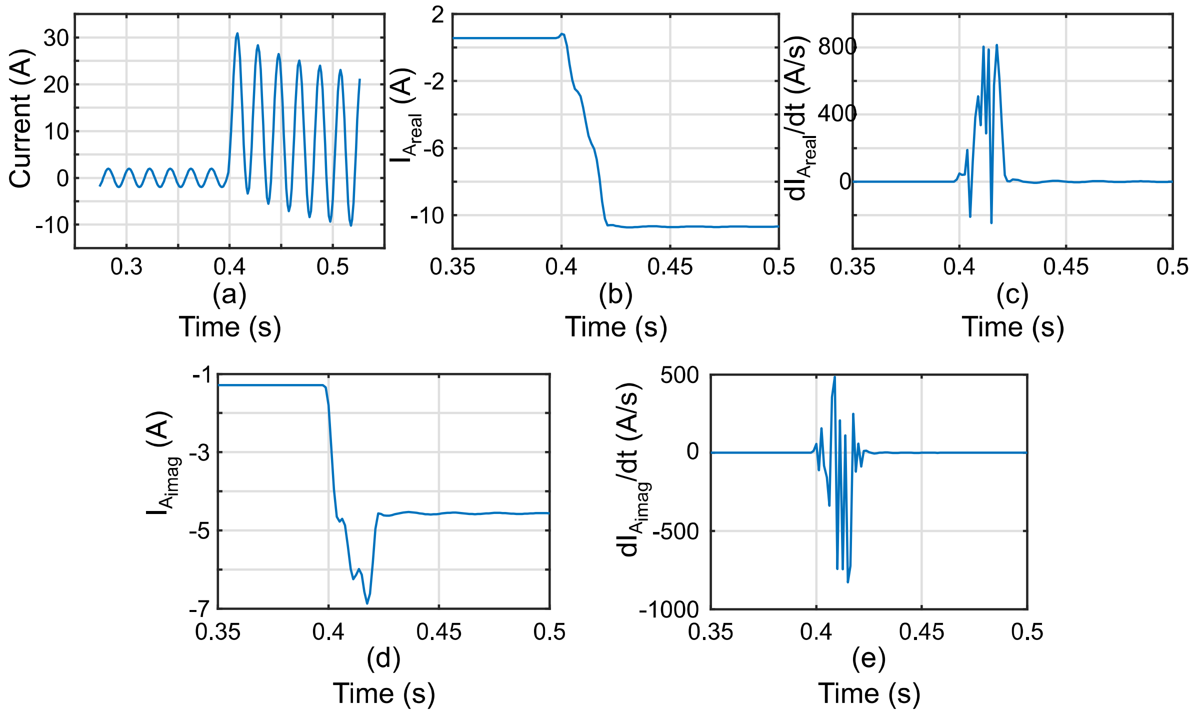

Fig 3.3 Variation Of (a) Instantaneous Current Signal (b) Real Component, (c) Derivative of The Real Component, (d) Imaginary Component, And (e) Derivative of The Imaginary Component

3.3 Dynamic Phasor Model of Faulted Transmission Lines

The fundamentals of dynamic phasors were introduced in Chapter 2. Using these fundamental principles, the dynamic phasor model of the transmission line is derived and fault loop equations for the dynamic phasor model of the transmission line are derived in this subsection.

The transmission line can be modeled using dynamic phasors as a simple R-L model, π-section model, or a T-section model. The transmission line is represented using the simple R-L model assuming it provides sufficiently accurate results under fault conditions. Typically, Phase-to-Phase and Phase-to-Ground fault loops are considered when deriving distance relay equations. A similar approach was considered when deriving the dynamic phasor-based distance relay equations. The

Phase-to-Phase-to-Ground fault loop can be treated as a special case of the Phase-to-Phase fault loop.

The following assumptions were made when deriving the fault loop equations: (i) all the considered fault scenarios are short circuits, (ii) faults were applied on a system with a single infeed, (iii) distance to a fault from the relay location is expressed by multiplier *n* (p.u) of line length, (iv) the total line resistance and inductance are assumed as *R* and *L* respectively and represented using the positive sequence values R_1 and L_1. These assumptions are similar to those made when deriving the traditional distance relay equations.

In the equations given in the following subsections, the variables denoted by simple letters refer to instantaneous values whereas the variables denoted by capital letters refer to respective dynamic phasor quantities. The instantaneous differential equation is provided for the considered fault loop first, and the respective dynamic phasor equation is presented next to present how the dynamic phasor domain equations are obtained.

3.3.1 Phase-to-Phase Fault Loop

The derivation of the dynamic phasor equation for Phase-to-Phase fault loops is demonstrated using the fault loop formed during a Phase-B-to-Phase-C short circuit as shown in Fig 3.4 (a). The fault loop is defined by the following first-order differential equation:

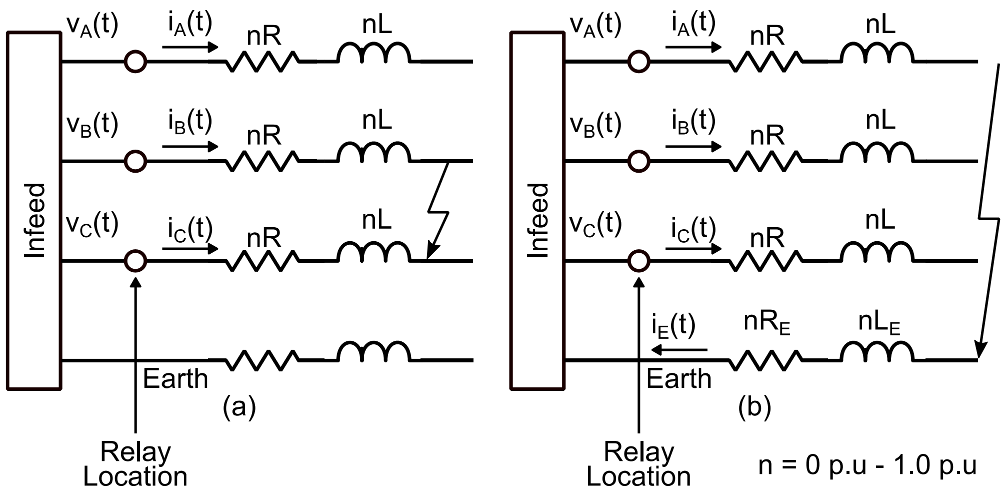

Fig 3.4 (a) Phase-B-to-Phase-C Short Circuit (b) Phase-A-to-Ground Short Circuit Fault

$$v_B(t) - v_C(t) = nRi_B(t) + nL\frac{di_B(t)}{dt} - nRi_C(t) - nL\frac{di_C(t)}{dt} \quad (3.9)$$

By writing ((3.9) in terms of the dynamic phasors and using the derivative property given ((2.36), the dynamic phasor equation of the Phase-B-to-Phase-C fault loop can be written as:

$$\begin{aligned} V_B(t) - V_C(t) = {} & nRI_B(t) + nL\frac{dI_B(t)}{dt} + j\omega nLI_B(t) - nRI_C(t) - nL\frac{dI_C(t)}{dt} \\ & - j\omega nLI_C(t) \end{aligned} \quad (3.10)$$

where $V_B(t)$ is the dynamic phasor of $v_B(t)$ and so on. Equation ((3.10) can be further simplified as:

$$V_B(t) - V_C(t) = nR[I_B(t) - I_C(t)] + nL\left[\frac{dI_B(t)}{dt} - \frac{dI_C(t)}{dt}\right] + j\omega nL[I_B(t) - I_C(t)] \quad (3.11)$$

Separating the real and imaginary parts of ((3.11) results in ((3.12) and ((3.13):

$$\begin{aligned} & V_{B(Re)} - V_{C(Re)} \\ & \quad = nR\left(I_{B(Re)} - I_{C(Re)}\right) + nL\left(\frac{dI_{B(Re)}}{dt} - \frac{dI_{C(Re)}}{dt}\right) \\ & \quad - \omega nL\left(I_{B(Im)} - I_{C(Im)}\right) \end{aligned} \quad (3.12)$$

$$V_{B(Im)} - V_{C(Im)} \\ = nR\left(I_{B(Im)} - I_{C(Im)}\right) + nL\left(\frac{dI_{B(Im)}}{dt} - \frac{dI_{C(Im)}}{dt}\right) \\ + \omega nL\left(I_{B(Re)} - I_{C(Re)}\right) \tag{3.13}$$

Here, the subscripts (Im) and (Re) represent the time-varying real and imaginary components of the dynamic phasors, and (*t*) is omitted for simplicity. Solutions for *nL* and *nR* can be obtained by solving ((3.12) and ((3.13). With $p, q \in [A, B, C]$ denoting phases, the general solution for the apparent inductance *nL* and the apparent resistance *nR* for a Phase-to-Phase fault loop can be written as,

$$nL = \frac{\lambda}{\mu - \nu} \tag{3.14}$$

$$nR = \frac{\zeta - \psi}{\mu - \nu} \tag{3.15}$$

where,

$$\lambda = \left(V_{p(Im)} - V_{q(Im)}\right)\left(I_{p(Re)} - I_{q(Re)}\right) - \left(I_{p(Im)} - I_{q(Im)}\right)\left(V_{p(Re)} - V_{q(Re)}\right)$$

$$\mu = \left(\frac{dI_{p(Im)}}{dt} - \frac{dI_{q(Im)}}{dt}\right)\left(I_{p(Re)} - I_{q(Re)}\right) + \omega\left(I_{p(Re)} - I_{q(Re)}\right)^2$$

$$\nu = \left(\frac{dI_{p(Re)}}{dt} - \frac{dI_{q(Re)}}{dt}\right)\left(I_{p(Im)} - I_{q(Im)}\right) - \omega\left(I_{p(Im)} - I_{q(Im)}\right)^2$$

$$\zeta = \left(V_{p(Re)} - V_{q(Re)}\right)\left[\left(\frac{dI_{p(Im)}}{dt} - \frac{dI_{q(Im)}}{dt}\right) + \omega\left(I_{p(Re)} - I_{q(Re)}\right)\right]$$

$$\psi = \left(V_{p(Im)} - V_{q(Im)}\right)\left[\left(\frac{dI_{p(Re)}}{dt} - \frac{dI_{q(Re)}}{dt}\right) - \omega\left(I_{p(Im)} - I_{q(Im)}\right)\right]$$

3.3.2 Phase-to-Ground Fault Loop

Deriving dynamic phasor equations for the Phase-to-Ground fault loop is demonstrated using the fault loop formed during a Phase-A-to-Ground short circuit as shown in Fig 3.4 (b) where R_E and L_E represent the earth return path resistance and inductance. Furthermore, $i_A(t)$ is the Phase-

A instantaneous current and $i_E(t)$ is the instantaneous residual current. Applying KVL for the fault loop, the first-order differential equation in ((3.16) can be obtained:

$$v_A(t) = nRi_A(t) + nL\frac{di_A(t)}{dt} + nR_E i_E(t) + nL_E\frac{di_E(t)}{dt} \tag{3.16}$$

Equation ((3.16) can be written using the dynamic phasors as:

$$V_A(t) = nRI_A(t) + nL\frac{dI_A(t)}{dt} + j\omega nLI_A(t) + nR_E I_E(t) + nL_E\frac{dI_E(t)}{dt} + j\omega nL_E I_E(t) \tag{3.17}$$

Equation ((3.17) can be further simplified as:

$$\begin{aligned} V_A(t) = nRI_A(t) + nL\frac{dI_A(t)}{dt} + j\omega nLI_A(t) + k_{RE}nRI_E(t) + k_{IM}nL\frac{dI_E(t)}{dt} \\ + j\omega k_{IM}nLI_E(t) \end{aligned} \tag{3.18}$$

where, k_{RE} and k_{IM} are the earth-impedance compensation resistance ratio and earth-impedance compensation reactance ratio [65] respectively as defined in ((3.19)

$$\begin{gathered} k_{RE} = \frac{1}{3}\left(\frac{R_0}{R_1} - 1\right) = \frac{R_E}{R_1} = \frac{R_E}{R} \\ k_{IM} = \frac{1}{3}\left(\frac{X_0}{X_1} - 1\right) = \frac{X_E}{X_1} = \frac{L_E}{L_1} = \frac{L_E}{L} \end{gathered} \tag{3.19}$$

where, R_0, R_1, X_0, X_1, R_E, and X_E are line zero-sequence resistance, line positive sequence resistance, line zero sequence reactance, line positive sequence reactance, earth resistance, and earth reactance respectively. Equations similar to ((3.12) and ((3.13) can be obtained by separating real and imaginary components of ((3.18) and solving for nL and nR. General equations for fault loop inductance and resistance for a Phase-to-Ground fault are given in ((3.20) and ((3.21).

$$nL = \frac{\gamma}{\alpha - \beta} \tag{3.20}$$

$$nR = \frac{\rho - \sigma}{\beta - \alpha} \tag{3.21}$$

where:

$$\gamma = V_{p(Re)}\left(I_{p(Im)} + k_{RE}I_{E(Im)}\right) - V_{p(Im)}\left(I_{p(Re)} + k_{RE}I_{E(Re)}\right)$$

$$\alpha = \left(I_{p(Im)} + k_{RE}I_{E(Im)}\right)\left[\frac{dI_{p(Re)}}{dt} + k_{IM}\frac{dI_{E(Re)}}{dt} - \omega\left(I_{p(Im)} + k_{IM}I_{E(Im)}\right)\right]$$

$$\beta = \left(I_{p(Re)} + k_{RE}I_{E(Re)}\right)\left[\frac{dI_{p(Im)}}{dt} + k_{IM}\frac{dI_{E(Im)}}{dt} + \omega\left(I_{p(Re)} + k_{IM}I_{E(Re)}\right)\right]$$

$$\rho = V_{p(Re)}\left[\frac{dI_{p(Im)}}{dt} + k_{IM}\frac{dI_{E(Im)}}{dt} + \omega\left(I_{p(Re)} + k_{IM}I_{E(Re)}\right)\right]$$

$$\sigma = V_{p(Im)}\left[\frac{dI_{p(Re)}}{dt} + k_{IM}\frac{dI_{E(Re)}}{dt} - \omega\left(I_{p(Im)} + k_{IM}I_{E(Im)}\right)\right]$$

Even though ((3.14), ((3.15), ((3.20), and ((3.21) are derived for a single-infeed short circuit scenario, they would hold if a short circuit occurred in a system with an infeed at the remote end. However, when a fault occurs with a finite fault resistance, the conditions would deviate from the original assumptions.

3.4 Comparator-Based Line Distance Protection

The dynamic phasor-based distance elements for the implementation of Phase-to-Phase and Phase-to-Ground fault loops were developed using magnitude comparators that compare scaler quantities derived based on real and imaginary parts of the dynamic phasors and their derivatives.

3.4.1 Phase-to-Phase Fault Loop

The inductance and resistance for a Phase-to-Phase fault can be estimated using ((3.14) and ((3.15). If the distance relay is to be operated, then the estimated resistance and reactance should be inside a predefined reach as shown in Fig 3.5. Therefore, two inequalities in ((3.22) and ((3.23) should hold if the fault is inside the protected zone.

$$-L_{Reverse\ Reach} < L_{Estimate} < L_{Forward\ Reach} \tag{3.22}$$

$$-R_{Reverse\ Reach} < R_{Estimate} < R_{Forward\ Reach} \tag{3.23}$$

Using ((3.22), the comparator signals for inductance reach can be defined with the help of ((3.14) as:

$$S1L_{PP} = -L_{Reverse\ Reach}(\mu - \nu) \tag{3.24}$$

$$S2L_{PP} = L_{Forward\ Reach}(\mu - \nu) \tag{3.25}$$

$$S3L_{PP} = \lambda \tag{3.26}$$

Similarly, using ((3.23) three comparator signals can be defined for the resistance reach with the help of ((3.15):

$$S1R_{PP} = -R_{Reverse\ Reach}(\mu - \nu) \tag{3.27}$$

$$S2R_{PP} = R_{Forward\ Reach}(\mu - \nu) \tag{3.28}$$

$$S3R_{PP} = \ \zeta - \psi \tag{3.29}$$

where; $\lambda, \mu, \nu, \zeta,$ and ψ are defined in section 3.3.1.

Therefore, using the comparator signals defined in ((3.24), ((3.25), ((3.26), ((3.27), ((3.28), and ((3.29) following trip logic can be defined:

$Trip = 1$:

$$if \begin{Bmatrix} [(S3R_{PP} > S1R_{PP})\ AND\ (S3R_{PP} < S2R_{PP})]\ AND \\ [(S3L_{PP} > S1L_{PP})\ AND\ (S3L_{PP} < S2L_{PP})] \end{Bmatrix} \tag{3.30}$$

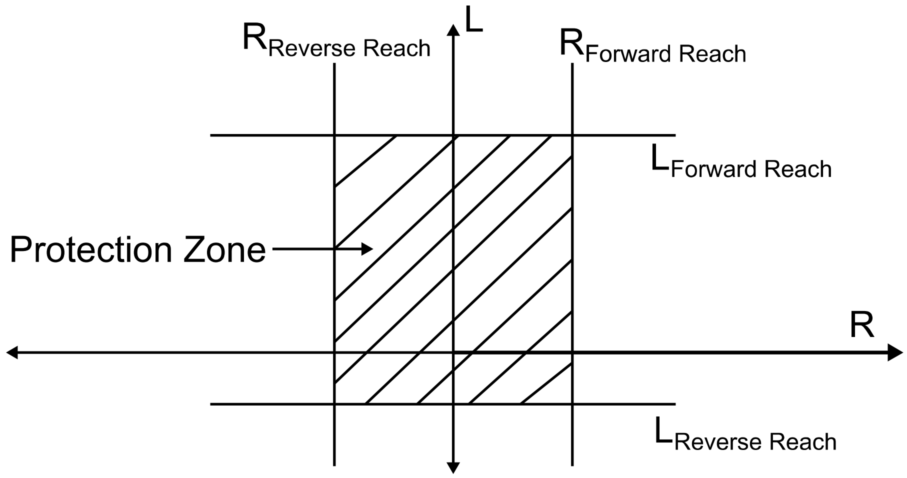

Fig 3.5 Protection Zone Defined on L-R Plane [66]

3.4.2 Phase-to-Ground Fault Loop

The inductance and resistance for the Phase-to-Ground fault loop can be estimated using ((3.20) and ((3.21). The inequalities that are given in ((3.22) and ((3.23) will still hold for the Phase-to-Ground fault loop as well. Therefore, using ((3.22) the comparator signals for the inductance reach defined in Fig 3.5 can be written with the help of ((3.20) as:

$$S1L_{PG} = -L_{Reverse\ Reach}(\alpha - \beta) \tag{3.31}$$

$$S2L_{PG} = L_{Forward\ Reach}(\alpha - \beta) \tag{3.32}$$

$$S3L_{PG} = \gamma \tag{3.33}$$

Similarly, using ((3.23), three comparator signals can be defined for the resistance reach with the help of ((3.21):

$$S1R_{PG} = -R_{Reverse\ Reach}(\alpha - \beta) \tag{3.34}$$

$$S2R_{PG} = R_{Forward\ Reach}(\alpha - \beta) \tag{3.35}$$

$$S3R_{PG} = \rho - \sigma \tag{3.36}$$

Hence, similar to the Phase-to-Phase fault loop, the following logic can be developed for Phase-to-Ground fault using ((3.31) – ((3.36).

$Trip = 1$:

$$iif \begin{Bmatrix} [(S3R_{PG} > S1R_{PG})\ AND\ (S3R_{PG} < S2R_{PG})]\ AND \\ [(S3L_{PG} > S1L_{PG})\ AND\ (S3L_{PG} < S2L_{PG}\ )] \end{Bmatrix} \tag{3.37}$$

Phase-to-Phase-to-Ground fault conditions are considered a special condition of Phase-to-Phase fault.

3.5 Validation of the Method

3.5.1 Test System and Reach Setting Calculation

The performance of the protection scheme was evaluated and compared with the standard distance relaying algorithm using the power system depicted in Fig 3.6 (a), simulated in the electromagnetic transient (EMT) simulation program PSCAD/EMTDC™ with 50 μs time steps. Fault-generated waveforms were sampled at 16 samples/cycle sampling rate, saved as CSV files, and later fed into the dynamic phasor-based distance protection scheme implemented in MATLAB/ Simulink. The sources were represented as three-phase voltage sources with different positive and zero sequence impedances. The transmission lines were represented using the frequency-dependent phase model available in the PSCAD/EMTDC™ transmission line library with default settings. The 3-conductor delta tower type was used, and the line design is shown in Fig 3.6 (b). Chukar conductors having a DC resistance of 0.0203 Ω/km and a radius of 0.032m were used for phase conductors. The DC resistance and radius of ground conductors are 2.8645 Ω/km and 0.0055 m, respectively. Instead of enabling ideal transposition, the transmission lines were transposed by connecting three-line segments as shown in Fig 3.7. The ground plane component available in the Transmission Library in PSCAD/EMTDC™ was used to represent the earth ground return path of the system and it was approximated with a constant resistivity of 100 Ωm. The current transformer (CT) was modeled using the Jiles-Atherton (JA) model[67] and the potential transformer (PT) was modeled using the Lucas model [68] available in the protection library in PSCAD/EMTDC™. The parameters of the line at 50 Hz are given in Table 3.1. The source impedances are given in Table 3.2. The three-phase transformer data are provided in Table 3.3. The parameters of CT and PT models are given in Tables 3.4 and 3.5.

Table 3.1 Transmission Line Parameters (230 kV, 100 MVA Base)

Parameter	**Value (p.u)**	**Parameter**	**Value (p.u)**
R_1	0.0098	R_0	0.0851
X_1	0.1200	X_0	0.3240

Table 3.2 Source Impedance Data

Source	$\boldsymbol{Z_1}$ **(Ω)**	$\boldsymbol{Z_0}$ **(Ω)**
Source 1	$1.077\angle 87.65^o$	$0.897\angle 80.86^o$
Source 2	$3.8\angle 87.69^o$	$6.02\angle 80.9^o$

Table 3.3 Transformer Data

Parameter	**Value**
Line-to-Line Voltages: Winding-1/Winding-2	13.8 kV/230 kV
Transformer MVA	100
Positive Sequence Leakage Reactance	0.1 p.u
Magnetizing Current	2.0 %
Air Core Reactance/Knee Voltage	0.2 p.u /1.17 p.u

Table 3.4 Current Transformer Parameters

Parameter	Value
Nominal Ratio	1200 A:5 A
Primary Turns/ Secondary Turns	240
Secondary Resistance/ Inductance	0.5 Ω / 0.8×10^{-3} H
Core Area	2.601×10^{-3} m^2
Burden Resistance / Inductance	0.5 Ω / 0.8×10^{-3} H

Table 3.5 Potential Transformer Parameters

Parameter	Value
Nominal Ratio	230 kV:115 V
Primary Resistance/Inductance (on secondary)	0.05 Ω / 0.47×10^{-3} H
Secondary Resistance/Inductance	0.18 Ω / 0.47×10^{-3} H
Hysteresis/Eddy Current Loss	5.0 W / 2.5 W
Secondary Operating Voltage/Frequency	115 V/50 Hz
Operating Flux Density	0.8 T
Burden Resistance/Inductance – Series	301.0 Ω/2.4 H
Burden Resistance – Parallel	785.0 Ω

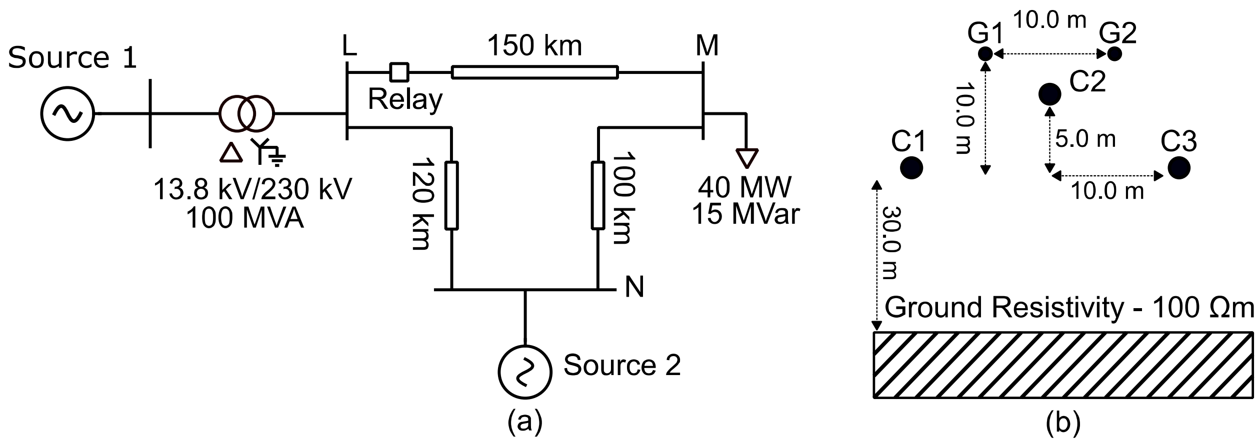

Fig 3.6 (a) Power system simulated in PSCAD/EMTDC™ and (b) design of transmission line

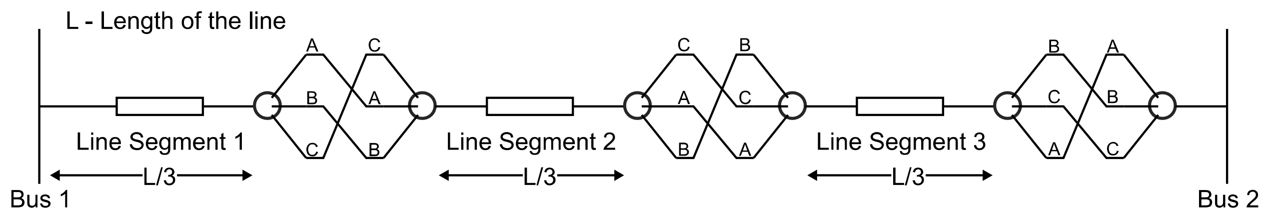

Fig 3.7 The 1/3-1/3-1/3 Transmission Line Transposition Scheme Used in Transmission Lines in PSCAD/EMTDC™

The characteristic of the proposed distance protection scheme is a quadrilateral. Therefore, the setting calculation procedure proposed in [69] for a quadrilateral relay was followed when calculating the reach settings. The relay consists of 3 forward zones and one reverse zone. The reactance and resistive reach settings are calculated as follows:

3.5.1.1 Reactance Reach Calculation

The general equation for reactance reach for the nth zone is given by ((3.38) where L_1 is the line positive sequence reactance. Reach values for zones 1,2,3, and 4 are set to 80 %, 120 %, 150 %, and 30 %. Reactance reach settings are given in Table 3.6.

$$L_{reach} = L_1 \times nth\ Zone\ Reach\ \% \times \frac{CT\ Ratio}{PT\ Ratio}\ \Omega\ (secondary) \tag{3.38}$$

Table 3.6 Reactance Reach Settings

	Zone 1 (H)	Zone 2 (H)	Zone 3 (H)	Zone 4 (H)
L_{Reach} *(forward)*	0.0194	0.0291	0.0364	0
L_{Reach} *(reverse)*	0	0	0	0.0073

3.5.1.2 Resistive Reach Calculation

Several factors need to be considered when setting the resistive reach setting. All distance elements must avoid the heaviest system loading. Taking the 5A CT secondary rated current as the maximum load current and PT secondary rated voltage as 115 V, the minimum load impedance seen by the relay would be [69]:

$$\frac{V_{phase\ neutral}}{I_{rated}} = \frac{115/\sqrt{3}}{5} = 13.3\ \Omega\ (Secondary)$$

According to [69], phase distance zones would avoid the minimum load impedance by a margin of 40% and earth fault zones by a margin of 20%. Hence the maximum resistive reaches would be 7.9 **Ω** and 10.6 **Ω** respectively. Additionally, typical resistive coverage for earth faults would be 40 **Ω** (primary) [69]. For phase faults, assuming a minimum load current of 1 kA, arc resistance can be calculated using the Warrington formula as 18.1 **Ω**. Therefore, the minimum secondary resistive reaches become:

$$R_{phase\ to\ phase} = 18.1 \times \frac{240}{2000} = 2.172\ \Omega\ (secondary)$$

$$R_{phase\ to\ ground} = 40 \times \frac{240}{2000} = 4.8\ \Omega\ (secondary)$$

Furthermore, zone 2 resistive reach should be less than 80 % of the zone 3 resistive reach [69]. The resistive reach settings are given in Table 3.7.

Table 3.7 Resistive Reach Settings

	Zone 1 (Ω)	**Zone 2 (Ω)**	**Zone 3 & 4 (Ω)**
R_{PP}	3	4.5	8
R_{PG}	5	7	10

Zone 1 was set as an instantaneously operating zone and zones 2-, 3-, and 4-time settings were set as 0.3 s, 0.8 s, and 1.5 s respectively.

3.5.2 Evaluation of the Protection Scheme

3.5.2.1 Complete Algorithm

Fig 3.8 depicts the implemented dynamic phasor-based distance protection algorithm. Current and voltage buffers are filled at the initiation of the algorithm, dynamic phasor calculation begins once the buffers are full. A moving window is used to store voltage and current measurements. Upon calculating the dynamic phasors and their derivatives the calculated values are used in the comparator equations to make the trip decisions. Then the voltage and current buffers are updated when the new measurements are available.

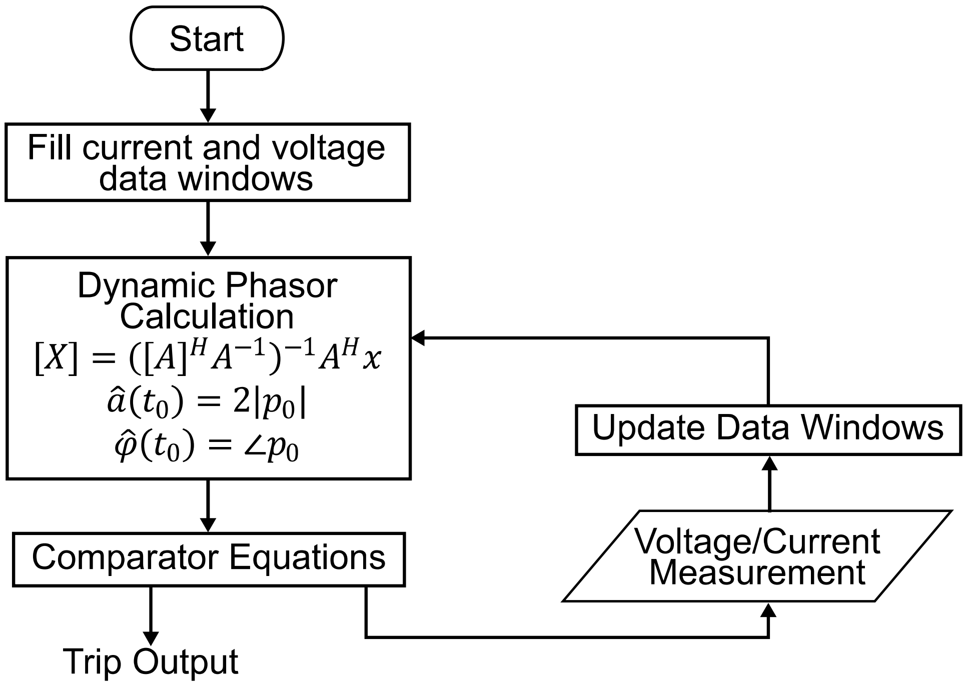

Fig 3.8 Dynamic phasor distance protection algorithm

3.5.2.2 Demonstration of Basic Operation

To demonstrate the operation of the proposed algorithm, the short circuit faults listed in Table 3.8 were applied on the protected line L-M at 0.4 s.

Table 3.8 Considered Fault Scenarios

Scenario	**Fault Type**	**Location**
Scenario-1	AG	33.3 % of Line MN
Scenario-2	BCG	33.3 % of Line MN
Scenario-3	AC	33.3 % of Line MN
Scenario-4	ABC	33.3 % of Line MN

Fig 3.9 (a-d), Fig 3.9 (e-h), Fig 3.10 (a-d), and Fig 3.10 (e-h) show the Zone 1 comparator signals for Scenarios -1, 2, 3, and 4 respectively. Since Scenario-1 is a Phase-to-Ground Fault, it should hold the logic explained in ((3.37) during the fault condition. In the first, second, and fourth subfigures in Fig 3.9 which depict the comparator signals calculated for the Phase-A-to-Ground

fault loop, before the fault, the comparator signals $S1L_{PG}$, $S2L_{PG}$, $S3L_{PG}$, $S2R_{PG}$, and $S3R_{PG}$ hold $S1L_{PG} > S3L_{PG}$, $S2L_{PG} < S3L_{PG}$, and $S2R_{PG} < S3R_{PG}$ confirming a non-fault condition. However, upon applying the fault at 0.4 s, the above-mentioned inequalities invert confirming a Phase-A-to-Ground fault condition.

Fig 3.9 (e-h) shows the comparator signals calculated for the Phase-B-to-C fault loop which is been used to issue trip signals for the Phase-B-to-C-to-Ground fault. Before the fault, the comparator signals $S1L_{PP}$, $S3L_{PP}$, $S2R_{PP}$, and $S3R_{PP}$ hold $S1L_{PP} > S3L_{PP}$ and $S2R_{PP} < S3R_{PP}$ conditions confirming a non-fault condition which is depicted in the first and fourth subfigures. Upon applying the fault, these conditions get inverted.

Fig 3.10 (a-d) depicts the variation of Phase-A-to-C fault loop comparator signals with time. Before the fault, the comparator signals $S1L_{PP}$, $S3L_{PP}$, $S2R_{PP}$, and $S3R_{PP}$ hold $S1L_{PP} > S3L_{PP}$ and $S2R_{PP} < S3R_{PP}$ conditions confirming non-fault conditions. As with the other fault cases, these two conditions get inverted upon applying the fault to issue the trip signal.

Fig 3.10 (e-h) depicts the variation of Phase-B-to-C fault loop comparator signals with time for a Three-Phase fault. In this scenario, out of the four comparator logics in ((3.30) that verify the existence of a Phase-to-Phase fault three remain false during the non-fault period. Upon applying the fault, these three logics become true to confirm the existence of a Phase-to-Phase fault. A similar variation can be observed in the comparator signals calculated for the other two fault loops during a Three-Phase fault condition.

Observation of the variation of comparator signals for different fault types verifies the logic scheme developed in Section 3.4. Furthermore, at least two sets of logical equations defined in ((3.30) and ((3.37) remain false during non-fault conditions which ensure the reliability of the proposed line protection scheme. Furthermore, during the fault condition, except for the corresponding relay element, (AG element during Phase-A-to-Ground fault), all the other relay elements do not pick up a fault condition except in the case of Three-Phase faults helping to avoid misoperation during a fault scenario. The oscillations in the comparator signals are caused by the real and imaginary parts of the estimated dynamic phasors. The trip decisions are made only after two consecutive sampling points satisfy the trip logic to avoid spurious tripping and improve security (this approach is typical even in commercial relays). But it also delays the tripping when oscillations cause the logical conditions tested in the relay to alternate from one sample point to the other.

3.5.2.3 Close-in Three-Phase Faults

Fig 3.11 (a-d) shows the Zone 1 Phase-to-Phase comparator signals for a close in Three-Phase short circuit fault applied at 1 km away from the relay in the forward direction. Whereas Fig 3.11 (e-h) shows the Zone 4 Phase-to-Phase comparator signals for close in Three-Phase short circuit fault applied at 1 km away from the relay in the reverse direction. As shown in the figures, comparator signals correctly pick up the fault in both the forward and reverse directions. Furthermore, during the forward fault, neither the phase nor ground reverse elements pick up the fault, and the same behavior was observed in forward elements during the reverse fault as well, ensuring the correct operation of the distance protection algorithm.

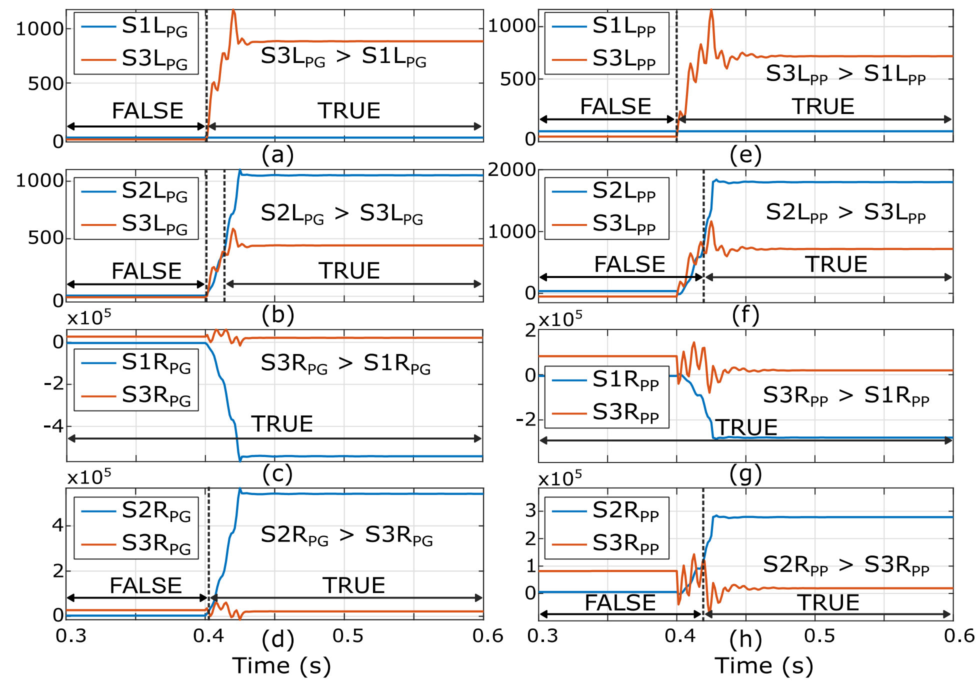

Fig 3.9 Comparator signals for fault Scenario 1 (a-d), and Scenario 2 (e-h).

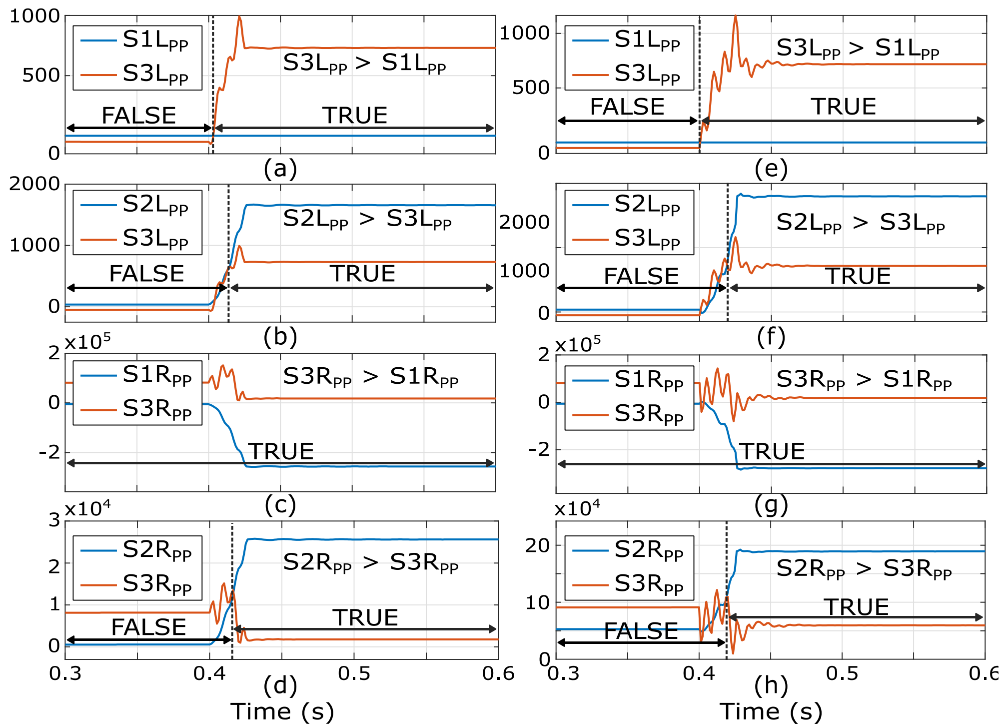

Fig 3.10 Comparator signals for fault Scenario 3 (a-d) and Scenario 4 (e-h)

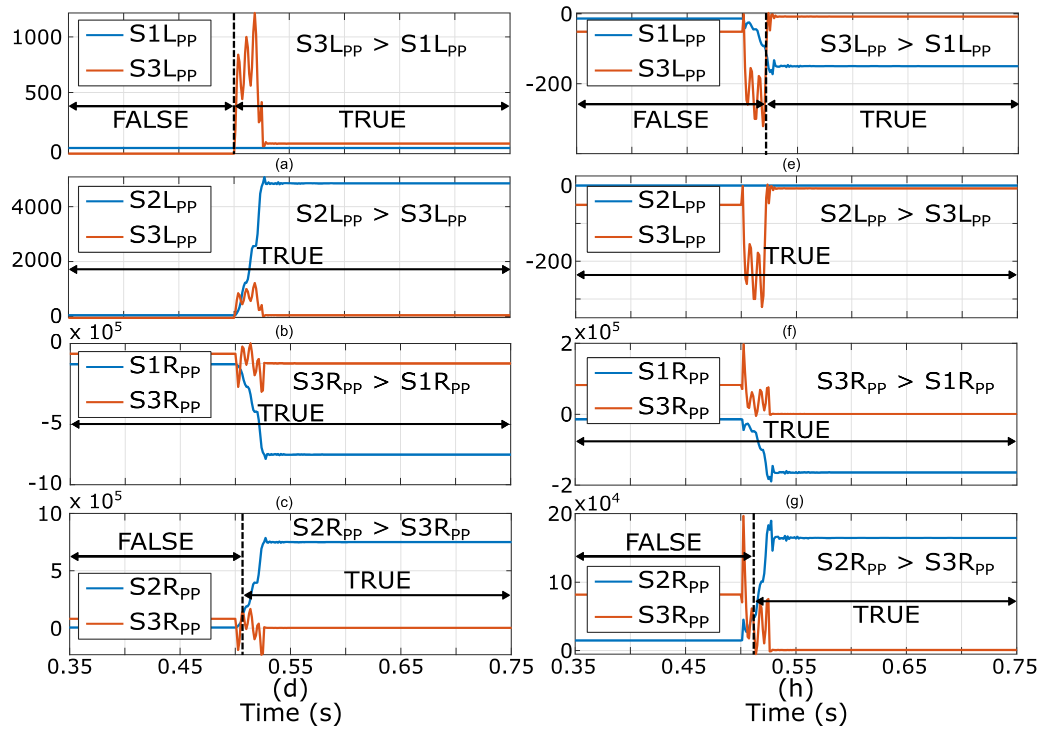

Fig 3.11 Comparator signals for close in Three-Phase short circuit in the forward direction (a-d) and the reverse direction (e-h)

3.5.2.4 Comparison With Traditional Distance Protection

The performance of the proposed dynamic phasor-based line distance protection scheme was compared with a quadrilateral relay model developed in PSCAD/EMTDC™ software. This relay model was implemented based on the algorithms available in commercial relay manuals [70] and therefore, provides a more accurate response compared to the relay models available in the PSCAD master library. The main purpose of using a conventional relay model is that one of the main aims of this study was to investigate whether a dynamic phasor-based distance relay provides any advantage over conventional distance protection. Settings were calculated using the same basis as in Sections 3.5.1.1 and 3.5.1.2 for the quadrilateral distance relay model, which uses standard one-cycle DFT for phasor estimation and a mimic filter to remove the decaying DC component. Operating times of the DP-based method and the quadrilateral relay were compared by applying

Zone 1 short circuit and high impedance (35 Ω) Phase-A-to-Ground faults at three different locations (10%, 50%, and 70% of line length) and three fault inception angles (0º, 45º and 90º). Table 3.9 and Table 3.10 summarize the results obtained from these tests. Operating times when the window width increased up to 1.5 cycles are also shown in the same tables.

Fig 3.12 shows the operating point on the L-R plane during a Phase-A-to-Ground short circuit fault in the forward direction. Zone 1 reach and the line is plotted on the same diagram. The operating point is calculated using both the dynamic phasor-based method and the quadrilateral relay model settles at the same point after the initial post-fault transient period. Compared to the quadrilateral relay model, the operating point calculated using the dynamic phasor model shows an oscillatory behavior before settling at the fault point. Further investigations revealed that the oscillatory behavior was caused by the phasor estimates and not by the derivative terms in the comparator equations. However, the actual decision-making is done using the comparator equations given in ((3.30) and ((3.37). These oscillations are visible in comparator signals shown in Fig 3.9 - Fig 3.11. Even in the quadrilateral distance relay model implemented in PSCAD, the decisions are based on the equivalent angle comparators. In both traditional and dynamic phasor-based relay models, trip signals are issued only after the respective trip criteria are satisfied for two consecutive sampling points to ensure high reliability.

DP-based distance relay operates faster than the standard quadrilateral relay for both short circuits and high impedance fault conditions for close-up faults at the fault inception angles of 0° and 45° even when a 1.5-cycle window was used in the dynamic phasor estimation stage. However, this speed advantage of DP-based relay tends to diminish for faults away from the relay location, especially at 90º fault inception angles. Investigations also showed that the operating times for

Phase-to-Phase and Three-Phase faults are equal to the standard quadrilateral relay for close-up faults and tend to slow down for faults away from the relay location.

Further analysis showed that the operating times for both Phase-to-Phase and Phase-to-Phase-to-Ground faults are mainly limited by $S3R_{PP}$ comparator signal. The decaying DC component creates oscillations in the real and imaginary components of the currents during the transition period which increases the transition time from non-fault condition to fault condition. Even though the 1.5-cycle window seemed to have a better rejection of decaying DC components, the longer window length results in slower performance overall. However, for Phase-to-Ground faults, the presence of the DC component seems to accelerate the operating time.

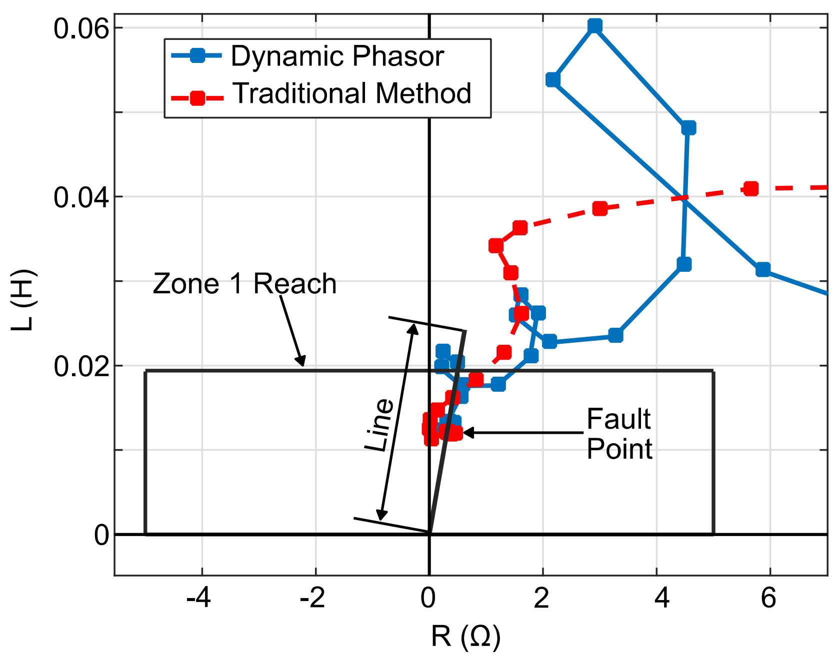

Fig 3.12 Operating point on L-R plane for Phase-to-Ground short circuit in the forward direction

Additional tests were done to compare the performance for reverse faults, but the dynamic phasor method did not show any speed advantage for reverse faults irrespective of the window length. The dynamic phasor-based relay operated correctly as expected for all cases. However, the dynamic phasor-based relay did not provide a consistent speed advantage over the traditional distance relay as initially hypothesized.

Table 3.9 Operating Time in Cycles for R_f= 0

Inception angle	**Fault Location**	**DP based Relay**		**DFT-based Standard Quadrilateral Relay**
		1.25 Cycles	**1.5 Cycles**	
0º	10 %	0.375	0.4375	0.4375
	50 %	0.8125	0.9375	0.875
	70 %	1.25	1.375	1.0625
45º	10 %	0.3125	0.4375	0.4375
	50 %	1.0625	0.875	0.8125
	70 %	1.125	1.25	1
90º	10 %	0.3125	0.5625	0.5625
	50 %	1.0	1.125	0.875
	70 %	1.25	1.25	1.0625

Table 3.10 Operating Time in Cycles R_f = 35 Ω

Inception angle	**Fault Location**	**DP based Relay**		**DFT-based Standard Quadrilateral Relay**
		1.25 Cycles	**1.5 Cycles**	
0º	10 %	0.5	0.625	0.75
	50 %	0.625	0. 8125	0.9375
	70 %	1.1875	1.25	1.5
45º	10 %	0.375	0.5	0.625
	50 %	0.6875	0.6875	0.8125
	70 %	1.0625	1.1875	1.375
90º	10 %	0.5	0.5625	0.5625
	50 %	1	1.0625	1
	70 %	1.25	1.1875	1.125

3.5.2.5 Line Length and Pre-Fault Load Conditions Considerations

To investigate the effect of the line length on the performance of the proposed algorithm, the length of the protected line in the test system was increased to 300 km. Forward and reverse faults were applied after recalculating the relay settings for the increased line length. For all applied faults, the relay operated as expected as shown in Table 3.11. The trajectory of fault points for Phase-A-to-Ground, Phase-B-to-C, and Phase-A-to-C-to-Ground forward faults applied at 10%, 50%, 70%, and 85% of line length are shown in Fig 3.13.

Table 3.11 Relay Operating for 300 km Transmission Line

Applied Fault	**Forward Direction**	**Reverse Direction**
AG	Operated	Operated
BG	Operated	Operated
CG	Operated	Operated
AB	Operated	Operated
AC	Operated	Operated
BC	Operated	Operated
ABG	Operated	Operated
BCG	Operated	Operated
ACG	Operated	Operated
ABC	Operated	Operated

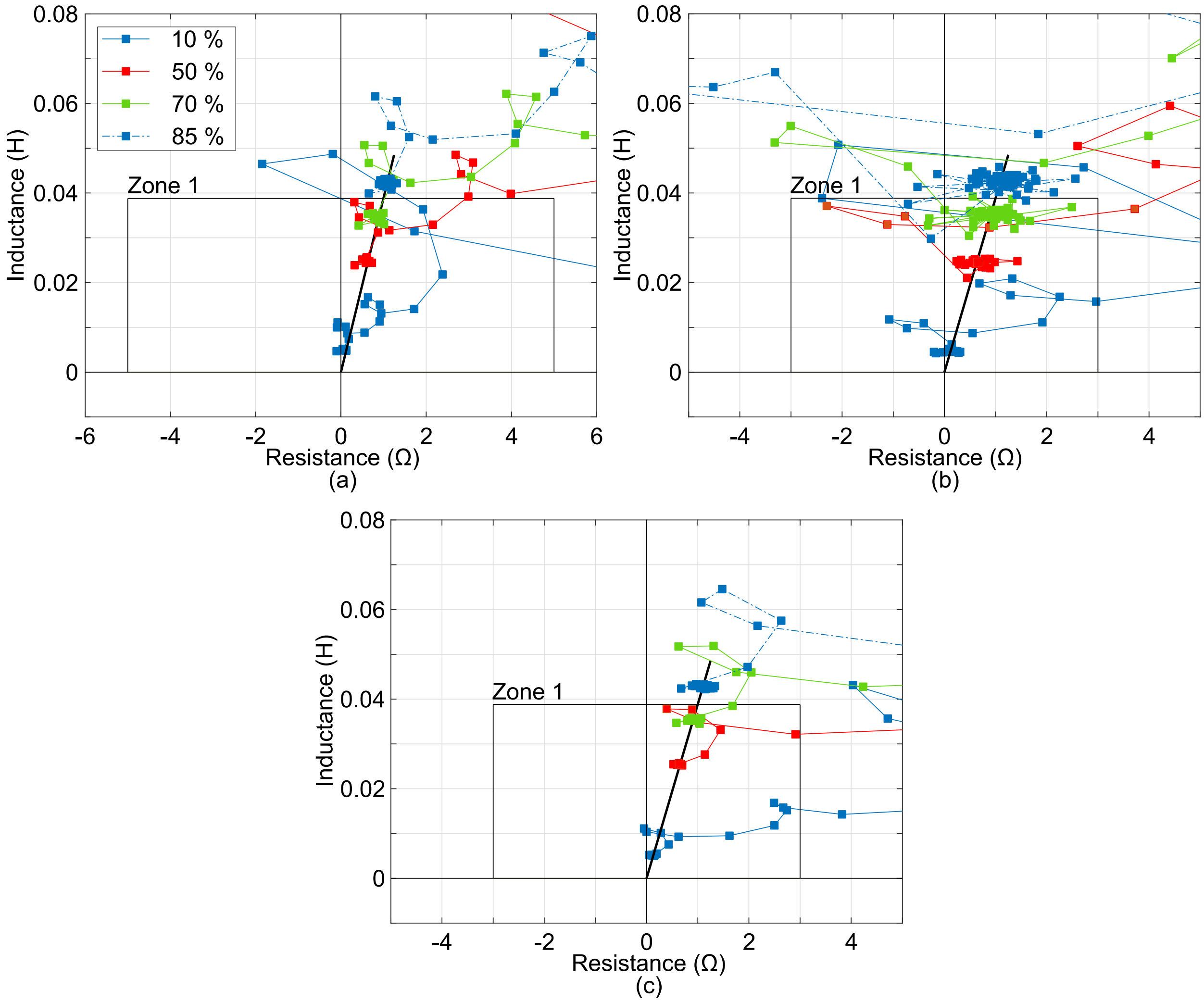

Fig 3.13 The Impedance Trajectory for (a) Phase-A-to-Ground, (b) Phase-B-to-C, and (c) Phase-A-to-C-to-Ground Faults at 10%, 50%, 70% and 85% of Line Length of 300 km Line

The proposed method was also tested under different pre-fault load flow conditions. The pre-fault load flow directions were changed by changing the phase angles of the two sources and applying faults in the forward and reverse directions. The method operated as expected even after changing the initial load flow conditions. The results are shown in Table 3.12.

Table 3.12 Relay Operation for Different Pre-Fault Load Conditions

Applied Fault	$\angle\boldsymbol{Source}\ \mathbf{1} > \angle\boldsymbol{Source}\ \mathbf{2}$		$\angle\boldsymbol{Source}\ \mathbf{2} > \angle\boldsymbol{Source}\ \mathbf{1}$	
	Forward	**Reverse**	**Forward**	**Reverse**
BG	Operated	Operated	Operated	Operated
BCG	Operated	Operated	Operated	Operated
AC	Operated	Operated	Operated	Operated

3.5.2.6 SIR and Evolving Faults

The proposed dynamic phasor-based line protection scheme was tested by applying a Phase-A-to-Ground evolving fault. The fault resistance R_f was modeled as:

$$R_f = 10 \times 10^6 \times e^{-7(t-t_f)}\Omega \qquad 3.39$$

where t is the time and t_f is the time of fault inception. The dynamic phasor-based method was able to successfully detect and issue a trip signal for the simulated evolving fault. Furthermore, the method can work for a wide range of source-to-line impedance ratios (5 – 20)

3.6 Concluding Remarks

The merits of applying the concept of dynamic phasors for line distance protection were studied. Starting from the fundamental principles, fault loop equations were derived using the DP relationships. Using these fault loop equations, an amplitude comparator-based line distance protection scheme with directional capabilities was developed. A method to extract the dynamic phasors and their first derivative from time-domain sampled current and voltage signals was implemented to simulate the proposed DP-based distance protection scheme.

The DP-based distance protection operates correctly for all tests performed and proved robust under evolving faults and for a wide range of source-to-line impedance ratios. However, the speed of operation, the factor that motivated examining the DP-based distance protection, was not always faster when compared to the traditional distance protection. Although some speed advantage can be achieved with the DP approach for closeup faults, contrary to the initial expectation, there is no clear advantage of the DP-based approach over traditional distance protection, especially when considering the additional complexity in the algorithms and the phasor estimation process. Even in the cases where the dynamic phasor-based relay operated faster than the traditional distance relay, the speed advantage is limited to a few sampling intervals. This is mainly arising from having to use of 1.25 cycle estimation window in the dynamic phasor extraction algorithm to suppress the second harmonic whereas the traditional distance relay uses one cycle to estimate the phasor quantities.

Chapter 4

Distance Protection Using Incremental Clarke Components of Instantaneous Measurements

4.1 Background

Chapter 3 explored the concept of dynamic phasors in improving the speed of distance protection by developing a distance protection scheme based on the dynamic phasor model of the transmission line. However, the results showed that only a limited speed advantage was achieved for close-up faults and provided no clear advantage over traditional protection. Chapter 1 introduced the alternative approaches considered in recent literature and their advantages and drawbacks. Most of the alternative approaches introduced in recent literature use traveling waves or instantaneous currents and voltages including incremental quantities. This chapter proposes a line protection scheme that uses instantaneous incremental quantities of voltages and currents and is founded on Clarke's equivalent networks of transmission lines.

The Clarke transform [71] is a popular transformation method in power systems that is been used to decouple ac three-phase quantities and break down the complex system into its natural or characteristic modes, which are denoted as α, β, and 0 components. It was introduced in 1917 to simplify the determination of system currents and voltages during Phase-to-Ground faults by eliminating cross-coupling terms in the system equations. Similar to sequence components, decoupled α, β, and 0 equivalent circuits can be derived to replace an actual three-phase circuit. This chapter attempts to use the beneficial properties of the Clarke transform and Clarke equivalent circuits to develop a fast and reliable line protection scheme similar to the familiar distance protection.

The main original contributions of this chapter include formulation of the Clarke domain fault loop equations and the relevant Clarke equivalent circuits for different fault types and devising a method to determine the inductance (L) and resistance (R) of the Clarke equivalent circuit of the respective fault loop using Clarke components of the instantaneous values of currents and voltages. Furthermore, a decision-making process that is very familiar to protection engineers is proposed through protection zones defined on the L-R plane, with a systematic approach for setting selection. To choose the correct fault loop, it is proposed to use the Clarke component-based faulted phase identification scheme, which will be described in Chapter 5.

4.2 Clarke Equivalent Networks

The standard Clarke transform equation is defined concerning Phase A only. To handle all types of possible faults, the transform given in ((4.1) which combines Clarke transforms with respect to Phases A, B, and C, can be used.

$$\begin{bmatrix} X_{\alpha^A} \\ X_{\alpha^B} \\ X_{\alpha^C} \\ X_{\beta^A} \\ X_{\beta^B} \\ X_{\beta^C} \\ X_0 \end{bmatrix} = \frac{1}{3} \begin{bmatrix} 2 & -1 & -1 \\ -1 & 2 & -1 \\ -1 & -1 & 2 \\ 0 & \sqrt{3} & -\sqrt{3} \\ -\sqrt{3} & 0 & \sqrt{3} \\ \sqrt{3} & -\sqrt{3} & 0 \\ 1 & 1 & 1 \end{bmatrix} \begin{bmatrix} X_a \\ X_b \\ X_c \end{bmatrix} \tag{4.1}$$

where X can be either voltage or current represented either by instantaneous values or their phasors. The term X_{Q^P} term in ((4.1) is defined as the α or β component of the current or voltage calculated with respect to Phases A or B or C. For example, i_{α^A} is the α component of the instantaneous current calculated with respect to Phase A.

Different boundary conditions are imposed by different types of short circuit faults. Based on these boundary conditions, a unique set of equations can be derived in terms of the Clarke transform quantities. Considering these equations, Clarke networks for each fault category (Phase-to-Ground, Phase-to-Phase-to-Ground, Phase-to-Phase, and Three-Phase) can be derived. The process is explained in the subsequent subsections considering a fault from each type.

4.2.1 Three-Phase Fault

During a Three-Phase short-circuit, conditions at the fault point are given in ((4.2) and ((4.3):

$$v_{aF}(t) = v_{bF}(t) = v_{cF}(t) = 0 \tag{4.2}$$

$$\Delta i_a(t) + \Delta i_b(t) + \Delta i_c(t) = 0 \tag{4.3}$$

where, $\Delta i_a(t), \Delta i_b(t)$, and $\Delta i_c(t)$ are the components of line currents flowing into the fault and $v_{aF}(t), v_{bF}(t)$, and $v_{cF}(t)$ are the instantaneous voltages across the fault (the same notation applies to all the other fault types considered hereafter). Substituting the boundary conditions into ((4.1), the results in ((4.4) and ((4.5) can be obtained for the fault point:

$$\begin{gathered} v_{\alpha^A F}(t) = v_{\alpha^B F}(t) = v_{\alpha^C F}(t) = 0 \\ v_{\beta^A F}(t) = v_{\beta^B F}(t) = v_{\beta^C F}(t) = 0 \end{gathered} \tag{4.4}$$

$$\Delta i_0(t) = 0 \tag{4.5}$$

The conditions described in ((4.4) and ((4.5) can be depicted using the fault loops shown in Fig 4.1 (a) and (b) respectively for α^A and β^A networks. In Fig 4.1, $\Delta v_{\alpha^A}(t)$ and $\Delta v_{\beta^A}(t)$ are the component of voltages at the relay point due to respective fault current components $\Delta i_{\alpha^A}(t)$ and $\Delta i_{\beta^A}(t)$. The parameters R_α, L_α, R_β, and L_β are the per unit α and β resistance and inductance of the circuit calculated taking Phase-A as the reference, which is equal to line positive sequence resistance and inductance. The suffix (S) in circuit parameters denotes the source quantities, and x is the per unit distance to the fault from the relay point. Similar fault loops can be generated for α^B, β^B and α^C, β^C fault loops.

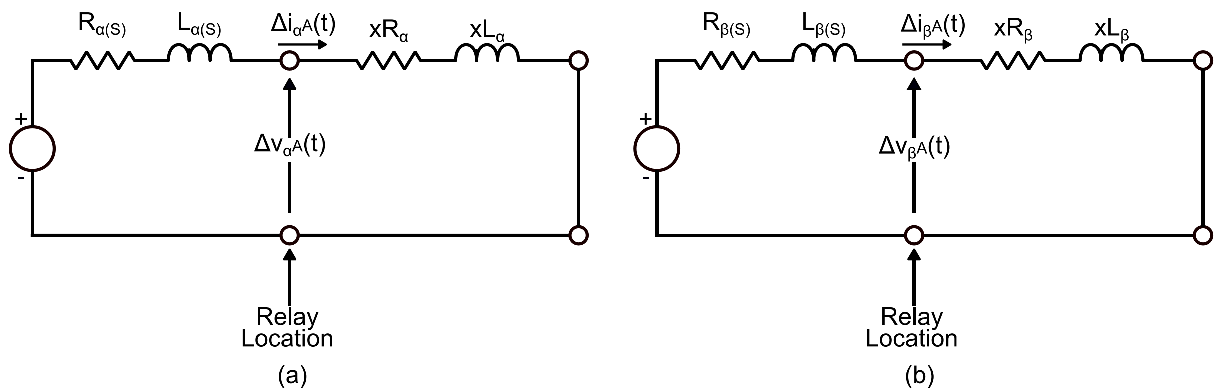

Fig 4.1(a) α^A, and (b) β^A Networks During a Three-Phase Fault

The time domain equations for the fault loops depicted in Fig 4.1 (a) and (b) are:

$$\Delta v_{\alpha^A}(t) = xR_\alpha \cdot \Delta i_{\alpha^A}(t) + xL_\alpha \cdot \frac{d\Delta i_{\alpha^A}(t)}{dt} \tag{4.6}$$

$$\Delta v_{\beta^A}(t) = xR_\beta \cdot \Delta i_{\beta^A}(t) + xL_\beta \cdot \frac{d\Delta i_{\beta^A}(t)}{dt} \tag{4.7}$$

4.2.2 Phase-to-Phase Fault

The boundary conditions at the fault point for a Phase-B-to-C short-circuit, are given in ((4.8) and ((4.9).

$$\Delta i_a(t) = 0; \quad \Delta i_b(t) + \Delta i_c(t) = 0 \tag{4.8}$$

$$v_{bF}(t) = v_{cF}(t) \quad (4.9)$$

Considering the Clarke components calculated with respect to Phase A ($X_{\alpha^A}, X_{\beta^A}; X \in v\ or\ i$) the following relationships can be derived at the fault point by applying the boundary conditions defined in ((4.8) and ((4.9) into ((4.1):

$$\Delta i_0(t) = \Delta i_{\alpha^A}(t) = 0 \quad (4.10)$$

$$v_{\beta^A F}(t) = 0 \quad (4.11)$$

From the conditions given in ((4.10) and ((4.11), it is evident that neither the α nor 0 networks are involved in the fault since there is no current flowing in those two networks. Only the β network is involved in the fault as shown in Fig 4.2.

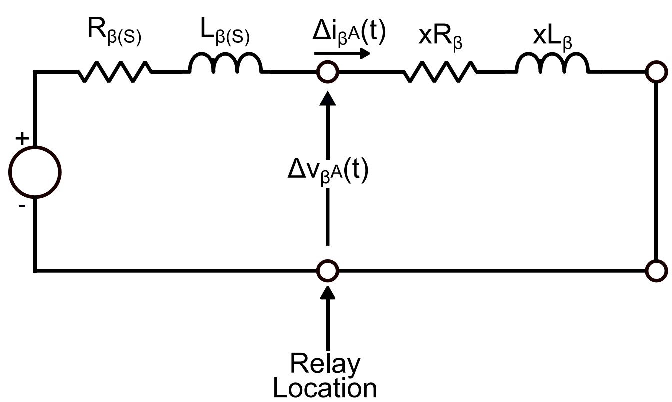

Fig 4.2 The β^A Network During Phase-B-to-C Fault

Therefore, the time domain equation for the β network fault loop formed by the β component calculated with respect to Phase-A is:

$$\Delta v_{\beta^A}(t) = xR_\beta \cdot \Delta i_{\beta^A}(t) + xL_\beta \cdot \frac{d\Delta i_{\beta^A}(t)}{dt} \quad (4.12)$$

Two other fault loops can be formed considering the Clarke components calculated with reference to Phase-B and Phase-C (faulted phases) as well. However, these fault loops will be more complex compared to the fault loop formed by the components calculated with respect to the non-faulted phase. Thus, for a Phase-A-to-B fault, the simplest fault loop is formed by the β components calculated with respect to Phase-C whereas for a Phase-C-to-A fault, the simplest fault loop is formed by the β components calculated with respect to Phase-B. In both cases, the fault loop structure is similar to the one shown in Fig 4.2.

4.2.3 Phase-to-Ground Fault

The conditions at the fault point for a Phase-A-to-Ground short circuit are given in ((4.13) and ((4.14).

$$v_{aF}(t) = 0 \tag{4.13}$$

$$\Delta i_b(t) = \Delta i_c(t) = 0 \tag{4.14}$$

Applying the boundary conditions given in ((4.13) and ((4.14) in ((4.1) would result in:

$$v_{\alpha^A F}(t) + v_{0F}(t) = 0 \tag{4.15}$$

$$\Delta i_{\beta^A}(t) = 0 \tag{4.16}$$

$$\Delta i_{\alpha^A}(t) = 2\Delta i_0(t) \tag{4.17}$$

From the conditions given in ((4.16), it is evident that the β network is not involved in the fault since there is no current flowing in the β network. Equation ((4.15) indicates a series interconnection between the α and 0 component networks, but ((4.17) conflicts with such a series connection. This can be circumvented by expressing Δv_0 as:

$$\Delta v_{0F}(t) = -\left(\frac{R_0}{2}\right)(2\Delta i_0(t)) - \left(\frac{L_0}{2}\right)\frac{d}{dt}(2\Delta i_0(t)) \tag{4.18}$$

This implies that the zero-sequence network can be modified by considering $2\Delta i_0$ as the network current and halving the network resistance and inductance values. Fig 4.3 shows the resulting

Clarke component network interconnection for a Phase-A-to-Ground fault. The suffixes (L) and (S) in parameters denote the line and source components respectively.

Therefore, the time domain fault loop equation for the Phase-A-to-Ground fault is as follows.

$$\Delta v_{\alpha^A}(t) = xR_\alpha \cdot \Delta i_{\alpha^A}(t) + xL_\alpha \cdot \frac{d\Delta i_{\alpha^A}(t)}{dt} + \left(\frac{R_0}{2} \cdot \Delta i_{\alpha^A}(t) + \frac{L_0}{2} \cdot \frac{d\Delta i_{\alpha^A}(t)}{dt}\right) \tag{4.19}$$

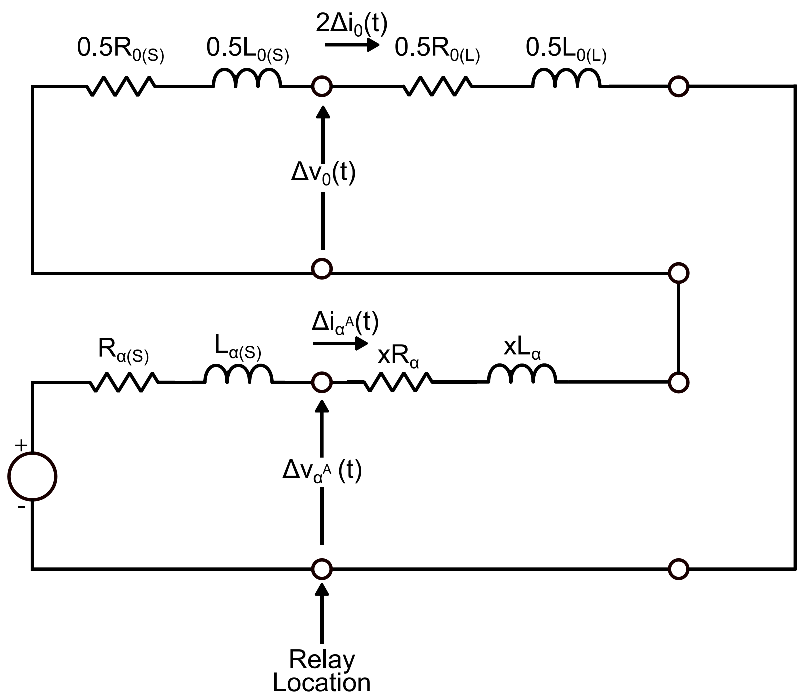

Fig 4.3 Phase-A-to-Ground Fault Loop in Clarke Domain

For a Phase-A-to-ground fault, two other fault loops can be formed considering the α components calculated by taking Phase-B and C as references ($X_{\alpha^B}, X_{\alpha^C}; X \in v, i$). However, the simplest fault loop is formed when the X_{α^A} components are used. In general, for Phase-to-Ground faults, α components computed considering the faulted phase as the reference should be used to get the simplest fault loop. Therefore, for Phase-B-to-Ground faults and Phase-C-to-Ground faults, the fault loops are formed by considering X_{α^B} and X_0 components and X_{α^C} and X_0 components respectively, using a structure similar to the one shown in Fig 4.3.

4.2.4 Phase-to-Phase-to-Ground Fault

The conditions at the fault point for a Phase-B-to-C-to-G short circuit are given in ((4.20) and ((4.21).

$$v_{bF} = v_{cF} = 0 \tag{4.20}$$

$$\Delta i_a = 0 \tag{4.21}$$

Applying the conditions defined in ((4.20) and ((4.21) into ((4.1) shows that at the fault point.

$$\Delta v_{\alpha^A F} = 2\Delta v_{0F}, \qquad \Delta v_{\beta^A F} = 0 \tag{4.22}$$

$$\Delta i_{\alpha^A} = -\Delta i_0 \tag{4.23}$$

According to ((4.22) and ((4.23), during a Phase-to-Phase-to-Ground fault, all three networks are involved in the fault. The expression in ((4.23) indicates a parallel connection between α and 0 component networks during the fault. However, to satisfy ((4.22), the 0-component voltage needs to be amplified by a factor of 2 before the parallel connection. This can be achieved by expressing $2\Delta v_0(t)$ as:

$$2\varDelta v_0(t) = (2R_0)\varDelta i_0(t) + (2L_0)\frac{d}{dt}\varDelta i_0 \tag{4.24}$$

This implies that the 0-network resistance and inductance need to be doubled before connecting in parallel with the α network. Fig 4.4 shows the appropriate Clarke component network connection for a Phase-B-to-C-to-Ground fault. The β network formed for a Phase-to-B-to-C-to-Ground fault is similar to the network formed in a Phase-B-to-C fault. Similar Clarke components networks can be obtained for Phase-A-to-B-to-Ground and Phase-C-to-A-to-Ground faults considering the α-components computed using non-faulted phase as the reference.

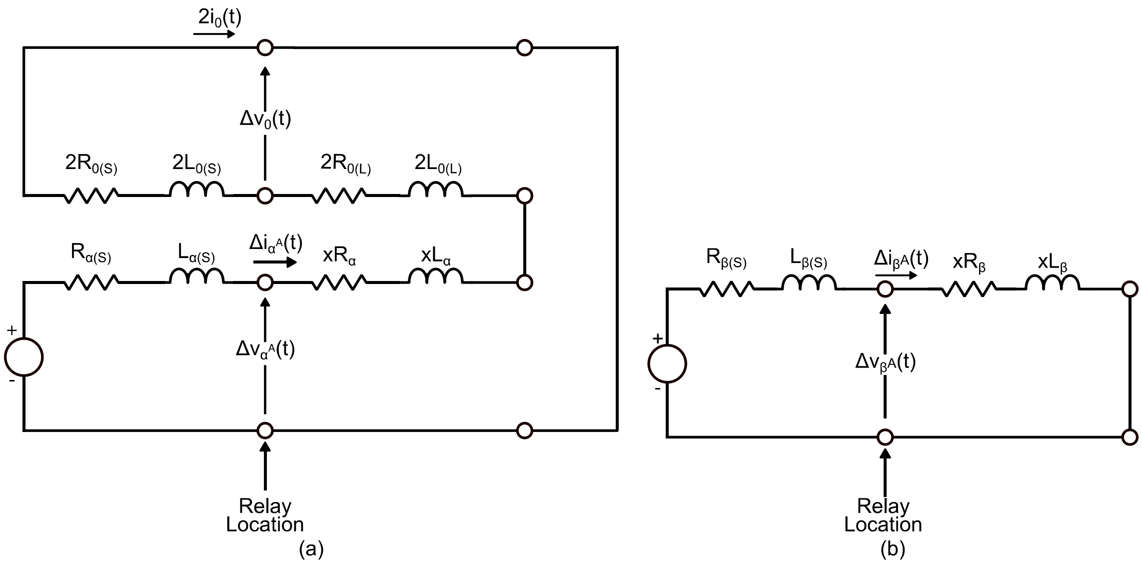

Fig 4.4 (a) Fault Loop Formed Consisting Of α and 0 Network and (b) β Fault Loop Network During Phase-to-Phase-to-Ground Fault

The time domain equations derived for the Clarke fault loops are depicted in Fig 4.4 (a) and (b) as follows. The β loop will be considered when forming the protection scheme since it is much less complex than the α loop.

$$\Delta v_{\alpha^A}(t) = xR_\alpha \cdot \Delta i_{\alpha^A}(t) + xL_\alpha \frac{d\Delta i_{\alpha^A}(t)}{dt} + 2\left(R_0 \cdot \Delta i_{\alpha^A}(t) + L_0 \frac{d\Delta i_{\alpha^A}(t)}{dt}\right) \tag{4.25}$$

$$\Delta v_{\beta^A}(t) = xR_\beta \cdot \Delta i_{\beta^A}(t) + xL_\beta \cdot \frac{d\Delta i_{\beta^A}(t)}{dt} \tag{4.26}$$

Based on the equations presented, a specific fault loop can be used to estimate the resistance and inductance. In the case of three-phase faults, a fault loop consisting of either α or β network can be used to estimate the resistance and inductance of the fault loop. For Phase-to-Phase faults, the fault loop consists of only β network. For Phase-to-Ground faults, the fault loop is formed by combining α and 0 networks. For Phase-to-Phase-to-Ground faults, it is simple to use the fault loop involving only β network. As noted before, the voltages and currents used in the fault loop equations are dependent on the specific phases involved in the fault. Table 4.1 summarizes the Clarke voltages and currents applicable for different fault types.

Table 4.1 Clarke Voltages and Currents Used in Fault Loops

Fault	Clarke Voltage	Clarke Current
AG	$\Delta v_{\alpha^A}(t)$	$\Delta i_{\alpha^A}(t)$
BG	$\Delta v_{\alpha^B}(t)$	$\Delta i_{\alpha^B}(t)$
CG	$\Delta v_{\alpha^C}(t)$	$\Delta i_{\alpha^C}(t)$
ABG/AB	$\Delta v_{\beta^C}(t)$	$\Delta i_{\beta^C}(t)$
ACG/AC	$\Delta v_{\beta^B}(t)$	$\Delta i_{\beta^B}(t)$
BCG/BC	$\Delta v_{\beta^A}(t)$	$\Delta i_{\beta^A}(t)$
ABCG/ABC	$\Delta v_{\alpha^A}(t)/\Delta v_{\beta^A}(t)$	$\Delta i_{\alpha^A}(t)/\Delta i_{\beta^A}(t)$

4.2.5 Incorporating Fault Resistance and Remote Infeed

Boundary conditions and network equations defined in Sections 4.2.1 to 4.2.4 for the considered faults can be used to estimate the resistance and inductance of a fault loop. However, these equations are defined for short circuit faults in a single-ended system. Faults occurring in real power systems are always not short circuits and often there is a source at the remote end resulting in an infeed. Thus, the relationships in ((4.17) and ((4.22) need to be modified to account for nonideal conditions. The ratio between $\Delta i_{\alpha}(t)$ and $i_0(t)$ or $\Delta v_{\alpha^A F}$ and Δv_{0F} will not be exactly equal to 0.5 or 2.0. Therefore ((4.6), ((4.7), ((4.12), ((4.19), ((4.25), and ((4.26) need to be modified to account for fault resistance.

Three-Phase Faults:

$$\Delta v_{\alpha^A}(t) = (xR_\alpha + R_{F\alpha})\Delta i_{\alpha^A}(t) + xL_\alpha \frac{d\Delta i_{\alpha^A}(t)}{dt} \tag{4.27}$$

$$\Delta v_{\beta^A}(t) = \left(xR_\beta + R_{F\beta}\right)\Delta i_{\beta^A}(t) + xL_\beta \frac{d\Delta i_{\beta^A}(t)}{dt} \tag{4.28}$$

Phase-B-to-C Fault:

$$\Delta v_{\beta^A}(t) = \left(xR_\beta + R_{F\beta}\right)\Delta i_{\beta^A}(t) + xL_\beta \frac{d\Delta i_{\beta^A}(t)}{dt} \tag{4.29}$$

Phase-A-to-Ground Fault:

$$\Delta v_{\alpha^A}(t) = (xR_\alpha + k_0 R_0 + R_{F\alpha})\Delta i_{\alpha^A}(t) + (xL_\alpha + k_0 L_0)\frac{d\Delta i_{\alpha^A}(t)}{dt} \tag{4.30}$$

Phase-B-to-C-to-Ground Fault:

$$\Delta v_{\alpha^A}(t) = (xR_\alpha + k_0 R_0 + R_{F\alpha})\Delta i_{\alpha^A}(t) + (xL_\alpha + k_0 L_0)\frac{d\Delta i_{\alpha^A}(t)}{dt} \tag{4.31}$$

$$\Delta v_{\beta^A}(t) = \left(xR_\beta + R_{F\beta}\right)\Delta i_{\beta^A}(t) + xL_\beta \frac{d\Delta i_{\beta^A}(t)}{dt} \tag{4.32}$$

Here, $R_{F\alpha}$ and $R_{F\beta}$ is the fault resistance in each fault loop seen by the relay and k_0 is the actual ratio between $\Delta i_\alpha(t)$ and $\Delta i_0(t)$ as defined in ((4.33).

$$k_0 = \frac{\Delta i_0(t)}{\Delta i_\alpha(t)} \tag{4.33}$$

Since zero sequence voltages and currents do not exist in the balanced steady state, typically $\Delta v_0 = v_0$ and $\Delta i_0 = i_0$. As mentioned in Section 4.2.3, the 0-component network consists of both the source and line zero-sequence parameters. Therefore R_0 and L_0 terms in ((4.30) and ((4.31) can be expanded as:

$$\begin{aligned} k_0 R_0 &= k_0\left(xR_{0(L)} + R_{0(S)}\right) \\ k_0 L_0 &= k_0\left(xL_{0(L)} + L_{0(S)}\right) \end{aligned} \tag{4.34}$$

The source zero sequence resistance and inductance can be estimated using a least square-like approach from the measured zero sequence incremental quantities at the relay point [72] considering ((4.35).

$$\Delta v_0(t) = -\left(R_{0(S)}\Delta i_0(t) + L_{0(S)}\frac{d\Delta i_0(t)}{dt}\right) \tag{4.35}$$

4.3 Protection Algorithm

Section 4.2 introduced the Clarke equivalent networks formed during different fault conditions and the relationship between fault loop voltage and currents in the Clarke domain for each fault type. Furthermore, the practical considerations related to these equations were also explored in the previous section. Developing the protection algorithm is explained hereafter.

4.3.1 Estimation of Clarke Fault Loop Components

Consider the signal is sampled at a frequency of f_s with a window of N_w samples, the least square method can be applied to estimate Clarke fault loop resistance and inductances.

$$[C] = ([\Delta I]^T \Delta I)^{-1} \Delta I^T \Delta V \tag{4.36}$$

where,

$$C = [\hat{R}_{TC} \quad \hat{L}_{TC}]^T$$

$$\Delta I = \begin{bmatrix} \Delta i_C(0) & \frac{d}{dt}\Delta i_C(0) \\ \vdots & \vdots \\ \Delta i_C(N_w - 1) & \frac{d}{dt}\Delta i_C(N_w - 1) \end{bmatrix}$$

$$\Delta V = [\Delta v_C(0) \quad \cdots \quad \Delta v_C(N_w - 1)]^T$$

where, Δv_C and Δi_C incremental Clarke voltages and currents, and $\hat{R}_{TC}$ and $\hat{L}_{TC}$ are the total resistance and inductance of the applicable Clarke equivalent circuit, with $C \in [\alpha, \beta]$. For α fault loop (fault loop generated during Phase-to-Ground fault),

$$\hat{R}_{T\alpha} = xR_\alpha + k_0 R_0 + R_{F\alpha}$$

$$\hat{L}_{T\alpha} = xL_\alpha + k_0 L_0$$

By subtracting the source side parts contained in R_0 and L_0, the fault loop resistance and inductance seen on the line side of the relay can be written as,

$$\begin{aligned} \hat{R}_{T\alpha\,(Fwd)} &= \hat{R}_{T\alpha} - k_0 R_{0(S)} \\ \hat{R}_{T\alpha\,(Fwd)} &= xR_\alpha + k_0 x R_{0(L)} + R_{F\alpha} \end{aligned} \tag{4.37}$$

$$\begin{aligned} \hat{L}_{T\alpha(Fwd)} &= \hat{L}_{T\alpha} - k_0 L_{0(S)} \\ \hat{L}_{T\alpha(Fwd)} &= xL_\alpha + k_0 x L_{0(L)} \end{aligned} \tag{4.38}$$

$R_{0(S)}$ and $L_{0(S)}$ can be estimated using ((4.35).

For β fault loop (fault loop generated during Phase-to-Phase, Phase-to-Phase-to-Ground, and Three-Phase faults) equations, there is no involvement of source side parameters, thus,

$$\hat{R}_{T\beta(Fwd)} = \hat{R}_{T\beta} = xR_\beta + R_{F\beta} \tag{4.39}$$

$$\hat{L}_{T\beta(Fwd)} = xL_\beta \tag{4.40}$$

4.3.2 Estimation of Fault Location

The fault location can also be estimated as an additional output from ((4.38) and ((4.40). If line zero sequence and positive sequence inductances are known, ((4.38) can be rewritten considering that α network inductance of the line is equal to its positive sequence inductance:

$$\hat{L}_{T\alpha(Fwd)} = xL_1(1 + k_0 k') \tag{4.41}$$

where $k' = L_{0(L)}/L_{1(L)}$ is the ratio of the line zero sequence and positive sequence inductances. Then the fault location in α fault loop can also be estimated as:

$$x = \frac{\hat{L}_{T\alpha(Fwd)}}{L_{1(L)}(1 + k_0 k')} \tag{4.42}$$

Similarly, the fault location in β fault loop can be estimated assuming that the β network inductance of the line is equal to its positive sequence inductance:

$$x = \frac{\hat{L}_{T\beta(Fwd)}}{L_{1(L)}} \tag{4.43}$$

4.3.3 Defining Protection Zones and Zone Setting Calculations

For the Clarke equivalent network-based line protection scheme, the use of protection zones defined on the L-R plane is proposed. To implement the scheme, magnitude comparators are used, because, in the proposed methodology, *L* and *R* are directly estimated as two scalar values. Also, for the forward direction, only positive values of *L* and *R* are expected, and therefore, no negative resistance reach is needed in the forward zones; similarly, no positive resistance reach is needed in the reverse zones. However, a safety margin can be left to account for measurement and numerical errors. Fig 4.5 (a) and (b) show the protective zones for Phase-to-Ground and Phase-to-Phase / Phase-to-Phase-to-Ground / Three-Phase faults.

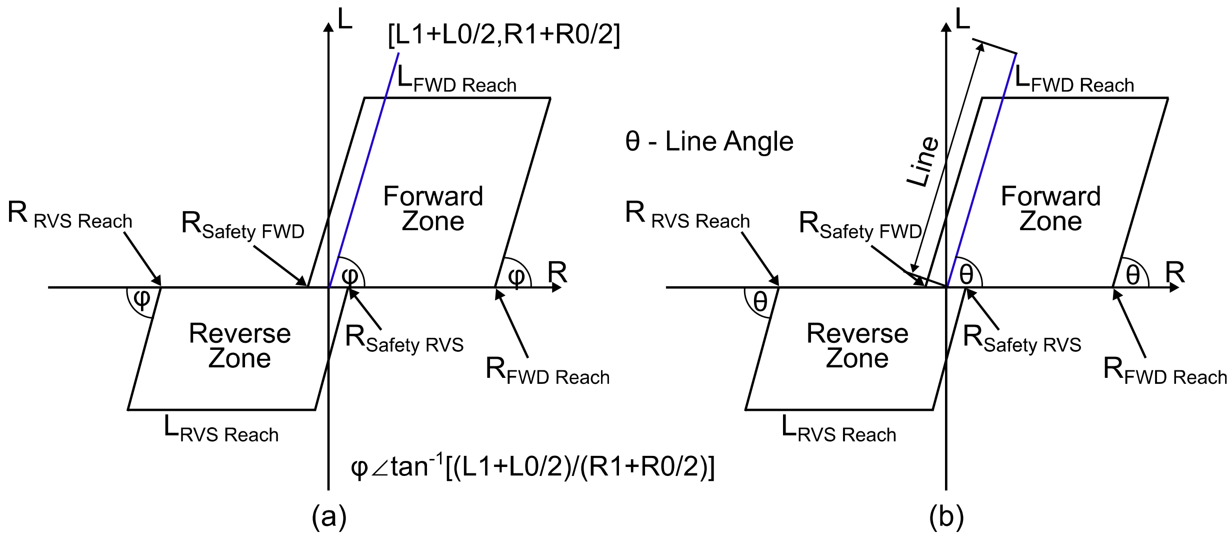

Fig 4.5 Defined Protective Zone for (a) Phase-to-Ground Faults and (b) Phase-to-Phase/ Phase-to-Phase-to-Ground/ Three-Phase Faults

4.3.3.1 Phase-to-Phase Faults

Using ((4.39) and ((4.40), the apparent inductance and resistance of a Phase-to-Phase fault are estimated. The distance relay should operate if the coordinate of estimated resistance and inductance lies inside an operating zone defined by the respective reach settings as shown in Fig 4.5. Two inequalities in ((4.44) and ((4.45) will be true for a fault inside the protected zone.

$$0 < \hat{L}_{T\beta} < L_{reach} \tag{4.44}$$

$$R_{safety} < \hat{R}_{T\beta} < R_{reach} \tag{4.45}$$

4.3.3.2 Phase-to-Ground Faults

The inequalities relevant to Phase-to-Ground faults are specified in ((4.46) and ((4.47), where $\hat{L}_{T\alpha}$ and $\hat{R}_{T\alpha}$ represent the estimates of inductance and resistance for the Phase-to-Ground fault loop using ((4.37) and ((4.38).

$$0 < \hat{L}_{T\alpha} < L_{reach} \tag{4.46}$$

$$R_{safety} < \hat{R}_{T\alpha} < R_{reach} \tag{4.47}$$

4.3.3.3 Reach Settings

The n[th] zone reach for α loops is given by ((4.48) where L_1 and L_0 are the line positive sequence inductance and line zero-sequence inductance respectively.

$$L_{reach} = (L_1 + L_0/2) \times \ (Zone_n Reach\ \%) \times \frac{CTR}{PTR} \tag{4.48}$$

The equation to calculate the inductance reach for the n[th] zone in β fault loop is given by ((4.49) where L_1 is the line positive sequence inductance.

$$L_{reach} = L_1 \times (Zone_n\ Reach\ \%) \times \frac{CTR}{PTR} \tag{4.49}$$

The resistive reach is set based on the amount of fault resistance that needs to be covered. Hence the resistive reach settings were calculated as follows.

$$R_{reach} = Covered\ Reach \times \frac{CTR}{PTR} (sec. \Omega) \tag{4.50}$$

Here, covered reach is the expected fault resistance to be covered.

The angle Θ in Fig 4.5 (b) denotes the line angle $\varphi = \tan^{-1}\left(\frac{L1+L0/2}{R1+R0/2}\right)$.

4.3.4 Algorithm Implementation

Fig 4.6 depicts the implemented instantaneous distance protection algorithm. First, the instantaneous current and voltage samples are measured and transformed into Clarke components using the transformation given in ((4.1). High-frequency signal components in the sampled voltages and currents are removed by low-pass filtering. Incremental Clarke component currents are calculated after transforming the filtered currents using the equation given in ((4.51)

$$\Delta i(n) = i(n) - i(n - kN) \tag{4.51}$$

where Δi is the instantaneous incremental current, k is the number of periods and N is the period of the measured quantity.

Incremental quantities last for k power cycles. After k power cycles the quantities expire since historical values slide into the fault period. Since the power system sources remain stationary for a short period typically around a few tens of milliseconds [7], a frequency tracking algorithm is not required when calculating instantaneous incremental quantities.

Since Clarke voltages denoted in the equations are the voltage drops in the Clarke networks, it is equivalent to the measured voltages. The incremental Clarke currents are used for fault detection. A fault is detected by comparing the incremental Clarke currents against a predefined threshold. This adaptive threshold is set to 5% of the pre-fault RMS current.

Transformed voltage and current samples are stored in a moving window. Then the 0, α, and β loop resistances and inductances are calculated using least-square estimation. It is assumed that the phase selection decision received from a phase selection logic is used to identify the correct fault loop. Upon identifying the correct fault loop, the check is performed to determine whether the fault point (on the L-R plane) is within the protection zone or not. If it is inside the zone, a trip is issued after confirming the condition for a pre-set number of consecutive calculations. The decision to issue an instantaneous trip or a time-delayed trip is based on whether the fault point is inside the instantaneous zone (Zone 1) or in a time-delayed zone. Although it is not necessary to apply fast instantaneous incremental currents-based protection for zones operating with time delay, faster operation of Zone 2 and reverse zone can be advantageous when transfer trip schemes are used. Since the proposed method allows providing backup protection to forward and reverse zones without additional calculations except for the comparison of already estimated apparent L and R

values with the respective backup zone reach values, it is proposed to implement a forward Zone 2 and a reverse zone (Zone 3).

If a trip is not issued, the algorithm checks for a fault in the system and if there is a fault, then the buffers are updated with new measurements, and the k_0 value is updated. If there is no fault in the system, the algorithm waits for a new fault to happen. To avoid the occurrence of transient tripping, a trip command is not issued unless twelve consecutive points are inside the defined zone boundary. The number of consecutive calculations required to confirm a decision was determined through a trial-and-error approach, and it was found that the number of samples covering about 15% of a cycle provides sufficient security without significantly slowing down the operating time. If the speed is more important, the number can be decreased to cover about 10% of a cycle without significant degradation in security. This is a very common practice that is been used in protection relays to improve security, but when using phasor quantities, only two or three consecutive calculations are sufficient for confirmation.

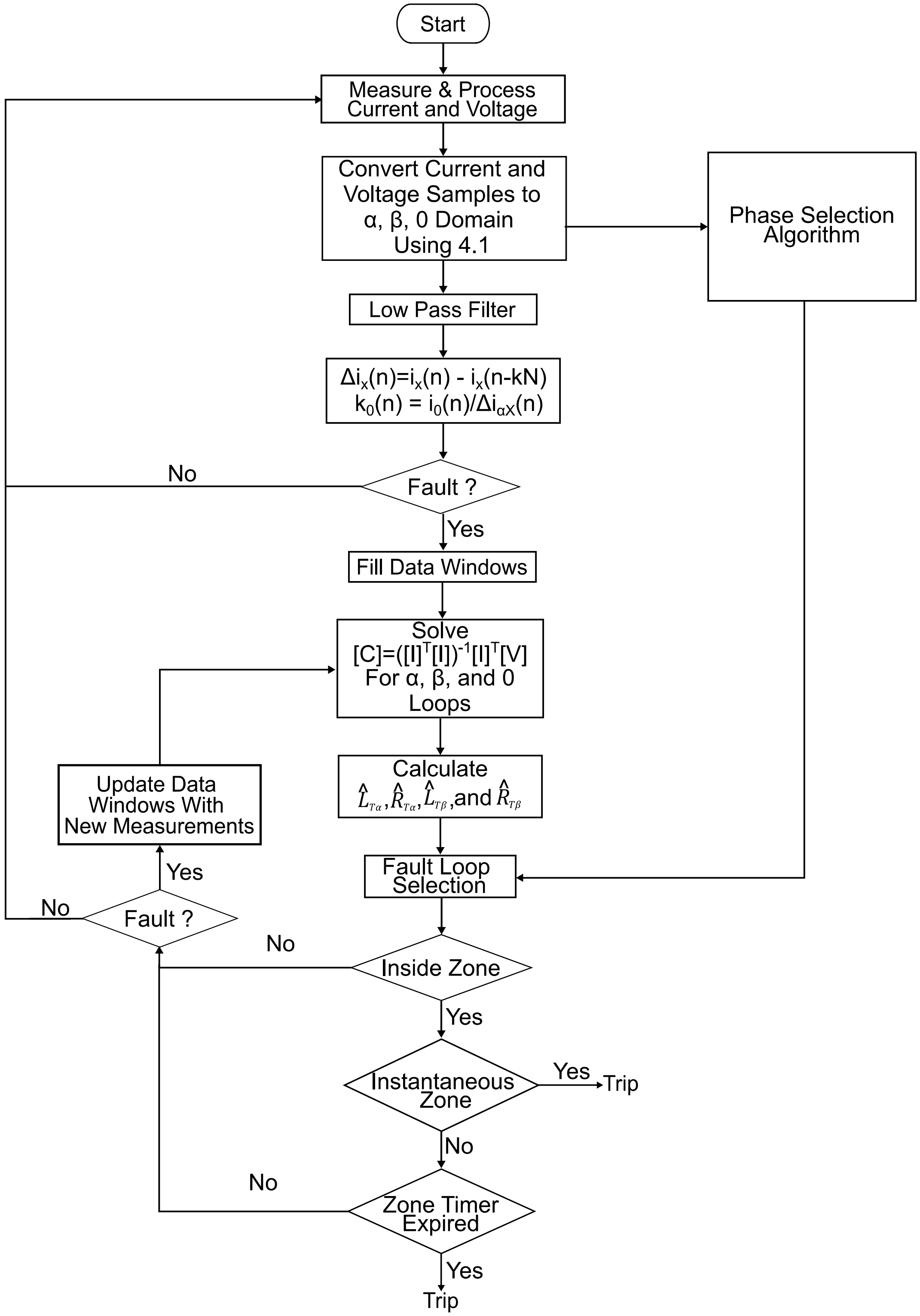

Fig 4.6 Protection Algorithm

4.3.5 Test System and Reach Setting Calculation

The power system depicted in Fig 4.7 (a) was simulated in PSCAD/EMTDC™ with a 10 μs time step to evaluate the proposed method. The main reason for using a small time step of 10 μs was to enable simulating close-in faults. In EMT simulations, the shortest transmission line segment that can be simulated using frequency dependent models is determined by the time step, as the wave travel time needs be longer than the simulation time step. The local and remote systems of the power system were portrayed as three-phase voltage sources. The source impedances for local and remote systems are provided in Table 4.4. The transmission lines were configured as 3-conductor flat tower type as illustrated in Fig 4.7 (b) and represented using frequency-dependent phase domain models. The ground return path was approximated using a ground plane with a resistivity of 100 Ωm.

The JA model [67] and Lucas model [68] from the PSCAD/EMTDC protection library were utilized to simulate the CT and PT. The CT had a ratio of 1000:5, and the PT had a ratio of 230000:115. Details regarding the transmission line parameters at 50 Hz and conductor data can be found in Tables Table 4.2 and Table 4.3. CT and PT model parameters are presented in Tables Table 4.5 and 4.6, respectively.

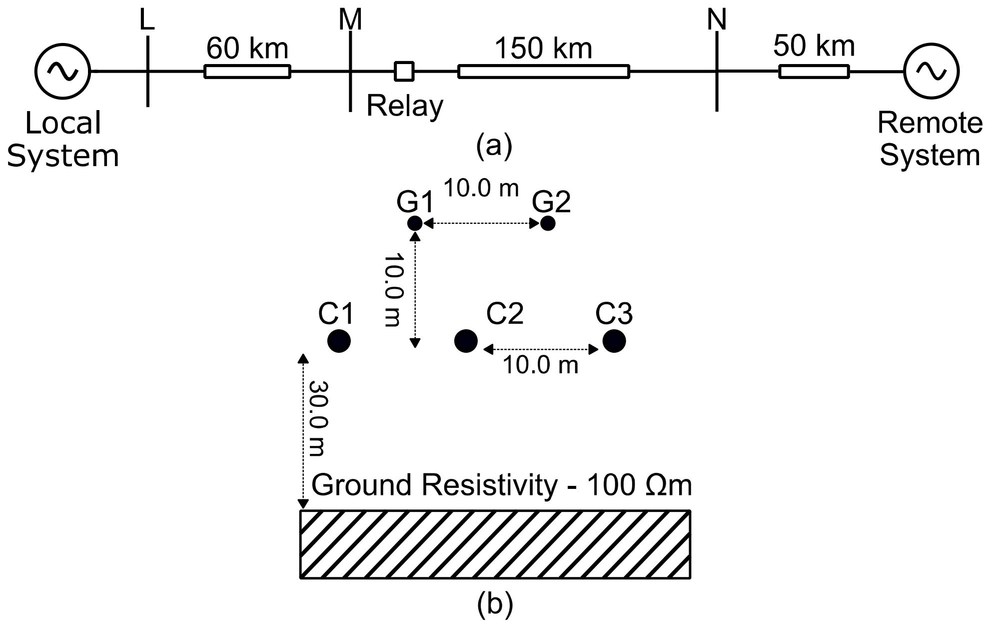

Fig 4.7 (a) Considered Power System and (b) Transmission Line Design

Table 4.2 Transmission Line Parameters (230 kV, 100 MVA Base)

Parameter	**Value (p.u)**	**Parameter**	**Value (p.u)**
R_1	0.00967	R_0	0.08160
X_1	0.11839	X_0	0.32614

Table 4.3 Transmission Line Conductor Data

Conductor	**Resistance**	**Radius**
Phase	0.0203 Ω/km	0.032 m
Ground	2.8645 Ω/km	0.0055 m

Table 4.4 Local and Remote Source Impedances

Source	Z_1 **(Ω)**	Z_0 **(Ω)**
Local System	$1.077\angle 87.65^{o}$	$0.897\angle 80.86^{o}$
Remote System	$3.8\angle 87.69^{o}$	$6.02\angle 80.9^{o}$

Table 4.5 Parameters of the Current Transformer

Parameter	Value
Turns Ratio	240
Resistance (Secondary)	0.5 Ω
Inductance (Secondary)	0.8×10^{-3} H
Core Section Area	2.601×10^{-3} m^2
Burden Resistance	0.5 Ω
Burden Inductance	0.8×10^{-3} H

Table 4.6 Parameters of the Potential Transformer

Parameter	Value
Primary Resistance (on secondary)	0.05 Ω
Primary Inductance (on secondary)	0.47×10^{-3} H
Resistance (Secondary)	0.18 Ω
Inductance (Secondary)	0.47×10^{-3} H
Hysteresis Loss	5.0 W
Eddy Current Loss	2.5 W
Operating Voltage (Secondary)	115 V
Nominal Frequency	50 Hz
Operating Flux Density	0.8 T
Series Burden Resistance	301.0 Ω
Series Burden Inductance	2.4 H
Parallel Burden Resistance	785.0 Ω

The waveforms generated by faults were sampled at a rate of 80 samples per cycle and saved as CSV files. Subsequently, these CSV files were fed into the Clarke equivalent network-based instantaneous distance protection scheme implemented in MATLAB/Simulink. The delay used for computing incremental quantities was three cycles (k = 3). Two sets of settings need to be calculated considering the α and β loops. The relay comprises two forward zones and a reverse zone. Zone settings are set as Zone 1 = 80%, Zone 2 = 120%, and Zone 3 = -30% of line length for both α and β loops. Reach settings are determined as described in the next sub-sections.

4.3.5.1 Inductance Reach Calculation

Settings for α fault loop were computed using ((4.48). The resulting inductance reach settings are given in Table 4.7.

Table 4.7 Inductance Reach Setting for α Loop

	Zone 1	**Zone 2**	**Zone 3**
L_{Reach} *(forward)*	0.0401	0.0602	0
L_{Reach} *(reverse)*	0	0	-0.015

The inductance reach values for the β fault loop were computed using ((4.49). The computed inductance reach settings are given in Table 4.8.

Table 4.8 Inductance Reach Setting for β Loop

	Zone 1	**Zone 2**	**Zone 3**
L_{Reach} *(forward)*	0.0159	0.0239	0
L_{Reach} *(reverse)*	0	0	-0.006

4.3.5.2 Resistive Reach Calculation

The resistive reach was set using ((4.50) considering the required fault resistance coverage. The forward Zone 1 was set to cover 25 Ω fault resistance and Zone 2 was set to cover 50 Ω resistance. The reverse zone resistance reach was set to cover 20 Ω fault resistance. The value of R_{safety} mentioned in Section 4.3.2 was set to 30% of the respective forward/reverse value. The settings calculated for α and β loops are given in Tables Table 4.9 and Table 4.10.

Table 4.9 Resistance Reach Settings for α Loop

	Zone 1	**Zone 2**	**Zone 3**
R_{Reach} *(forward)*	5.167 Ω	7.667 Ω	1.400 Ω
R_{Reach} *(reverse)*	-1.550 Ω	-2.300 Ω	–4.667 Ω

Table 4.10 Resistance Reach Settings for β Loop

	Zone 1	**Zone 2**	**Zone 3**
R_{Reach} *(forward)*	3.01 Ω	5.51 Ω	0.7530 Ω
R_{Reach} *(reverse)*	–0.903 Ω	–1.653 Ω	–2.51 Ω

4.3.5.3 Least Squares Computational Complexity, Window Length, and Low Pass Filter Cutoff Frequency

The proposed algorithm uses linear least squares (LLS) to estimate the fault loop inductance and resistance. The total cost of solving the LLS problem is approximately $mn^2 + \frac{n^3}{3}$ where m is the number of samples and *n* is the number of features. Therefore, the proposed algorithm requires 42 floating point operations for each new sample in one of the Clarke fault loops. Considering the 80 samples per cycle sampling rate, 1 million floating point operations per second (MFLOPS) would be required to calculate the six Clarke fault loops. In comparison, 100 MFLOPS were used in conventional IEDs more than ten years ago [73]. Furthermore, the matrix $[\Delta I]^T[\Delta I]$ in the least square equation is a 2×2 non-singular, real-valued, symmetrical matrix irrespective of the number of measurements, and thus the inverse of the matrix can be calculated easily reducing the computational burden.

A compromise between speed and accuracy needs to be made when selecting a reasonable least square data window. A longer data window width would ensure accurate estimates of fault loop inductance and resistance at the cost of speed. Whereas a shorter window length would increase the speed while reducing the accuracy which could lead to spurious tripping. Therefore, a data window of 10 samples, i.e., $N_w = 10$ (1/8$^{\text{th}}$ of a cycle at 80 samples/cycle) was used in the least square estimation as a compromise between the faster response and reliable operation.

Instantaneous incremental quantities contain all the frequency components including the decaying dc component, the fault component of the fundamental frequency, and the high-frequency transients. The proposed algorithm is only interested in the fundamental component of the instantaneous incremental quantities. Therefore, the low-pass filter's cutoff frequency was set to 150 Hz. This cutoff frequency is effective for both 50 Hz and 60 Hz systems and removes the higher-order harmonics and signal noise that can impact the *L* and *R* estimations. These reasonable values for the sample window length and low-pass filter cutoff frequency were selected and confirmed through simulation studies, employing a methodical sensitivity study.

4.3.6 Demonstration of Algorithm

4.3.6.1 Forward Faults

The operation for forward faults was demonstrated using Phase-A-to-Ground, Phase-B-to-C-to-Ground, Phase-A-to-C, and Three-Phase short circuits applied at 10 % of the protected line (Line MN). The trajectory of fault loop inductance against the fault loop resistance is plotted in Fig 4.8 for the applied faults. The plotted values are obtained from the applicable fault loop: from α loops for Phase-A-to-Ground; and β loops for Phase-B-to-C-to-Ground, Phase-A-to-C, and Three-Phase faults.

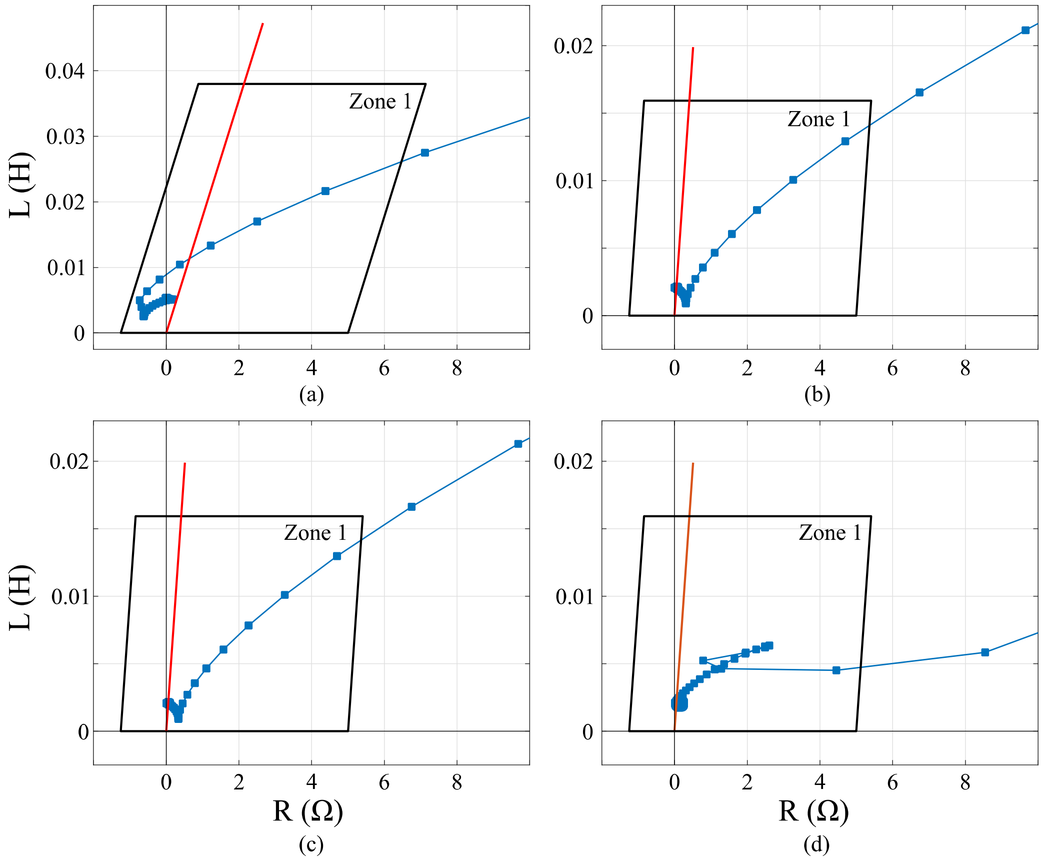

Fig 4.8 Trajectory of Fault Loop Inductance against Fault Loop Resistance for (a) Phase-A-to-Ground, (b) Phase-B-to-C-to-Ground, (c) Phase-A-to-C, and (d) Three-Phase Short Circuit Faults on Forward Direction

4.3.6.2 Reverse and Zone 2 Faults

a) Reverse Faults

To illustrate the operation for reverse faults, short circuit faults were applied at the middle of the line LM, which is within Zone 3. The trajectory of fault loop inductance against fault loop resistance is depicted in Fig 4.9 for Phase-A-to-Ground (Fig 4.9 (a)), Phase-B-to-C-to-Ground (Fig 4.9 (b)), Phase-A-to-C (Fig 4.9 (c)), and Three-Phase (Fig 4.9 (d)) faults respectively.

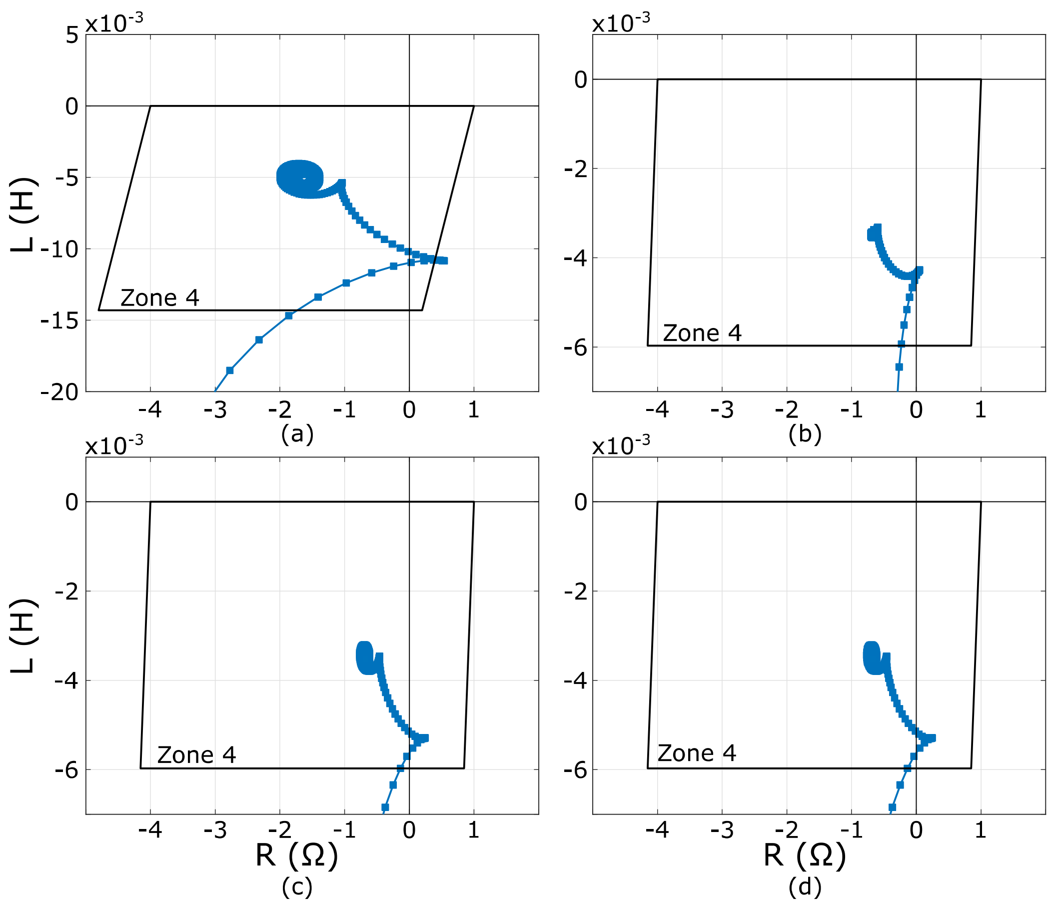

Fig 4.9 Trajectory of Fault Loop Inductance against Fault Loop Resistance for (a) Phase-A-to-Ground, (b) Phase-B-to-C-to-Ground, (c) Phase-A-to-C, and (d) Three-Phase Short Circuit Faults on Reverse Direction

b) Zone 2 Faults

Fig 4.10 shows the impedance trajectory for Zone 2 faults applied in the power system. Faults were applied at 100% of the line length of the protected line. Fig 4.10 (a), Fig 4.10 (b), and Fig 4.10 (c) show the impedance trajectories for Phase-B-to-Ground, Phase-A-to-C-to-Ground, and Phase-A-to-B short circuit faults respectively. In Fig 4.10, the inductance-resistance trajectories enter Zone 1 momentarily. However, it does not lead to a trip signal since there needs to be at least 12 consecutive points (at 80 samples/cycle) inside the zone to issue a trip signal. In addition to that, the inductance-resistance trajectory tends to move away from the line as the fault location moves away from the relay location due to the effect of infeed in the system. When the fault location moves toward the remote end of the line, the contribution to the fault current from the remote source increases. This will lead to an increase in estimation error since the estimation equation is derived assuming the system is single-ended.

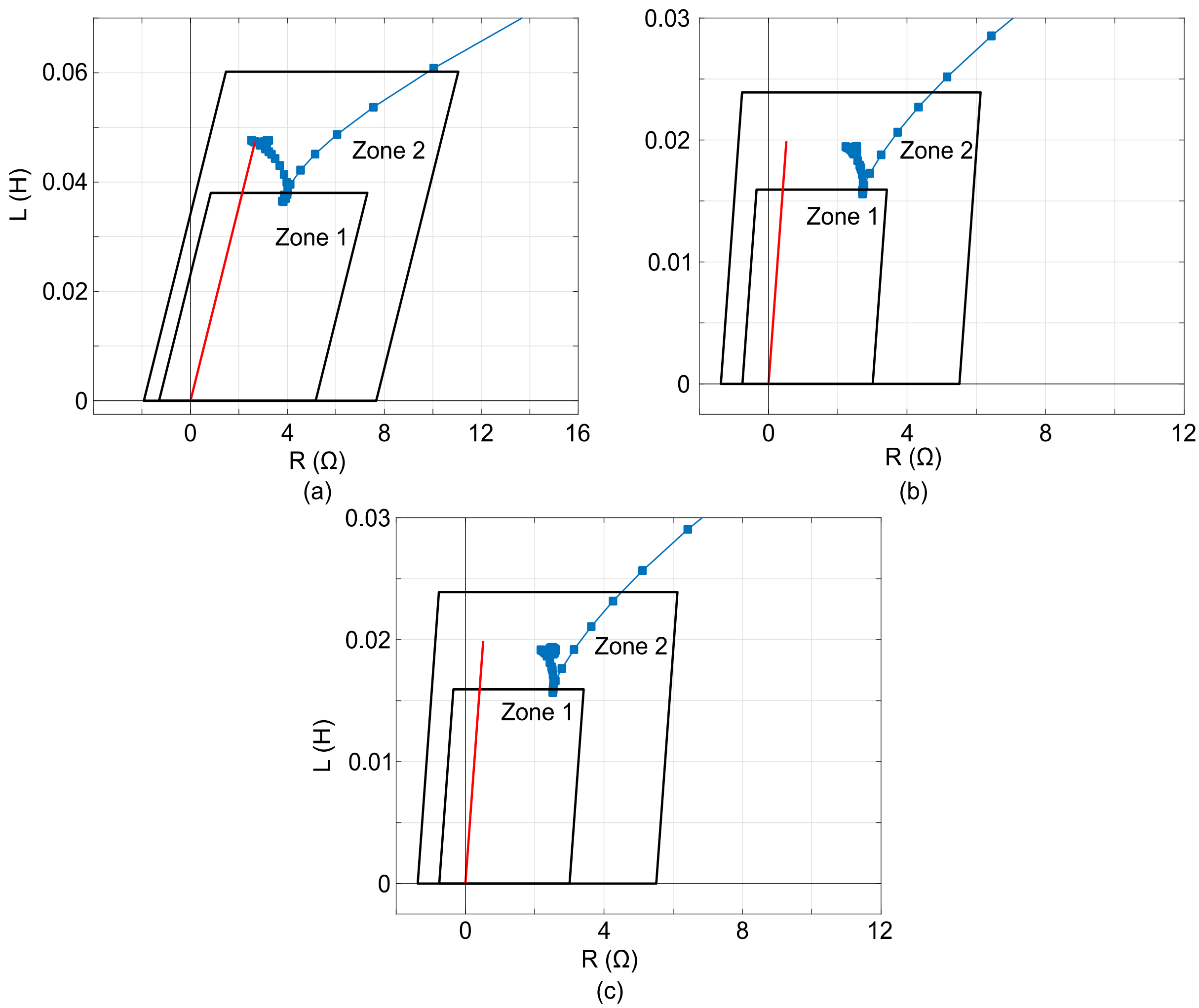

Fig 4.10 Zone 2 Short Circuit Faults Applied on the Power System (a) Phase-B-to-Ground, (b) Phase-A-to-C-to-Ground, and (c) Phase-A-to-B Fault

4.3.6.3 Performance Analysis of the Proposed Method

a) Short Circuit Faults

Table 4.11 shows operating times for Zone 1 Phase-to-Ground, Phase-to-Phase-to-Ground, and Phase-to-Phase faults for faults applied on Line-MN at four different fault locations (10%, 50%, 75%, and 90% of Line Length).

Table 4.11 Zone 1 Operating Time for Short Circuit Faults

Fault Type	**10%**	**50%**	**75%**	**90%**
AG	7.5 ms	8.25 ms	9.0 ms	-
BG	7.5 ms	8.25 ms	9.0 ms	-
CG	7.5 ms	8.25 ms	9.0 ms	-
ABG	7.5 ms	8.5 ms	9.25 ms	-
ACG	7.5 ms	8.5 ms	9.25 ms	-
BCG	7.5 ms	8.5 ms	9.25 ms	-
AB	7.5 ms	8.5 ms	9.25 ms	-
BC	7.5 ms	8.5 ms	9.25 ms	-
AC	7.5 ms	8.5 ms	9.25 ms	-

The protective zone was defined as 80% of the line length for Zone 1 which trips instantaneously. As seen from the results for fault locations less than 80% of the line length, the proposed method trips within 10 ms of fault inception whereas for 90% of line length Zone 1 element does not issue a trip signal as expected.

b) Effects of Fault Resistance and Infeed

Tables Table 4.12 and Table 4.13 show the operating times obtained for Phase-to-Ground, Phase-to-Phase-to-Ground, and Phase-to-Phase faults applied with fault resistances of 5 Ω, and 25 Ω respectively. The coverage of the proposed methods was reduced with increasing fault resistance. This is not unusual, even in the traditional phasor-based distance relays, the coverage is reduced with increasing fault resistance. The coverage for Phase-to-Ground and Phase-to-Phase-to-Ground faults was reduced to 60% of the line and this is partly due to $k_0 x R_{0(L)}$ component in

((4.37), which was not considered in the resistive reach setting. However, it should be noted that the fault resistance of most of the faults that occur at transmission levels is less than 5 Ω.

The effect of the fault resistance on the estimated inductance and resistance is depicted in Fig 4.11. At 10% of line length, a Phase-A-to-Ground fault was applied with four different fault resistances (Short Circuit, 5 Ω, 10 Ω, and 25 Ω). With increasing fault resistance, the final settling point of the inductance-resistance trajectory shifts to the right on the L-R plane.

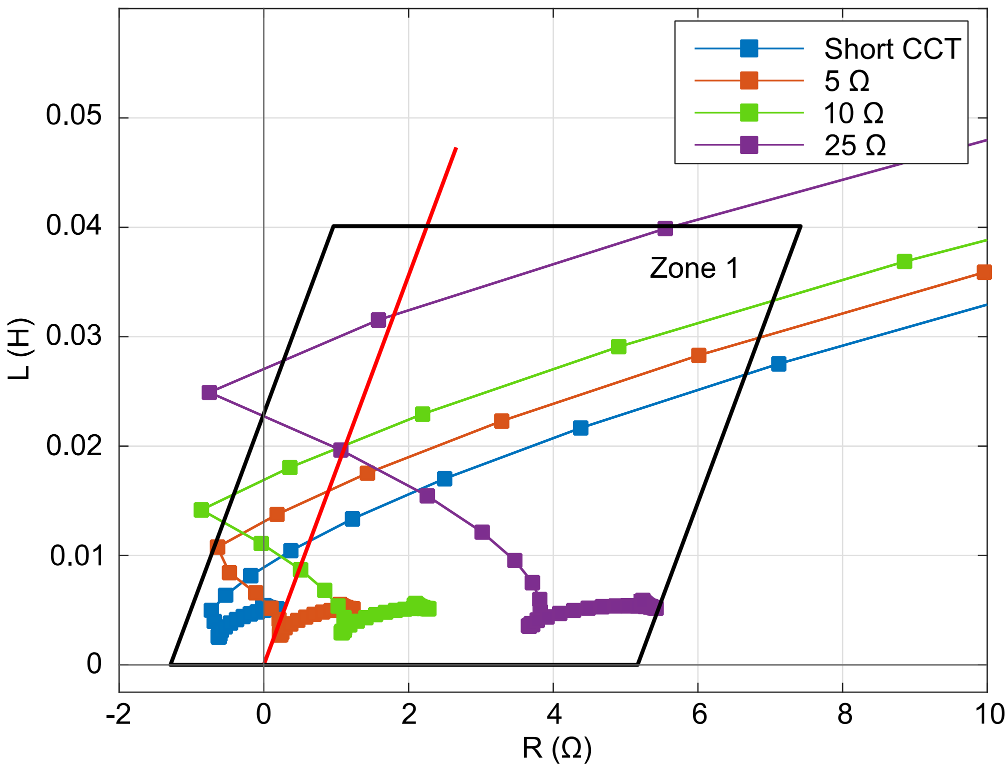

Fig 4.11 Effect of Fault Resistance on the Estimated Fault Loop Inductance and Resistance

However, the proposed method still covers up to 70% of the line length for Phase-to-Phase faults for fault resistances up to 10 Ω. An increase of fault resistance up to 50 Ω further reduced the protection coverage to 50% in Phase-to-Ground and Phase-to-Phase-to-Ground faults and up to 60% in Phase-to-Phase faults. However, the operating time remained almost constant even with high resistance fault scenarios.

Table 4.12 Zone 1 Operating Time for Faults With 5 Ω Resistance

Fault Type	**10%**	**50%**	**75%**	**90%**
AG	7.5 ms	8.25 ms	9.0 ms	-
BG	7.5 ms	8.25 ms	9.0 ms	-
CG	7.5 ms	9.75 ms	9.725 ms	-
ABG	7.5 ms	8.5 ms	9.25 ms	-
ACG	7.5 ms	8.5 ms	9.25 ms	-
BCG	7.5 ms	8.5 ms	9.25 ms	-
AB	7.5 ms	8.5 ms	9.25 ms	-
BC	7.5 ms	8.5 ms	9.25 ms	-
AC	7.5 ms	8.5 ms	9.25 ms	-

Table 4.13 Zone 1 Operating Time for Faults With 25 Ω Resistance

Fault Type	**10%**	**50%**	**75%**	**90%**
AG	8.0 ms	8.5 ms	-	-
BG	8.0 ms	8.5 ms	-	-
CG	8.0 ms	8.5 ms	-	-
ABG	7.5 ms	8.75 ms	-	-
ACG	7.5 ms	8.75 ms	-	-
BCG	7.5 ms	8.75 ms	-	-
AB	7.5 ms	8.5 ms	-	-
BC	7.5 ms	8.5 ms	-	-
AC	7.5 ms	8.5 ms	-	-

As observed from Table 4.13, the proposed method fails to provide coverage for faults at 75% of line length at 25 Ω fault resistance. This is due to the impact of remote infeed in the system. The inductance and resistance estimation equations were derived for the single-infeed short circuit faults, but in the test system, there is a contribution to fault current from a remote infeed. The effect of infeed is depicted in Fig 4.12 where the inductance-resistance trajectory of a Phase-A-to-Ground fault with 25 Ω fault resistance is plotted with infeed and without infeed. The without-infeed scenario was simulated by disconnecting the remote system at bus N in the power system shown in Fig 4.7 (a). As depicted in Fig 4.12, the final settling point of the inductance-resistance trajectory moves away from the Zone 1 boundary when the remote system is connected. Whereas, when the remote system is disconnected, the point moves inside the Zone 1 boundary which leads to a trip decision. This effect is present even in the traditional distance relays. It is possible to devise some approximate compensation based on the remote system equivalent inductance to reduce this effect, but this was not attempted.

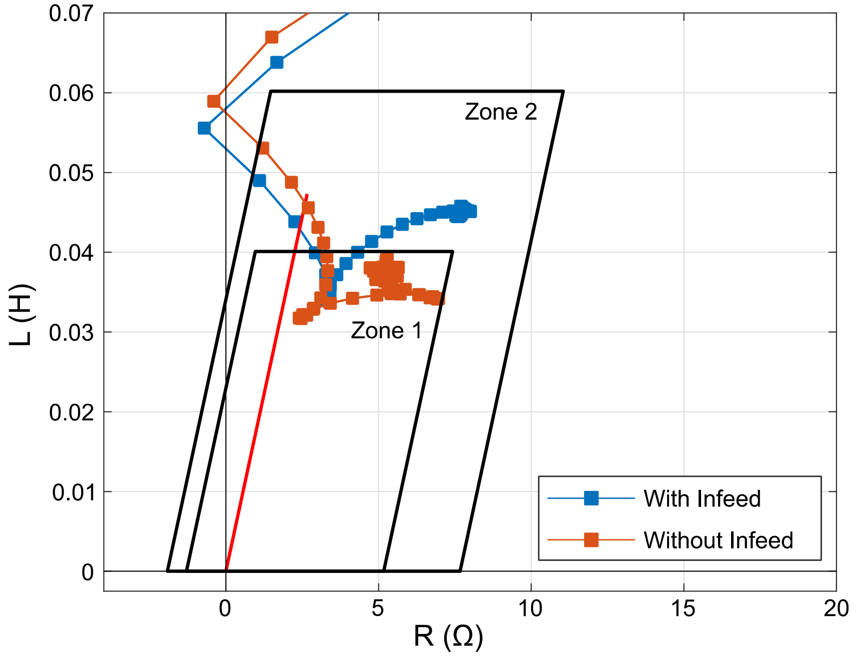

Fig 4.12 Estimated Inductance-Resistance Trajectory with and without the Remote Infeed

4.3.6.4 Effect of Line Transposition

The line transposition scheme or non-transposed transmission lines influence Clarke transformation equations as they are defined for ideally transposed transmission lines. This is common to sequence components as well. Since real-world transmission lines are either non-transposed or non-ideally transposed transmission lines, the effect of transposition on the proposed scheme must be investigated.

a) Non-ideally (Manually) Transposed Transmission Line

The non-ideally transposed transmission line was simulated by manually transposing the protected transmission line MN in the power system depicted in Fig 4.7 (a) as shown in Fig 4.13.

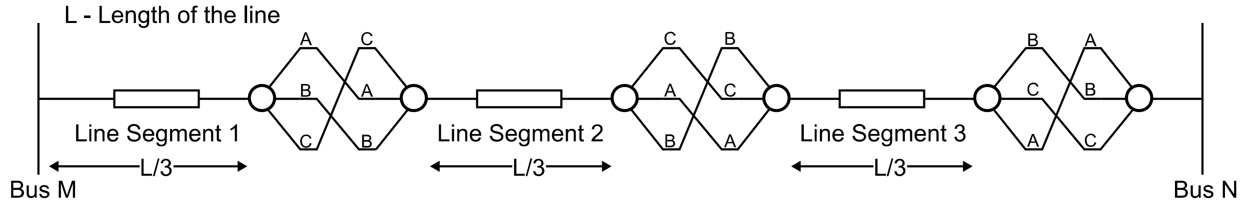

Fig 4.13 Manual Transposition of Transmission Line

Fig 4.14 shows the variation of instantaneous incremental currents of Clarke currents calculated with respect to Phase-A (Δi_{α^A}, Δi_{β^A}, and Δi_0) for ideally transposed transmission line and manually transposed transmission line. Fig 4.14 (a), (d), and (g) depicts the waveforms for a fault applied at 10% of line length. Fig 4.14 (b), (e), and (h) depict the waveforms for a fault applied at 50% of line length whereas Fig 4.14 (c), (f), and (i) depict the waveforms for a fault applied at 90% of line length. Even though the current waveforms of Δi_{β^A} currents for all shown fault conditions deviates from the ideally transformed transmission line cases, very little deviation can be observed in Δi_{α^A} and Δi_0 currents which forms the Clarke fault loop for Phase-A-to-Ground faults. A similar observation can be made for instantaneous Clarke currents for other Phase-to-Ground faults as well.

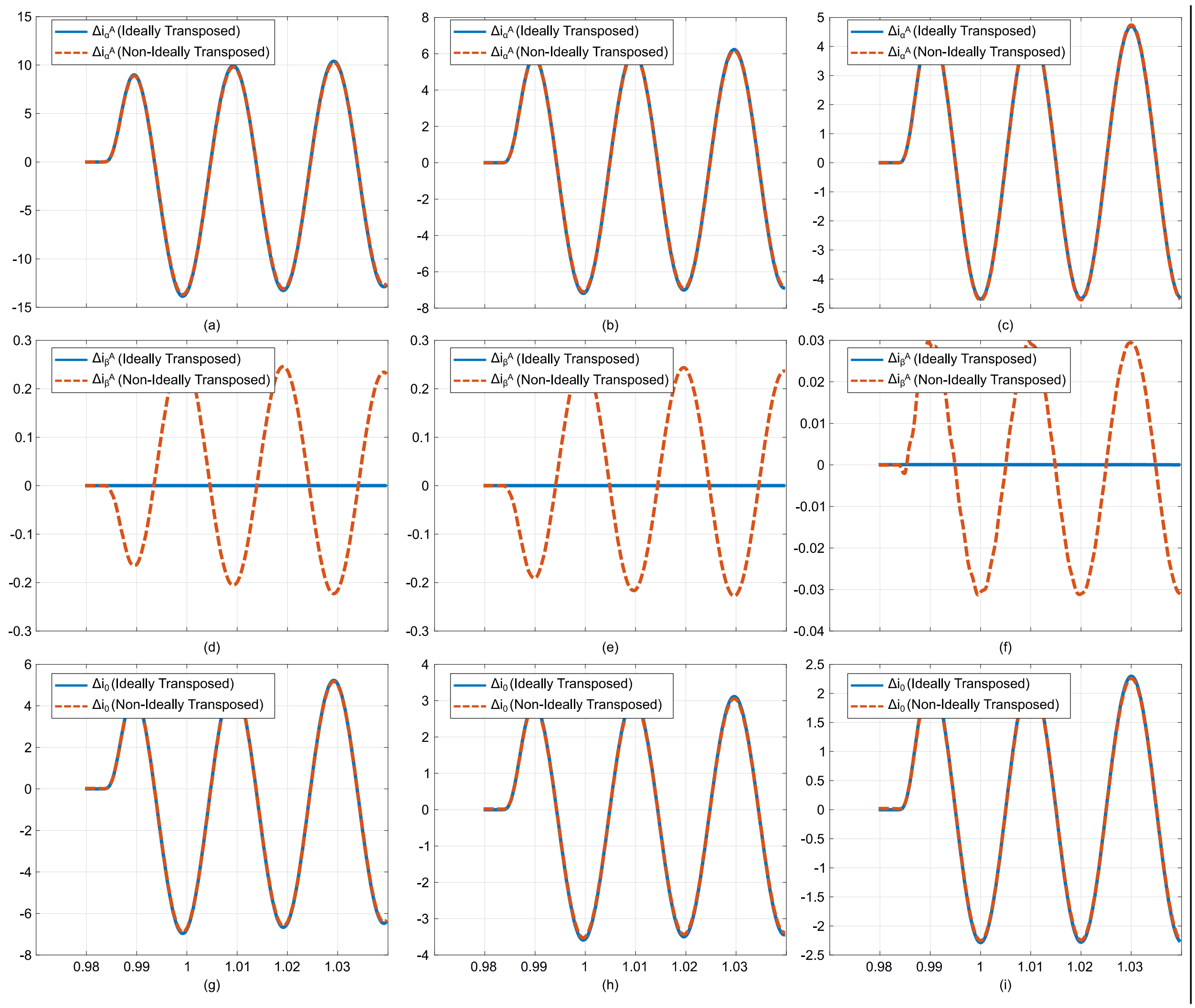

Fig 4.14 Incremental Clarke Currents for Phase-A-to-Ground Faults Applied at 10%, 50%, and 90% of Line Length

Fig 4.15 depicts the variation of instantaneous incremental Clarke currents calculated with respect to Phase-A for Phase-B-to-C-to-Ground faults applied at 10%, 50%, and 90% of line length. Variations for the ideally transposed transmission line and manually transposed transmission line are plotted in the same plot. A slight difference can be observed in Δi_{α^A} current components. However, Δi_{β^A} and Δi_0 current variations are almost identical for ideally transposed and manually transposed transmission lines.

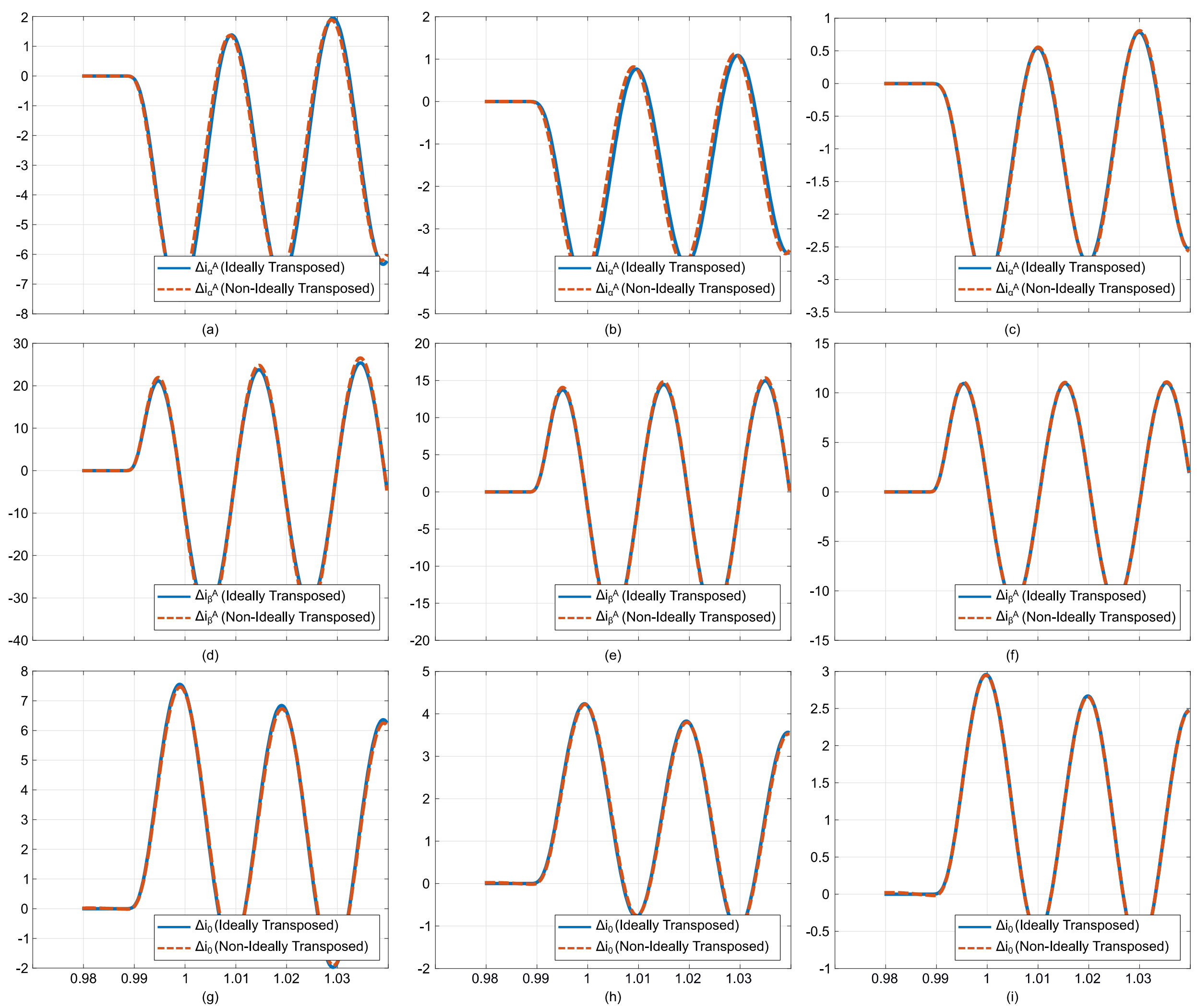

Fig 4.15 Incremental Clarke Currents for Phase-B-to-C-to-Ground Faults Applied at 10%, 50%, and 90% of Line Length

Variation of instantaneous incremental Clarke currents calculated with respect to Phase-B during Phase-A-to-C faults applied at 10%, 50%, and 90% of line length are depicted in Fig 4.16 for both ideally transposed and manually transposed transmission lines. Fig 4.16 (a), (d), and (g) show the current waveforms for the fault at 10% line length. Fig 4.16 (b), (e), and (h) show the current waveforms for the fault at 50% of the line length whereas Fig 4.16 (c), (f), and (i) show the current waveforms for the fault at 90% of line length respectively. Some deviation can be observed in both Δi_α and Δi_0 current components due to the unbalance caused by transposition. However,

Δi_{β^B} components calculated for manually transposed transmission line have little deviation from the ideally transposed transmission line. Therefore, the effect on fault loop inductance and resistance is minimized.

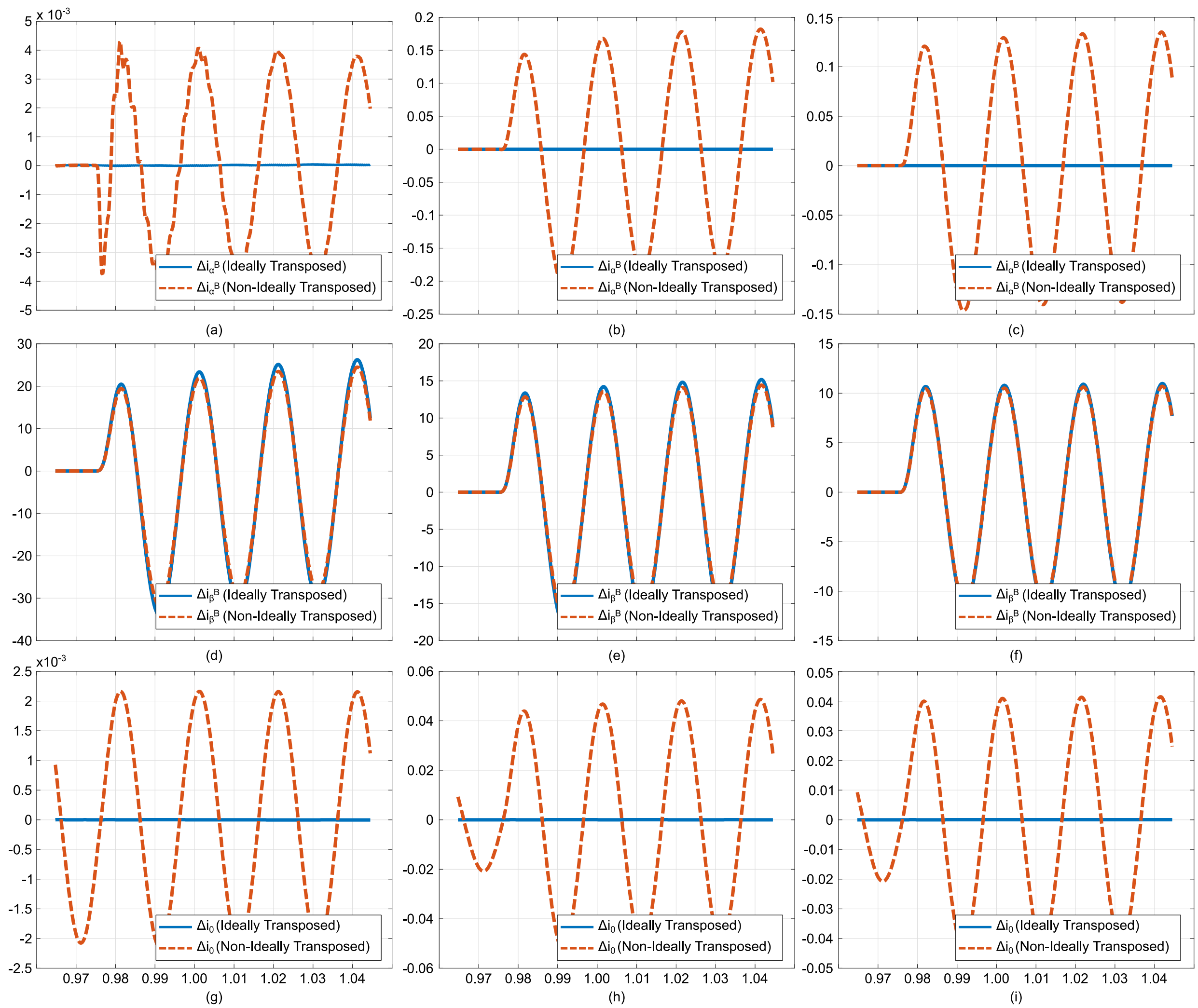

Fig 4.16 Incremental Clarke Currents for Phase-A-to-C Faults Applied at 10%, 50%, and 90% of Line Length

Table 4.14 summarizes the operating times for short circuit faults applied at 10%, 50%, 80%, and 90% line lengths in the manually transposed transmission line. Compared to the ideally transposed transmission line results shown in Table 4.11, the difference between the operating times is insignificant. This is due to the fact that there is little difference between the variation of instantaneous incremental Clarke currents forming the fault loop in ideally transposed and manually transposed transmission lines.

Table 4.14 Operating Times for Short Circuit Faults Applied on the Manually Transposed Transmission Line Model

Fault Type	**10%**	**50%**	**80%**	**90%**
AG	8.0 ms	8.5 ms	9.25 ms	-
BG	8.0 ms	8.5 ms	9.25 ms	-
CG	8.0 ms	8.75 ms	9.5 ms	-
ABG	8.0 ms	8.75 ms	9.5 ms	-
ACG	8.25 ms	8.75 ms	9.5 ms	-
BCG	8.0 ms	8.75 ms	9.5 ms	-
AB	8.0 ms	8.75 ms	9.5 ms	-
BC	8.25 ms	8.75 ms	9.5 ms	-
AC	8.0 ms	8.75 ms	9.5 ms	-

b) Non-transposed Transmission Line

The protected transmission line in the system was modeled as a non-transposed transmission line by disabling the ideal transposition in the PSCAD/EMTDC™ frequency-dependent transmission line component.

Fig 4.17 shows the variation of instantaneous incremental Clarke current components calculated Phase-A-to-Ground, Phase-B-to-C-to-Ground, and Phase-A-to-C faults applied at 10% of the protected line. Compared to the manually transposed transmission line, a considerable deviation can be observed in the current measured in the non-transposed transmission line. Thus, it would lead to reduced performance in non-transposed transmission lines compared to manually transposed transmission lines.

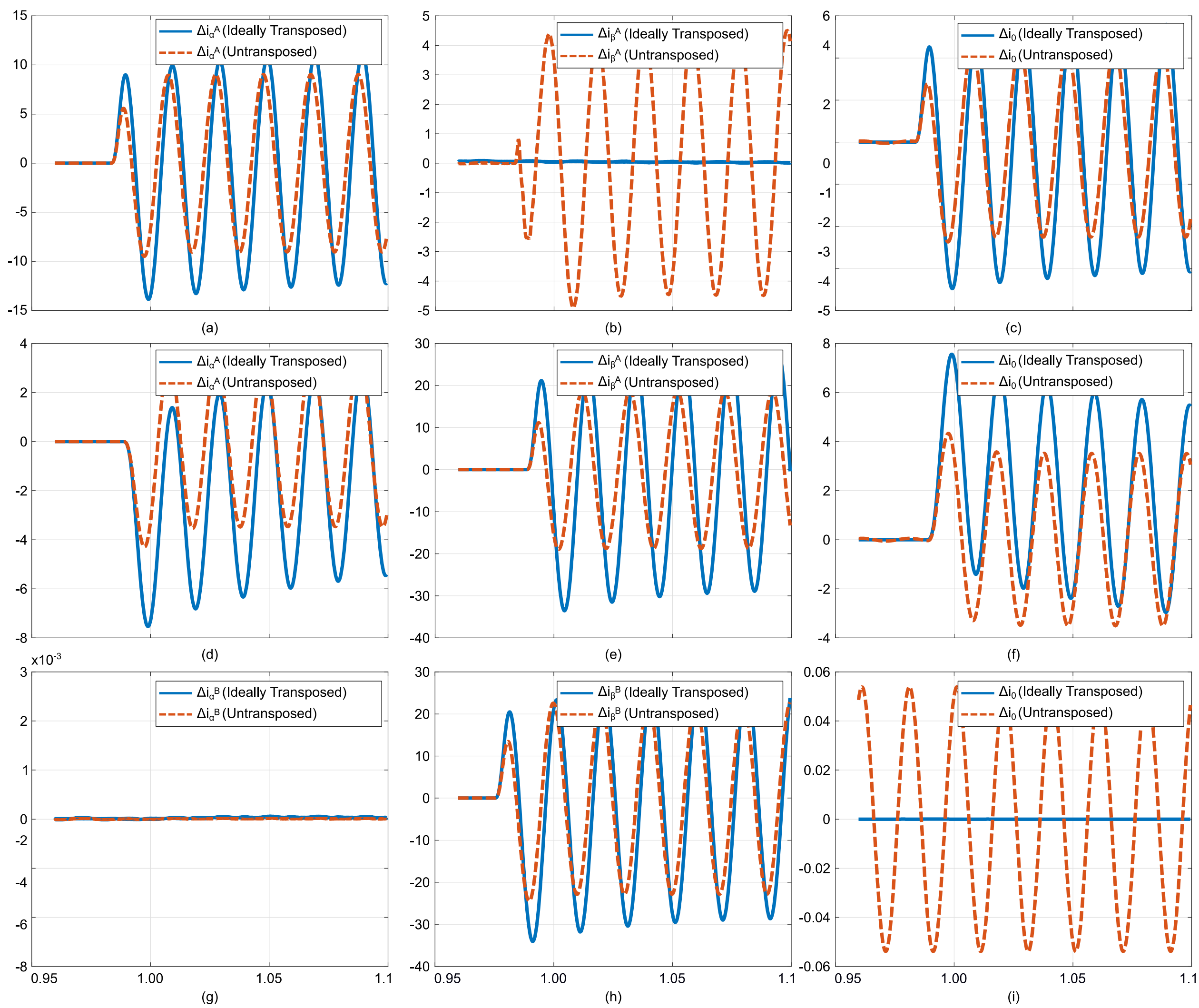

Fig 4.17 Instantaneous Incremental Clarka components Calculated for Phase-A-to-Ground Fault (a) – (c), Phase-B-to-C-to-Ground Fault (d) – (f), and Phase-A-to-C-Fault (g) – (i).

Table 4.15 summarizes the operating times for short circuit faults applied at 10%, 50%, 60%, 70%, and 80% line lengths in the manually transposed transmission line. Compared to the ideally transposed transmission line results shown in Table 4.11, a reduction in coverage for non-transposed transmission lines can be observed where the algorithm only covers up to 60% of the line length.

Table 4.15 Operating Times for Short Circuit Faults Applied on the non-transposed Transmission Line Model

Fault Type	10%	50%	60%	70%	80%
AG	8.3 ms	8.8 ms	9.0 ms	-	-
BG	8.2 ms	8.8 ms	9.0 ms	-	-
CG	8.3 ms	8.8 ms	9.0 ms	-	-
ABG	7.7 ms	9.0 ms	9.2 ms	-	-
ACG	8.0 ms	9.0 ms	9.2 ms	-	-
BCG	7.8 ms	8.8 ms	9.3 ms	-	-
AB	7.7 ms	8.7 ms	9.0 ms	-	-
BC	7.8 ms	8.8 ms	9.0 ms	-	-
AC	7.8 ms	9.0 ms	9.2 ms	-	-

4.3.6.5 Performance Comparison with Standard Distance Relay

The proposed protection scheme's performance was evaluated by utilizing MHO and QUAD relay models, developed using algorithms outlined in relay manuals [70], and integrated into the PSCAD/EMTDC™ software. As a result, the developed relay models provide a response that is similar to relay models available in the real world. Only the Zone 1 MHO and QUAD elements in the PSCAD relay model were enabled to compare the operating time of the proposed method against the standard distance relay mode. Zone 1 reach setting was set at 80% of the line length. For phasor estimation, the PSCAD relay model utilizes DFT with a mimic filter to filter out the decaying DC component. Zone 1 Phase-A-to-Ground faults were applied to compare the operating times of the proposed Clarke component-based distance relay and the standard MHO and QUAD distance relays. Faults were applied at 10%, 50%, and 75% of the line length with fault inception angles of 0º, 45º and 90º. Both short circuit faults and high impedance (25 Ω) faults were considered. Table 4.16 and provide the results.

Table 4.16 Operating Time for $R_f = 0\ \Omega$

Inception angle	**Fault Location**	**CCN Protection Scheme**	**DFT-based Standard Mho Relay**	**DFT-based Standard Quad Relay**
0º	10%	1.875 ms	2.3 ms	7.0 ms
	50%	8.1 ms	9.8 ms	15.25 ms
	75%	10.9 ms	15.0 ms	20.5 ms
45º	10%	5.35 ms	5.25 ms	7.0 ms
	50%	6.35 ms	11.0 ms	13.5 ms
	75%	7.85 ms	16.8 ms	18.75 ms
90º	10%	7.5 ms	9.5 ms	9.0 ms
	50%	8.25 ms	17.0 ms	15.0 ms
	75%	9.0 ms	20.75 ms	19.5 ms

Table 4.17 Operating Time for $R_f = 25\ \Omega$

Inception angle	Fault Location	CCN Protection Scheme	DFT-based Standard Mho Relay	DFT-based Standard Quad Relay
0º	10%	2.1 ms	9.0 ms	10.75 ms
	50%	5.6 ms	-	14.25 ms
	75%	-	-	22.25 ms
45º	10%	4.85 ms	8.75 ms	8.75 ms
	50%	6.6 ms	17.0 ms	13.75 ms
	75%	-	-	20.0 ms
90º	10%	8.0 ms	12.0 ms	9.0 ms
	50%	8.5 ms	19.0 ms	17.25 ms
	75%	-	-	20.5 ms

The proposed method demonstrates quicker operation compared to the MHO and QUAD relays for faults across all examined fault inception angles, resistances, and locations. Furthermore, the proposed method provides equal or better coverage compared to the standard MHO relay for high-impedance fault conditions at all considered fault inception angles. However, the QUAD relay model provided coverage for all high-resistive faults proving it to be the better option to cover high resistive faults. Compared to both MHO and QUAD relays, the proposed method is twice as fast for remote faults in most cases. This is more prominent in faults with high fault resistance. Hence the objective of fast-tripping is achieved by the proposed Clarke components-based instantaneous line protection scheme. Although a direct comparison was not made, the operating time of the proposed algorithm is slower than the published results for the time domain protection method proposed in [74] - [76]. This is because the proposed method needs a short data window to estimate apparent L and R values using the least square estimation and waits for multiple points to be inside the zone boundary to provide robust decisions. However, the tripping times of the proposed method are well within the half-cycle time, which is considered the most beneficial, from an overall power system perspective [77].

4.3.6.6 Fault Location Estimation

Fig 4.18 demonstrates the proposed method's ability to estimate the fault location. Fault location estimates for Phase-A-to-B short circuit faults applied in 10% increments from 10% to 90% of line length are depicted in Fig 4.18. During the initial transient period, the fault location estimates are underestimated. However, after the initial transient period that lasts for about 5 ms, the location estimates settle around the expected location fairly accurately as shown in Fig 4.18. Accuracy slightly drops when the fault is closer to the remote end, due to the impact of remote infeed.

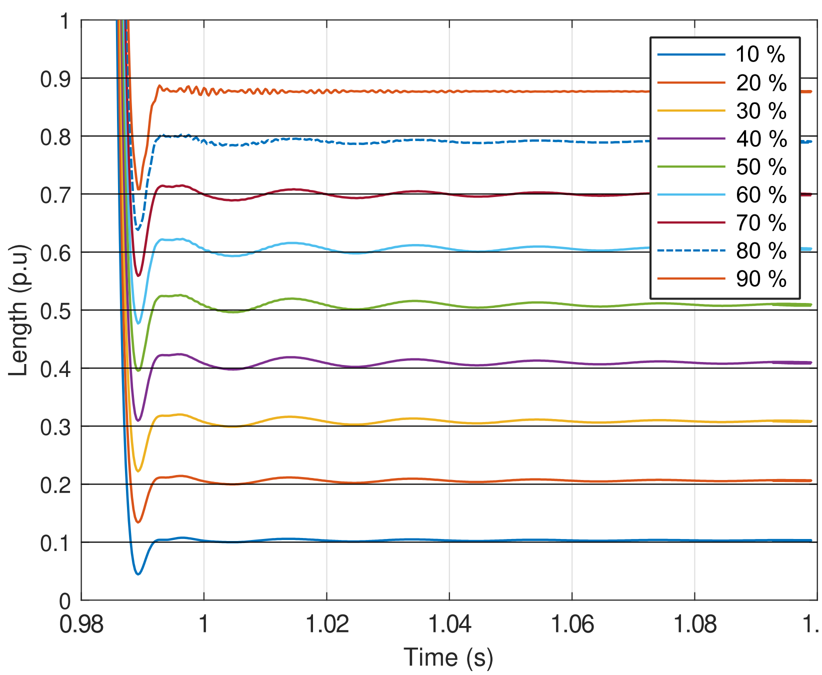

Fig 4.18 Fault Location Estimate for Short Circuit Phase-A-to-B Fault with Time

4.4 Concluding Remarks

This chapter proposed a new Clarke component-based instantaneous line protection algorithm. Using the fundamental principles as a starting point, fault loop equations were derived for each fault type to estimate the resistance and inductance. Additionally, equations were derived to estimate the fault location. Fault loop inductance and resistance were estimated using least-squares estimation using time-domain sampled values. A line distance protection scheme with directional capabilities was implemented using the estimated inductance and resistance values.

The proposed method has the following features/advantages: It can be set up to implement multiple protection zones using amplitude comparators enabling the provision of backup protection for remote and reverse faults. The protection zones can be configured to provide coverage for a desired fault resistance. Unlike some of the other instantaneous quantities-based protection algorithms proposed in the literature, the proposed method does not require additional thresholds or knowledge of the source impedance as an input parameter for the calculations. The use of Clarke components is expected to minimize the impacts of mutual coupling between the conductors.

In comparison with the standard Mho and Quad distance relays, the proposed relay showed improved operating time, especially for remote faults where the operating time improved by twice as much as the standard phasor-based relay models. The proposed Clarke component network-based method operated satisfactorily for high impedance faults but with a slightly reduced coverage. However, performance was still better than the standard Mho distance relay both in terms of operating time and dependability and has a faster operating time than the standard Quad distance relay, but with slightly lower dependability. Even though the operating time of the proposed relay is slower than some of the published literature, it still lies within the half-cycle time which is considered the most beneficial. The proposed method provides accurate results on manually transposed transmission lines. However, long non-transposed transmission lines can have a noticeable effect on the performance of the proposed protection element, which is not a concern as the long lines are always transposed in practice.

Chapter 5

Fault Type and Faulted Phase Identification Using Clarke Components of Transient Currents

Chapter 4 introduced a line protection algorithm using Clarke components of the instantaneous voltages and current measurements. Integrating this algorithm into a practical line protection scheme requires a fast method to identify the fault type and phases involved in the fault, a task generally referred to as the phase selection in the protection literature, to identify the correct fault loop. This chapter presents a very fast phase selection algorithm that utilizes the Clarke components of the fault-generated current transients.

5.1 Introduction

A properly implemented phase selection scheme should (i) allow the faulted loops in the distance relay to operate while blocking the healthy loops and (ii) enable single-pole tripping and reclosing schemes by differentiating single-phase faults from multi-phase faults. With the growing penetration of IBRs, the inertia of power systems is reduced, and strict stability margins are introduced to maintain the system stability. Therefore, critical clearing times are reduced and the faults in the system must be cleared faster. Hence faulted phase selection schemes must operate within a short time window after the inception of a fault to ensure the prompt and correct operation of protection schemes.

Faulted phase selection schemes can be categorized into three groups: i) phasor-based methods; ii) superimposed component-based methods [78], [79]; and iii) transient component-based methods [80]. The problem of fault classification can be divided into a multistep process consisting of two major steps: (i) identification of the 'fault type', and (ii) identification of the 'faulted phases'. The term 'fault type identification' refers to the process of determining whether a fault is a, (i) Phase-to-Ground fault, (ii) Phase-to-Phase fault, (iii) Phase-to-Phase-to-Ground fault, or a, (iv) Three-Phase fault. The term 'faulted phase identification' refers to the process of identifying the phases involved in a fault, after the identification of its type.

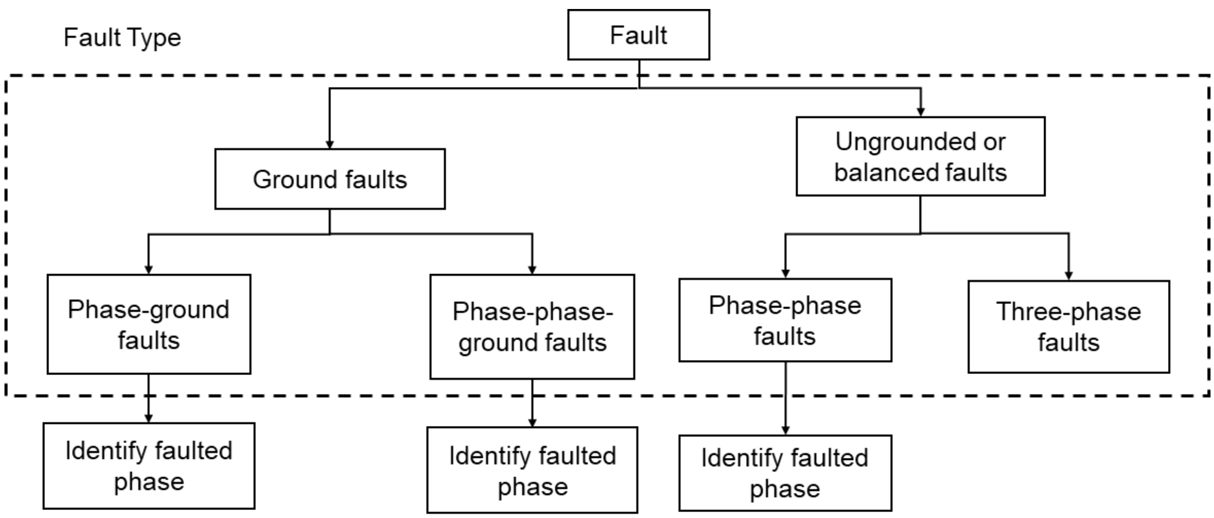

Fig 5.1 Steps in the Process of Identifying Fault Type and Faulted Phases

5.1.1 Phasor-Based Faulted Phase Selection Methods

Conventional phasor-based protection algorithms rely on the typical characteristics of fault currents from the synchronous generators and the reactive nature of the network impedances. These algorithms exploit the fact that the currents during faults exhibit certain characteristics such as higher magnitudes (than load currents), asymmetry (for asymmetrical faults), and predictable phase angle relationships between voltages and currents. Many of the relay manufacturers use symmetrical component-based techniques for faulted phase identification [81], [82]. Different relay manufacturers use slightly modified versions of this method, but all its variants measure the phase angles between sequence currents and/or voltages to determine the phase(s) involved in a fault.

The most commonly used faulted phase selection algorithms used in conventional phasor-based algorithms determine the phases involved in a fault based on the phase angle signature of Phase-A sequence currents. The symmetrical component theory and the boundary conditions at the fault dictate that the phase angle difference between negative and zero sequence currents (α) lies within the distinct regions for different types of ground faults as shown in Fig 5.2 (a). Different but unique regions exist for the phase angle difference between the negative and the positive sequence current phasors (β) during ground faults as shown in Fig 5.2 (b).

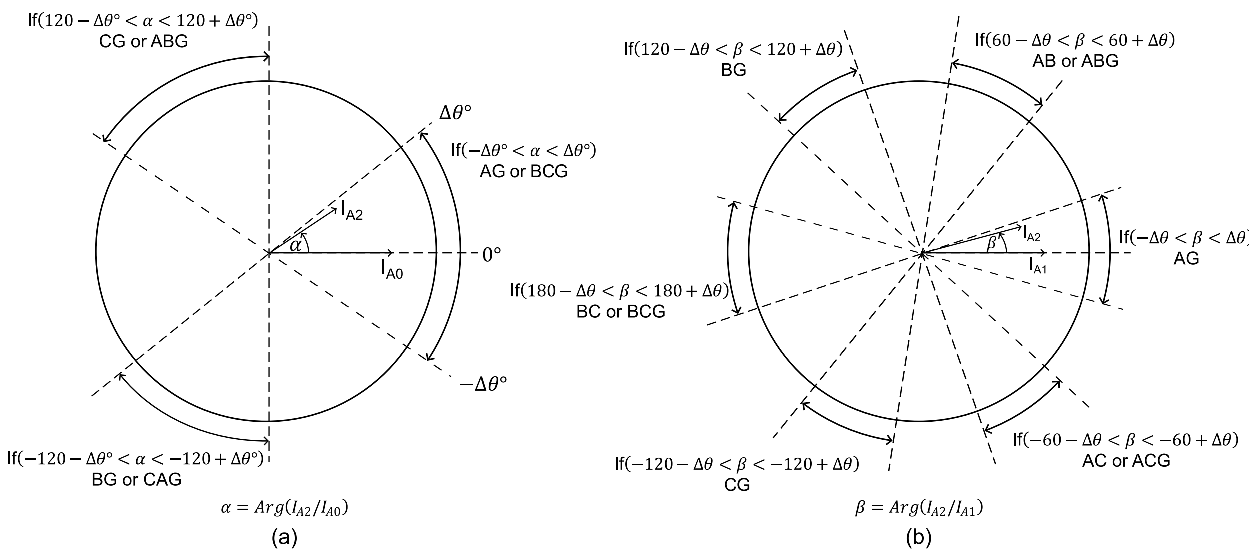

Fig 5.2 (a) Angle Difference Between Phase-A Negative and Zero Sequence Current Phasors During Bolted Faults (b) Angle Difference Between Phase-A Negative and Positive Sequence Current Phasors During Bolted Faults

However, these phase selection algorithms are severely affected in power systems with high penetration of IBRs. Mainly due to the lack of negative sequence current contributions during fault conditions leading to inaccurate decisions.

Furthermore, phasor-based phase selection algorithms typically take at least one cycle to decide. If the HV circuit breaker operating time of 2-3 cycles is considered [5], the typical fault clearance time would be in the range of 3 – 4.5 cycles after considering the time of 1-1.5 cycles [5] to issue a trip signal of phasor-based methods. This can create unfavorable system conditions in a system with strict stability margins and short critical clearing times.

5.2 Clarke Transient Current Based Faulted Phase Selection Scheme

Identification of the fault type and the phases involved in a fault is a challenging task when using faster protection schemes such as transient-based protection algorithms that have sub-cycle operating times, but it is important if the advantages of single-pole tripping are to be exploited [83]. Furthermore, utilities value features such as fault type identification when selecting protection equipment including transient-based relays [84]. Since the phasor-based faulted phase selection algorithms discussed in Section 5.1.1 cannot be guaranteed to operate within sub-cycle time frame, researchers have proposed transient-based fault type classification schemes, however, most of these previously proposed algorithms [80], [85] - [87] in the literature have limitations.

The challenging part of fault detection and classification in AC systems using transient signals is the dependability of the strength of the transients with the fault inception angle, fault resistance, and the fault location. Therefore, at some combinations of the above three variables, the strength of the transient observed in a phase that is not involved in a fault may be stronger than the strength of the transient observed in the phase that is involved in the fault. Hence, faulted phase identification cannot be reliably achieved with a simple approach like a comparison of transient magnitudes against a threshold. To address this challenge, machine learning-based classification algorithms such as artificial neural networks, decision trees, and support vector machines are often proposed [88] - [91]. However, such methods require a large set of field measurements or examples of fault transients generated through simulations for the training phase. For example, in [92] approximately 30000 data sets were used for training a neural network. Therefore, such methods with extensive time-domain simulations with accurate system models come with a high engineering cost and need to be repeated whenever the system is substantially upgraded.

Wavelet transformation is commonly used for extracting transients in fault classification schemes [80], [85], [86], [89], [90], [93] - [95]. Many of these schemes require high sampling rates. For example, a sampling rate of 400 kHz is used in [80], and a sampling rate of 1 MHz is used in [89]. Furthermore, voltage or remote terminal measurements are considered in some of the proposed algorithms [96], [97] which may not be available in most cases.

5.2.1 Faulted Phase Selection Using Clarke Currents

Modal transformations have been used to simplify the fault classification process by decoupling the three-phase system since using direct measurement of phase currents and voltages is prone to failures due to mutual coupling between phase conductors. Clarke transformation [71] is one such transformation among other methods to decouple the three-phase system. As mentioned in Chapter 4, the standard Clarke transformation equation is defined only to handle Phase-A. To generate Clarke currents relevant to all types of faults, the transformation given in ((5.1) can be used.

$$\begin{bmatrix} i_{\alpha^A} \\ i_{\alpha^B} \\ i_{\alpha^C} \\ i_{\beta^A} \\ i_{\beta^B} \\ i_{\beta^C} \\ i_\gamma \end{bmatrix} = \frac{1}{3}\begin{bmatrix} 2 & -1 & -1 \\ -1 & 2 & -1 \\ -1 & -1 & 2 \\ 0 & \sqrt{3} & -\sqrt{3} \\ -\sqrt{3} & 0 & \sqrt{3} \\ \sqrt{3} & -\sqrt{3} & 0 \\ 1 & 1 & 1 \end{bmatrix}\begin{bmatrix} i_a \\ i_b \\ i_c \end{bmatrix} \tag{5.1}$$

5.2.2 Definition of Fault Classification Indices

Using the transformed current components in ((5.1), nine indices are defined. The first three indices are defined by taking the ratio between the maximum absolute values of i_{α^X} and i_{β^X} within a short time window with a length of T_w.

$$F_{\beta_X}^{\alpha_X} = \max\left(\left|i_{\alpha^X}\right|\right)/\max\left(\left|i_{\beta^X}\right|\right) \tag{5.2}$$

where $X \in [A, B, C]$ is the reference phase. Three more indices are defined as the inverse of the ratios defined in ((5.2):

$$F_{\alpha_X}^{\beta_X} = \max\left(\left|i_{\beta^X}\right|\right)/\max\left(\left|i_{\alpha^X}\right|\right) \tag{5.3}$$

The last three indices are defined as the ratios of i_γ to i_{α^X}.

$$F_{\alpha_X}^{\gamma} = \max\left(\left|i_\gamma\right|\right)/\max\left(\left|i_{\alpha_X}\right|\right) \tag{5.4}$$

Identification of the fault type and faulted phases are carried out by considering the expected values of the indices defined in ((5.2), ((5.3), and ((5.4) for each fault type. The criteria for discriminating the fault type and faulted phases are derived considering the boundary conditions for each fault type.

5.2.2.1 Discriminating Ground Faults from Ungrounded Faults

The logic for discriminating a ground fault from an ungrounded fault is explained by considering a Phase-A-to-ground fault and a Phase-A-to-B fault. If the load currents are assumed much smaller than the fault currents, the boundary conditions defined in ((5.5) hold for Phase-A-to-ground faults, and the conditions in ((5.6) hold for Phase-A-to-B faults.

$$i_b \approx i_c \approx 0 \tag{5.5}$$

$$i_b \approx -i_a \text{ and } i_c \approx 0 \tag{5.6}$$

The transformed current components for the Phase-A-to-ground fault and the Phase-A-to-B fault are obtained by substituting ((5.5) and ((5.6) in ((5.1). The corresponding results are depicted in ((5.7) and ((5.8) respectively.

$$\begin{bmatrix} i_{\alpha^A} \\ i_{\alpha^B} \\ i_{\alpha^C} \\ i_{\beta^A} \\ i_{\beta^B} \\ i_{\beta^C} \\ i_\gamma \end{bmatrix}_{A\to G} \approx \begin{bmatrix} \frac{2}{3} i_a \\ -\frac{1}{3} i_a \\ -\frac{1}{3} i_a \\ 0 \\ -\frac{1}{\sqrt{3}} i_a \\ \frac{1}{\sqrt{3}} i_a \\ \frac{1}{3} i_a \end{bmatrix} \tag{5.7}$$

$$\begin{bmatrix} i_{\alpha^A} \\ i_{\alpha^B} \\ i_{\alpha^C} \\ i_{\beta^A} \\ i_{\beta^B} \\ i_{\beta^C} \\ i_\gamma \end{bmatrix}_{A\to B} \approx \begin{bmatrix} i_a \\ i_a \\ 0 \\ -\frac{1}{\sqrt{3}} i_a \\ -\frac{1}{\sqrt{3}} i_a \\ -\frac{2}{\sqrt{3}} i_a \\ 0 \end{bmatrix} \tag{5.8}$$

As $[i_\gamma]_{A\to G} \approx \frac{1}{3} i_a$ in ((5.7) indices $F^{\gamma}_{\alpha_X}$ calculated for Phase-A-to-ground fault are such that $\left(F^{\gamma}_{\alpha_A}\right)_{A\to G} \approx 0.5$ and $\left(F^{\gamma}_{\alpha_B}\right)_{A\to G} \approx \left(F^{\gamma}_{\alpha_C}\right)_{A\to G} \approx 1$. Similar consideration of the other types of Phase-to-Ground faults shows that $F^{\gamma}_{\alpha_X}$ index of the faulted phase remains around 0.5 while the other two $F^{\gamma}_{\alpha_X}$ indices remain around 1.0. Furthermore as $[i_\gamma]_{A\to B} \approx 0$ in ((5.8), the indices $F^{\gamma}_{\alpha_A}$and $F^{\gamma}_{\alpha_B}$ calculated for Phase-A-to-B fault are such that $\left(F^{\gamma}_{\alpha_A}\right)_{A\to B} \approx \left(F^{\gamma}_{\alpha_B}\right)_{A\to B} \approx 0$, whereas the index

$\left(F_{\alpha_C}^{\gamma}\right)_{A\to B}$ would be some arbitrary value since both $\left[i_{\alpha_C}\right]_{A\to B}$ and $\left[i_{\gamma}\right]_{A\to B}$ are approximately equal to zero. Similar analysis of other types of Phase-to-Phase faults shows that for any ungrounded fault, at least two of the $F_{\alpha_X}^{\gamma}$ indices would be very small values. For a three-phase fault, $\left[i_{\gamma}\right]_{A\to B\to C}\approx 0$, and all maximum absolute values of i_{α_X}components will be non-zero, resulting in nearly zero values for all three $F_{\alpha_X}^{\gamma}$ indicies. Therefore, any ground fault can be discriminated from an ungrounded or a three-phase fault using the criteria in ((5.9).

$$\begin{gathered} if\ \left\{\left(F_{\alpha_A}^{\gamma}>k_0\right)\&\left(F_{\alpha_B}^{\gamma}>k_0\right)\&\left(F_{\alpha_C}^{\gamma}>k_0\right)\right\}:\ \text{ground fault} \\ else: ungrounded\ fault \end{gathered} \tag{5.9}$$

The threshold k_0 is a constant in the range $[0.05-0.1]$

5.2.2.2 Discriminating Phase-to-Ground Faults from Phase-to-Phase-to-Ground Faults

The basis for the discrimination criteria is explained by considering a metallic Phase-A-to-ground fault and a Phase-A-to-Phase-B-to-ground fault as examples. The boundary conditions defined in ((5.5) hold for the Phase-A-to-ground fault while ((5.10) holds for the Phase-A-to-Phase-B-to-ground fault.

$$i_c\approx 0 \tag{5.10}$$

The transformed current components for the phase A-to-ground fault are given in ((5.7) and those for the phase A-to-phase B-to-ground fault can be obtained by substituting ((5.10) into ((5.1):

$$\begin{bmatrix} i_{\alpha^A} \\ i_{\alpha^B} \\ i_{\alpha^C} \\ i_{\beta^A} \\ i_{\beta^B} \\ i_{\beta^C} \end{bmatrix}_{A-B\to G} \approx \begin{bmatrix} \frac{2}{\sqrt{3}}i_a-\frac{1}{3}i_b \\ \frac{-i_a}{3}+\frac{2i_b}{3} \\ \frac{-i_a}{3}-\frac{i_b}{3} \\ \frac{i_b}{\sqrt{3}} \\ \frac{-i_a}{\sqrt{3}} \\ \frac{i_a}{\sqrt{3}}-\frac{i_b}{\sqrt{3}} \end{bmatrix} \tag{5.11}$$

As $\left[i_{\beta^A}\right]_{A\to G}\approx 0$ in ((5.7), index $F_{\beta_A}^{\alpha_A}$ calculated for the Phase-A-to-ground fault becomes a very high value, while $[F_{\beta_B}^{\alpha_B}]_{A\to G}\approx[F_{\beta_C}^{\alpha_C}]_{A\to G}\approx 1/\sqrt{3}$. On the other hand, all $F_{\beta_X}^{\alpha_X}$ indices calculated for the Phase-A-to-B-to-ground fault will be much smaller than $[F_{\beta_A}^{\alpha_A}]_{A\to G}$. Therefore, the sums of the indices satisfy the inequality given in ((5.12).

$$\left[F_{\beta_A}^{\alpha_A}+F_{\beta_B}^{\alpha_B}+F_{\beta_C}^{\alpha_C}\right]_{A\to G}>\left[F_{\beta_A}^{\alpha_A}+F_{\beta_B}^{\alpha_B}+F_{\beta_C}^{\alpha_C}\right]_{A\to B\to G} \tag{5.12}$$

For any Phase-to-Ground fault, the sum on the left-hand side (LHS) of ((5.12) becomes very large because one of the indices on the left-hand side of ((5.12) is always very large (the other two remain around $1/\sqrt{3}$) while the sum on the right-hand side (RHS) of ((5.12) for any other type of Phase-to-Phase-to-Ground fault remains in the same range as for the Phase-A-to-B-to-ground fault. Therefore, any Phase-to-Ground fault can be identified using the criterion in ((5.13).

$$\begin{gathered} if\ \left\{\left(F_{\beta_A}^{\alpha_A}+F_{\beta_B}^{\alpha_B}+F_{\beta_C}^{\alpha_C}\right)>k_1\right\}\text{ :Phase-to-Ground fault} \\ else\text{:Phase-to-Phase-to-Ground fault} \end{gathered} \tag{5.13}$$

where k_1 is a threshold constant.

5.2.2.3 Discriminating Phase-to-Phase Faults from Three-Phase Faults

The basis behind discriminating a Phase-to-Phase fault from a Three-Phase fault is explained with the help of the expected values of $F_{\alpha_X}^{\beta_X}$ for a Phase-A-to-Phase-B fault. The boundary condition given in ((5.6) holds for a Phase-A-to-Phase-B fault. Thus, values of α and β components given in ((5.8) can be expected for a Phase-A-to-Phase-B fault.

As $i_{\alpha^C}\approx 0$ in ((5.8), the value of the index $F_{\alpha_C}^{\beta_C}$ calculated for a Phase-A-to-Phase-B fault becomes very large, whereas $[F_{\alpha_B}^{\beta_B}]_{A\to B}\approx[F_{\alpha_A}^{\beta_A}]_{A\to B}\approx 1/\sqrt{3}$. On the other hand for a Three-Phase fault, all maximum absolute values of i_{α_X} and i_{β_X} components will be non-zero, resulting in $F_{\alpha_X}^{\beta_X}$ indices which are much smaller than $F_{\alpha_C}^{\beta_C}$ calculated for the Phase-A-to-Phase-B fault. Thus, the sums of the indices hold the condition ((5.14).

$$\left[F_{\alpha_A}^{\beta_A} + F_{\alpha_B}^{\beta_B} + F_{\alpha_C}^{\beta_C}\right]_{A\to B} > \left[F_{\alpha_A}^{\beta_A} + F_{\alpha_B}^{\beta_B} + F_{\alpha_C}^{\beta_C}\right]_{A\to B\to C} \tag{5.14}$$

The condition given in ((5.14) satisfies any type of Phase-to-Phase fault as one of the indices on LHS of ((5.14) is always very large, and therefore much larger than the sum of three indices calculated for any three-phase fault. Thus, any Phase-to-Phase fault can be discriminated from a Three-Phase fault using the criterion in ((5.15).

$$\begin{array}{c} if\ \left\{\left(F_{\alpha_A}^{\beta_A} + F_{\alpha_B}^{\beta_B} + F_{\alpha_C}^{\beta_C}\right) > k_n\right\} \text{:Phase-to-Phase fault} \\ else\text{:three-phase fault} \end{array} \tag{5.15}$$

where k_1 is a threshold constant.

The threshold k_n can be set to be the same as k_1 since the conditions tested are similar, and in practice a single threshold (k_1) can be used.

5.2.3 Identification of Faulted Phases

The values for $F_{\beta_X}^{\alpha_X}$ and $F_{\alpha_X}^{\beta_X}$ are mostly determined by the phase(s) involved in the fault. Therefore, depending on the fault type, the faulted phases are identified by comparing the values of $F_{\beta_X}^{\alpha_X}$ and $F_{\alpha_X}^{\beta_X}$ as described in the following sections.

5.2.3.1 Faulted Phase Identification for Phase-to-Ground Faults

According to ((5.7), for a Phase-A-to-ground fault, $F_{\beta_B}^{\alpha_B} = F_{\beta_C}^{\alpha_C} \approx 1/\sqrt{3}$. Furthermore, $F_{\beta_A}^{\alpha_A} \gg F_{\beta_B}^{\alpha_B}$ and $F_{\beta_A}^{\alpha_A} \gg F_{\beta_C}^{\alpha_C}$. As a result, phase involved in the fault has the highest magnitude among the

$F_{\beta_X}^{\alpha_X}$ values. Hence, once the fault type is determined as a Phase-to-Ground with the help of ((5.13), the faulted phase can be determined using the criteria in ((5.16), with $k_2 > 1/\sqrt{3}$; a value in the range of 1-10 is recommended.

$$\begin{array}{r}
if\left\{\left(F_{\beta_A}^{\alpha_A} \geq k_2\right) \& \left(F_{\beta_B}^{\alpha_B} < k_2\right) \& \left(F_{\beta_C}^{\alpha_C} < k_2\right)\right\} : A - G\ Fault \\
else\ if\ \left\{\left(F_{\beta_B}^{\alpha_B} \geq k_2\right) \& \left(F_{\beta_A}^{\alpha_A} < k_2\right) \& \left(F_{\beta_C}^{\alpha_C} < k_2\right)\right\} : B - G\ Fault \\
else\ if\ \left\{\left(F_{\beta_C}^{\alpha_C} \geq k_2\right) \& \left(F_{\beta_A}^{\alpha_A} < k_2\right) \& \left(F_{\beta_B}^{\alpha_B} < k_2\right)\right\} : C - G\ Fault
\end{array} \tag{5.16}$$

5.2.3.2 Faulted Phases Identification for Phase-to-Phase Faults

For a Phase-A-to-Phase-B fault, according to ((5.8), $F_{\alpha_A}^{\beta_A} = F_{\alpha_B}^{\beta_B} \approx 1/\sqrt{3}$. Furthermore, since $i_{\alpha^C} \approx 0$, $F_{\alpha_C}^{\beta_C} \gg F_{\alpha_A}^{\beta_A}$ and $F_{\alpha_C}^{\beta_C} \gg F_{\alpha_B}^{\beta_B}$. Once a Phase-to-Phase fault is identified with the help of ((5.15), the faulted phases can be determined using ((5.17).

$$\begin{array}{r}
if\ \left\{\left(F_{\alpha_A}^{\beta_A} < k_2\right)\&\left(F_{\alpha_B}^{\beta_B} < k_2\right)\&(F_{\alpha_C}^{\beta_C} \geq k_2)\right\}\text{: A-B fault} \\
else\ if\ \left\{\left(F_{\alpha_A}^{\beta_A} \geq k_2\right)\&\left(F_{\alpha_B}^{\beta_B} < k_2\right)\&(F_{\alpha_C}^{\beta_C} < k_2)\right\}\text{: B-C fault} \\
else\ if\ \left\{\left(F_{\alpha_A}^{\beta_A} < k_2\right)\&\left(F_{\alpha_B}^{\beta_B} \geq k_2\right)\&(F_{\alpha_C}^{\beta_C} < k_2)\right\}\text{: C-A fault}
\end{array} \tag{5.17}$$

where k_2 is constant in the range of [1-10].

5.2.3.3 Faulted Phases Identification for Phase-to-Phase-to-Ground Faults

Consider a Phase-A-to-Phase-B-to-ground fault. A significantly larger current can be expected in the faulted phases when compared with the current in the healthy phase, and the phase angle between the currents through the faulted phases is above 90° (≈120°). According to ((5.1), i_{α^C} component becomes significantly smaller than all other components. Therefore, for this fault $F_{\beta_A}^{\alpha_A} \gg F_{\beta_C}^{\alpha_C}$ and $F_{\beta_B}^{\alpha_B} \gg F_{\beta_C}^{\alpha_C}$. Using a similar argument, the criteria in ((5.18) can be developed to identify the faulted phases of a Phase-to-Phase-to-Ground fault.

$$if\ (F_{\beta_A}^{\alpha_A} > F_{\beta_C}^{\alpha_C})\&(F_{\beta_B}^{\alpha_B} > F_{\beta_C}^{\alpha_C})\text{: A-B-G fault} \tag{5.18}$$

$else\ if\ (F_{\beta_B}^{\alpha_B} > F_{\beta_A}^{\alpha_A})\&(F_{\beta_C}^{\alpha_C} > F_{\beta_A}^{\alpha_A})$: B-C-G fault
$else\ if\ (F_{\beta_C}^{\alpha_C} > F_{\beta_B}^{\alpha_B})\&(F_{\beta_A}^{\alpha_A} > F_{\beta_B}^{\alpha_B})$: C-A-G fault

5.2.4 Use of Rate of Change of Currents (ROCOC) for Calculation of Fault Indices

The criteria to identify the fault type and faulted phases were derived using the fault classification indices computed using the transformed currents. However, boundary conditions such as ((5.5), ((5.6), and ((5.10) can deviate from the assumed ideal values during high resistance faults due to load currents. This undesirable impact of load currents can be minimized by using the incremental values of the respective transformed currents for calculating the fault indices. The incremental current values within a short time window of T_W can be approximately expressed in terms of the derivatives of the respective currents: $\Delta i = (di/dt)T_W$. When taking the ratios of the incremental currents expressed in terms of their derivatives, the window length parameter, T_W, cancels out. Hence, the indices proposed in ((5.2), ((5.3) and ((5.4) can be redefined using derivatives of the respective currents to obtain a new set of nine fault classification indices as:

$$G_{\alpha_X}^{\gamma} = \frac{max\left(\left|\frac{di_\gamma(t)}{dt}\right|\right)}{max\left(\left|\frac{di_{\alpha X}(t)}{dt}\right|\right)} \tag{5.19}$$

$$G_{\beta_X}^{\alpha_X} = \frac{max\left(\left|\frac{di_{\alpha X}(t)}{dt}\right|\right)}{max\left(\left|\frac{di_{\beta X}(t)}{dt}\right|\right)} \tag{5.20}$$

$$G_{\alpha_X}^{\beta_X} = \frac{max\left(\left|\frac{di_{\beta X}(t)}{dt}\right|\right)}{max\left(\left|\frac{di_{\alpha X}(t)}{dt}\right|\right)} \tag{5.21}$$

where X is the reference phase. These peak ROCOC-based indices facilitate minimizing the effects of load currents and faster identification of fault type and faulted phases. The transformed current quantities are band-pass filtered to separate incremental values before computing the derivatives. The cutoff frequencies of the band pass filter are selected to remove the power frequency signal components and noisy high-frequency components. In order to avoid the effect of the reflected secondary current waves, the maximums of the respective time derivatives observed within a short time window of length T_W after detecting a fault are used.

The steps involved in the classification of fault type are shown in Fig 5.3. In the first step, the values of $G_{\alpha_X}^{\gamma}$ is compared against the threshold k_0 to discriminate the ground faults from the non-ground faults. If it is a ground fault, the sum of $G_{\beta_A}^{\alpha_A}$, $G_{\beta_B}^{\alpha_B}$ and $G_{\beta_C}^{\alpha_C}$ is compared against the threshold k_1 to discriminate the Phase-to-Ground faults from the Phase-to-Phase-to-Ground faults. If it is a non-ground fault, the sum of $G_{\alpha_A}^{\beta_A}$, $G_{\alpha_B}^{\beta_B}$, and $G_{\alpha_C}^{\beta_C}$, is compared against the threshold k_1 to discriminate between the Phase-to-Phase faults and the Three-Phase faults. No discrimination is made between the three-phase faults and the Three-Phase-to-Ground faults. After identifying the fault type, the faulted phase(s) are identified using the criteria in ((5.16), ((5.17), and ((5.18), but with the indices computed using current derivatives as defined in ((5.19) – ((5.21).

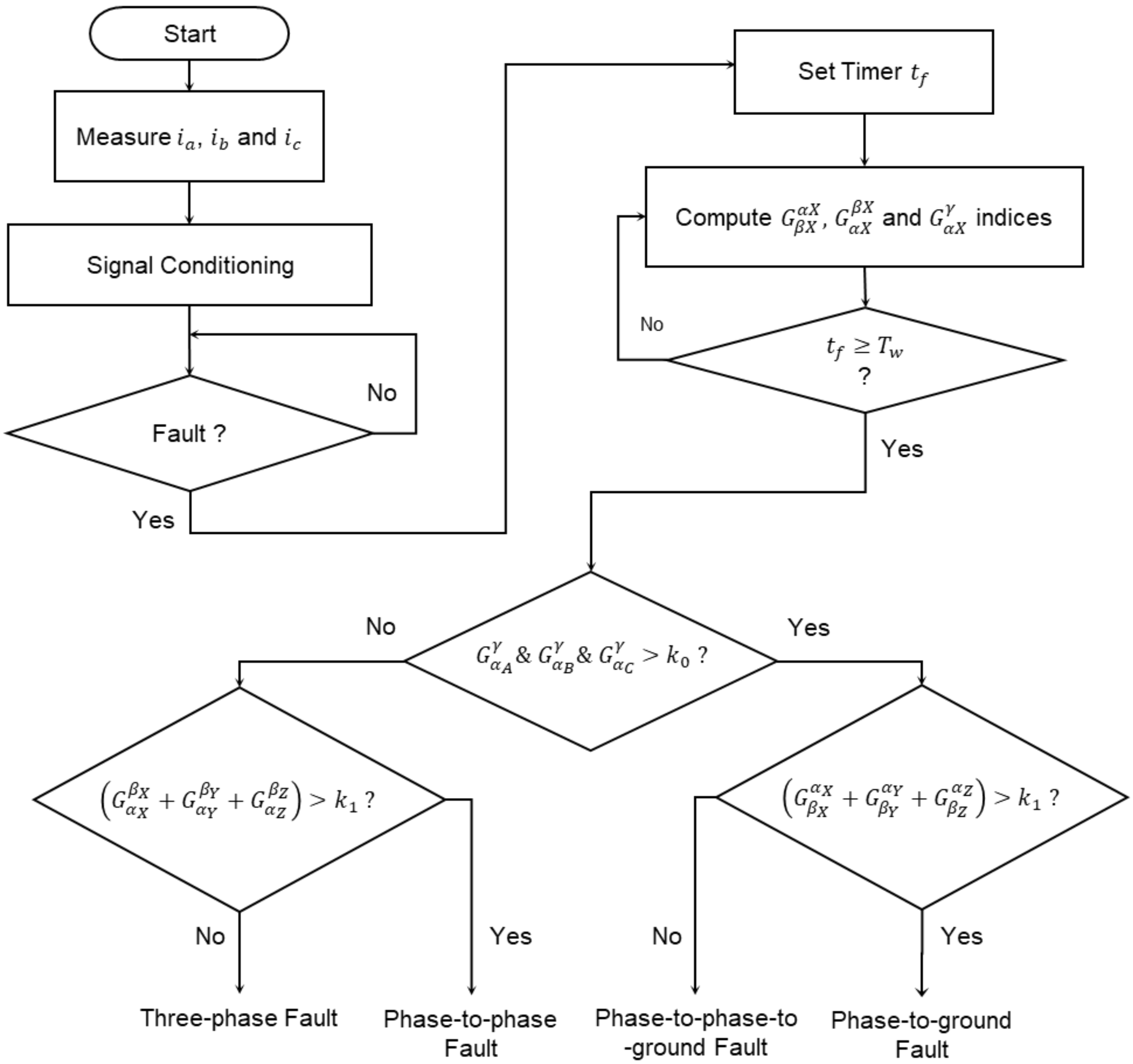

Fig 5.3 Fault Type Identification Algorithm

The signal processing involved in calculating the indices is shown in Fig 5.4. The process is triggered when the sum of the absolute values of the derivatives of α and β components become greater than a certain threshold level (k_d) in the range of 0.1 – 0.5, at least for one of the reference phases. From that point, the maximum values of the current derivatives are tracked over a period of T_W.

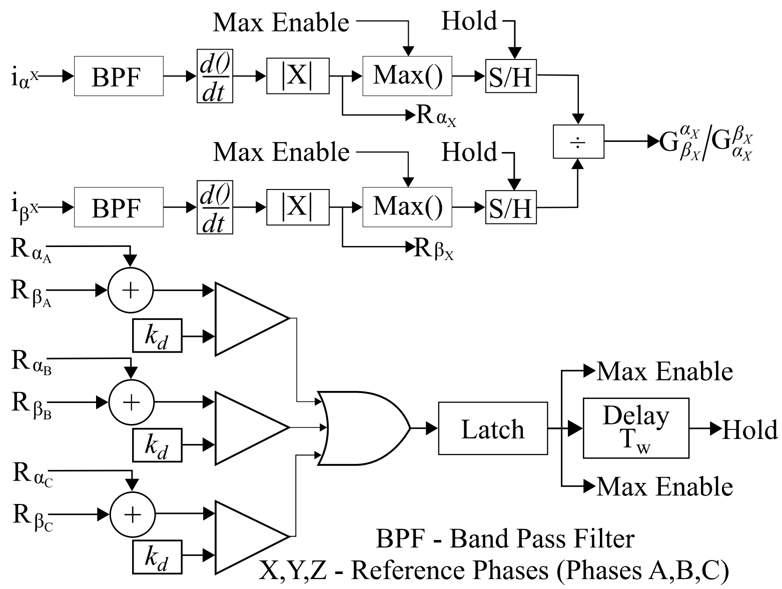

Fig 5.4 Signal Processing Involved in Calculating the Fault Indices

5.3 Algorithm Validation

5.3.1 Test System

The algorithm was validated using the 230 kV power system shown in Fig 5.5, simulated in PSCAD/EMTDC^{TM} with a 25 μs time step. The transmission lines were represented using detailed line models available in PSCAD/EMTDC. The parameters of the line at 60 Hz are given in Table 5.1. The source impedances are given in Table 5.2.

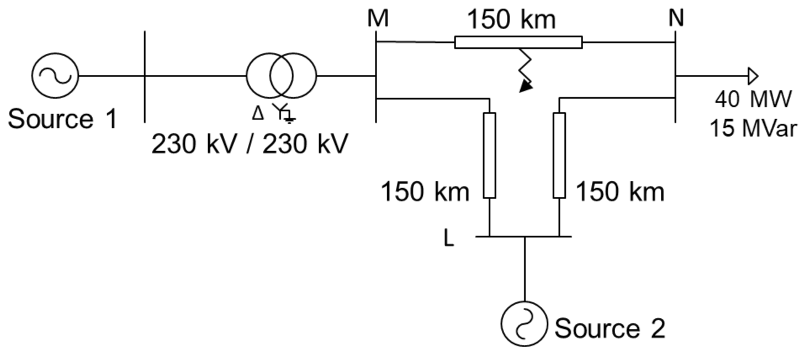

Fig 5.5 Test System Simulated in PSCAD/EMTDC™

Table 5.1 Transmission Line Parameters

Parameter	**Value**	**Parameter**	**Value**
R_1 (Ω/km)	5.0677×10^{-2}	R_0 (Ω/km)	2.14428×10^{-1}
X_{L1} (Ω/km)	4.8217×10^{-1}	X_{L0} (Ω/km)	1.525662
X_{C1} (MΩ/km)	0.29469	X_{C0} (MΩ/km)	0.414412

Table 5.2 Source Impedance Data

Source	$\boldsymbol{Z_1}$ **(Ω)**	$\boldsymbol{Z_0}$ **(Ω)**
Source 1	$17.95\angle 87.65^o$	$14.95\angle 80.86^o$
Source 2	$3.8\angle 87.69^o$	$6.02\angle 80.9^o$

5.3.2 Selection of Filter Frequency, Bandwidth, and Time Window

The filter cutoff frequencies and the time window were set in such a way that the discrimination margin between the Phase-to-Ground and Phase-to-Phase-to-Ground faults (M_{GND}) and that between the Phase-to-Phase and Three-Phase faults (M_{UGND}) is sufficiently large. The discrimination margins for the ground and ungrounded faults are defined as ((5.22) and ((5.23) respectively.

$$M_{GND} = \sum \left[G_{\beta_X}^{\alpha_X}\right]_{X\to G} \Big/ \sum \left[G_{\beta_X}^{\alpha_X}\right]_{X\to Y\to G} \quad (5.22)$$

$$M_{UGND} = \sum \left[G_{\alpha_X}^{\beta_X}\right]_{X\to Y} \Big/ \sum \left[G_{\alpha_X}^{\beta_X}\right]_{X\to Y\to Z} \quad (5.23)$$

In order to identify the pass band for the filters, faults were applied on line M-N at different fault inception angles while changing one of the factors; the filter bandwidth, filter lower cutoff frequency, or the peak detection time window (T_W) at a time. The mean values of the nine M_{GND} indices (A-G/A-B-G, B-G/A-B-G, …, C-G/C-A-G) and three M_{UGND} indices (A-B/A-B-C, B-C/A-B-C, C-A/A-B-C) were calculated at 40 different fault inception angles and the minimums of the respective mean values M_{GND}^* and M_{UGND}^* were reported.

The effect of the filter's lower cutoff frequency on the discrimination margin was evaluated first while maintaining the filter bandwidth at 1 kHz and the length of time window at 2 ms. The faults were applied at two locations, 12.5 km and 135 km away from busbar M. Table 5.3 shows the results which led to the selection of a lower cutoff frequency of the band pass filter as 2500 Hz, since it gives a sufficiently large discrimination margin.

Next, the length of the time window was varied while maintaining the lower cut-off frequency at 2500 Hz and filter band width at 1 kHz. In addition to M_{GND} and M_{UGND} values, $G_{\alpha_A}^{\gamma}$, $G_{\alpha_B}^{\gamma}$ and $G_{\alpha_C}^{\gamma}$ were also calculated. Table 5.4 presents the minimums of the mean values of respective factors. Although a time window of 0.5 ms is the best for M_{GND}^* and M_{UGND}^*, a 0.75 ms time window is more appropriate when considered ${G_{\alpha_X}^{\gamma}}^*$ values as well.

Table 5.3 Effect of Lower Cutoff Frequency on Discrimination margin (bandwidth=1 kHz. T_{dw} = 2 ms)

Lower Cut-off Frequency (Hz)	12.5 km Away		135 km Away	
	M_{GND}*	M_{UGND}*	M_{GND}*	M_{UGND}*
1000	528.212	513.379	431.39	289.24
1500	946.802	721.375	572.84	364.80
2000	1056.356	663.856	849.66	472.08
2500	1095.556	584.368	1077.43	525.60
3000	1161.228	657.799	1312.47	605.39

Table 5.4 Effect of Time Window on Discrimination Margin (lower cutoff = 2500 Hz, bandwidth = 1 kHz)

Time Window	Ground Faults		Ungrounded Faults	
	M_{GND}*	$G_{\alpha_X}^{\gamma\,*}$	M_{UGND}*	$G_{\alpha_X}^{\gamma\,*}$
2 ms	830.30	0.75	438.63	0.1175
1 ms	1149.99	0.92	1147.72	0.0755
0.75 ms	1246.35	0.92	1405.50	0.0765
0.5 ms	1413.94	0.72	1572.50	0.0287
0.25 ms	1285.76	0.28	1511.37	0.0001

After selecting the optimum time window and filter lower cut-off frequency, the effect of filter bandwidth was analyzed using the same approach with the selected time window (0.75 ms) and the filter's lower cutoff frequency (2500 Hz). The results indicated that 1 kHz bandwidth gives the best discrimination margins. The threshold settings k_0, k_1, and k_2 were respectively set to 0.05, 100, and 10 for the system considered.

5.3.3 Demonstration of Operation

In order to demonstrate the basic operation of the algorithm, the faults listed in Table 5.5 were applied on Line M-N at 0.3 s.

Table 5.5 Fault Scenarios Considered

Scenario	**Fault Type**	**Fault Resistance**	**Location**
Scenario – 1	AG	300 Ω	50 % of Line MN
Scenario – 2	ABG	300 Ω	50 % of Line MN
Scenario – 3	AB	300 Ω	50 % of Line MN
Scenario – 4	ABC	300 Ω	50 % of Line MN

Fig 5.6 shows the instantaneous phase current signals (Fig 5.6 (a)) and their band pass filtered versions (Fig 5.6 (b)) for Scenario-1. The change in Phase-A current is minor due to high fault resistance. Furthermore, band pass filtered current waveforms in Fig 5.6 (b) show that strong transients are induced on the healthy phases due to coupling and highlight the need for decoupling before faults can be classified. Fig 5.7 depicts the transformed current components obtained from the currents in Fig 5.6 (b). From the decoupled transient currents shown in Fig 5.7, it is clear that i_{β_A} is nearly zero as expected for a Phase-A-to-ground fault, the feature important for identifying the fault type and the faulted phase, in spite of 300 Ω fault resistance. As a result, $G_{\beta_A}^{\alpha_A}$ index remains more than 1000 times larger than the other two indices.

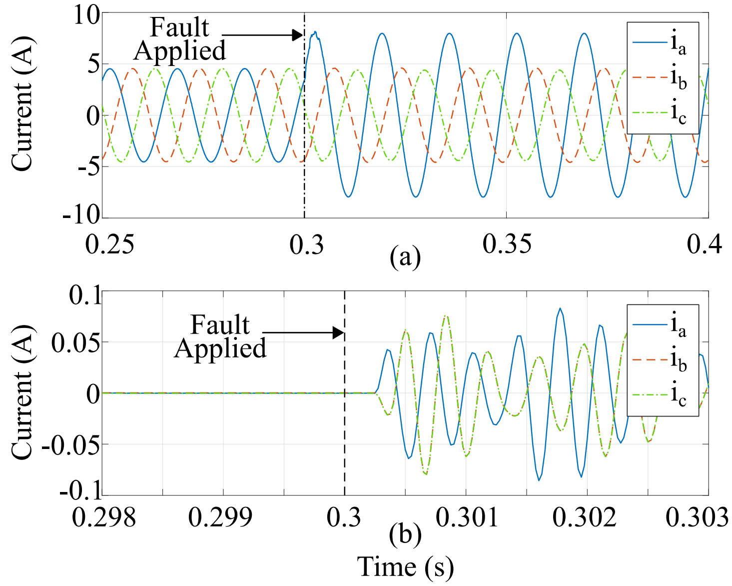

Fig 5.6 Three Phase Currents During Fault Scenario-1 (a) Before and (b) After Band Pass Filtering

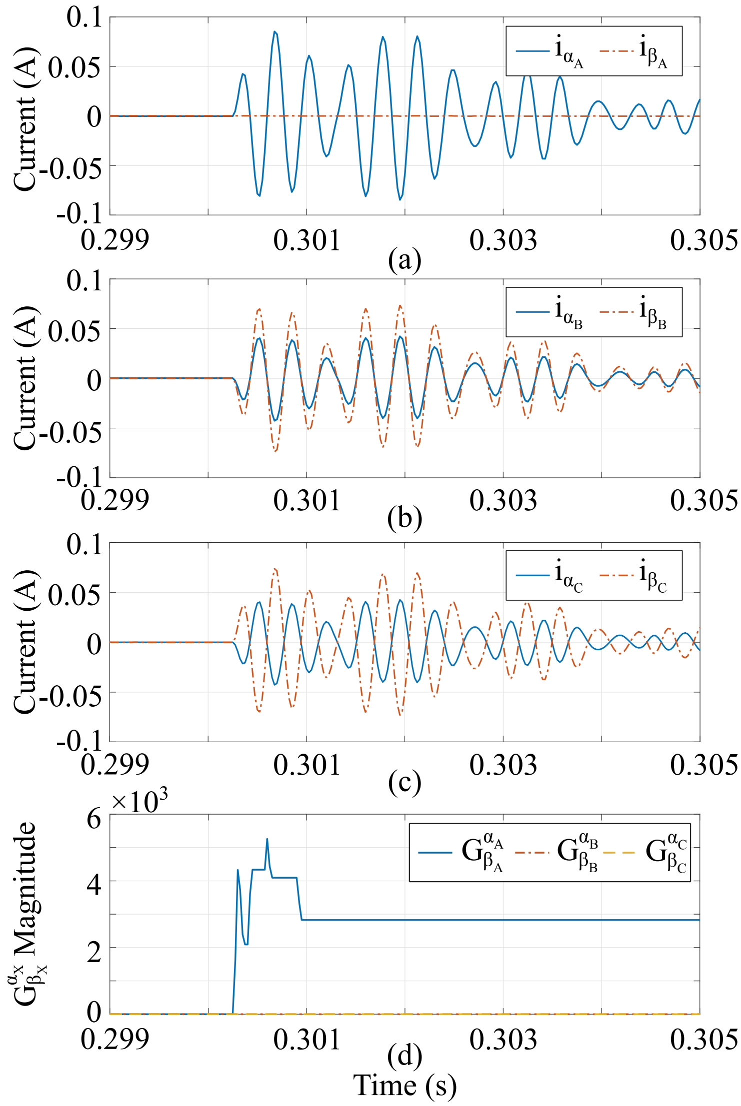

Fig 5.7 Transformed Currents Components Reference to (a) Phase A, (b) Phase B (c) Phase C, and (d) $G_{\beta X}^{\alpha x}$ Ratios for Scenario-1.

Fig 5.8 shows the calculated $G_{\alpha_X}^{\gamma}$ indices for four types of faults (Scenarios 1-4). All three $G_{\alpha_X}^{\gamma}$ indices exceed the respective thresholds in Fig 5.8 (a) and Fig 5.8 (b), indicating ground faults in Scenarios 1 and 2. Table 5.6 presents $G_{\beta X}^{\alpha X}$ indices and the sum of $G_{\beta X}^{\alpha X}$ values for Scenarios 1 and 2, for which all three $G_{\alpha_X}^{\gamma}$ indices are greater than the threshold k_0. Scenario 1 has a sum of $G_{\beta X}^{\alpha X}$ values greater than k_1 (=100), and therefore, according to ((5.13), this fault is classified as a Phase-to-Ground fault. Furthermore, $G_{\beta_A}^{\alpha_A} > k_2$ (=10) and both $G_{\beta_B}^{\alpha_B}$ and $G_{\beta_C}^{\alpha_C}$ are less than k_2. According to ((5.16) the faulted phase for Scenario-1 can be identified as Phase-A.

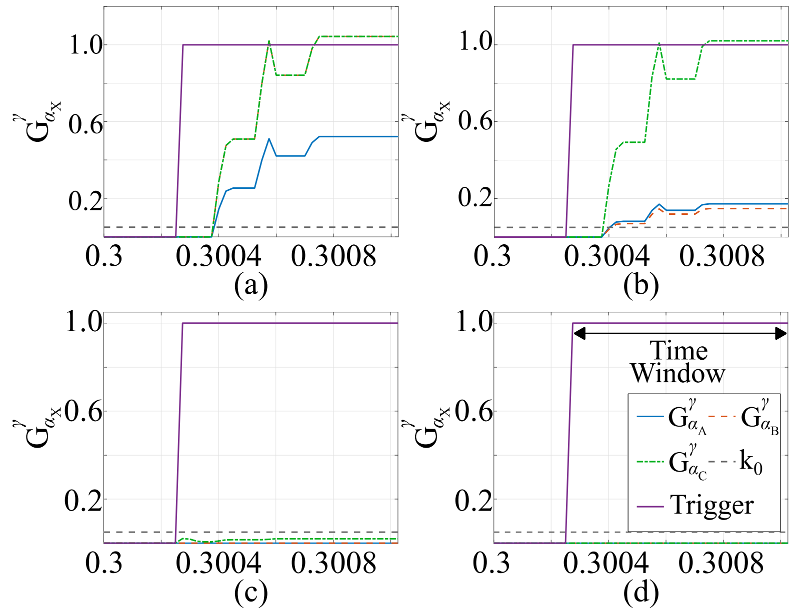

Fig 5.8 $G_{\alpha_X}^{\gamma}$ Indices for Four Types of Faults Applied at Middle of Line M-N (a) Scenario 1 (b) Scenario 2 (c) Scenario 3 and (d) Scenario 4

For the fault of Scenario-2, the sum of $G_{\beta_X}^{\alpha_X}$ indices are lower than k_1 (=100). According to ((5.13), this should be a Phase-to-Phase-to-Ground fault. Moreover, both $G_{\beta_B}^{\alpha_A}$ and $G_{\beta_B}^{\alpha_B}$ are larger than $G_{\beta C}^{\alpha C}$, and therefore, as per ((5.18), Phase-A and Phase-B are involved in this fault.

Table 5.7 gives $G_{\alpha X}^{\beta X}$ values and the sum of $G_{\alpha X}^{\beta X}$ values calculated for Scenarios 3 and 4. According to Fig 5.7 (c) and Fig 5.7 (d), all three $G_{\alpha_X}^{\gamma}$ indices is less than k_0 threshold, thus they are not ground faults. The sum of $G_{\alpha X}^{\beta X}$ values is higher than the threshold k_1 (=100) for Scenario 3. Therefore, according to ((5.15), Scenario 3 is classified as a Phase-to-Phase fault. Furthermore, $G_{\alpha_C}^{\beta_C} > k_2$ (=10) while both $G_{\alpha_A}^{\beta_A}$ and $G_{\alpha_B}^{\beta_B}$ are less than k_2 (=10) indicates that Phase-C is not involved in the fault. In conclusion, fault Scenario 3 can be identified as a Phase-A-to-Phase-B fault. Fault Scenario 4 can be identified as a three-phase fault since the sum of $G_{\alpha_X}^{\beta_X}$ ratios are less than threshold k_1.

Table 5.6 $G_{\beta_X}^{\alpha_X}$ Values for Ground Faults

Fault Type	$G_{\beta_A}^{\alpha_A}$	$G_{\beta_B}^{\alpha_B}$	$G_{\beta_C}^{\alpha_C}$	Sum
Scenario 1	2824.572	0.577	0.577	2825.727
Scenario 2	1.294	2.439	0.135	3.868

Table 5.7 $G_{\alpha_X}^{\beta_X}$ Values for Ungrounded Faults

Fault Type	$G_{\alpha_A}^{\beta_A}$	$G_{\alpha_B}^{\beta_B}$	$G_{\alpha_C}^{\beta_C}$	Sum
Scenario 3	0.577	0.577	12841.63	12842.784
Scenario 4	1.574	0.051	1.915	3.54

5.3.4 Evaluating Fault Type Discrimination Performance

To verify the robustness and accuracy of the fault type identification criteria, fault classifications were conducted for different fault locations and different fault inception angles under different system conditions.

a) Discrimination of Phase-to-Ground Faults from Phase-to-Phase-to-Ground Faults

Fig 5.9 shows the typical variation of the sum of $G_{\beta X}^{\alpha X}$ values with the fault inception angle for Phase-A-to-Ground and three possible Phase-to-Phase-to-Ground faults. The fault inception angle is varied between 0 to 180 degrees in 1-degree steps. Fig 5.9 (a) and Fig 5.9 (b) show the calculated sum of $G_{\beta X}^{\alpha X}$ values for fault resistances of 0.05 Ω and 300 Ω, respectively. In Fig 5.9 (b), two additional curves corresponding to 50 Ω and 100 Ω Phase-A-to-Ground faults are also included. Fig 5.9 shows that discrimination remains robust except during a narrow range of fault inception angles, regardless of the fault resistance. According to Fig 5.9 (b), fault discrimination becomes unreliable at the worst-case fault inception angle for faults with more than 300 Ω arc resistance, which is above the typical fault resistances expected at 230 kV level and considered unusually high even for 525 kV level [98].

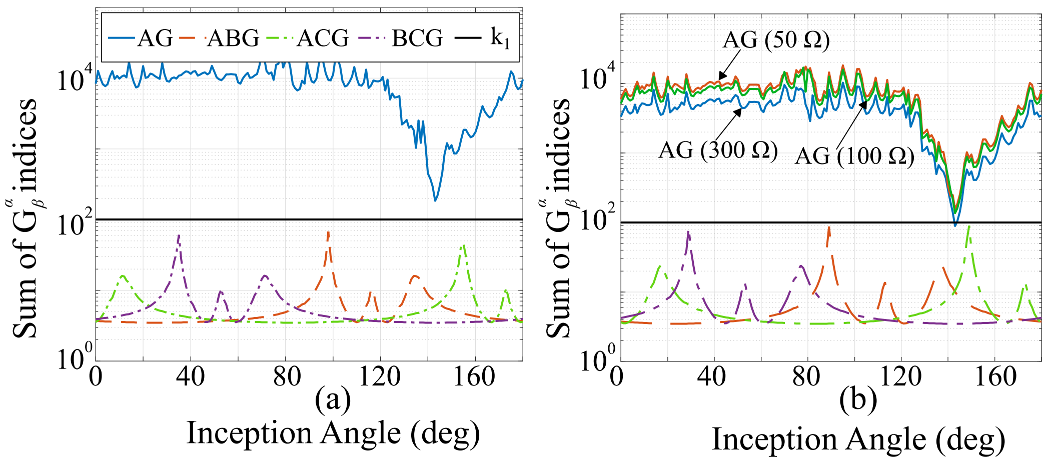

Fig 5.9 Variation of the Sum of $G_{\beta X}^{\alpha X}$ Indices for Phase-to-Ground and Phase-to-Phase-to-Ground Faults at 10% of Line M-N for Faults with (a) 0.05 Ω and (b) 300 Ω Fault Resistance.

The sum of $G_{\beta X}^{\alpha X}$ indices calculated for four fault events (fault resistances of 50 Ω), two closer to near end and the other two closer to the far end, are shown in Table 5.8 and Table 5.9. It can be verified that the Phase-to-Ground faults can be successfully discriminated from the Phase-to-Phase-to-Ground faults regardless of the fault location.

Table 5.8 $G_{\beta X}^{\alpha X}$ Ratios for Ground Faults Applied at 5%

Fault Type	$G_{\beta_A}^{\alpha_A}$	$G_{\beta_B}^{\alpha_B}$	$G_{\beta_C}^{\alpha_C}$	**Sum**
B-to-G Fault	0.5773	20384.92	0.5773	20386.07
A-to- -C-to-G Fault	0.994	0.271	3.774	5.039

Table 5.9 $G_{\beta X}^{\alpha X}$ Ratios for Ground Faults Applied at 95%

Fault Type	$G_{\beta_A}^{\alpha_A}$	$G_{\beta_B}^{\alpha_B}$	$G_{\beta_C}^{\alpha_C}$	**Sum**
B-to-G Fault	0.57703	16220.5	0.5773	16221.65
A-to- -C-to-G Fault	1.125	0.206	2.994	4.325

b) Discrimination of Phase-to-Phase and Three-Phase Faults

Fig 5.10 shows the variation of the sum of $G_{\alpha X}^{\beta X}$ values with the fault inception angle for different Phase-to-Phase faults and three-phase faults. A robust discrimination margin can be observed for the whole range of fault inception angles even at 300 Ω fault resistance.

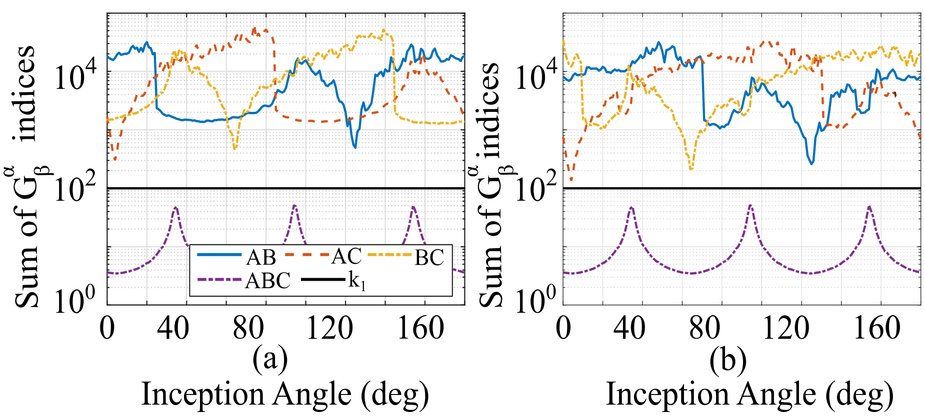

Fig 5.10 Variation of the Sum of $G_{\alpha X}^{\beta X}$ Indices for Phase-to-Phase and Three Phase Faults at 90% of Line M-N with (a) 0.05 Ω and (b) 300 Ω Fault Resistances

Table 5.10 and Table 5.11 show the $G_{\alpha X}^{\beta X}$ values calculated for four different Phase-to-Phase and Three-Phase faults with 50 Ω fault resistance, applied closer to the near and far ends of Line M-N. Thus, it can be concluded that the Phase-to-Phase faults can be successfully discriminated from the Three-Phase faults with a large discrimination margin, regardless of the fault resistance, fault inception angles, and fault location.

Table 5.10 $G_{\alpha X}^{\beta X}$ Ratios for Ungrounded Faults Applied at 5%

Fault Type	$\boldsymbol{G_{\alpha_A}^{\beta_A}}$	$\boldsymbol{G_{\alpha_B}^{\beta_B}}$	$\boldsymbol{G_{\alpha_C}^{\beta_C}}$	**Sum**
B-to- C Fault	23153.11	0.5774	0.5773	23154.26
Three Phase Fault	6.693	0.394	0.795	7.882

Table 5.11 $G_{\alpha X}^{\beta X}$ Ratios for Ungrounded Faults Applied at 95%

Fault Type	$\boldsymbol{G_{\alpha_A}^{\beta_A}}$	$\boldsymbol{G_{\alpha_B}^{\beta_B}}$	$\boldsymbol{G_{\alpha_C}^{\beta_C}}$	**Sum**
B-to-C Fault	9946.01	0.5773	0.5773	9947.16
Three Phase Fault	1.854	0.037	1.622	3.513

c) Overall Accuracy of Fault Type Identification

Table 5.12 summarizes the performance of fault type identification evaluated for various ground faults and non-grounded faults. The second column indicates the number of fault scenarios simulated for each fault type by varying the location in steps of 10% and the fault inception angle in steps of 3° for fault resistances of 0.05 Ω and 50 Ω. In summary, a hundred percent accurate fault type identification is observed for more than 10,000 faults simulated in the system shown in Fig 5.5 using the threshold settings given in Section 5.3.2.

Table 5.12 Fault Type Classification Accuracy

Applied Fault	Number of Cases	Correct Classification	Incorrect Classification	Accuracy
Phase-to-Phase Faults	3294	3294	0	100%
Three-Phase Faults	1098	1098	0	100%
Phase-to-Ground Faults	3294	3294	0	100%
Phase-to-Phase-to-Ground Faults	3294	3294	0	100%

5.3.5 Evaluating Faulted Phase Selection Performance

The accuracy of the faulty phase selection procedure is evaluated in this section.

a) Faulted Phase Identification for Phase-to-Ground Faults

Fig 5.11 (a) and (b) show the observed variation of $G_{\beta X}^{\alpha X}$ indices with the fault inception angle for Phase-A-to-Ground faults at the middle of Line M-N for 0.05 Ω and 50 Ω fault resistances respectively. According to Fig 5.11, regardless of the fault inception angle and fault resistance value, $G_{\beta_A}^{\alpha_A}$ is at least 75 times greater than the threshold k_2 (=10).

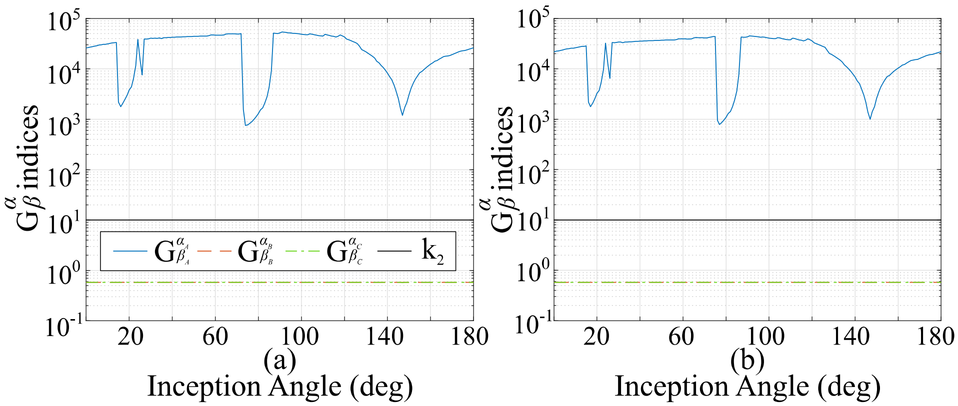

Fig 5.11 Fault Indices for Phase-A-to-Ground faults at 50% of the Line (a) 0.05 Ω Faults Resistance (b) 50 Ω Faults Resistance

The indices $G_{\beta_B}^{\alpha_B}$, $G_{\beta_C}^{\alpha_C}$ are approximately equal to 0.577 $(1/\sqrt{3})$ irrespective of the fault resistance and fault inception angle, and less than the threshold k_2. Hence for all cases, Phase-A can be easily identified as the faulted phase according to ((5.16). Further simulations showed that this property holds for all fault locations. The selected value of threshold $k_{2,}$ 10, gives reliable discrimination.

b) Faulted Phase Identification for Phase-to-Phase Faults

Once a Phase-to-Phase fault is identified, the faulty phases can be identified using ((5.17). The $G_{\alpha X}^{\beta X}$ index computed taking the healthy phase as the reference has a very high value, while the other two remain around 0.577. This condition is satisfied irrespective of the fault inception angle or the fault resistance, as can be seen in Fig 5.12 which shows the variations of three $G_{\alpha X}^{\beta X}$ indices with the fault inception angle during Phase-A-to-Phase-B faults. The selected value of k_2 ensures correct decisions are made.

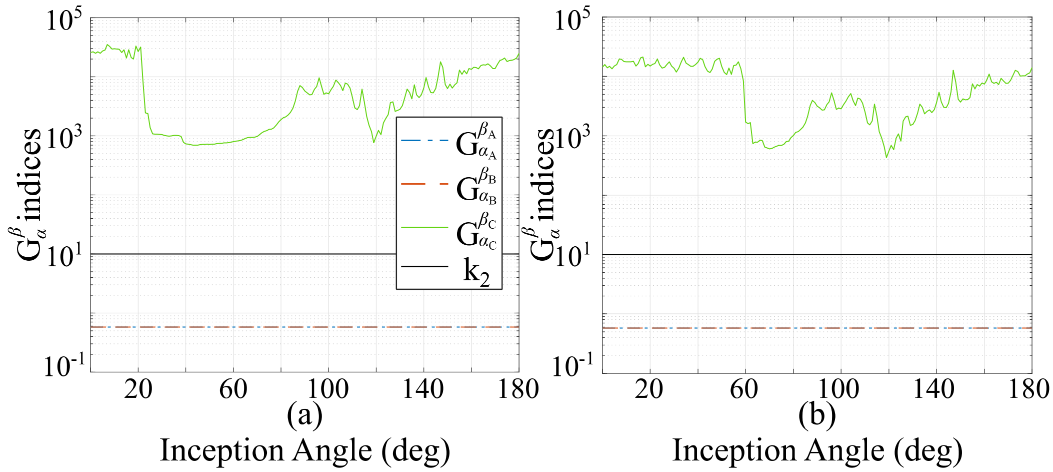

Fig 5.12 Fault Indices for a Phase-A-to-B Fault at 75% of Line M-N for (a) 0.05 Ω Resistance and (b) 50 Ω Fault Resistance

c) Faulted Phase Identification for Phase-to-Phase-to-Ground Faults

Fig 5.13 shows the variations of $G_{\beta X}^{\alpha X}$ indices with the fault inception angle for Phase-A- Phase-B-to-ground faults at two different fault resistance values.

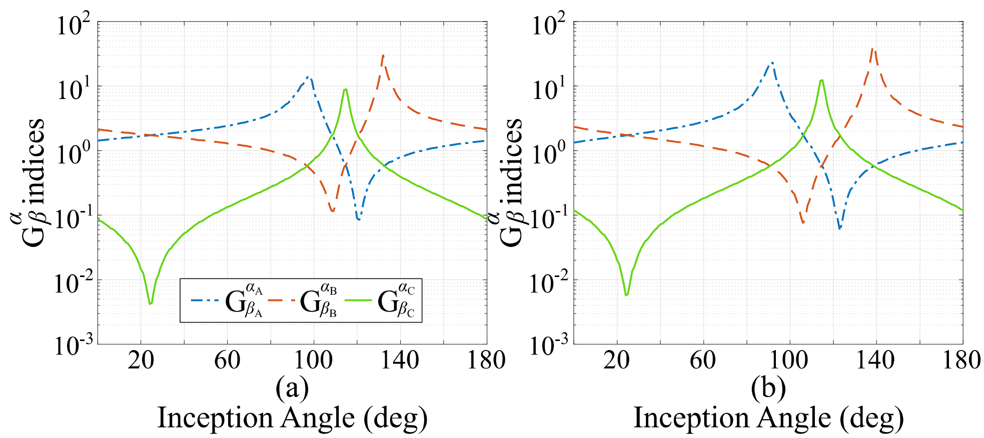

Fig 5.13 Variation of Fault Indices for Phase-A-to-B-to-Ground Faults at 25% of Line M-N (a) 0.05 Ω Fault Resistance and (b) 50 Ω Fault Resistance

According to Fig 5.13 (a), the values of $G_{\beta_C}^{\alpha_C}$ remains below $G_{\beta_A}^{\alpha_A}$ and $G_{\beta_B}^{\alpha_B}$ as expected for a Phase-A-Phase-B-to-Ground fault, when the inception angle is in the ranges of 0° to 97° and 134° to 180° facilitating correct faulty phase identification. However, the discrimination criteria in ((5.18) give incorrect results for the fault inception angles in the range of 97° to 115° (Phase-A and

Phase-C), and 115° to 133° (Phase-B and Phase-C). Careful examination showed that this incorrect faulty phase identification happens if a fault occurs at a point where the voltage difference of the faulted phases is close to zero. Thus, there is a region of fault inception angles that blinds the faulty phase identification criteria for Phase-to-Phase-to-Ground faults. According to Fig 5.13 (a) and Fig 5.13 (b), this region spans for about 40° when considering 50 Ω faults.

It should be noted that from the protection perspective, this incorrect identification of faulted phases is not a major drawback since the fault type is correctly established as a Phase-to-Phase-to-Ground fault in the fault type identification step. Incorrect identification of faulted phases is inconsequential to trip decisions because three-phase tripping is usually employed for any fault involving two or more phases. However, the relay may provide wrong faulted phase information, for example, to repair crews or engineers doing post-mortem analysis.

d) Overall Accuracy of Faulted Phase Identification

Table 5.13 shows the observed accuracy of the proposed faulted phase identification algorithm for over 9,000 fault scenarios simulated in the system shown in Fig 5.5 using the threshold values selected in Section 5.3.2. According to Table 5.13, faulted phases were correctly identified 100% of the time for Phase-to-Ground and Phase-to-Phase faults. The accuracy remained over 80% for Phase-to-Phase-to-Ground faults. However, it should be noted that the incorrect decisions in Table 5.13 refer to the incorrect identification of faulted phases involved in the fault and not the fault type.

Table 5.13 Faulted Phase Identification

Applied Fault	Number of Cases	Correct decisions	Incorrect decisions	Accuracy
A-to-B	1098	1098	0	100%
A-to-C	1098	1098	0	100%
B-to-C	1098	1098	0	100%
A-to-G	1098	1098	0	100%
B-to-G	1098	1098	0	100%
C-to-G	1098	1098	0	100%
A-to-B-to-G	1098	915	183	83.3%
A-to-C-to-G	1098	894	204	81.42%
B-to-C-to-G	1098	913	185	83.15%

5.3.6 Practical Consideration of Proposed Algorithm

5.3.6.1 Effect of Sampling Rate

The effect of sampling rate on the accuracy of the algorithm was evaluated considering 100 kHz, 40 kHz, and 10 kHz sampling frequencies. The EMT model of the power system depicted in Fig 5.5 was simulated with 5 μs time steps (less than the period of highest sampling frequency) and the current measurements were obtained through a 500/5A current transformer modeled in PSCAD/EMTDC^{TM}. Signal processing was modeled as shown in Fig 5.14. The Low Pass Filter (LPF) cutoff frequency was set to half the sampling frequency and Analog to Digital Conversion (ADC) resolution was set to 16 bits. The variations of two selected transformed current components

(i_{α_A} and i_{β_A}) computed from signals sampled at different rates are compared for a Phase-B-to-Ground fault example in Fig 5.14.

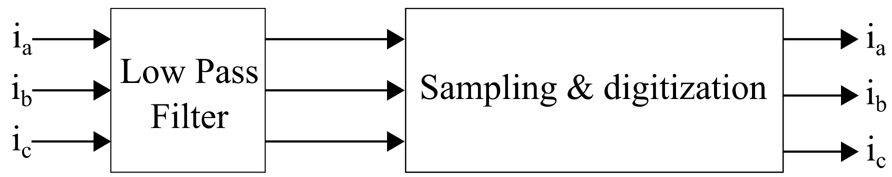

Fig 5.14 Analog to Digital Conversion Process

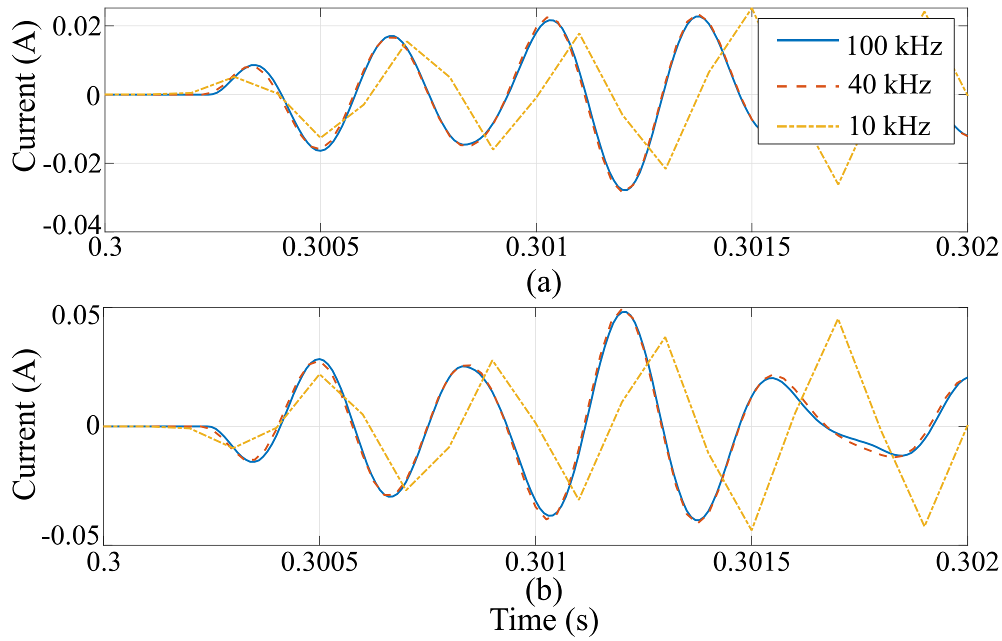

Fig 5.15 Transformed Current Components (a) i_{α_A} and (b) i_{β_A} Calculated with Different Sampling Frequencies.

According to Fig 5.15, the variations of the current components are almost the same at 100 kHz and 40 kHz sampling rates. It is similar to the other current components and remains so for sampling frequencies above 20 kHz. The signals sampled at 10 kHz deviate significantly from the rest but produce consistent fault type and faulted phase identification results because indices are calculated as ratios. However, the discrimination margins were reduced at 10 kHz. The results presented in Section 5.3.6 correspond to 40 kHz sampling, which is more than adequate for the algorithm.

5.3.6.2 *Effect of Non-Ideal Transposition*

The Clarke's transform does not perfectly decouple the phase quantities in non-transposed and non-ideally transposed systems. Simulation studies were carried out on the power system shown in Fig 5.5 by replacing the transmission lines with completely non-transposed transmission lines and realistically transposed (1/3-1/3-1/3 scheme) transmission lines to analyze the effect of line transposition on the proposed algorithm.

The simulation results showed that appreciable differences occur only in the transformed components which are expected to be approximately equal to zero for a particular fault type: the peak magnitudes of these components increase when the line is non-ideally transposed. This in turn can affect the indices ($G_{\beta_X}^{\alpha_X}$ and $G_{\alpha_X}^{\beta_X}$) and reduce the discrimination margin in the fault type identification criteria given in ((5.13) and ((5.15). However, the criteria for faulted phase identification given in ((5.16), ((5.17), and ((5.18) are not much affected by the transposition scheme used.

5.3.6.3 *Selection of Thresholds k_0, k_1 and k_2*

The suitable ranges of the thresholds k_0 and k_2 were recommended based on the theoretical expectations of the fault indices, and they are expected to be system-independent. The condition in ((5.9) is in effect looking for a significant percentage of ground mode current compared to aerial mode current. The theoretically expected minimum value for $G_{\alpha X}^{\gamma}$ indices during a ground fault are 0.5, and therefore k_0 should be below 0.5. Considering the principles used in setting ground overcurrent relays, a value in the range 0.05-0.1 was proposed, and the simulations confirmed the appropriateness of the values used for k_0. This setting should apply to any power system which is not highly unbalanced. Theoretically, the threshold k_2 should be set above 0.577, because during the Phase-to-Ground faults, $G_{\beta_X}^{\alpha_X}$ indices of the non-faulted phases are approximately equal to 0.577 and during the Phase-to-Phase faults, $G_{\alpha_X}^{\beta_X}$ indices of the faulted phases are approximately equal to 0.577. A value in the range [1-10] is suggested, and the simulations showed that $G_{\alpha_X}^{\beta_X}$ virtually remain at the theoretically expected values and there is an ample margin of discrimination with the value used for k_2 (=10).

However, the value of threshold k_1 is not system-independent as thresholds k_0 and k_2. Simulation studies showed that the discrimination margins of the fault type identification criteria given in ((5.13) and ((5.15) are affected by the line transposition scheme. Thus, the threshold k_1 should be selected appropriately for a given system through an engineering study considering the worst-case fault resistance and fault inception angles.

5.3.6.4 Performance for Remote and Reverse Faults

To examine fault type and faulted phase identification for faults happening outside the protected line, Phase-A-to-ground faults were applied at 50% of Line M-N (protected line for relays at M and N) and Line N-L (remote faults for relay at M and reverse faults for relay at N). The currents in Line M-N were measured at both ends (M and N) and fed to the algorithm. A total of 31 faults per scenario were applied varying the fault inception angle by 6 degrees. For all cases, the fault type and the faulted phase were identified correctly. Hence it is apparent that the algorithm works irrespective of the measurement location and direction.

5.3.6.5 Effect of Noise

Noise in the signals is a major issue for transient-based algorithms. The effect of noise on the proposed algorithm was analyzed by adding high-frequency uniform random noise to the input signals. The effect of noise was negligible for signal-to-noise ratios higher than 10 dB. This very high immunity to noise is expected because the noise is filtered out by the bandpass filter. Only higher-order harmonics or inter-harmonics that fall within the pass band of the filter can degrade the performance. The effect of quantization noise was also examined by changing the ADC resolution. The algorithm could satisfactorily perform at 12-bit resolution, but below that performance becomes unreliable.

5.3.7 Performance Evaluation Using Digital Real-Time Simulator

To evaluate the real-time performance of the proposed algorithm, the algorithm was implemented as a real-time process on a Digital Real Time Simulator (DRTS) unit as depicted in Fig 5.16. The algorithm was implemented in the DRTS using standard library components available in the DRTS software suite and received instantaneous current and voltage measurements as IEC 61850-9-2 LE sampled values (SV) from the DRTS unit simulating the power system. The two DRTS units were independent and connected only through an external, real communication link that serves as the IEC 61850 process bus. In addition, the simulation time step of both DRTS units was synchronized to a common GNSS (Global Navigation Satellite System) time reference.

IEC 61850-9-2 LE SV published by the network interface card of the DRTS unit 1 (simulating the power system) was directed through a Local Area Network (LAN) to DRTS unit 2, which ran the transient-based phase selection algorithm. The SV packets were published at a sampling rate of 256 samples per cycle (s/c), which translates to a sampling frequency of 15.36 kHz with a system nominal frequency of 60 Hz. The merging unit was modeled assuming an Analogue to Digital (A/D) converter bit resolution of 24 bits. Anti-aliasing filters of the merging unit were modeled as 6th-order low-pass Butterworth filters with the cutoff frequency set to half of the sampling frequency of 15.36 kHz. The lower and upper cutoff frequencies of the band-pass filter used in the phase selection algorithm were adjusted to 2.5 kHz and 3.5 kHz, respectively. Moreover, the threshold settings k_0, k_1, and k_2 were set as 0.05, 25, and 10, respectively. DRTS unit 2 decoded and fed the measurements in the subscribed SV to the transient-based phase selection algorithm. Upon identifying the fault type, the transient-based algorithm initiated a GOOSE message that carried the faulted phase information from DRTS unit 2 to DRTS unit 1. To increase the resolution of the voltage and current measurements fed to the algorithm, smaller SV channel scale factors than the ones defined in the standards IEC 61850-9-2LE/IEC 61869-9 were used. Lowering the scale factors enabled better utilization of the 32-bit representation of values used in SV communication for this application, where measurement resolution is of a higher significance than the dynamic range.

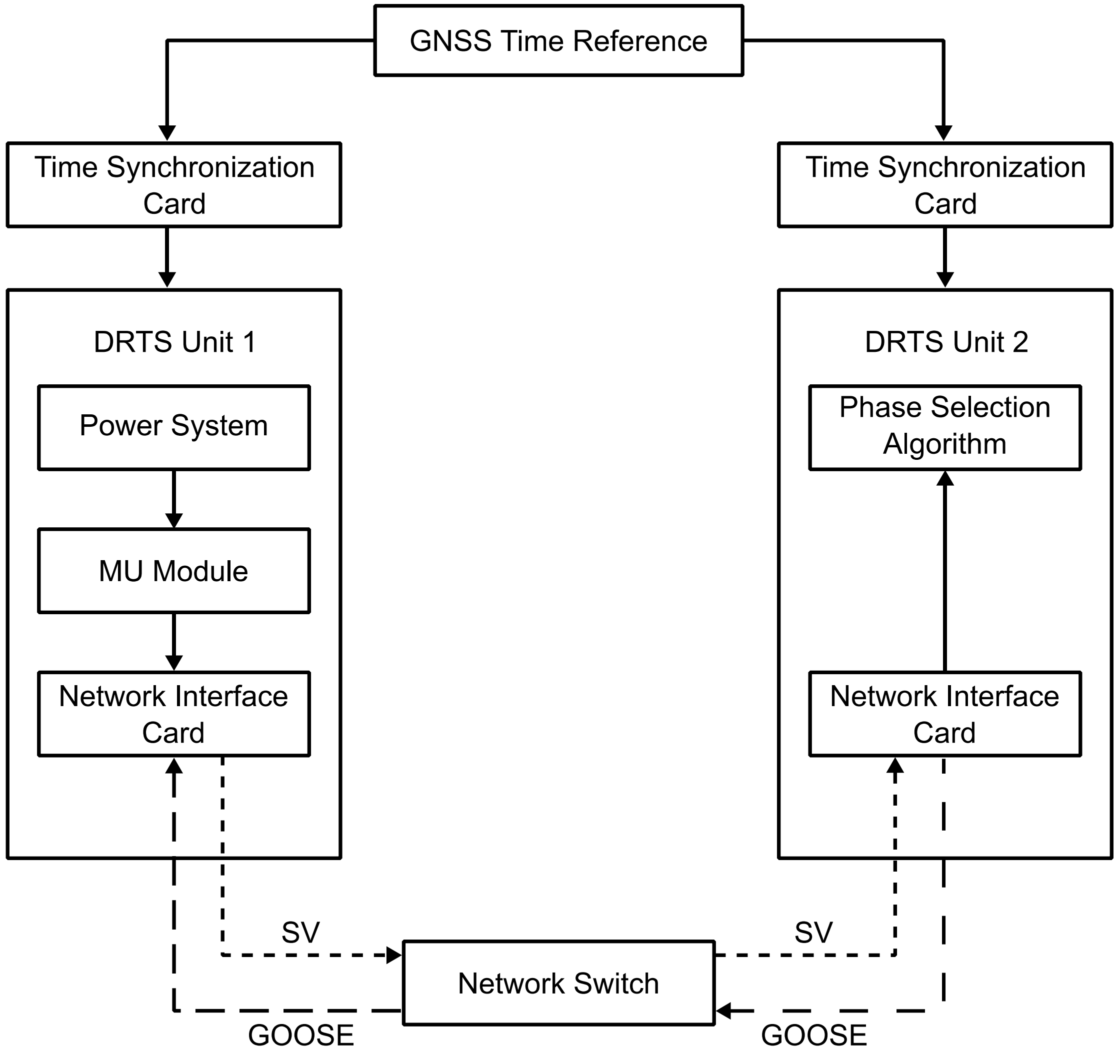

Fig 5.16 Schematic of the Setup for Testing the Proposed Algorithm in DRTS

The power system model used to test the transient-based consisted of a Type – IV windfarm as depicted in Fig A.1. High impedance and short circuit faults given in Table 5.14 were applied in the protected line several times in each test case to verify the reliability of the algorithm. The results are summarized in Table 5.14.

Table 5.14 Fault Type Identification of Transient-Based Faulted Phase Identification Algorithm

Applied fault		Short Circuit Faults	High Impedance Fault
Type	Location		
AG	5%	AG	AG
	50%	AG	AG
	75%	AG	AG
BC	5%	BC	BC
	50%	BC	BC
	75%	BC	BC
ACG	5%	ACG	ACG
	50%	ACG	ACG
	75%	ACG	ACG

Table 5.15 shows the overall performance of the transient-based algorithm for various fault types. Both short circuit and high impedance faults (50 Ω) were applied at three different fault locations (5%, 50%, and 75% of line length) while varying the fault inception angle from 0º to 180º in one-degree steps. The current transient-based method identified the fault type with an accuracy of more than 95% for most fault types. However, even in this scenario, the transient-based method delivered a higher accuracy (over 70%). Furthermore, the algorithm did not identify Phase-to-Phase-to-Ground faults as Phase-to-Ground faults. In addition to that, the transient-based scheme was capable of identifying the faulted phase within 1 ms of fault inception. Furthermore, the average round trip time of the test loop (including the GOOSE/SV message transfer times) was approximately 4 ms.

Table 5.15 Overall Performance of the Transient-Based Algorithm

Applied Fault	Number of Cases	Correctly Identified Cases	Incorrectly Identified Cases	Accuracy (%)
AG	1086	1062	24	97.79
BG	1086	1067	19	98.25
CG	1086	1062	24	97.29
Total	**3258**	**3191**	**67**	**97.94**
ABG	1086	796	290	73.29
ACG	1086	813	273	74.86
BCG	1086	811	275	74.67
Total	**3258**	**2420**	**838**	**74.28**
AB	1086	1079	7	99.36
AC	1086	1080	6	99.44
BC	1086	1080	6	99.45
ABC	1086	1028	58	94.66
Total	**4344**	**4267**	**76**	**98.22**

5.4 Concluding Remarks

This chapter introduces a faulted phase selection algorithm that relies on Clarke current transients produced during faults. The algorithm does not require very high sampling rates and is simple to implement. Hence, the method can be implemented on existing hardware without any issues.

The transient current-based faulted phase selection algorithm classifies faults much faster than phasor-based algorithms as the indices are calculated using a very short 0.75 ms measurement window. Since the fault discrimination indices are calculated using the signal components in the 2500 –3500 Hz range, the standard current transformers are adequate. Furthermore, the performance of the transient current-based faulted phase selection algorithm was evaluated in a real-time digital simulator to evaluate its real-time performance using IEC 61850-9-2 LE sampled values and GOOSE messages on a power system with high penetration of IBRs. The transient current-based algorithm delivered accurate results for faulted phase selection in the presence of IBRs. However, the accuracy of the algorithm was affected by the fault inception angle, especially in the case of Phase-to-Phase-to-Ground faults. Even though in the cases in which the algorithm incorrectly identified the phases involved in Phase-to-Phase-to-Ground faults, the algorithm accurately identified the fault type as a Phase-to-Phase-to-Ground fault. In addition to that the algorithm accuracy was also affected by the line transposition schemes.

Chapter 6

Fault Type and Faulted Phase Identification Using Incremental Phase Currents

The current transient-based faulted phase selection algorithm presented in Chapter 5 showed promising results. However, some drawbacks were identified during the validation stage. One of the main drawbacks is the effect of the fault inception angle. Especially in the case of Phase-to-Phase-to-Ground faults where the faulted phases are identified incorrectly even though the fault is identified as a Phase-to-Phase-to-Ground fault. Furthermore, the transposition scheme also affected the overall performance of the algorithm.

The incremental current-based faulted phase selection scheme proposed in this Chapter is immune to the fault inception angle and the effect of line transposition. It uses some of the concepts used in the transient current-based algorithms introduced in Chapter 5, especially the concept of comparing the peak values of the rate of change of currents to determine the faulted phase, but directly uses incremental phase currents instead of their Clarke components.

6.1 Instantaneous Incremental Current Based Faulted Phase Selection Indices

When a fault occurs in a transmission line, fault currents start to flow in the phases involved in the fault. Therefore, current magnitudes in the faulted phase or phases are significantly higher than the current magnitudes in the non-faulted phase or phases. However, trying to identify the faulted phase or phases using a simple magnitude comparison would not be successful under high resistance faults or when the system is heavily loaded.

On the other hand, the process of identifying faulted phases becomes much simpler if incremental components of the post-fault currents, which represent the fault-induced components, are used. Furthermore, the rate of change of incremental currents (ROCOIC) would indicate the change from non-faulted to faulted state faster than the incremental currents. Therefore, a pairwise comparison of the rate of change of incremental currents (ROCOIC) is proposed as a technique to identify the fault type and faulted phases. It will be shown that this approach results in a more robust, faster and simpler algorithm at the expense of a slight reduction in the speed.

The pair of indices defined in ((6.1) are proposed to compare ROCOIC values of two phases; thus, for a three-phase system, six indices can be calculated.

$$F_{xy} = \frac{max\left|\frac{d\Delta i_x(t)}{dt}\right|}{max\left|\frac{d\Delta i_y(t)}{dt}\right|} \quad F_{yx} = \frac{max\left|\frac{d\Delta i_y(t)}{dt}\right|}{max\left|\frac{d\Delta i_x(t)}{dt}\right|} \tag{6.1}$$

where $\Delta i_x(t)$ and $\Delta i_y(t)$ are instantaneous incremental currents of Phase-X and -Y respectively. This index is a measure of the relative strength of the incremental current of one phase to that of another phase and vice versa. The absolute maximum rate of change of incremental currents within a short time window of length T_W is used for computing the indices. Ground faults are identified by checking for the existence of zero sequence currents.

6.2 Faulted Phase Identification Using the Proposed Indices

The following three subsections describe the basis of criteria to identify the faulted phases.

6.2.1 Identifying the Faulted Phase in Phase-to-Ground Faults

Consider a Phase-A-to-Ground fault. During this fault, a significant incremental current can be observed in Phase A, and little to no incremental currents can be observed in Phases B and C. Hence the six indices during a Phase-A-to-Ground fault would have the following relationships: $F_{ab} \gg 1$, $F_{bc} \approx 1$, $F_{ca} \ll 1$, $F_{ba} \ll 1$, $F_{cb} \approx 1$, and $F_{ac} \gg 1$. Therefore, during a Phase-to-Ground fault, the two indices that have the faulted phase incremental current as the numerator (F_{ab} and F_{ac}) will be the largest two indices among six indices while the other four indices will be:

a) Approximately equal to one or

b) Less than one.

This would hold for other types of faults as well. Thus, the following logic can be used to determine the faulted phase in any Phase-to-Ground fault.

$$\begin{array}{c} if\{(max(F_{ab}, F_{bc}, F_{ca}) = F_{ab})\ \&\ (max(F_{ba}, F_{cb}, F_{ac}) = F_{ac})\}:\ AG\ Fault \\ else\ if\{(max(F_{ac}, F_{bc}, F_{ca}) = F_{bc})\ \&\ (max(F_{ba}, F_{cb}, F_{ac}) = F_{ba})\}:\ BG\ Fault \\ else\ if\{(max(F_{ab}, F_{bc}, F_{ca}) = F_{ca})\ \&\ (max(F_{ca}, F_{cb}, F_{ac}) = F_{cb})\}:\ CG\ Fault \end{array} \tag{6.2}$$

6.2.2 Identifying the Faulted Phases in Phase-to-Phase and Phase-to-Phase-to-Ground Faults

To explain the logic to identify the phases in Phase-to-Phase or Phase-to-Phase-to-Ground faults, consider a Phase-B-to-C fault. During a Phase-B-to-C fault, significant incremental currents can be observed in Phases-B and -C. Hence the six indices during a Phase-B-to-C fault would be related as: $F_{ab} \ll 1$, $F_{bc} \approx 1$, $F_{ca} \gg 1$, $F_{ba} \gg 1$, $F_{cb} \approx 1$, and $F_{ac} \ll 1$. Therefore, indices F_{ba} and F_{ca} will be the largest two indices among the six indices. Thus, in general, during a Phase-to-Phase or Phase-to-Phase-to-Ground fault, the two indices which have the incremental currents of the faulted phases in the numerator will be the largest two indices while the other four indices will be either less than one or approximately equal to one. Hence, a logic scheme can be developed to identify the faulted phases in Phase-to-Phase and Phase-to-Phase-to-Ground faults.

$$\begin{aligned} &if\{(max(F_{ab}, F_{bc}, F_{ca}) = F_{bc})\ \&\ (max(F_{ba}, F_{cb}, F_{ac}) = F_{ac})\}: AB/ABG\ Fault \\ &else\ if\{(max(F_{ab}, F_{bc}, F_{ca}) = F_{ab})\ \&\ (max(F_{ba}, F_{cb}, F_{ac}) = F_{cb})\}: AC/ACG\ Fault \\ &else\ if\{(max(F_{ab}, F_{bc}, F_{ca}) = F_{ca})\ \&\ (max(F_{ba}, F_{cb}, F_{ac}) = F_{ba})\}: BC/BCG\ Fault \end{aligned} \quad (6.3)$$

Phase-to-Phase-to-Ground faults can be discriminated from the Phase-to-Phase faults by checking the existence of zero sequence currents.

6.2.3 Identifying Three-Phase Faults

During a Three-Phase fault, incremental currents can be observed in all three phases. Therefore, all six indices will be approximately equal to one. Hence, the difference between the index and its inverse index should be theoretically equal to zero. The logic to identify the Three-Phase faults is given in ((6.4), with the threshold k_1 set to 1.

$$if\{(|F_{ab} - F_{ba}| < k_1)\ \&(|F_{bc} - F_{cb}| < k_1)\ \&\ (|F_{ca} - F_{ac}| < k_1)\}: Three - Phase\ Fault \quad (6.4)$$

The criteria to identify the faulted phases can be summarized in Table 6.1 where the largest two indices out of the six calculated indices during a fault are marked by an X.

Table 6.1 Largest Two Indices for Different Fault Types

Fault	**Index**					
	$\boldsymbol{F_{ab}}$	$\boldsymbol{F_{bc}}$	$\boldsymbol{F_{ca}}$	$\boldsymbol{F_{ba}}$	$\boldsymbol{F_{cb}}$	$\boldsymbol{F_{ac}}$
AG	X					X
BG		X		X		
CG			X		X	
AB/ABG		X				X
AC/ACG	X				X	
BC/BCG			X	X		

6.3 Signal Processing and Algorithm Implementation

As mentioned in Chapter 2, instantaneous incremental currents consist of all the frequency components including the decaying DC component, the fundamental frequency component of the fault component, and the high-frequency components. The proposed phase selection scheme works best when focused on the fundamental frequency component of the fault component. To eliminate DC components and high-frequency noise due to traveling waves, some amount of signal conditioning is required. The signal processing involved in the proposed algorithm is depicted in Fig 6.1 along with the index calculation stage. Fig 6.1 (a) shows the signal processing and maximum value calculation stage of the algorithm. The instantaneous current samples are first filtered using a digital mimic filter to remove the decaying DC component. Accurate knowledge of the system-dependent filter time constant is not critical for this application. Upon removing the DC component, the current samples are low-pass filtered to remove the high-frequency transients.

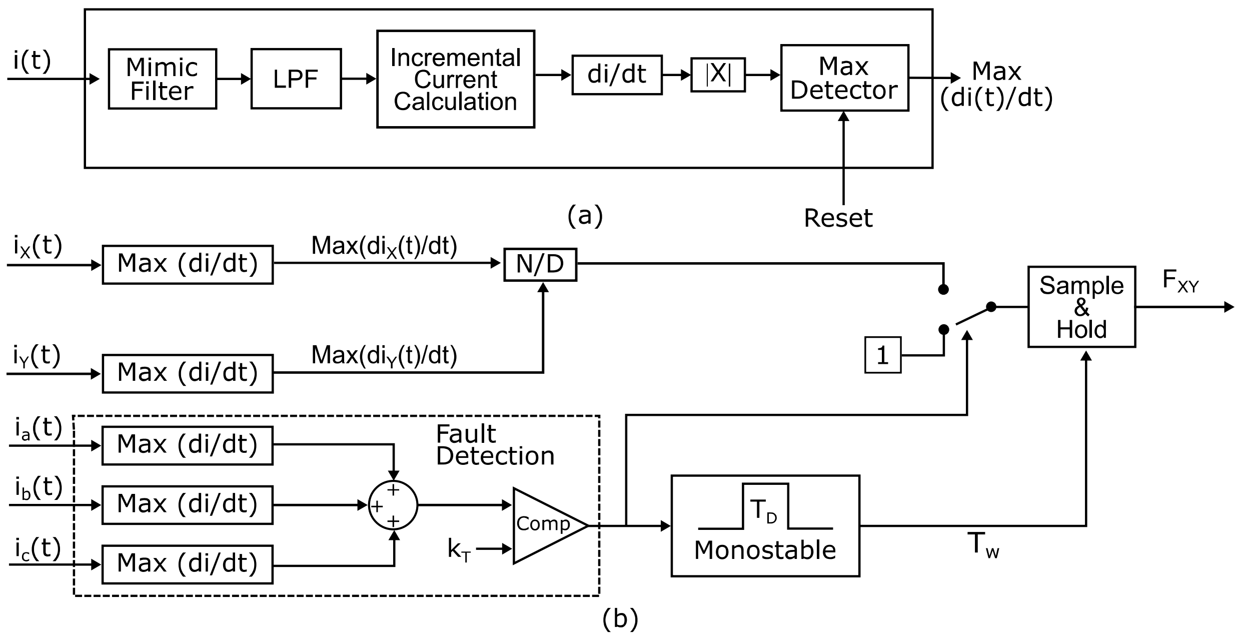

Fig 6.1 Calculating the Faulted Phase Identification Indices (a) Signal Conditioning and Max(di/dt) detector, (b) Index calculation.

Fig 6.1 (b) shows the fault detection logic and the index calculation stage of the algorithm. Until the fault is detected the indices are forced to 1. Once the fault is detected, the timer is activated. The value of the index at the end of the timer is held at the sample & hold circuit. A simple threshold-based comparison method is employed to detect the fault condition, and it works fast and reliably for all conditions. If desired, any other robust fault detection technique can be used.

Fig 6.2 shows the complete phase selection algorithm. Once the fault is detected, first the Three-Phase fault check is carried out to identify the existence of a Three-Phase fault. Then the ground faults are discriminated by checking for the existence of zero sequence current by comparing the zero-sequence current against threshold k_0. Then the logic conditions for each fault are checked until a decision is made.

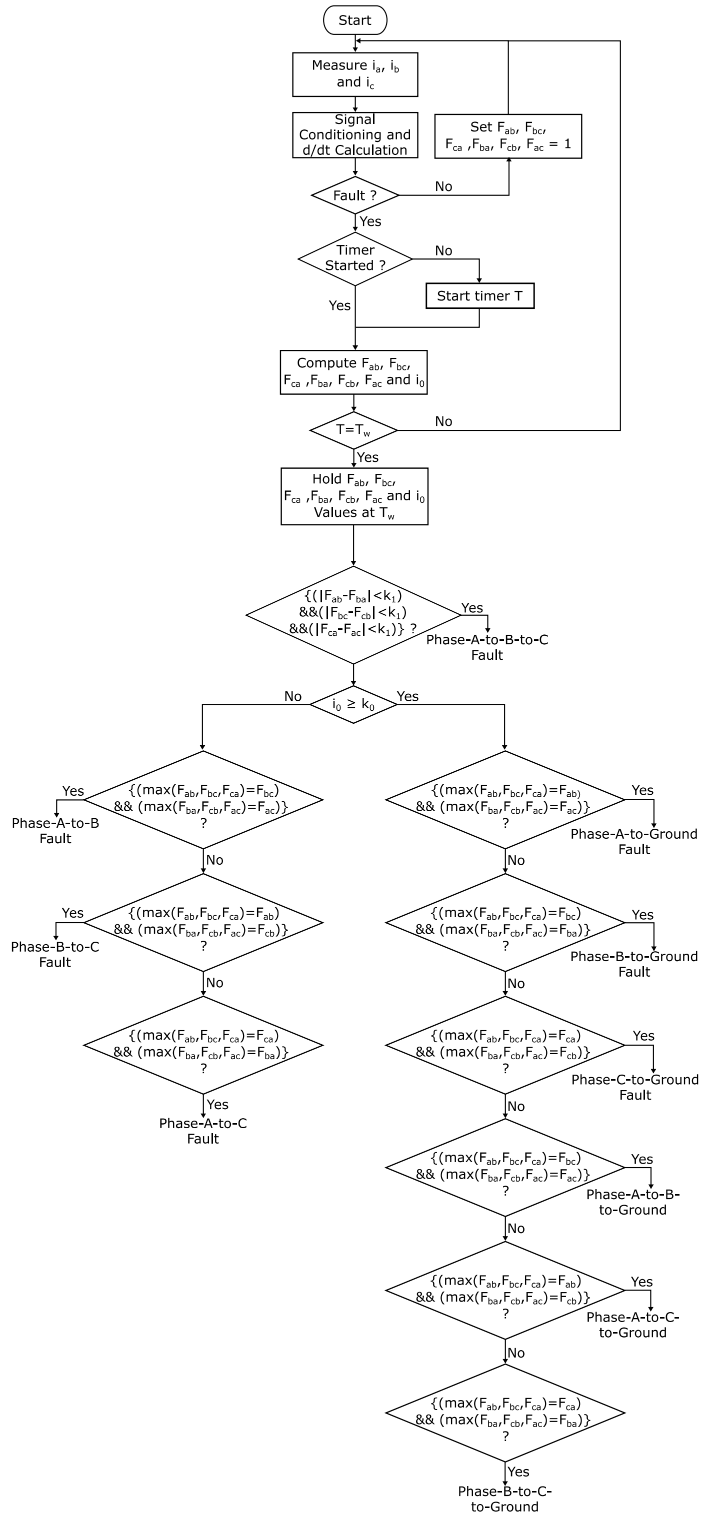

Fig 6.2 Incremental Current-Based Faulted Phase Selection Algorithm

6.4 Algorithm Evaluation

The power system used in Chapter 3 was used to evaluate the proposed algorithm with the same parameters. The parameters of the power system are given in Section 3.5. The simulation was run with 10 μs time steps in PSCAD/EMTDC™.

The three-threshold settings and the low pass filter cutoff frequency were verified through a simulation study. The proposed method uses the instantaneous incremental quantities around a narrow band around the fundamental frequency. Therefore, the low pass filter cutoff frequency was set to 150 Hz. This cutoff frequency works well for systems with 50 or 60 Hz nominal frequency, removing the high-frequency content and higher-order harmonics. The fault detection threshold (k_T) should be set above the absolute sum of peak di/dt values under normal operation, which is theoretically equal to zero since no incremental currents should be flowing in the circuit during a non-fault situation. Hence, the threshold setting was set to 1 A/s. In practice, this threshold can be adjusted during the commissioning so that it does not trigger due to normally present noise. The setting is also not critical, as it is not required for the faulted phase selection algorithm to discriminate between faults and other events (such as load or line switching, etc.). The ground fault discrimination threshold (k_0) was set to 5 % of the steady state RMS current to 0.1125 A.

The Three-Phase fault detection threshold (k_1) was set to 1.0. The index calculation time window (T_W) was set to 5 ms. The fault signals were sampled at 80 samples/cycle and do not require very high sampling rates since the algorithm relies on instantaneous values. A window length of about a quarter cycle ensures a fast response and minimizes any influence of CT saturation because, in properly designed systems, it is highly unlikely for DC saturation to occur in the first quarter cycle after a fault. The signal conditioning and algorithm parameters can be fine-tuned to a given system, for example, k_0 can be set more sensitively for systems with high impedance or resonance grounding.

6.4.1 Demonstration of Algorithm

To demonstrate the basic operation of the proposed algorithm, faults listed in Table 6.2 were applied in the middle of Line-LM at 0.5 s.

Table 6.2 Considered Fault Scenarios

Scenario	**Fault**	**Fault Resistance**	**Location**
Scenario-1	BG	150 Ω	50 % of Line LM
Scenario-2	AC	150 Ω	50 % of Line LM
Scenario-3	ABC	150 Ω	50 % of Line LM

Fig 6.3 shows the ROCOIC variations for the considered fault scenarios. Fig 6.3 (a) shows the ROCOICs for Scenario-1 where the ROCOIC of Phase-B is significantly larger than the ROCOIC of the other two phases. In addition to that, variations of ROCOIC of phases A and C are identical during the fault scenario. Hence, F_{ba} and F_{bc} will be much larger than F_{ab}, F_{ca}, F_{cb}, and F_{ab} which satisfies the condition given in ((6.2). Similar behavior can be observed for other Phase-to-Ground faults as well.

Fig 6.3 (b) depicts the variations of ROCOIC for fault Scenario-2. The ROCOIC of the two faulted phases (Phase-A and C) are much larger than the non-faulted phase (Phase-B). Since the magnitude variation of the two faulted phases is identical, F_{ca} and F_{ac} indices would be approximately equal to one whereas F_{ab} and F_{cb} would be much larger than the other four indices. Hence, using the logic given in ((6.3) the two faulted phases can be identified as Phase-A and C.

A similar kind of behavior can be observed in a Phase-A-to-Phase-C-to-Ground fault scenario as well. The only difference would be the existence of zero sequence current.

Fig 6.3 (c) shows the variation of ROCOIC for fault Scenario 3. In this case, all three phases show a significant amount of incremental currents compared to the other two fault scenarios. Furthermore, the magnitude variation of all three phases is similar to each other. Therefore, all six indices calculated during this fault scenario would be close to one satisfying the criteria given in ((6.4).

Table 6.3 shows the index values for the considered fault scenarios. Even with a high fault resistance value such as 150 Ω the proposed method can identify the correct faulted phase which is one of the main advantages of the proposed algorithm.

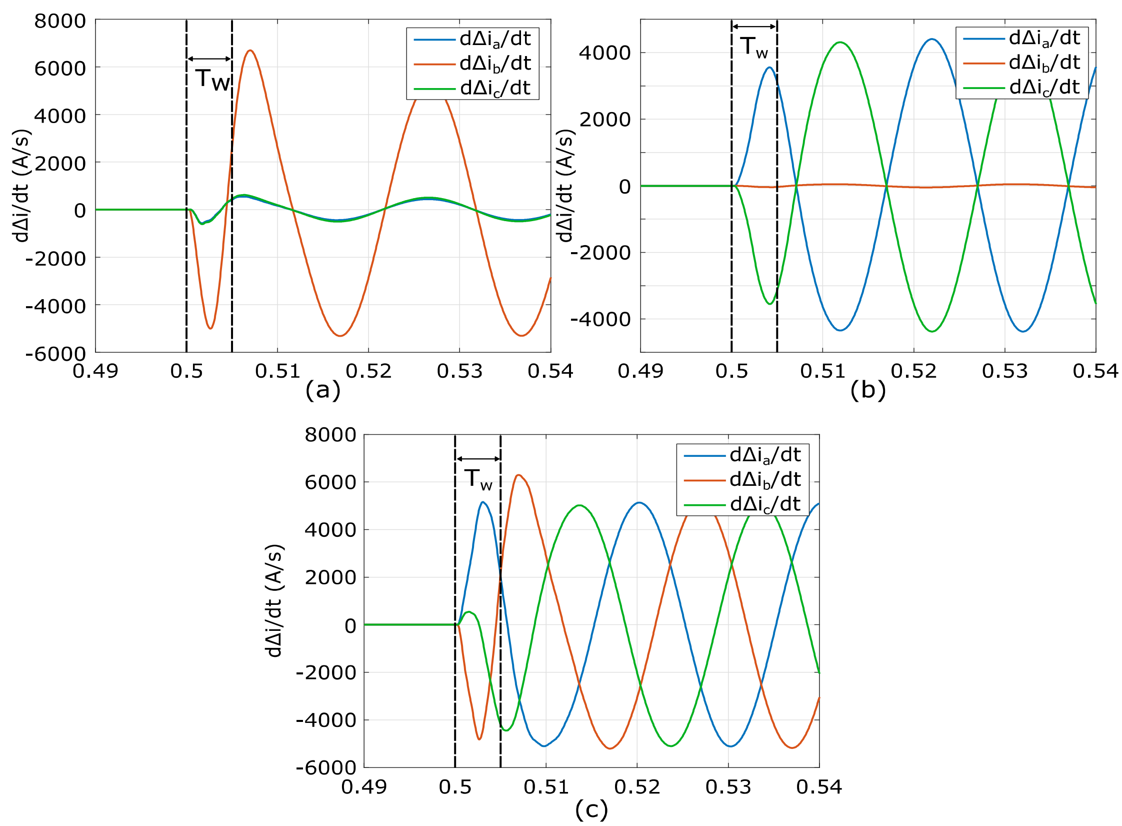

Fig 6.3 Rate of Change of Incremental Currents for (a) Scenario-1, (b) Scenario-2, and (c) Scenario-3

Table 6.3 Index Values for Considered Fault Scenarios

Scenario	F_{ab}	F_{bc}	F_{ca}	F_{ba}	F_{cb}	F_{ac}
Scenario-1	0.096	9.73	1.07	10.41	0.10	0.934
Scenario-2	77.62	0.013	0.99	0.013	77.62	1.00
Scenario-3	0.877	1.34	0.85	1.14	0.74	1.18

6.4.2 Identification of Phase-to-Ground Faults

Fig 6.4 shows the variation of fault indices for Phase-C-to-Ground fault for three different fault resistances (0.01 Ω, 100 Ω, and 300 Ω). The fault inception angle was varied in one-degree steps from zero to 180 degrees. The faults were applied at 50% of the length of Line-LM. Irrespective of the fault resistance value, the indices F_{ca} and F_{cb} remain the two largest indices while F_{ab} and F_{ba} are close to one and F_{ac} and F_{bc} remain the smallest indicating a Phase-C-to-Ground fault. The results prove the robustness of the proposed algorithm against the fault resistance and inception angle, one of the weaknesses of the transient-based phase selection algorithm proposed in Chapter 5.

The influence of fault location on the proposed algorithm was analyzed by applying Phase-A-to-Ground short circuit faults on Line-LM between 10% and 100% of the line length. Fig 6.5 depicts the variation of fault indices with 1-degree increments along the line. The indices F_{ab} and F_{ac} which are depicted in Fig 6.5 (a) and Fig 6.5 (f) remain as the two largest indices irrespective of the fault inception angle and fault location verifying the existence of a Phase-A-to-Ground fault.

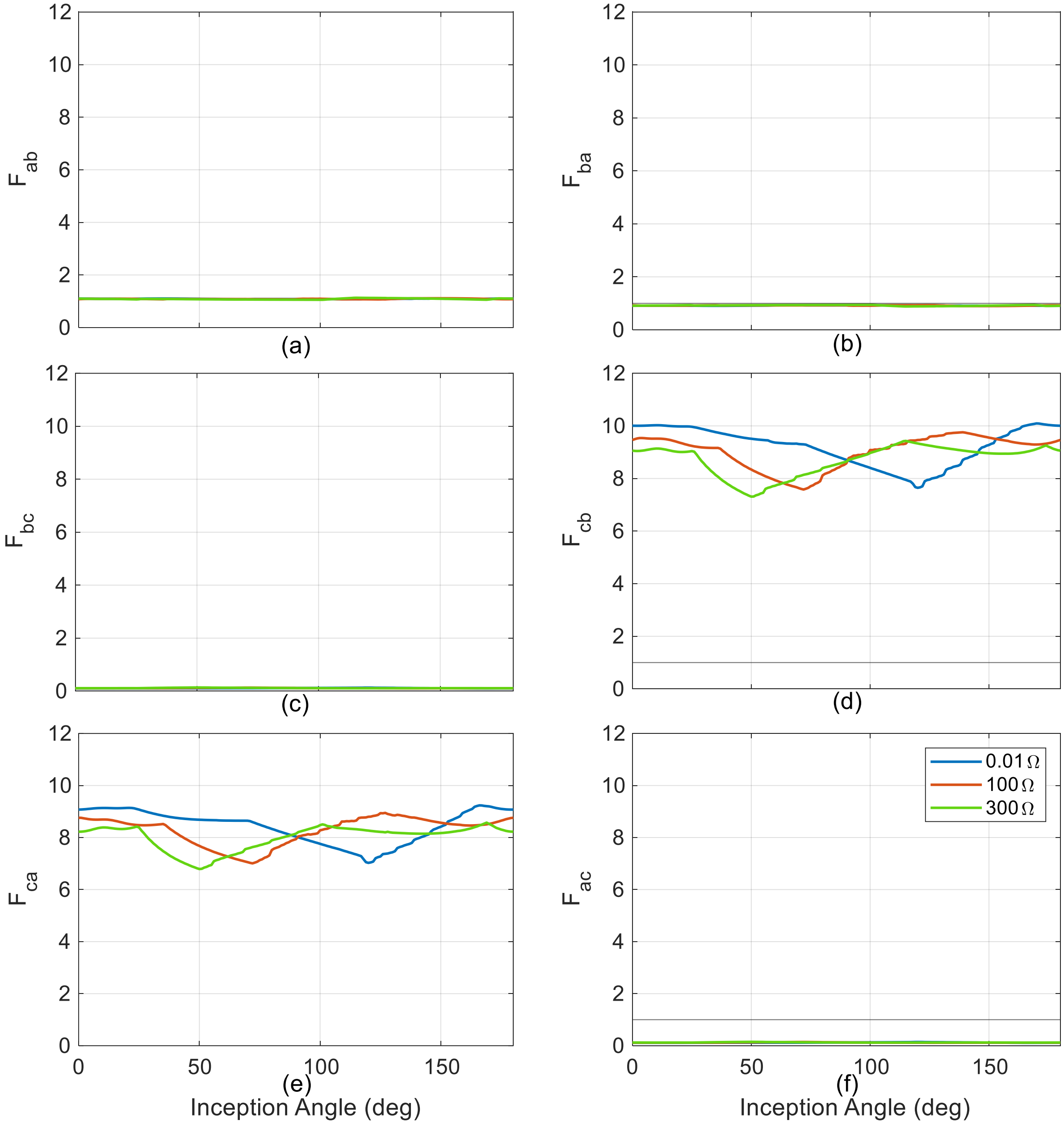

Fig 6.4 Variation of Fault Indices with Fault Inception Angle for Three Fault Resistances for Phase C-G faults (a) F_{ab}, (b) F_{bc}, (c) F_{ca}, (d) F_{ba}, (e) F_{cb}, and (f) F_{ac}

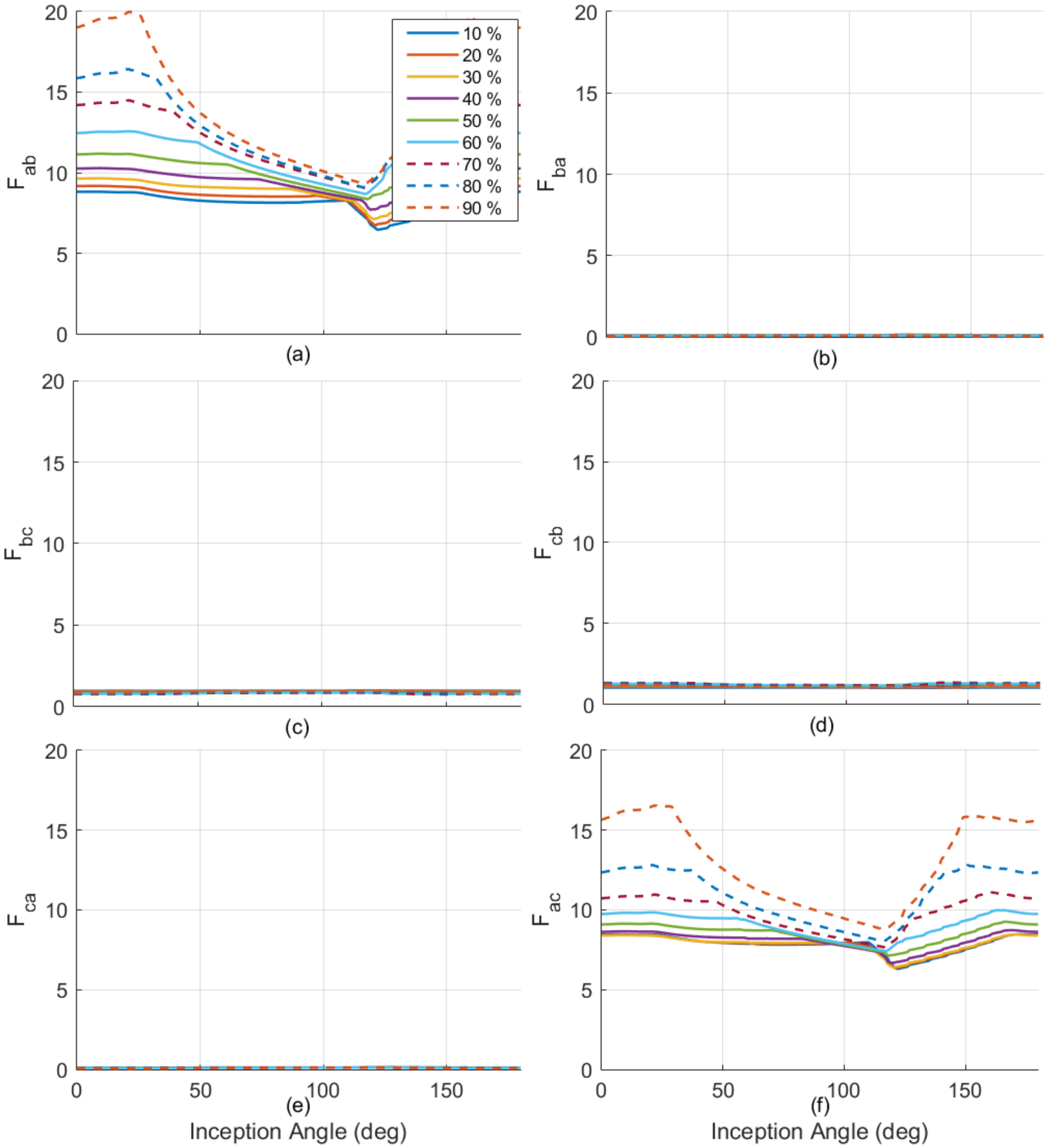

Fig 6.5 Variation of Fault Indices (a) F_{ab}, (b) F_{bc}, (c) F_{ca}, (d) F_{ba}, (e) F_{cb}, and (f) F_{ac} with Location for Phase-A-G Fault

6.4.3 Identification of Phase-to-Phase Faults

Fig 6.6 depicts the variation of fault indices for Phase-A-to-C fault applied at 80% of line length with fault inception angle for three different fault resistances (0.01 Ω, 100 Ω, and 300 Ω). The fault indices F_{ab} and F_{cb} remain as the two largest fault indices irrespective of the fault resistance and fault inception angle to verify the existence of Phase-A-to-C fault. For all three considered fault resistance values, F_{ab} and F_{cb} values vary within the same range which shows that the proposed method has a minimal effect from fault resistance.

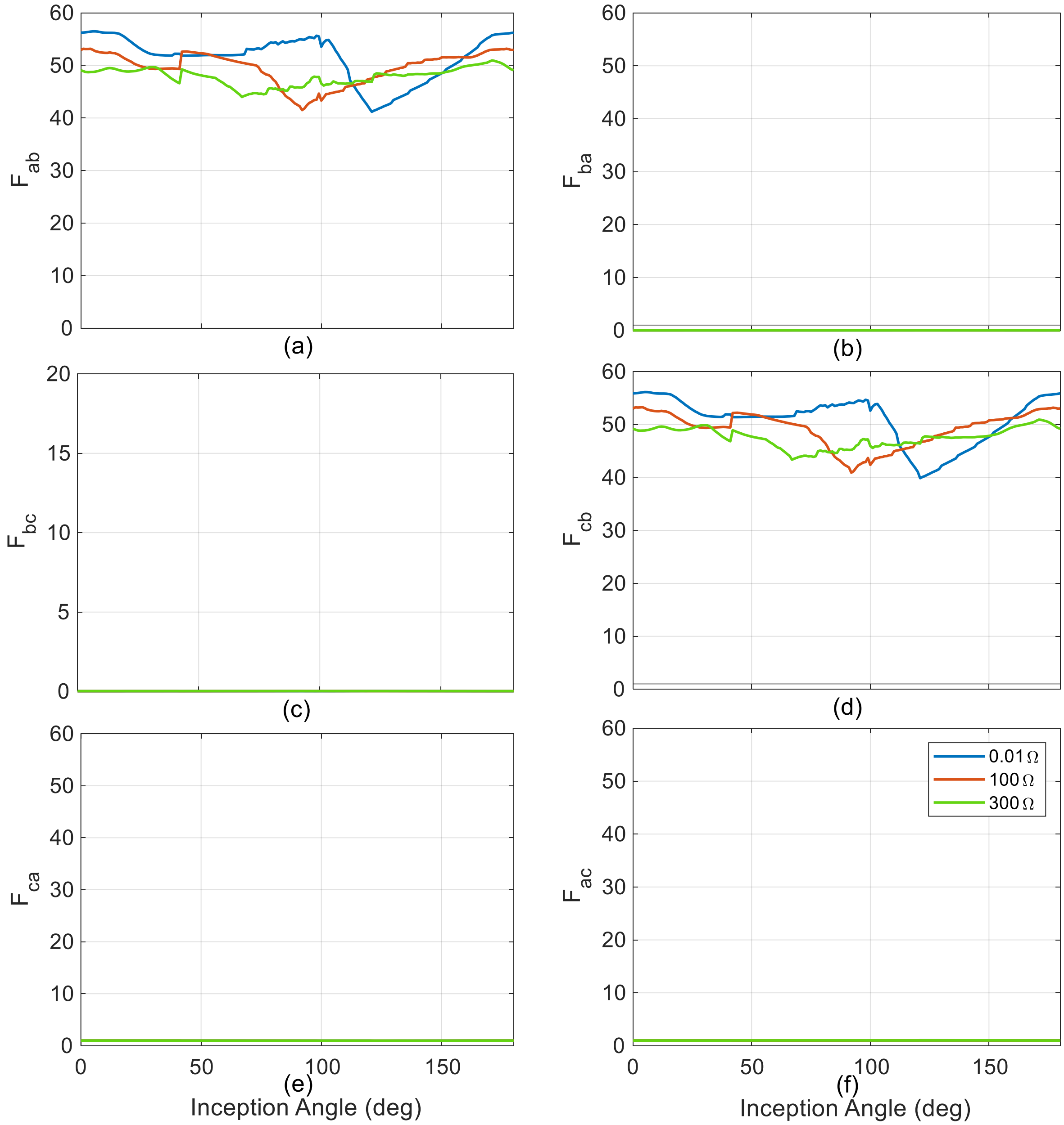

Fig 6.6 Variation of Fault Indices with Fault Inception Angle for Three Different Fault Resistances for Phase A-C fault (a) F_{ab}, (b) F_{bc}, (c) F_{ca}, (d) F_{ba}, (e) F_{cb}, and (f) F_{ac}

Fig 6.7 depicts the variation of fault indices for Phase-A-to-B short circuit faults applied on the Line-LM between 10% and 100% of the line length. The fault inception angle was incremented in

1-degree steps. Irrespective of the fault location, indices F_{bc} and F_{ac} remain the two largest indices verifying the existence of Phase-A-to-B fault irrespective of the fault location.

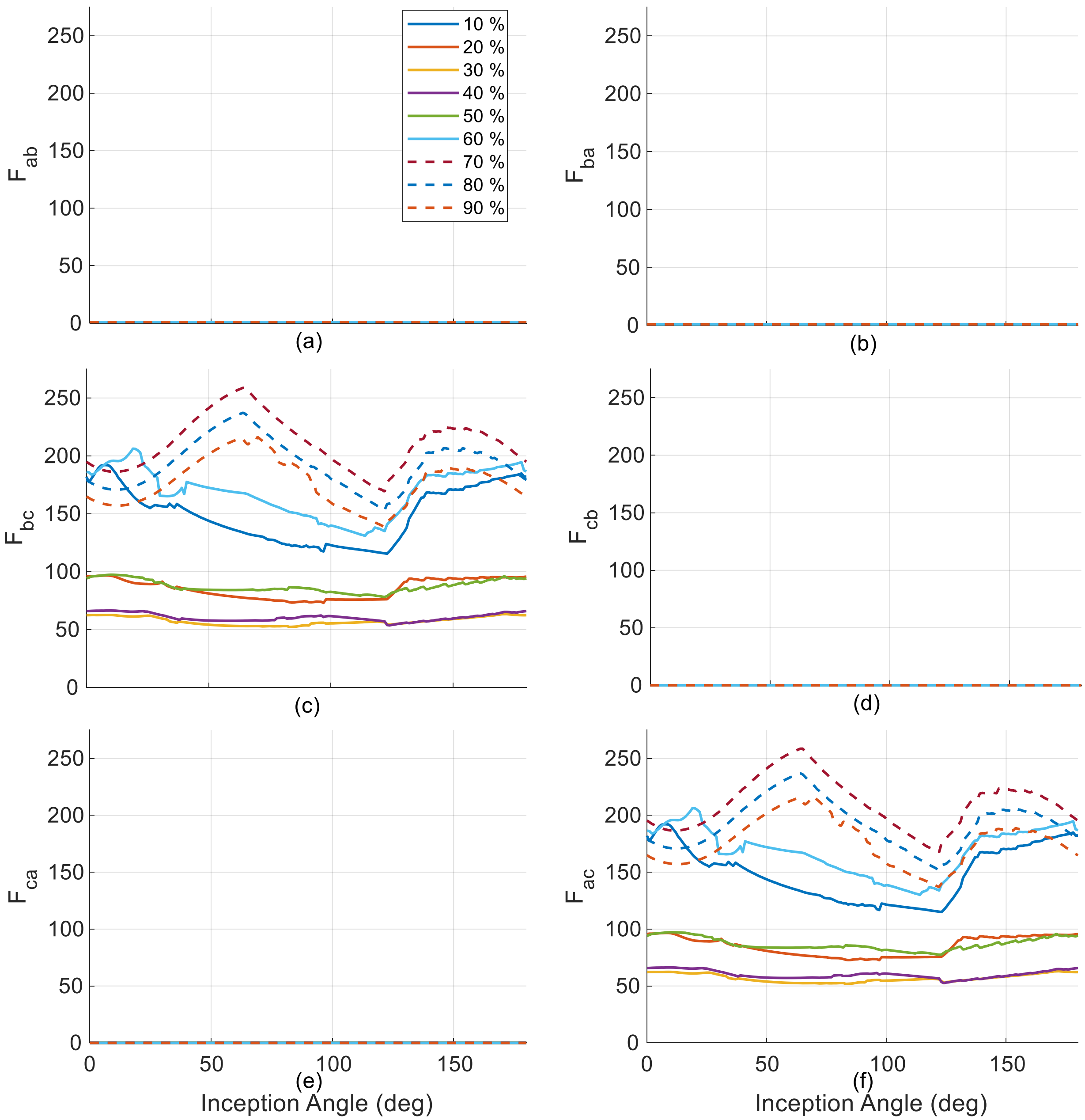

Fig 6.7 Variation of Fault Indices (a) F_{ab}, (b) F_{bc}, (c) F_{ca}, (d) F_{ba}, (e) F_{cb}, and (f) F_{ac} with Location for Phase A-B fault

6.4.4 Identification of Phase-to-Phase-to-Ground Faults

Fig 6.9 depicts the variation of fault indices for Phase-B-to-C-to-Ground short circuit faults applied on the Line-LM between 10% and 100% of line length. The zero-sequence current component confirms it is a ground fault as shown in Fig 6.8. Then F_{ba} and F_{ca} remain the two largest indices irrespective of the fault location and the fault inception angle, verifying the existence of a phase B-to-C-to-Ground fault,

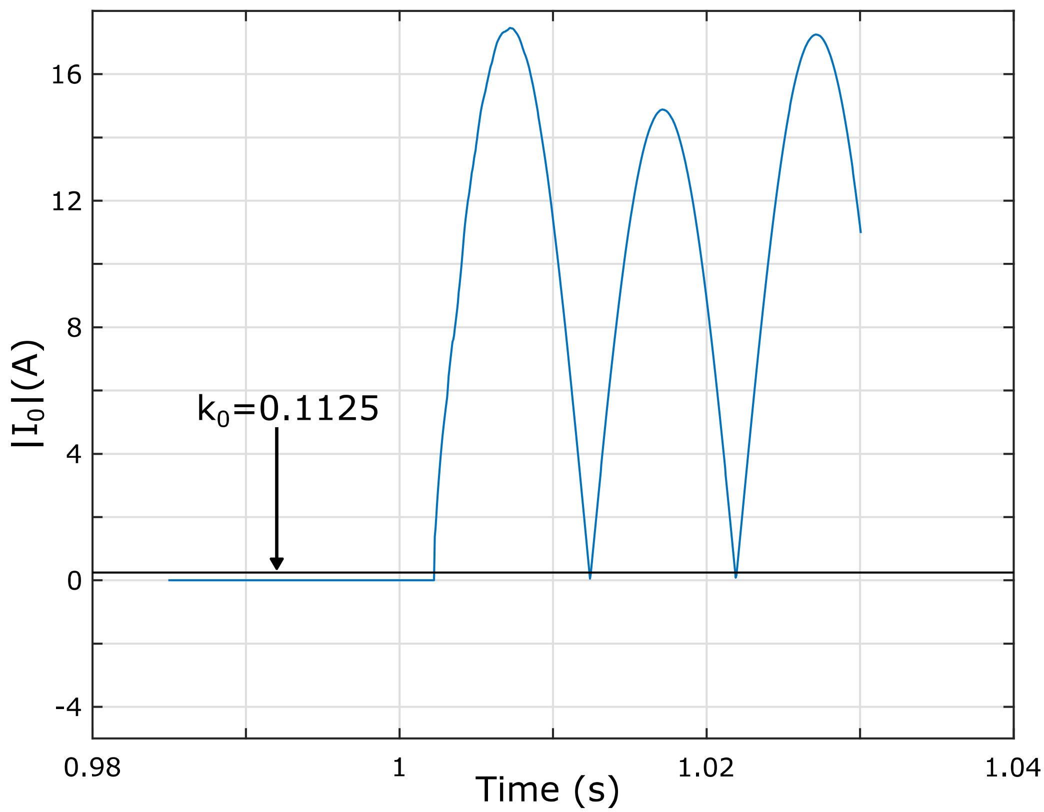

Fig 6.8 Variation of Zero Sequence Current During Phase-B-C-G Fault

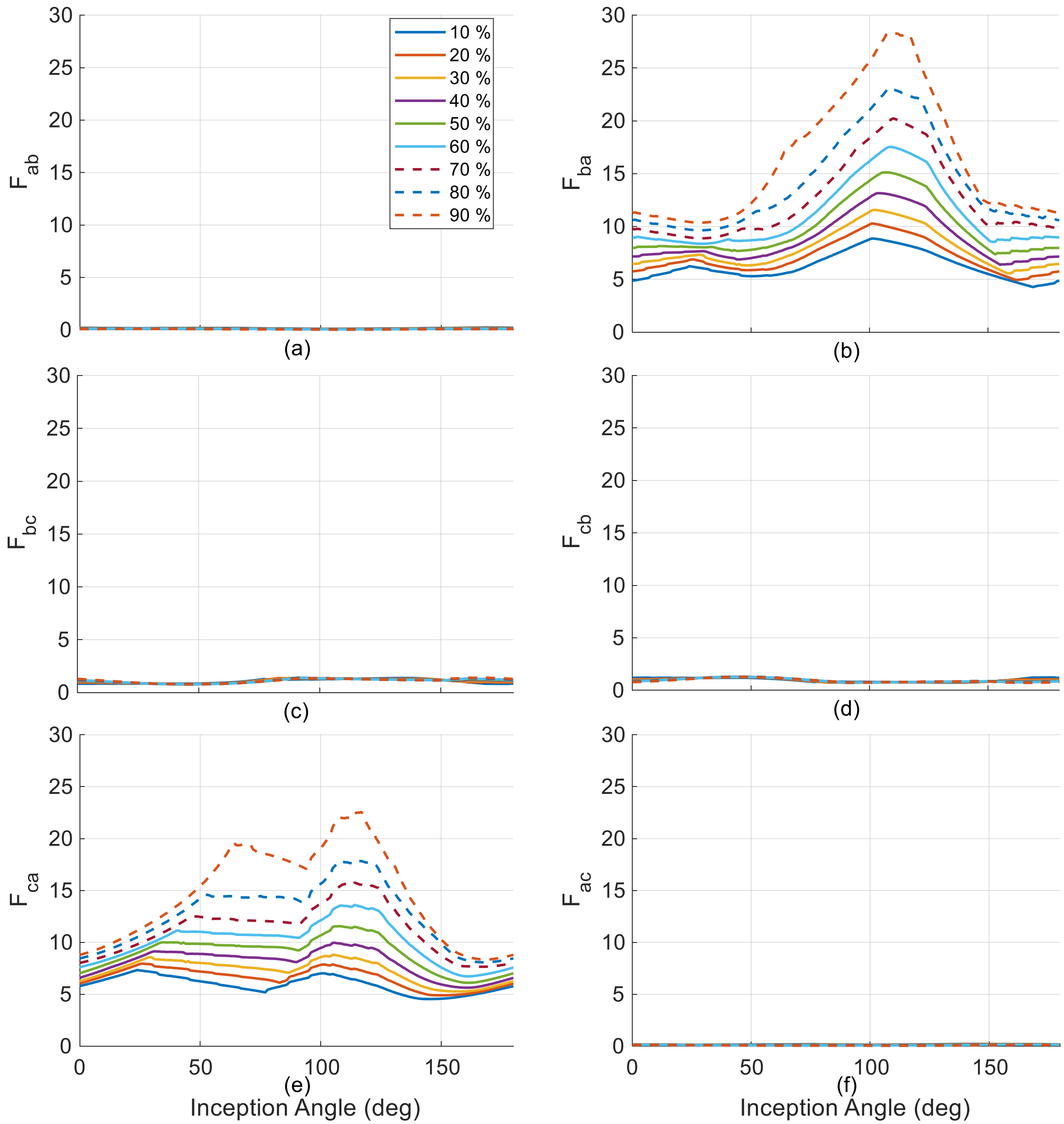

Fig 6.9 Variation of Fault Indices (a) F_{ab}, (b) F_{bc}, (c) F_{ca}, (d) F_{ba}, (e) F_{cb}, and (f) F_{ac} with the location for Phase-B-C-G fault

6.4.5 Three Phase Faults

The variations of Three-Phase fault detection indices ($|F_{ab} - F_{ba}|$, $|F_{bc} - F_{cb}|$ and $|F_{ca} - F_{ac}|$) for a Three-Phase fault applied at 90% of the line length at three different fault resistances (0.01 Ω, 100 Ω, and 300 Ω) are depicted in Fig 6.10. Further investigations confirmed that the algorithm is capable of identifying Three-Phase faults at least up to faults with 100 Ω fault resistance irrespective of the fault inception angle.

At 300 Ω fault resistance, the proposed algorithm fails to identify the Three-Phase fault within an approximate fault inception angle window of 100 degrees. Further analysis showed that this is due to the transients introduced by the mimic filter at some fault inception angles when no decaying DC component is present. This can be alleviated by blocking the index calculation for a specific period. However, this would come at the cost of speed. However, fault resistances of such high values are extremely rare occurrences at the transmission level.

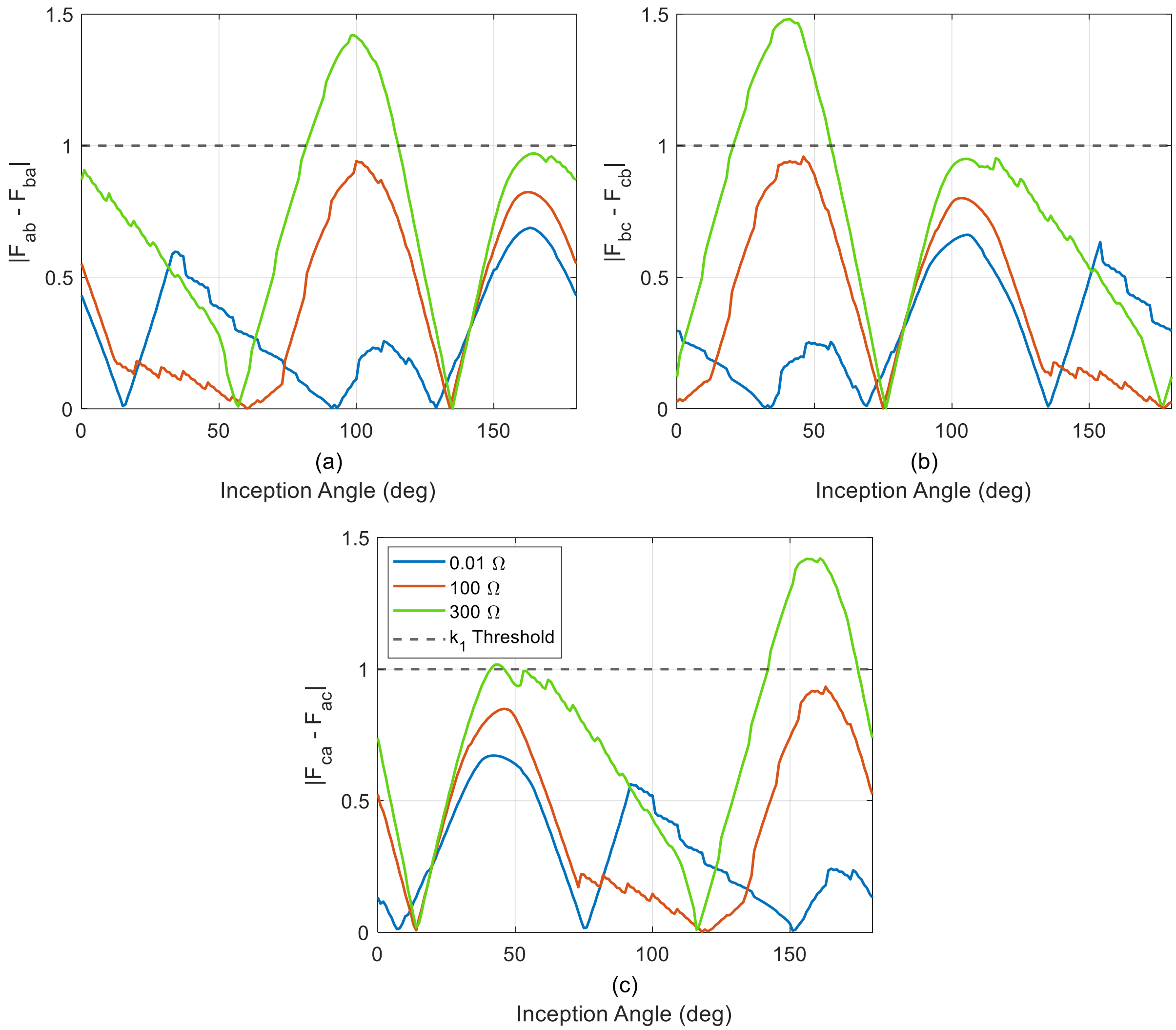

Fig 6.10 Variation of Three Phase Detection Threshold with Increasing Fault Resistance (a) $|F_{ab} - F_{ba}|$, (b) $|F_{bc} - F_{cb}|$, and (c) $|F_{ca} - F_{ac}|$ for Three-Phase Faults Applied at 90 % Line Length

6.4.6 Evaluating the Performance in a System With IBR

To investigate the performance of the proposed method on a system with IBR, the system shown in Fig 3.6 (a) was modified by replacing source 1 with a Type-IV 125 MW wind farm model [99] and opening the line MN. For the grid-side converter, the d-axis control mode was set to V_{dc} control, and the q-axis control model was set to Q control mode with priority set to I_q control during ride-through conditions. Whereas in the machine side converter, the d-axis control mode was set to P control the q-axis control mode was set to V_{ac} control and the priority was set to I_d control. The same threshold settings and filter parameters were used in the algorithm. Phase-to-Ground and Phase-to-Phase faults were applied at 90% of the length of Line-LM with a fault resistance of 50 Ω. The index values for each fault type are given in Table 6.4. The proposed algorithm was able to correctly identify the faulted phases in the applied faults.

With line MN open, the fault current contribution from the synchronous source was gradually reduced by changing the source strength, and the faulted phase selection performance for a 50 Ω line-ground fault at 90% of line L-M was evaluated repeatedly. When the fault current is supplied predominantly from the wind farm (i.e. the fault current contribution from the synchronous source is less than 5%), the proposed method was unable to correctly identify the faulted phases. This is due to the lack of significant incremental currents present in the faulted phases as a result of the control actions of the IBR controls. This is a limitation of the proposed method when protecting a radial line fed only from an IBR.

Table 6.4 Fault Index Values for Each Fault Type in a System with IBR

Fault	$\boldsymbol{F_{ab}}$	$\boldsymbol{F_{bc}}$	$\boldsymbol{F_{ca}}$	$\boldsymbol{F_{ba}}$	$\boldsymbol{F_{cb}}$	$\boldsymbol{F_{ac}}$
AG	5.39	1.4	0.13	0.19	0.73	7.44
BG	0.14	8.26	0.87	7.17	0.12	1.1
CG	1.36	0.1	7.06	0.74	9.6	0.16
AB	1.02	21.2	0.05	0.98	0.05	21.63
AC	13.5	0.08	0.93	0.07	12.62	1.07
BC	0.076	0.96	13.73	13.13	1.05	0.073

6.5 Practical Considerations

Evolving faults and Switch-On-to-Fault conditions are some practical scenarios that need to be taken into consideration. To handle the evolving fault condition, the current index calculation logic can be modified by resetting the maximum calculation block after the index calculation time window has expired. Thus, it would detect the new fault condition when the evolving fault occurs.

Handling switch-on-to-fault conditions is more complex than evolving conditions since the algorithm needs to differentiate between normal line energization conditions and switch-on-to-fault conditions. Therefore, a special switch-on-to-fault condition detection logic needs to be implemented to detect the switch-on-to-fault conditions, as in the case of conventional distance relays.

6.6 Concluding Remarks

This chapter proposes a simple and novel faulted phase selection scheme based on a set of indices determined using the peak rate of change of incremental currents around the fundamental frequency and the accuracy of the method is not affected by fault inception angle, fault resistance, and fault location and is applicable for both transposed and non-transposed transmission lines.

The decision-making time which is constrained by time window and filter delays is less than 6 ms. Even though it is slower than the transient-based method the proposed method is more reliable compared to the transient-based method proposed in Chapter 5. However, the proposed method fails to operate correctly in fault scenarios where the fault current is purely supplied from IBRs due nonexistence of significant incremental currents.

The results obtained during the algorithm validation have shown that this method is able to overcome the challenges faced by the transient-based faulted phase selection algorithm proposed in Chapter 5 proving it to be a robust and simple algorithm at the expense of a slight reduction in speed.

Chapter 7

Evaluation of the Complete Line Protection Scheme

Previous chapters proposed and investigated several algorithms to improve the speed of line protection. Two line protection algorithms were proposed in Chapters 3 and 4. Two-phase selection algorithms were proposed in Chapters 5 and 6. The algorithms were evaluated extensively as individual algorithms. This chapter evaluates the complete line protection scheme combining the algorithms proposed in Chapters 4 and 5. The algorithm proposed in Chapter 4 is used to estimate the fault loop inductance and resistance and for the phase selection scheme, the algorithm proposed in Chapter 5 is used. The performance of the complete line protection scheme was evaluated using a larger power system with IBR generation in this Chapter.

7.1 Test System

This chapter demonstrates the complete protection scheme which combines the Clarke quantities-based line distance protection algorithm and the transient current-based faulted phase selection algorithm. The completed algorithm was validated on a larger system [100] that includes a Type-IV wind farm that pushes 200 MW power to the system, derived by modifying the IEEE 14-bus system shown in Fig 7.1. The power system consists of six 230 kV buses, two 345 kV buses, and four 22 kV buses. The 100 km transmission line connecting Bus 4 and 5 is protected by the algorithm proposed in Chapter 4. Transmission lines are modeled using the Bergeron model.

The Type–IV wind turbine generator (WTG) used in the test system is based on the detailed model presented in [101]. The model consists of two sections: mechanical system and electrical system. The mechanical system extracts available mechanical power from the wind and yields mechanical torque. The electrical system converts the mechanical torque to the electrical torque. The interface between the mechanical and electrical systems is the permanent magnet (PM) machine, which converts the mechanical energy into electrical energy. The mechanical and electrical systems consist of the following components:

1. Mechanical System
    a. Wind Turbine
    b. Pitch Angle Controller
2. Electrical System
    a. Grid-side Converter and Controls
    b. Machine-side Converter and Controls
    c. DC-link Chopper Protection
    d. Low Pass Filters
    e. Transformer
    f. Scaling component

For the grid-side converter, the d-axis control mode was set to V_{dc} control, and the q-axis control model was set to Q control, with priority set to I_q control during ride-through conditions. In the machine side converter, the d-axis control mode was set to P control, the q-axis control mode was set to V_{ac} control and the priority was set to I_d control. Parameters of the Type–IV wind farm model are given in Table 7.1.

Table 7.1 Type–IV Wind Farm Model Parameters

Parameter	**Value**
Rated power of one unit	2 MVA
Number of Units	100
Frequency	60 Hz
Turbine RPM at machine nominal speed	12
Input Wind Speed	10 m/s
Cut in Wind Speed	3 m/s
Cut out Wind Speed	25 m/s
PM Machine Rated Voltage	0.69 kV
PM Machine base frequency	25 Hz

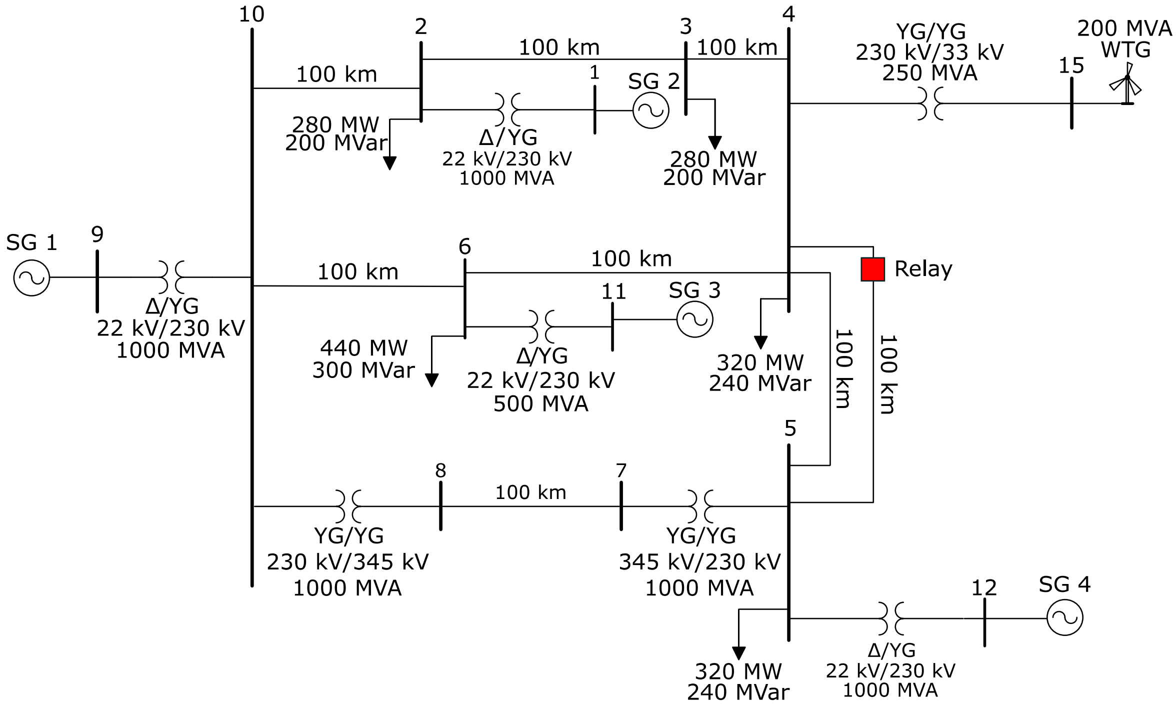

Fig 7.1 Modified IEEE 14-Bus Test System with Wind Farm

The positive and zero sequence per unit values of the protected transmission line are given in Table 7.2. Bus and transmission line data of the complete system are given in Appendix B – 14 Bus System.

Table 7.2 Positive and Zeros Sequence Per Unit Values of the Protected Transmission Line (Base Voltage = 230 kV, Base MVA = 100 MVA)

Parameter	**Value**
Positive Sequence Resistance (R_1)	0.0114 p.u
Positive Sequence Reactance (X_1)	0.0909 p.u
Zero Sequence Resistance (R_0)	0.1187 p.u
Zero Sequence Reactance (X_0)	0.2443 p.u

7.2 Details of the Relay Model

7.2.1 Phase Selection Algorithm

The proposed protection relay model uses the Clarke transient current-based faulted phase selection algorithm proposed in Chapter 5 as the preferred phase selection algorithm. The detection thresholds of the phase selection algorithm were modified according to the power system configuration. The settings of the phase selection algorithm are given in Table 7.3.

Table 7.3 Phase Selection Algorithm Parameter Settings

Parameter Setting	**Value**
Ground Detection Threshold (k_0)	0.1
Fault Type Identification Threshold (k_1)	25
Fault Detection Threshold	5 A/s
Phase Selection Time Window	0.75 ms

7.2.2 Protection Algorithm

A single zone was configured in the Clarke Equivalent Network-based protection scheme. The zone settings for the α network (Phase-to-Ground Faults) and β network (Phase-to-Phase/ Phase-to-Phase-to-Ground/ Three-Phase) are given in Table 7.4. The resistance reach setting was set to cover 25 Ω arc resistance on the primary side.

Table 7.4 Zone 1 Setting for α and β Networks

Network	$\boldsymbol{R}$ **(Ω)**	$\boldsymbol{L}$ **(H)**
α - Network	4.9939	0.0287
β - Network	2.9822	0.0122

The same fault detection logic used in the faulted phase selection algorithm was used to trigger the Clarke equivalent protection algorithm.

The phase selection algorithm uses a sampling rate of 10 kHz whereas the protection algorithm operates at a sampling rate of 80 Samples/Cycle (4.8 kHz). The protection algorithm waits for 12 consecutive sample points to satisfy the protection logic to issue a trip signal.

7.3 Results

To demonstrate the operation of the complete algorithm including the Clarke transient current-based faulted phase selection scheme and the Clarke equivalent network-based line protection algorithm, four fault scenarios were considered from each type of fault (Phase-to-Ground, Phase-to-Phase-to-Ground, Phase-to-Phase and Three-Phase faults). Faults were applied at three different locations in the protected line.

7.3.1 Phase-to-Ground Faults

Phase-A-to-Ground fault was applied at 10% of the protected line. As shown in Fig 7.2, the fault is applied at 4.0 s and the phase selection algorithm detects the fault after 0.5 ms and the phase selection algorithm identifies a Phase-A-to-Ground fault within 0.75 ms after detecting the fault.

The Clarke equivalent network-based line protection algorithm starts to estimate the Phase-A α loop inductance after detecting the fault. The trip decision is made 8.3 ms after detecting the fault in the system.

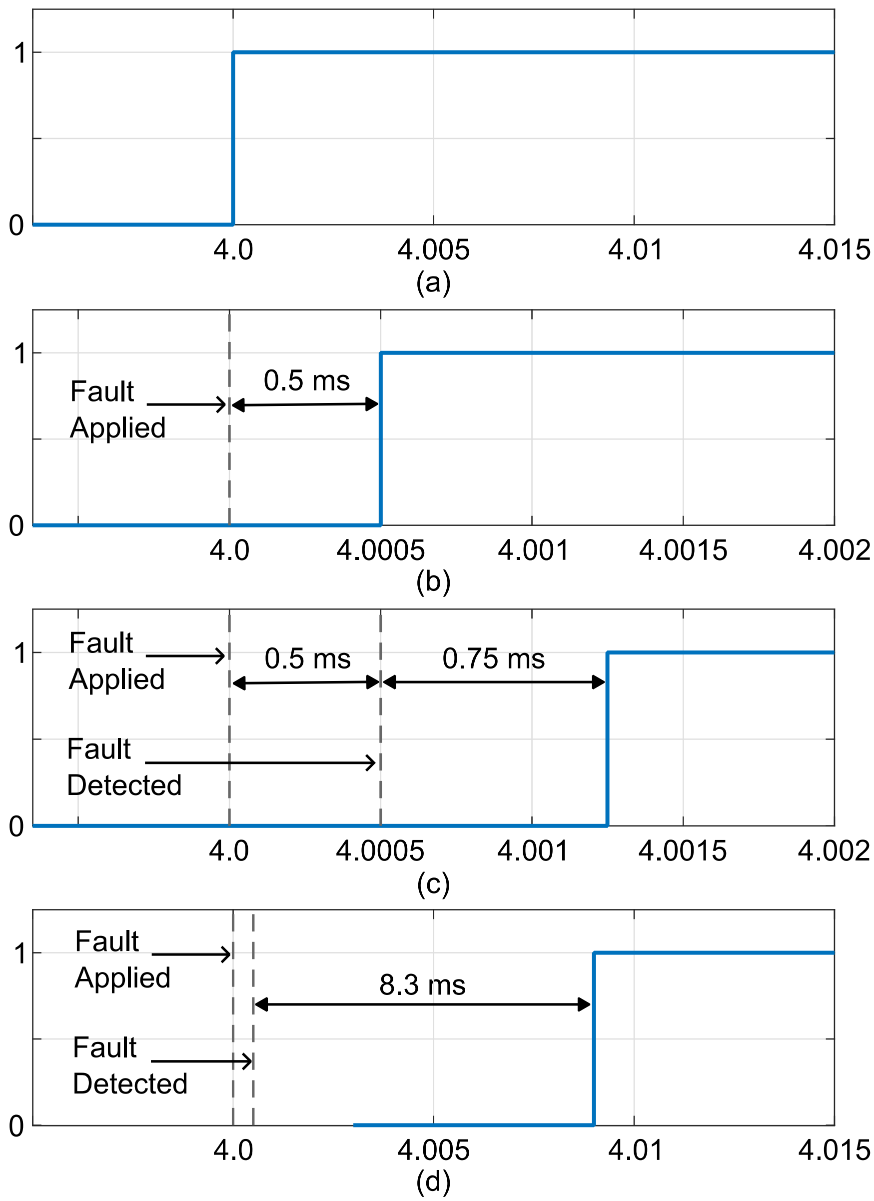

Fig 7.2 (a) Fault Inception, (b) Fault Detection, (c) Phase Selection, and (d) Trip Decision Waveforms of the Complete Algorithm for a Phase-A-to-Ground Fault

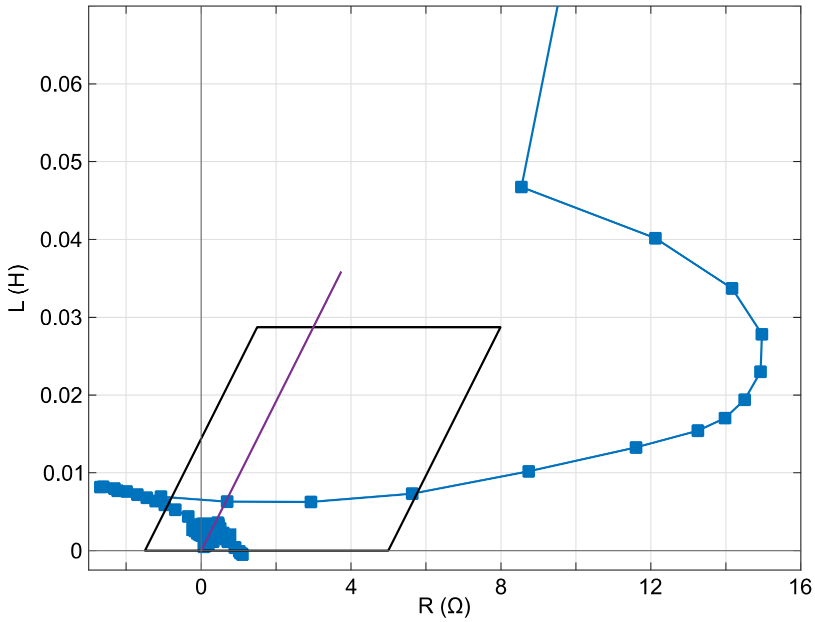

Fig 7.3 L – R Plot of the Phase-A-to-Ground Fault

7.3.2 Phase-to-Phase-to-Ground Faults

A Phase-B-to-C-to-Ground fault was applied at 75% of the line length of the protected line at 4.0 s. The faulted phase selection algorithm identifies the existence of a fault after 0.75 ms of fault inception. Upon detecting the fault, the faulted phase selection algorithm identifies the Phase-B-to-C-to-Ground fault after 0.75 ms. The trip decision for this fault is issued by the protection algorithm after 10.25 ms upon fault detection bringing the operating time of the complete algorithm to 11 ms.

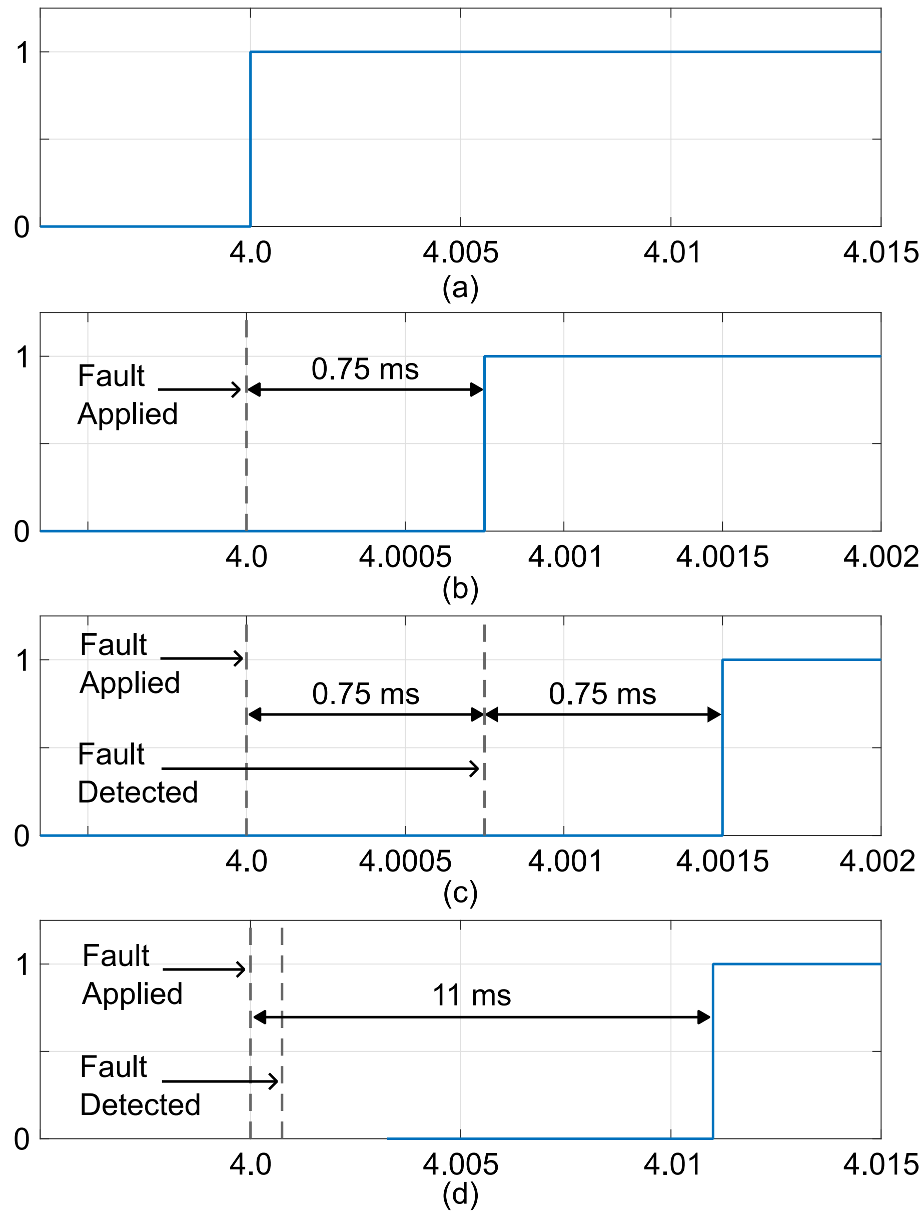

Fig 7.4 (a) Fault Inception, (b) Fault Detection, (c) Phase Selection, and (d) Trip Decision Waveforms of the Complete Algorithm for a Phase-B-to-C-to-Ground Fault

A Phase-A-to-B-to-Ground Fault was applied at 10% of the line length after disconnecting Line 3-4 of the power system. This makes most of the fault current fed into the fault from the WTG. The trajectory of L and R is depicted in Fig 7.5 and the trip plot is depicted in Fig 7.6. The proposed protection relay model operates accurately and issues a trip signal within 8.33 ms after applying the fault even when most of the fault current is fed by the WTG.

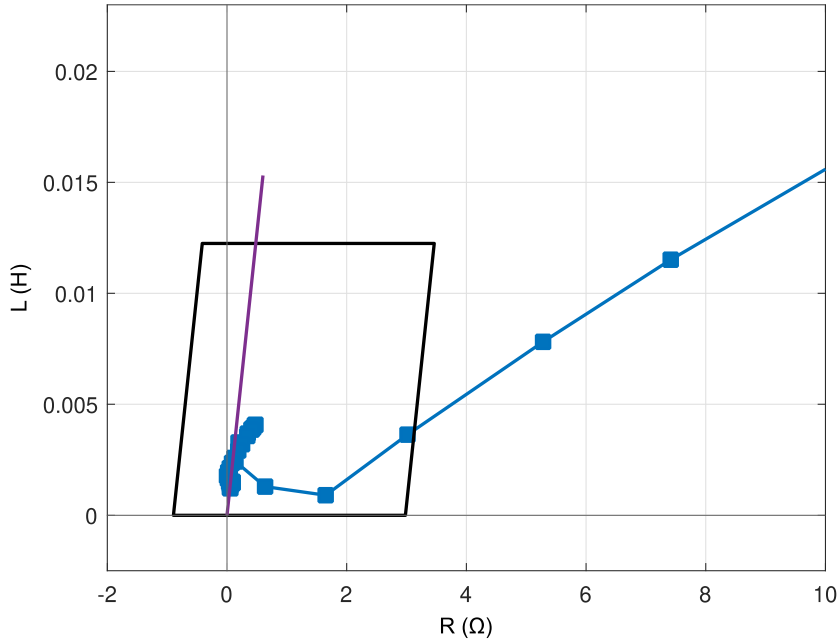

Fig 7.5 L – R Plot of the Phase-A-to-B-to-Ground Fault

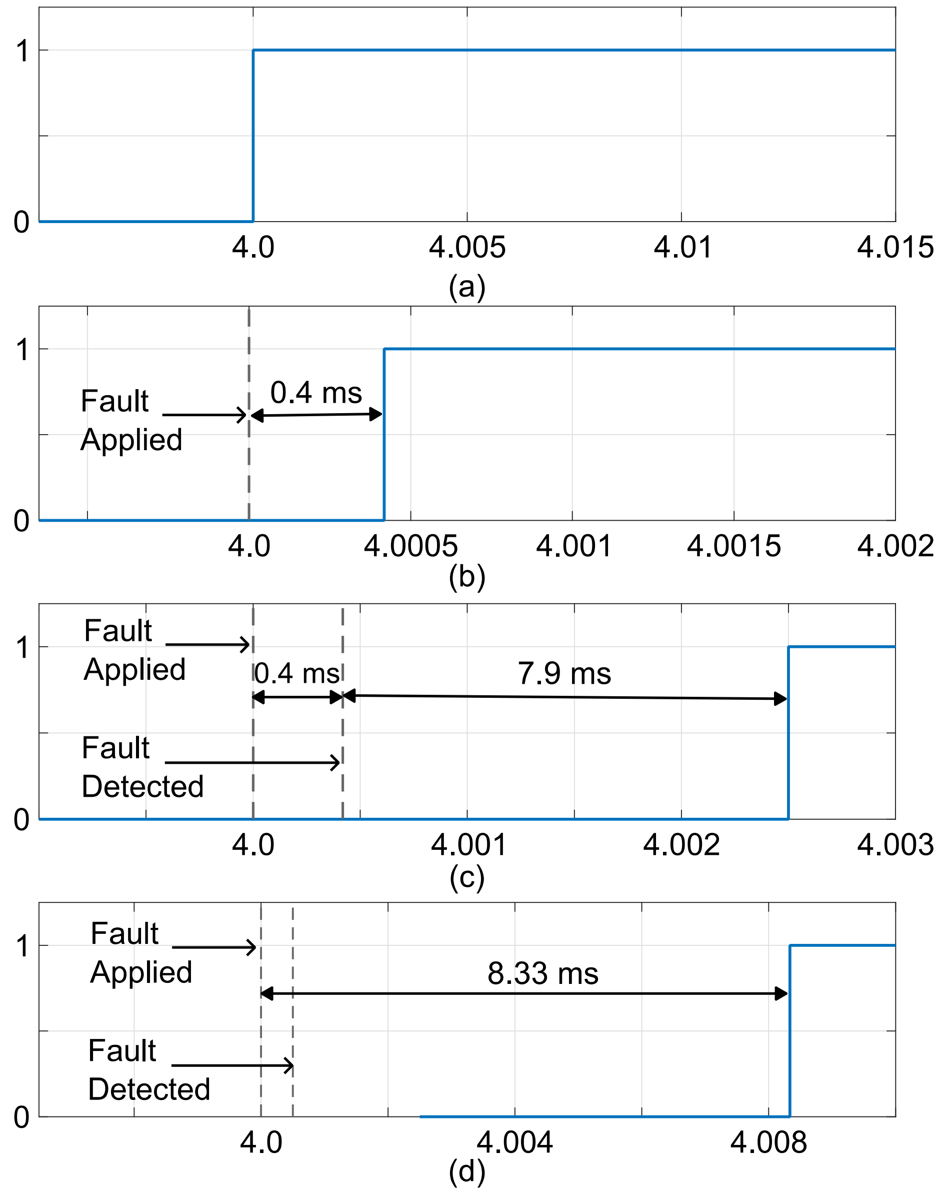

Fig 7.6 (a) Fault, (b) Fault Detection, (c) Phase Selection, and (d) Trip Decision Waveforms of the Complete Algorithm for a Phase-A-to-B-to-Ground Fault

7.3.3 Phase-to-Phase Faults

At 50% of the length of the protected line, a Phase-A-to-C fault was applied. The fault was applied 4 seconds after the start of the simulation. The fault is detected after 0.5 ms after applying the fault by the fault detection algorithm. The faulted phase selection algorithm identifies the

Phase-A-to-C fault 0.75 ms after detecting the fault and the trip decision is issued 9.5 ms after detecting the fault. The operating time of the complete algorithm for this fault scenario is 10 ms.

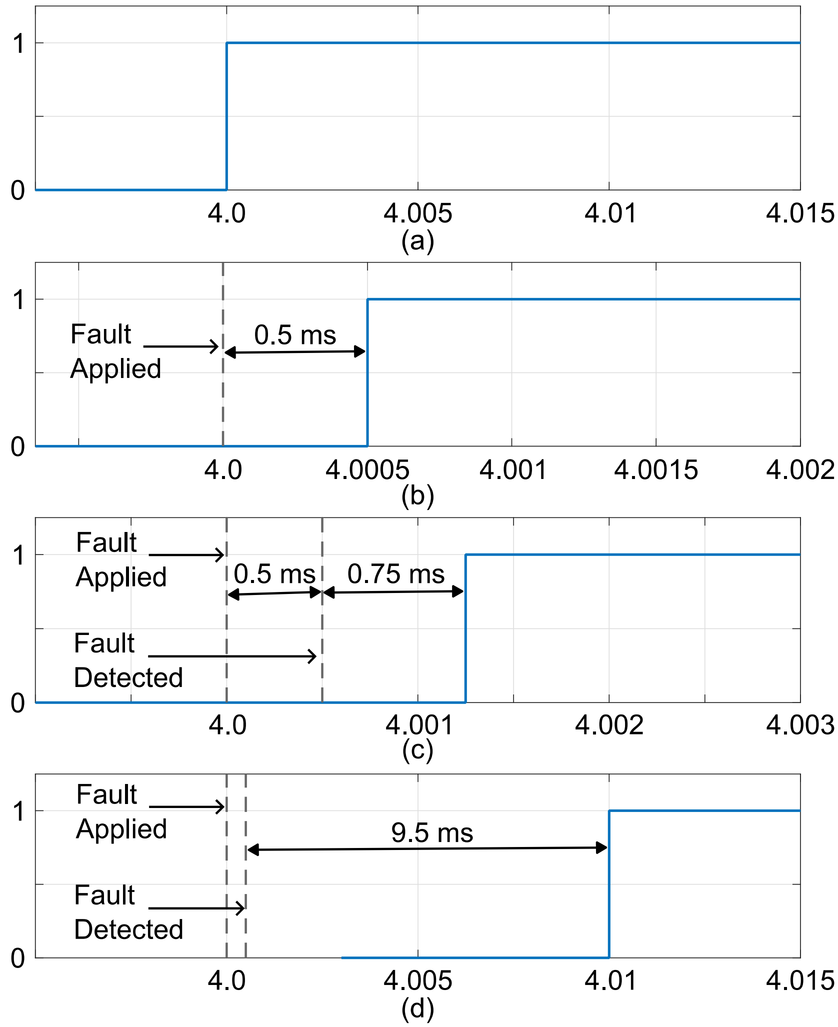

Fig 7.7 (a) Fault, (b) Fault Detection, (c) Phase Selection, and (d) Trip Decision Waveforms of the Complete Algorithm for a Phase-A-to-C Fault

The relay's operating time was compared by applying a Phase-B-to-C fault at the middle of the line and placing a relay at each end of the line at Bus 4 and Bus 5. The pre-fault power flow direction is reversed for the relay at Bus 5. The L-R trajectories for the two relays are plotted in Fig 7.8. In contrast with the traditional distance relays, the operating points enter the operating zone from the same direction of the L-R plane irrespective of the pre-fault power flow direction.

This is expected as the estimated R and L should be always positive for forward faults. The final point of the L-R trajectory settles at the same post-fault value. The phase selection and trip signals generated for the two considered scenarios are plotted in Fig 7.9 and Fig 7.10 respectively. In both cases, the relay issues a trip signal within 10 ms upon fault inception. The relay placed at Bus 4, which is closer to the wind farm, operates slightly slower compared to the relay placed at Bus 5. However, the operating time difference between the two relays is 0.4 ms.

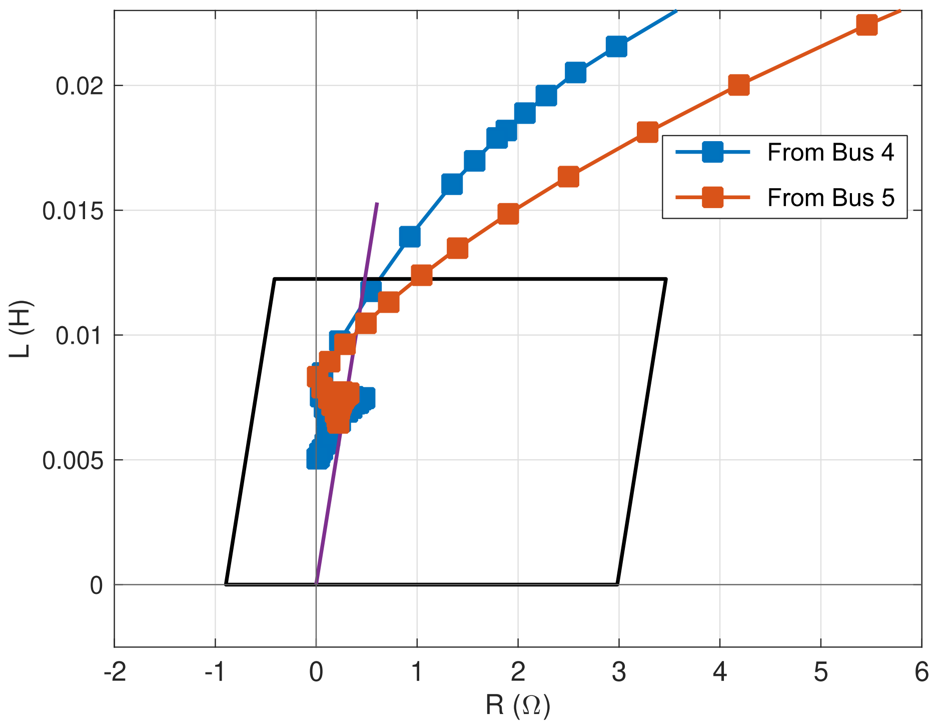

Fig 7.8 L – R Trajectories Phase-B-to-C Fault for Measurements Taken from Bus 4 and 5

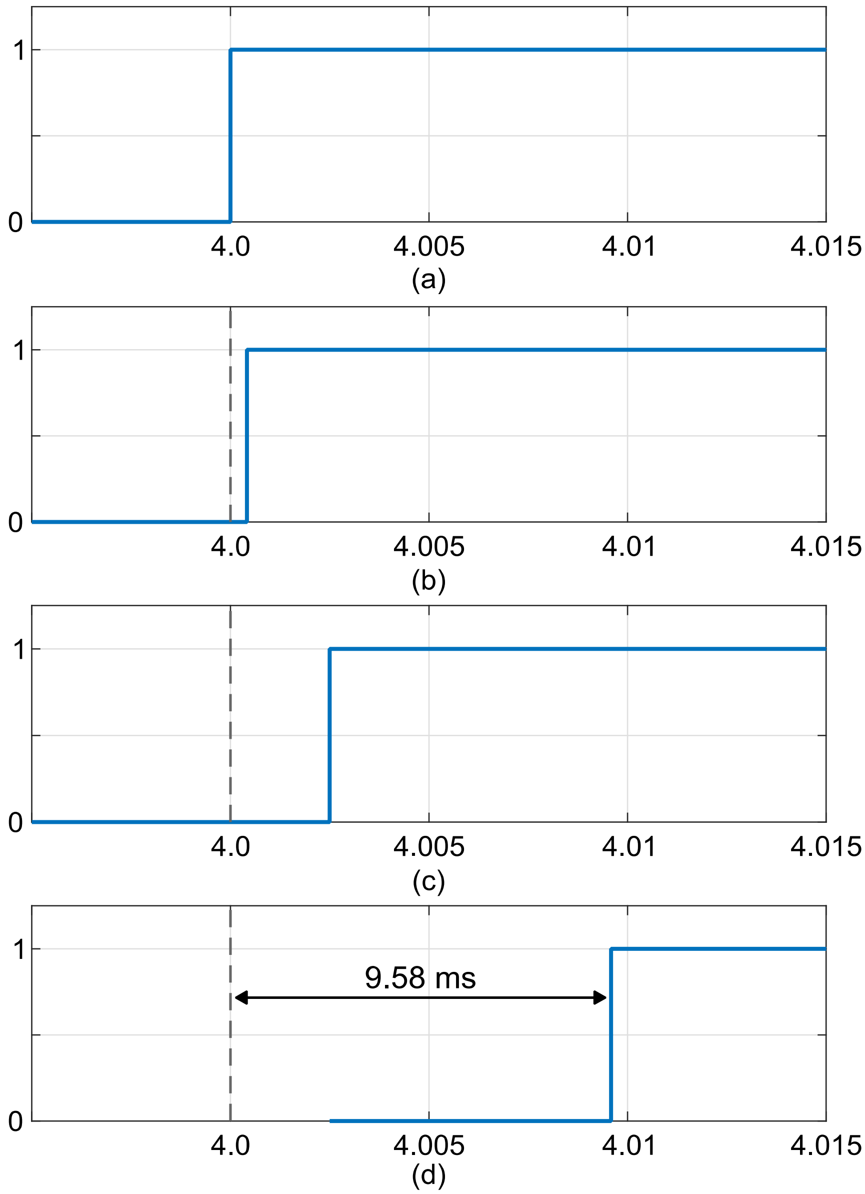

Fig 7.9 Phase-B-to-C Fault (a) Fault, (b) Fault Detection, (c) Phase Selection, and (d) Trip Signals Measured from Bus 4

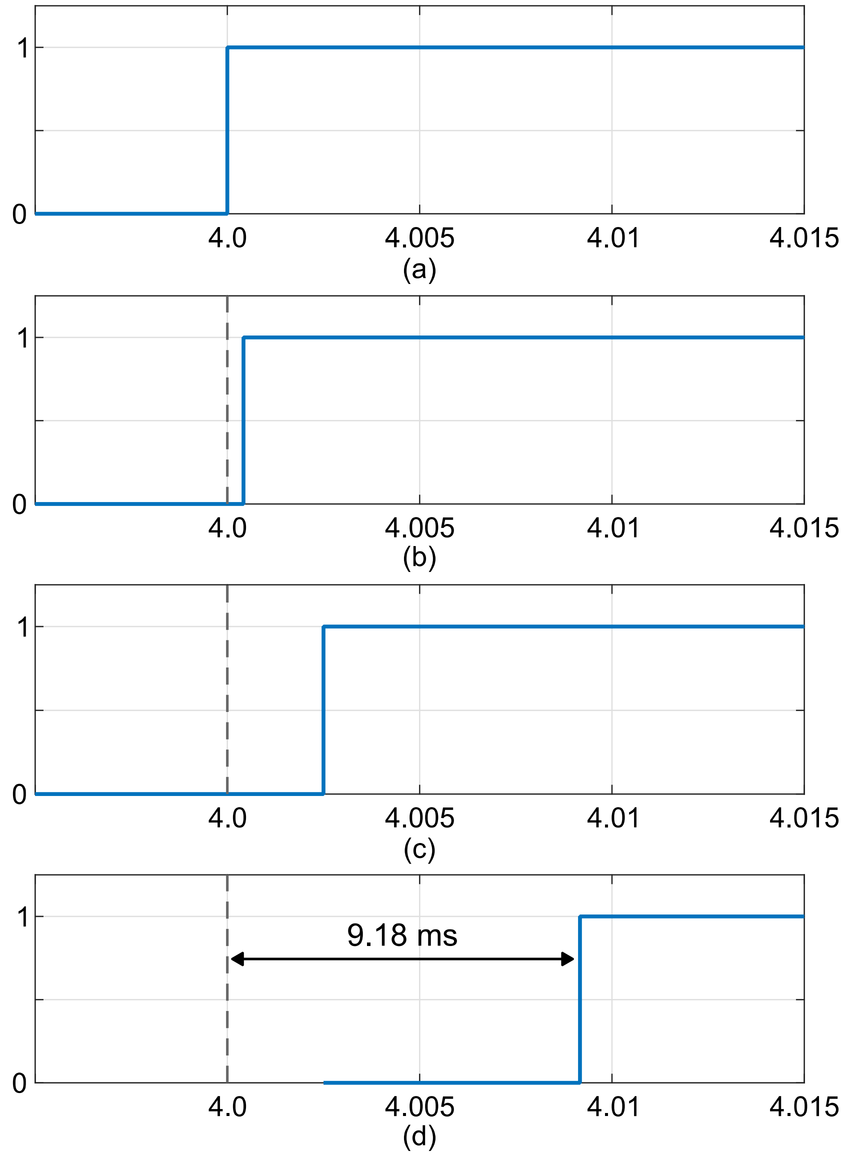

Fig 7.10 Phase-B-to-C Fault (a) Fault, (b) Fault Detection, (c) Phase Selection, and (d) Trip Signals Measured from Bus 5

7.3.4 Three-Phase Faults

The waveforms for the Three-Phase fault applied at 75% of the line length are shown in Fig 7.11. Similar to the other fault scenarios, the Three-Phase fault was applied at 4 seconds. The existence of a fault is detected after 0.5 ms and consequently, both the phase selection algorithm and line protection algorithm were triggered. The phase selection algorithm identifies the Three-Phase fault after its set 0.75 ms time window. The line protection algorithm issues the trip signal 10.25 ms after detecting the fault. The total operating time of the protection algorithm is 11 ms.

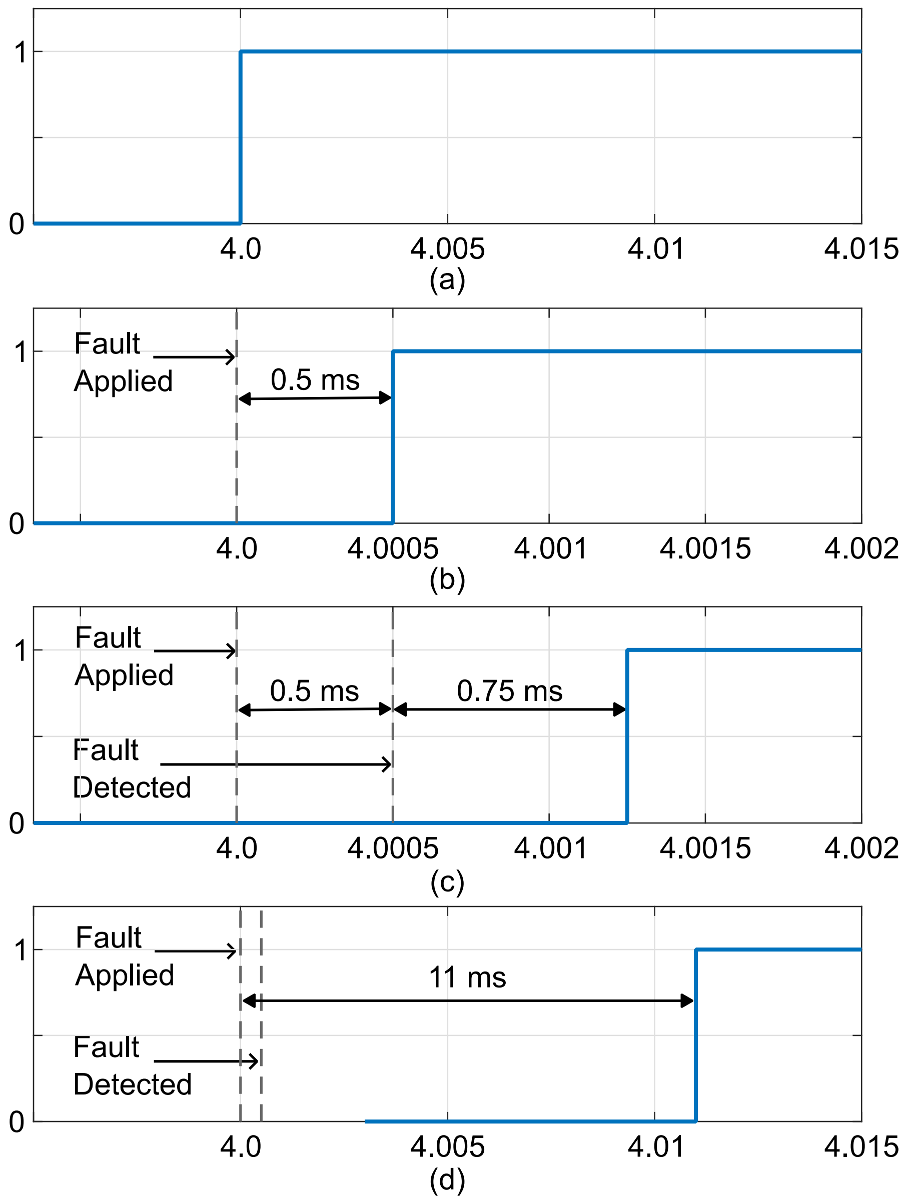

Fig 7.11 (a) Fault, (b) Fault Detection, (c) Phase Selection, and (d) Trip Decision Waveforms of the Complete Algorithm for a Three-Phase Fault

To demonstrate the relay's security a Three-Phase fault was applied on the parallel line at 50% of line length. The protection relay identifies the existence of a Three-Phase fault within a millisecond of fault inception. However, the relay determines that the fault is not within the protected zone and does not issue a trip signal as depicted in Fig 7.13. The L – R plot depicted in Fig 7.12 demonstrates this behavior. The trajectory transiently enters into the protected zone but moves out of the protected zone and settles outside the protected zone as expected. Since the relay waits for 12 consecutive points to be inside the protected zone, the transient movement of the operating point into the protected zone does not result in a trip signal maintaining the security of the relay.

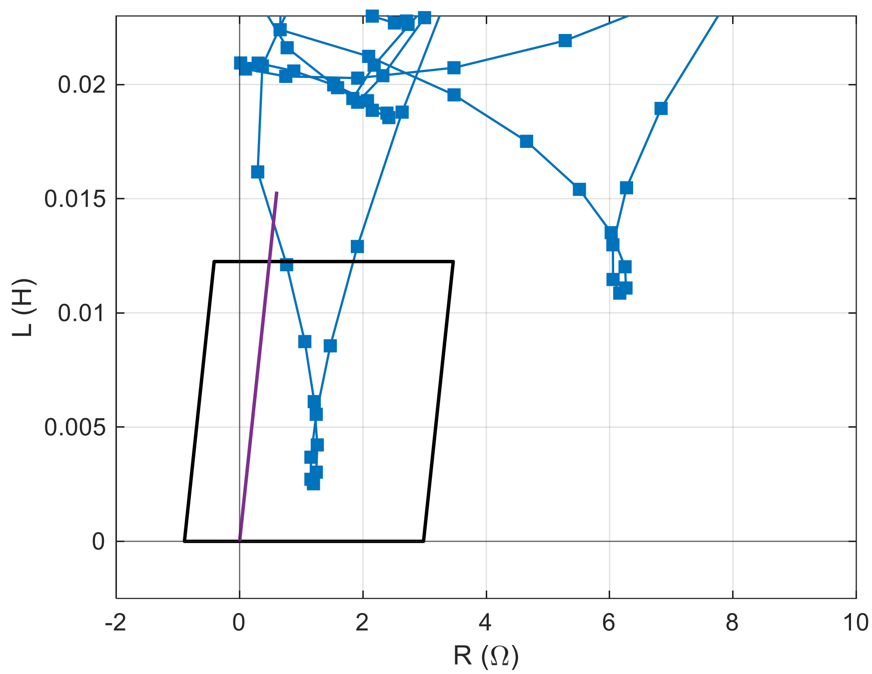

Fig 7.12 L – R Trajectory for the Three-Phase Fault Applied at the Parallel Line

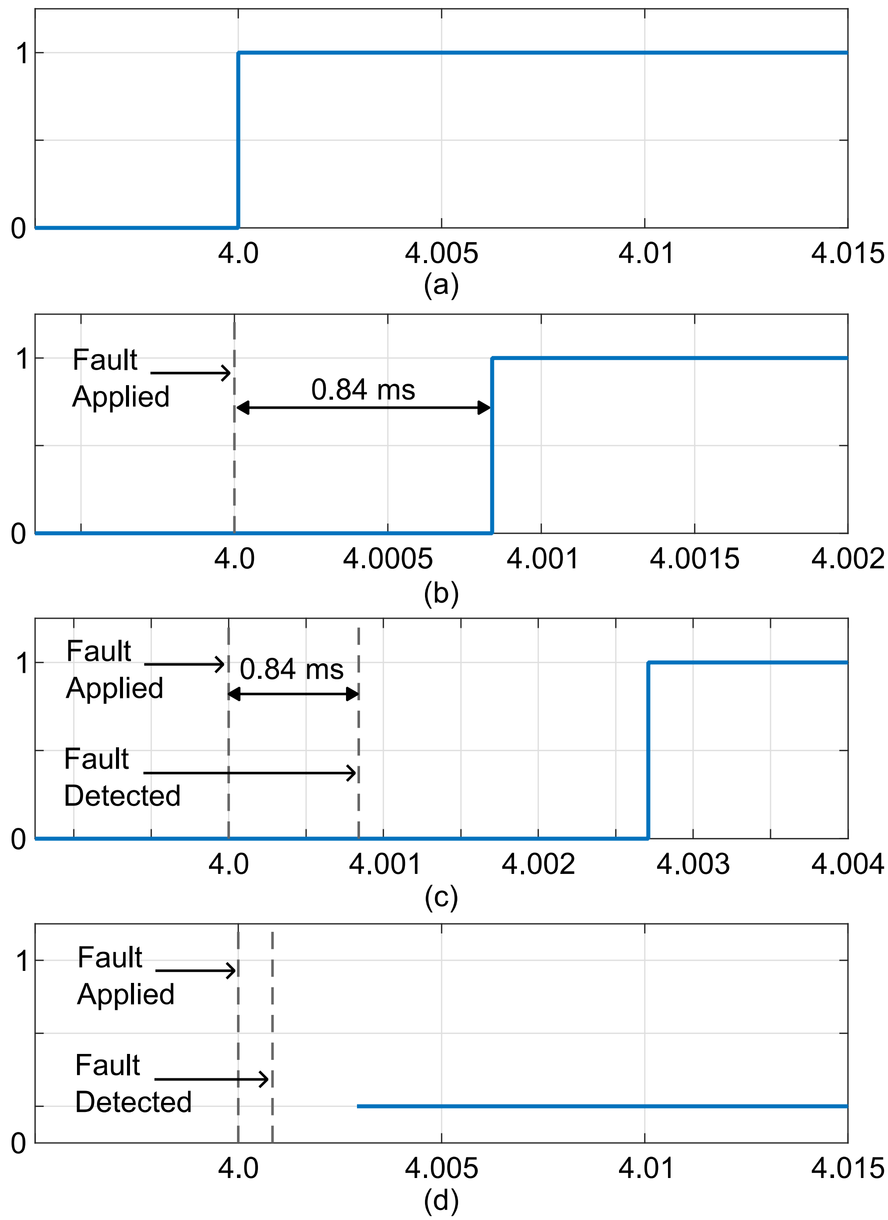

Fig 7.13 (a) Fault, (b) Fault Detection, (c) Phase Selection, and (d) Trip Signals for the Three-Phase Fault Applied at the Parallel Line

7.4 Concluding Remarks

This chapter evaluated the complete protection algorithm that combines the work presented in chapters 4 and 5. The algorithm was employed in a larger and more complex power system consisting of a Type-IV wind farm. Different aspects of the protection algorithm were investigated by creating different fault conditions and contingencies and the results showed the robustness of the proposed algorithm despite the size and complexity of the power system. The operating time of the complete protection algorithm remained to be around half a cycle of the power system frequency.

Chapter 8

Conclusions, Contributions, and Future Work

8.1 Summary and Conclusions

This thesis investigated several approaches to improve the speed of transmission line protection, including (i) the use of dynamic phasors for line distance protection (ii) the use of Clarke incremental current quantities for line distance protection, (iii) the use of Clarke current transient quantities for fault type and faulted phase identification, and (iv) use of incremental phase currents for fault type and faulted phase identification.

Chapter 3 studied the merits of applying the concept of dynamic phasors for line distance protection. Starting from the fundamental principles, fault loop equations were derived using the DP relationships. Using these fault loop equations, an amplitude comparator-based line distance protection scheme with directional capabilities was developed. A method to extract the dynamic phasors and their first derivative from time-domain sampled current and voltage signals was implemented to simulate the proposed DP-based distance protection scheme. Based on the study results presented in Chapter 3, the following conclusions are drawn:

- The DP-based distance protection operates correctly for all tests performed and proved robust under evolving faults and for a wide range of source-to-line impedance ratios.
- The speed of operation of the DP-based distance protection is not consistently faster than traditional distance protection; DP-based distance protection operates faster for

closeup faults, even then the speed advantage over traditional distance relays is limited to a few sampling intervals.

- The additional complexity in algorithms and the phasor estimation process of the DP-based approach outweigh its potential benefits.
- The limited speed advantage in the DP-based relay arises mainly due to the use of a 1.25-cycle estimation window in the dynamic phasor extraction algorithm to suppress the second harmonic; in contrast, the traditional distance relays employ one cycle DFT for phasor extraction.

Chapter 4 introduced a novel instantaneous Clarke component-based line protection algorithm considering the Clarke equivalent network model of the transmission lines. Fault loop equations were derived for each fault type to estimate the resistance and inductance of the fault loop. The algorithm determines the fault loop inductance and resistance using sampled values through least-squares estimation. These estimated inductance and resistance values enable the implementation of a directional line distance protection scheme. The algorithm can support multiple protection zones using amplitude comparators and provide backup protection for remote and reverse faults. These protection zones can be configured to cover specific fault resistances. Unlike other instantaneous line protection algorithms, the proposed algorithm does not require additional threshold or knowledge of source impedance. The performance of the algorithm was extensively analyzed by applying both short circuit and high impedance faults at different fault locations in both forward and reverse directions. A study was carried out to compare the proposed algorithm with traditional phasor-based distance protection relays. The performance of the algorithm on both manually transposed and non-transposed transmission lines was also evaluated. Based on the results presented in Chapter 4, the following conclusions can be drawn:

- Compared to standard Mho and Quadrilateral distance relays, the Clarke equivalent network-based distance relay algorithm showed improved operating time, particularly for faults farther from the relay location, with comparable dependability and security.
- The operating time of the proposed algorithm is consistent regardless of the fault location and fault resistance and remains within the half-cycle time window. The algorithm operated faster even for high impedance faults, though with slightly reduced coverage.
- The algorithm can operate and achieve the aforementioned speed advantage with a sampling rate of 80 samples/cycle, which is comparatively much lower than the sampling rates used by some of the faster algorithms reported in the literature.
- The performance of the proposed line protection algorithm may degrade if applied to long transmission lines that are not transposed. But this is not a serious limitation as long lines are transposed in practice.

Chapter 5 introduces a faulted phase selection algorithm that relies on the transients produced on Clarke current components during faults. The decision logic of the algorithm uses nine fault discrimination indices calculated as ratios of the derivatives of the different Clarke current components. The real-time performance of the proposed algorithm was tested by modeling the proposed algorithm as a real-time process in a DRTS and conducting hardware-in-the-loop simulation using a test power system with high penetration of inverter-based resources. Based on the results presented in Chapter 5, the following conclusions are drawn:

- The transient current-based faulted phase selection algorithm classifies fault types and identifies faulted phases much faster than phasor-based algorithms as the indices are calculated using a very short 0.75 ms measurement window.

- The algorithm can successfully identify fault types and faulted phases in systems with high IBR penetration.
- The results showed robust performance in fault type identification; the algorithm can always correctly determine the fault type.
- The algorithm correctly identifies faulted phases except for the Phase-to-Phase-to-Ground faults, where the accuracy of phase selection is affected by the fault inception angle.
- Since the fault indices are calculated using the signal components in the 2500 –3500 Hz range, the algorithm does not require very high sampling rates and is feasible to implement on the hardware of conventional relays.
- Due to bandpass filtering of input signals, the effect of noise is negligible for signal-to-noise ratios higher than 10 dB. The algorithm is not much affected by the quantization noise and could satisfactorily perform down to 12-bit A/D conversion resolution.
- The algorithm accuracy is affected by the discontinuities in the transmission line including the transposition points.

Chapter 6 presents another faulted phase selection algorithm based on the rate of change of incremental phase currents. This algorithm tries to overcome some of the shortcomings of the algorithm presented in Chapter 5. The fault type and faulted phase identification logic are based on six fault discrimination indices computed as ratios of ROCOIC values. The proposed algorithm was evaluated through extensive simulation studies. Based on these studies, the following conclusions can be drawn:

- The algorithm determines the faulted phases and fault type accurately regardless of the fault inception angle, fault resistance, fault location, and the discontinuities on the transmission line.
- The algorithm can make the decisions within 6 ms; while this is slower than the transient-based method proposed in Chapter 5, it is faster than the traditional phasor-based approaches.
- Since the algorithm relies on incremental currents, it does not require high sampling rates. A sampling rate of 80 samples/cycle is sufficient to generate accurate results.
- However, this method has limitations in scenarios where fault current is solely supplied by IBRs, understandably due to the lack of significant incremental currents.

Chapter 7 demonstrates the operation of the complete protection algorithm that combines the Clarke equivalent network-based line protection algorithm and the Clarke transient current-based faulted phase selection algorithm. The algorithm was validated on a 14-bus power system that has a Type-IV wind farm with a nominal capacity of 200 MW. Based on the results obtained, the following conclusions are drawn:

- The complete protection relay combining the algorithms proposed in Chapters 4 and 5 can generate trip signals within 10 ms of fault inception.
- The proposed protection scheme is immune to the problems caused by IBRs and performs robustly under a wide range of fault scenarios and provides adequate security.

8.2 Contributions

The main contributions of the work presented in this thesis are:

- Development of a dynamic phasor-based line protection scheme using the dynamic phasor model of the transmission line
- Development of a line distance protection algorithm using the Clarke components of instantaneous incremental quantities and the Clarke equivalent networks of a transmission line
- Development of a fast fault type and faulted phase selection algorithm using the transients in the Clark components of the instantaneous currents.
- Development of a robust fast fault type and faulted phase selection algorithm using the incremental components of the instantaneous currents.

8.3 Suggestions for Future Work

As an extension of the thesis, further research is recommended in the following areas:

- The accuracy of the proposed protection algorithms was validated using offline and real-time simulations in this thesis. Implementing the algorithm on a suitable hardware platform similar to those used in commercial relays and evaluating the performance using hardware-in-the-loop simulations and field tests can provide further insight into the suitability for practical application.
- The complete protection algorithm was tested on a 14-bus test system with IBRs. However, further testing in complex transmission systems with parallel lines, and series compensated transmission lines will provide more insight into the algorithm performance.
- The proposed protection algorithm only has the phase selection algorithm as a supervisory function. Developing other supervisory functions such as power swing blocking and load

encroachment functions using transients and incremental quantities to handle these situations will improve the security of the proposed protection relay.

References

[1] J. M. Gers and E. J. Holmes, *Protection of Electricity Distribution Networks*. Institution of Engineering and Technology (IET), 2004.

[2] V. Pathirana, “A Power System Protection Scheme Combining Impedance Measurement and Travelling Waves : Software and Hardware Implementation,” Ph.D Dissertation, Faculty of Graduate Studies, Univ. of Manitoba, Winnipeg, Canada, 2004.

[3] E. O. Schweitzer and B. Kasztenny, "Distance protection: Why have we started with a circle, does it matter, and what else is out there?," *2018 71st Annual Conference for Protective Relay Engineers (CPRE)*, College Station, TX, USA, 2018, pp. 1-19.

[4] N. D. Perera, “Detection , Localization , and Recognition of Faults in Transmission Networks Using Transient Currents,” Ph.D Dissertation, Faculty of Graduate Studies, Univ. of Manitoba, Winnipeg, Canada, 2012.

[5] R. Abboud and D. Dolezilek, “Time-Domain Technology – Benefits to Protection, Control, and Monitoring of Power Systems,” in *International Conference and Exhibition – Relay Protection and Automation for Electric Power Systems*, Saint-Petersburg, Russia, 2017, pp. 1–8.

[6] B. Kasztenny, J. Mazereeuw, and B. Campbell, “Phase Selection for Single-Pole Tripping :Weak Infeed Conditions and Cross-Country Faults,” *27th Annual Western Protective Relay Conference*, Spokane, WA, USA, 2000 , pp. 1-19.

[7] E. O. Schweitzer, B. Kasztenny, A. Guzmán, V. Skendzic and M. V. Mynam, "Speed of line protection - can we break free of phasor limitations?," *2015 68th Annual Conference for Protective Relay Engineers*, College Station, TX, USA, 2015, pp. 448-461.

[8] K. Babu, M. Tripathy, and A. Singh, “Recent techniques used in transmission line protection: A review,” *International Journal of Engineering, Science and Technology*, vol. 3, no. 3, pp. 1–8, 2011.

[9] M. Nagpal, M. Jensen, and M. Higginson, “TR – 81 - Protection Challenges and Practices for Interconnecting Inverter Based Resources to Utility Transmission Systems,” IEEE WG C32 Report, 2020.

[10] S. C. Johnson, J. D. Rhodes, and M. E. Webber, “Understanding the impact of non-synchronous wind and solar generation on grid stability and identifying mitigation pathways,” *Appl Energy*, vol. 262, p. 114492, Mar. 2020.

[11] K. S. Ratnam, K. Palanisamy, and G. Yang, “Future low-inertia power systems: Requirements, issues, and solutions - A review,” *Renewable and Sustainable Energy Reviews*, vol. 124, p. 109773, May 2020.

[12] A. Ulbig, T. S. Borsche, and G. Andersson, “Impact of Low Rotational Inertia on Power System Stability and Operation,” *IFAC Proceedings Volumes*, vol. 47, no. 3, pp. 7290–7297, 2014.

[13] T. S. Sidhu, D. S. Ghotra, and M. S. Sachdev, “An adaptive distance relay and its performance comparison with a fixed data window distance relay,” *IEEE Transactions on Power Delivery*, vol. 17, no. 3, pp. 691–697, Jul. 2002.

[14] H. Wang, G. Song, J. Ding and L. Yang, "Long line distance protection based on fast phasor calculation algorithm," *12th IET International Conference on Developments in Power System Protection (DPSP 2014)*, Copenhagen, Denmark, 2014, pp. 1-5.

[15] D. Finney, Z. Zhang and J. Cardenas, "Ultra fast distance protection," *10th IET International Conference on Developments in Power System Protection (DPSP 2010). Managing the Change*, Manchester, 2010, pp. 1-5.

[16] C. S. Chen, C. W. Liu, and J. A. Jiang, "Application of Combined Adaptive Fourier Filtering Technique and Fault Detector to Fast Distance Protection," *IEEE Transactions on Power Delivery*, vol. 21, no. 2, pp. 619–626, Apr. 2006.

[17] G. Benmouyal, N. Fischer and B. Smyth, "Performance comparison between Mho elements and incremental quantity-based distance elements," *2017 70th Annual Conference for Protective Relay Engineers (CPRE)*, College Station, TX, USA, 2017, pp. 1-19.

[18] H. L. Adharapurapu and R. Bhimasingu, "A novel algorithm for improving the differential protection of power transmission system," *Electric Power Systems Research*, vol. 181, p. 106183, Apr. 2020.

[19] "SEL-T400L Ultra-High-Speed Transmission Line Relay Instruction Manual", WA, USA, Schweitzer Engineering Laboratories, 2017.[Online]. Available: https://selinc.com/api/download/119049/

[20] A. H. Osman and O. P. Malik, "Transmission Line Distance Protection Based on Wavelet Transform," *IEEE Transactions on Power Delivery*, vol. 19, no. 2, pp. 515–523, Apr. 2004.

[21] R. Nandi and B. K. Panigrahi, "Detection of fault in a hybrid power system using wavelet transform," *Michael Faraday IET International Summit 2015*, Kolkata, 2015, pp. 203-206.

[22] R. Aguilar, F. Pérez, and E. Orduña, "High-speed transmission line protection using principal component analysis, a deterministic algorithm," *IET Generation, Transmission & Distribution*, vol. 5, no. 7, p. 712, 2011.

[23] E. Vazquez, J. Castruita, O. L. Chacon, and A. Conde, “A New Approach Traveling-Wave Distance Protection—Part I: Algorithm,” *IEEE Transactions on Power Delivery*, vol. 22, no. 2, pp. 795–800, Apr. 2007.

[24] M. Wen, D. Chen, and X. Yin, “A novel fast distance relay for long transmission lines,” *International Journal of Electrical Power and Energy Systems*, vol. 63, pp. 681–686, 2014.

[25] X. Qi, M. Wen, X. Yin, Z. Zhang, J. Tang, and F. Cai, “A novel fast distance relay for series compensated transmission lines,” *International Journal of Electrical Power and Energy Systems*, vol. 64, pp. 1–8, 2015.

[26] Y. Chen, M. Wen, Z. Wang, and X. Yin, “A novel instantaneous value based incremental quantities distance protection for AC transmission lines,” *International Journal of Electrical Power & Energy Systems*, vol. 135, pp. 1–15, Feb. 2022.

[27] G. Song, X. Chu, S. Gao, X. Kang, Z. Jiao, and J. Suonan, “Novel Distance Protection Based on Distributed Parameter Model for Long-Distance Transmission Lines,” *IEEE Transactions on Power Delivery*, vol. 28, no. 4, pp. 2116–2123, Oct. 2013.

[28] Y. Chen, M. Wen, Z. Wang, X. Yin, and D. Chen, “An Incremental Quantities Distance Protection Using Park’s Transformation,” *IEEE Transactions on Power Delivery*, vol. 8977, no. c, pp. 1–12, 2021.

[29] E. O. Schweitzer, B. Kasztenny, M. Mynam, A. Guzmán, and V. Skendzic, “New time-domain line protection principles and implementation,” *13th International Conference on Development in Power System Protection 2016 (DPSP)*, Edinburgh, UK, 2016, pp. 1–6.

[30] E. O. Schweitzer, B. Kasztenny and M. V. Mynam, "Performance of time-domain line protection elements on real-world faults," *2016 69th Annual Conference for Protective Relay Engineers (CPRE)*, College Station, TX, USA, 2016, pp. 1-17.

[31] B. Kasztenny, “Dependability of Transient-Based Line Protection Elements and Schemes,” in *PAC World Conference*, Glasgow, UK, 2023, pp. 1–13.

[32] H. Saadat, *Power System Analysis*. New York: McGraw-Hill, 1999.

[33] C. R. Paul, *Analysis of Multiconductor Transmission Lines*, 2nd ed. Hoboken: John Wiley & Sons Ltd, 2007.

[34] M. Steer, *Microwave and RF Design - A System Approach*. Raleigh: SciTech Publishing .INC, 2010.

[35] L. V. Bewley, *Traveling Waves on Transmission Systems*. Brooklyn: John Wiley & Sons Ltd, 1933.

[36] J. A. B. Faria and M. V. Guerreiro das Neves, “Nonuniform three-phase power lines: resonance effects due to conductor transposition,” *International Journal of Electrical Power & Energy Systems*, vol. 26, no. 2, pp. 103–110, Feb. 2004.

[37] V. Venkatasubramanian, “Tools for dynamic analysis of the general large power system using time-varying phasors,” *International Journal of Electrical Power and Energy Systems*, vol. 16, no. 6, pp. 365–376, 1994.

[38] S. R. Sanders, J. M. Noworolski, X. Z. Liu, and G. C. Verghese, “Generalized Averaging Method for Power Conversion Circuits,” *IEEE Trans Power Electron*, vol. 6, no. 2, pp. 251–259, 1991.

[39] U. D. Annakkage, C. Karawita, S. Arunprasanth, and H. Konara, “Dynamic phasor modeling of HVDC systems,” in *Modeling and Simulation of HVDC Transmission*, Institution of Engineering and Technology, 2020, pp. 213–243.

[40] M. Daryabak, S. Filizadeh, J. Jatskevich, A. Davoudi, M. Saeedifard, V. K. Sood, J. A. Martinez, D. Aliprantis, J. Cano, and A. Mehrizi-Sani, “Modeling of LCC-HVDC Systems

Using Dynamic Phasors," *IEEE Transactions on Power Delivery*, vol. 29, no. 4, pp. 1989–1998, Aug. 2014.

[41] P. Mattavelli, A. M. Stankovic and G. C. Verghese, "SSR analysis with dynamic phasor model of thyristor-controlled series capacitor," in *IEEE Transactions on Power Systems*, vol. 14, no. 1, pp. 200-208, Feb. 1999.

[42] K. M. H. K. Konara, "Interfacing a Transient Stability Model to a Real-Time Electromagnetic Transient Simulation Using Dynamic Phasors," Ph.D Dissertation, Faculty of Graduate Studies, Univ. of Manitoba, Winnipeg, Canada, 2019.

[43] A. M. Stankovic, S. R. Sanders and T. Aydin, "Dynamic phasors in modeling and analysis of unbalanced polyphase AC machines," in *IEEE Transactions on Energy Conversion*, vol. 17, no. 1, pp. 107-113, March 2002.

[44] K. Mudunkotuwa and S. Filizadeh, "Co-simulation of electrical networks by interfacing EMT and dynamic-phasor simulators," *Electric Power Systems Research*, vol. 163, pp. 423–429, Oct. 2018.

[45] B. Grcar, J. Ritonja, B. Poljzer, and M. Stankovic, A, "Estimation methods using dynamic phasors for numerical distance protection," *Generation, Transmission & Distribution, IET*, vol. 2, no. 3, pp. 433–443, 2007.

[46] V. Venkatasubramanian, H. Schattler and J. Zaborszky, "Fast time-varying phasor analysis in the balanced three-phase large electric power system," in *IEEE Transactions on Automatic Control*, vol. 40, no. 11, pp. 1975-1982, Nov. 1995.

[47] S. R. Sanders, J. M. Noworolski, X. Z. Liu and G. C. Verghese, "Generalized averaging method for power conversion circuits," in *IEEE Transactions on Power Electronics*, vol. 6, no. 2, pp. 251-259, April 1991.

[48] J. A. de la O Serna, "Dynamic phasor estimates for power system oscillations and transient detection," *2006 IEEE Power Engineering Society General Meeting*, Montreal, QC, Canada, 2006, pp. 1648–1657.

[49] J. A. de la O Serna and J. Rodríguez-Maldonado, "Taylor–Kalman–Fourier Filters for Instantaneous Oscillating Phasor and Harmonic Estimates," in *IEEE Transactions on Instrumentation and Measurement*, vol. 61, no. 4, pp. 941-951, April 2012.

[50] M. Radulovic, Z. Zecevic, and B. Krstajic, "Dynamic Phasor Estimation by Symmetric Taylor Weighted Least Square Filter," *IEEE Transactions on Power Delivery*, vol. 35, no. 2, pp. 828–836, 2020.

[51] C. Huang, X. Xie, and H. Jiang, "Dynamic Phasor Estimation Through DSTKF Under Transient Conditions," *IEEE Trans Instrum Meas*, vol. 66, no. 11, pp. 2929–2936, Nov. 2017.

[52] A. T. Munoz and J. A. de la O. Serna, "Shanks' Method for Dynamic Phasor Estimation," *IEEE Trans Instrum Meas*, vol. 57, no. 4, pp. 813–819, Apr. 2008.

[53] E. Vázquez M, A. Zamora-Mendez, M. R. Arrieta Paternina, L. A. Trujillo-Guajardo, and J. A. de la O Serna, "Dynamic phasor-driven digital distance relays protection," *Electric Power Systems Research*, vol. 184, no. September 2019, p. 106316, 2020.

[54] A. Zamora, J. M. Ramirez, M. R. Arrieta Paternina, and E. Vazquez-Martinez, "Digital filter for phasor estimation applied to distance relays," *IET Generation, Transmission and Distribution*, vol. 9, no. 14, pp. 1954–1963, 2015.

[55] D. Guillen, C. Salas, L. Fernando Sanchez-Gomez, and L. M. Castro, "Enhancement of dynamic phasor estimation-based fault location algorithms for AC transmission lines," *IET Generation, Transmission and Distribution*, vol. 14, no. 6, pp. 1091–1103, 2020.

[56] A. Zamora-Mendez, M. R. A. Paternina, M. E. Vazquez, J. M. Ramirez, and J. A. O. La De Serna, “Distance Relays Based on the Taylor-Kalman-Fourier Filter,” *IEEE Transactions on Power Delivery*, vol. 31, no. 3, pp. 928–935, 2016.

[57] J. A. De La O Serna and J. Rodríguez-Maldonado, “Instantaneous oscillating phasor estimates with TaylorK-Kalman filters,” *IEEE Transactions on Power Systems*, vol. 26, no. 4, pp. 2336–2344, 2011.

[58] S. Das and T. Sidhu, “A Simple Synchrophasor Estimation Algorithm Considering IEEE Standard C37.118.1-2011 and Protection Requirements,” *IEEE Trans Instrum Meas*, vol. 62, no. 10, pp. 2704–2715, Oct. 2013.

[59] B. Jafarpisheh, S. M. Madani, and S. Jafarpisheh, “Improved DFT-Based Phasor Estimation Algorithm Using Down-Sampling,” *IEEE Transactions on Power Delivery*, vol. 33, no. 6, pp. 3242–3245, Dec. 2018.

[60] J. K. Hwang, C. K. Song, and M. G. Jeong, “DFT-Based Phasor Estimation for Removal of the Effect of Multiple DC Components,” *IEEE Transactions on Power Delivery*, vol. 33, no. 6, pp. 2901–2909, Dec. 2018.

[61] B. R. Kumar, A. Mohapatra, and S. Chakrabarti, “A Novel Sub-Cycle-Based Method for Estimation of Decaying DC Component and Fundamental Phasor,” *IEEE Trans Instrum Meas*, vol. 70, pp. 1–10, 2021.

[62] D. Belega and D. Petri, “Dynamic synchrophasor estimation in the presence of decaying DC offsets,” in *Conference Record - IEEE Instrumentation and Measurement Technology Conference*, IEEE, 2014, pp. 502–507.

[63] G. Benmouyal, K. Zimmerman, G. Benmouyal, K. Zimmerman, and S. E. Laboratories, “Experience With Subcycle Operating Time Distance Elements in Transmission Line Digital

Relays," in *37th Annual Western Protective Relay Conference (CPRE)*, Spokane, WA, USA, 2010, pp. 1–12.

[64] D. Belega, D. Macii and D. Petri, "Fast Synchrophasor Estimation by Means of Frequency-Domain and Time-Domain Algorithms," in *IEEE Transactions on Instrumentation and Measurement*, vol. 63, no. 2, pp. 388-401, Feb. 2014.

[65] Q. Verzosa and J. Jun, "Ground Distance Relays – Understanding the Various Methods of Residual Compensation, Setting the Resistive Reach of Polygon Characteristics, and Ways of Modeling and Testing the Relay," *Methods*, vol. 1, no. 3, pp. 1–33.

[66] J. Wijekoon and A. D. Rajapakse, "Investigation of using dynamic phasors for improving the speed of distance protection," *IET Generation, Transmission & Distribution*, vol. 16, no. 16, pp. 3282–3296, Aug. 2022.

[67] U. D. Annakkage, P. G. McLaren, E. Dirks, R. P. Jayasinghe, and A. D. Parker, "A current transformer model based on the Jiles-Atherton theory of ferromagnetic hysteresis," *IEEE Transactions on Power Delivery*, vol. 15, no. 1, pp. 57–61, 2000.

[68] J. R. Lucas, "Representation of Magnetisation Curves over a Wide Region Using a Non-Integer Power Series," *The International Journal of Electrical Engineering & Education*, vol. 25, no. 4, pp. 335–340, Oct. 1988.

[69] Schneider Electric, "Easergy MiCOM P44x/EN M/Lb7 Numerical Distance Protection Relay Technical Manual" 2017. [Online]. Available: https://www.se.com/th/en/download/document/P44x_EN_M_Lb7__E1__M/

[70] ERLPhase Power Technologies Ltd., "L-PRO 4500 Transmission Line Protection Relay User Manual Version 2.0 Rev 0", 2018. [Online]. Available: https://www.erlphase.com/downloads/manuals/L_PRO_4500_manual.pdf

[71] E. Clarke, *Circuit analysis of A-C power systems*, Volume1 ed. New York: J. Wiley & Sons, 1943.

[72] G. Benmouyal, N. Fischer and B. Smyth, "Performance comparison between Mho elements and incremental quantity-based distance elements," *2017 70th Annual Conference for Protective Relay Engineers (CPRE)*, College Station, TX, USA, 2017, pp. 1-19.

[73] P. De Lima Vianna, G. Manassero, and R. R. Tiferes, “Distance Protection Functions Based on the Conic Section Equation and the Bayesian Inference: Implementation and Tests with Field Data,” in *2024 International Conference on Smart Energy Systems and Technologies (SEST)*, IEEE, Sep. 2024, pp. 1–6.

[74] Y. Chen, M. Wen, Z. Wang, X. Yin, and D. Chen, “An Incremental Quantities Distance Protection Using Park’s Transformation,” *IEEE Transactions on Power Delivery*, vol. 37, no. 4, pp. 3200–3212, Aug. 2022.

[75] O. D. Naidu, M. Krakowski and S. Zubic, "New time domain distance protection for renewable connected and series compensated transmission lines," *17th International Conference on Developments in Power System Protection (DPSP 2024)*, Manchester, UK, 2024, pp. 142-149.

[76] E. O. Schweitzer, B. Kasztenny and M. V. Mynam, "Performance of time-domain line protection elements on real-world faults," *2016 69th Annual Conference for Protective Relay Engineers (CPRE)*, College Station, TX, USA, 2016, pp. 1-17.

[77] S. Zubic, Z. Gajic and D. Kralj, "The impact of line protection operate time on circuit breaker wear," *16th International Conference on Developments in Power System Protection (DPSP 2022)*, Hybrid Conference, Newcastle, UK, 2022, pp. 404-409.

[78] G. Benmouyal and J. Roberts, “Superimposed Quantities: Their True Nature and Application in Relays,” *26th Annual Western Protective Relay Conference*, Spokane, WA, USA, 1999, pp. 1–18.

[79] G. Benmouyal and J. Mahseredjian, “A combined directional and faulted phase selector element based on incremental quantities,” *IEEE Transactions on Power Delivery*, vol. 16, no. 4, pp. 478–484, Oct. 2001.

[80] X. Dong, W. Kong and T. Cui, "Fault Classification and Faulted-Phase Selection Based on the Initial Current Traveling Wave," in *IEEE Transactions on Power Delivery*, vol. 24, no. 2, pp. 552-559, April 2009.

[81] D. Costello and K. Zimmerman, "Determining the faulted phase," *2010 63rd Annual Conference for Protective Relay Engineers*, College Station, TX, USA, 2010, pp. 1-20.

[82] E. M. Carrasco, M. P. C. Moreno, M. T. V. Martínez, and S. B. Vicente, “Improved faulted phase selection algorithm for distance protection under high penetration of renewable energies,” *Energies*, vol. 13, no. 3, pp. 1-19, 2020.

[83] A. Mahari and M. Sanaye-Pasand, "An Accelerated Single-Pole Trip Scheme for Zone-2 Faults of Distance Relays," in *IEEE Transactions on Power Delivery*, vol. 32, no. 2, pp. 678-687, April 2017.

[84] “SEL releases world’s fastest transmission line relay | Schweitzer Engineering Laboratories.” Accessed: Oct. 29, 2019. [Online]. Available: https://selinc.com/company/news/119068/

[85] Z. He, L. Fu, S. Lin and Z. Bo, "Fault Detection and Classification in EHV Transmission Line Based on Wavelet Singular Entropy," in *IEEE Transactions on Power Delivery*, vol. 25, no. 4, pp. 2156-2163, Oct. 2010.

[86] H. Livani and C. Y. Evrenosoğlu, "A Fault Classification and Localization Method for Three-Terminal Circuits Using Machine Learning," in *IEEE Transactions on Power Delivery*, vol. 28, no. 4, pp. 2282-2290, Oct. 2013.

[87] Y. Liu, D. Xie, W. Xiao, W. Wang and Y. Zheng, "Research of fault phase selection on UHV transmission lines based on wavelet analysis," *2016 International Conference on Smart Grid and Clean Energy Technologies (ICSGCE)*, Chengdu, China, 2016, pp. 284-289.

[88] N. S. D. B. Silva, K. M., B. A. Souza, "Fault Detection and Classification in Transmission Line Using Wavelet Transform and ANN," *IEEE Transactions on Power Delivery*, vol. 21, no. 4, pp. 2058–2063, 2006.

[89] A. Abdullah, "Ultrafast Transmission Line Fault Detection Using a DWT-Based ANN," in *IEEE Transactions on Industry Applications*, vol. 54, no. 2, pp. 1182-1193, March-April 2018.

[90] N. W. A. Lidula and A. D. Rajapakse, "A Pattern Recognition Approach for Detecting Power Islands Using Transient Signals—Part I: Design and Implementation," in *IEEE Transactions on Power Delivery*, vol. 25, no. 4, pp. 3070-3077, Oct. 2010.

[91] P. Jafarian and M. Sanaye-Pasand, "High-Frequency Transients-Based Protection of Multiterminal Transmission Lines Using the SVM Technique," in *IEEE Transactions on Power Delivery*, vol. 28, no. 1, pp. 188-196, Jan. 2013.

[92] A. Yadav and A. Swetapadma, "Improved first zone reach setting of artificial neural network-based directional relay for protection of double circuit transmission lines," *IET Generation, Transmission and Distribution*, vol. 8, no. 3, pp. 373–388, 2014.

[93] N. Perera and A. D. Rajapakse, "Development and Hardware Implementation of a Fault Transients Recognition System," in *IEEE Transactions on Power Delivery*, vol. 27, no. 1, pp. 40-52, Jan. 2012.

[94] A. Sharafi, M. Sanaye-Pasand, and P. Jafarian, “Ultra-high-speed protection of parallel transmission lines using current travelling waves,” *IET Generation, Transmission & Distribution*, vol. 5, no. 6, p. 656, 2011.

[95] A. I. Megahed, A. M. Moussa and A. E. Bayoumy, "Usage of wavelet transform in the protection of series-compensated transmission lines," in *IEEE Transactions on Power Delivery*, vol. 21, no. 3, pp. 1213-1221, July 2006.

[96] P. Dutta, A. Esmaeilian and M. Kezunovic, "Transmission-Line Fault Analysis Using Synchronized Sampling," in *IEEE Transactions on Power Delivery*, vol. 29, no. 2, pp. 942-950, April 2014.

[97] M. Kezunovic and B. Perunicic, "Automated transmission line fault analysis using synchronized sampling at two ends," in *IEEE Transactions on Power Systems*, vol. 11, no. 1, pp. 441-447, Feb. 1996.

[98] P. K. Maezono, E. Altman, K. Brito, V. A. dos Santos Mello Maria and F. Magrin, "Very high-resistance fault on a 525 kV transmission line - Case study," *2009 62nd Annual Conference for Protective Relay Engineers*, College Station, TX, USA, 2009, pp. 322-332.

[99] “PSCAD Knowledge Base - Type 4 Wind Turbine Generators.” Accessed: Oct. 19, 2022. [Online]. Available: https://www.pscad.com/knowledge-base/article/227

[100] S. Jiang, U. D. Annakkage, and A. M. Gole, “A platform for validation of FACTS models,” *IEEE Transactions on Power Delivery*, vol. 21, no. 01, pp. 484–491, 2006.

Appendix A – Test System with IBR

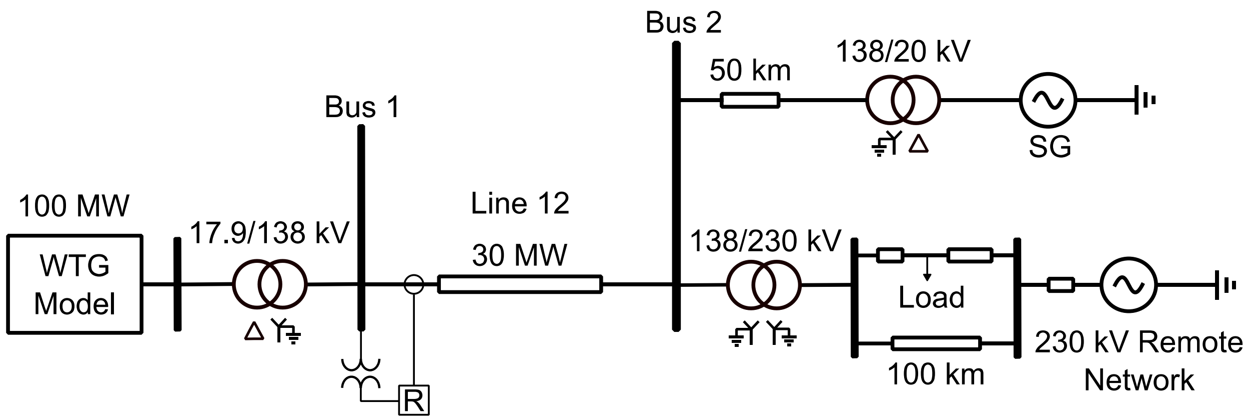

Fig A.1 Single Line Diagram of the Power System Model Used CHIL Testing of Current Transient Based Faulted Phase Selection Algorithm

Appendix B – 14 Bus System with Modified WTG

Table B.1 Transmission Line Data (230 kV, 100 MVA Base)

From Bus	To Bus	***R*** **(p.u)**	***X*** **(p.u)**	***B*** **(pu)**
2	3	0.03192	0.2601	0.5617
2	10	0.01138	0.09086	0.1829
3	4	0.03192	0.2601	0.5617
4	5	0.0114	0.0909	0.1828
4	5	0.0114	0.0909	0.1828
4	6	0.03192	0.2601	0.5617
6	10	0.03192	0.2601	0.5617
7	8	0.02940	0.3521	1.533

Table B.2 Transformer Data

From Bus	**To Bus**	***R*** **(p.u)**	***X*** **(p.u)**	**Tap Ratio**
1	2	0	0.1	10.45
4	15	0	0.025	6.96
5	7	0	0.1	1.5
5	12	0	0.1	10.45
6	11	0	0.1	10.45
8	10	0	0.1	0.67
9	10	0	0.1	10.45